Neutron and X-Ray 3D and 4D imaging of Fluid Transport within Natural and Lab-Deformed Carbonate Rocks

Mohammad Madankan

Submitted for the Degree
Doctor of Philosophy

Institute of GeoEnergy Engineering (IGE)
School of Energy, Geoscience, Infrastructure and Society (EGIS)
Heriot-Watt University
November 2021

Abstract:

Carbonate reservoir rocks are characterised by complexities in their void space caused by various processes involved in deposition and diagenesis occurring through chemical dissolution, reprecipitation, dolomitization, fracturing etc. These complexities affect the transport properties of these rocks and hinder an accurate estimation, and therefore all ensuing simulation, of their hydraulic behaviour. This PhD aims to deepen understanding of the influence of core-scale complexities of the pore system of carbonate rocks on fluid transport properties and processes. For this purpose, the complementary capabilities of X-ray and Neutron imaging along with quantitative image analysis are employed to experimentally investigate the miscible and immiscible fluid transport processes within carbonate rocks. Different types of textural variations due to the depositional and mechanical deformational features within four types of carbonate rocks, Coquina limestone, Biolithite, Travertine and Oolitic limestone are first characterised by analysing X-ray micro-CT images acquired from dry samples. Then, a series of High Speed Neutron Tomographies (HSNT) are acquired during miscible and immiscible fluid flow experiments in the selected carbonate rock samples (38mm diameter core) to explore different fluid transport processes affected by the characterised core-scale features. Image analysis techniques are employed that allow the extraction of quantitative data of pore system properties and fluid transport from the captured X-ray micro-CT images and HSNTs. The analysis on X-ray micro CT images revealed the significant influence of features like fractures, lamina or layering, layering orientation and different types of textural variations on the pore network properties like porosity, permeability, pore connectivity and tortuosity. The fluid transport processes and properties including morphology of the flow patterns, fluid speed distribution, saturation/relative concentration distribution of fluid phases, capillary heterogeneity trapping and fracture-matrix flow were resolved using the combination of HSNT and quantitative image analysis. The results also provide important insight on miscible transport processes including irregularity in the advancing fluid front and longitudinal dispersion.

To my parents, and my beloved wife.

Acknowledgement

First, I would like to express my deepest gratitude to my first supervisor, Dr Elli-Maria (Elma) Charalampidou for her dedicated support, guidance and continuous encouragement. She was always willing and enthusiastic to assist in any way she could throughout this PhD. I am also extremely thankful to my other three supervisors, Dr Helen Lewis, Dr Erika Tudisco and Dr Alessandro Tengattini for their support and guidance in every step of this PhD. I had a privileged opportunity of benefitting from the knowledge and experiences of my four valued supervisors in every step of this PhD. Special thanks to Maddi Etxegarai for providing me with the image analysis codes and training for using the experimental set-up. I am also very thankful to Prof Gary Couples for providing equipment for the experimental setup and for his consultation about experimental design. I would like to thank Dr Jim Buckman for providing the access to the Imaging Hub and Dr James Somerville for his incredible help and support in the Rock Mechanics laboratory of the Heriot-Watt University. I want to especially thank my friend, Dr Mehrdad Vasheghani Farahani for his collaboration in running the LBM simulations. The James-Watt scholarship provided by Heriot-Watt University is greatly appreciated. Also, the Neutron facilities of the Institut Laue-Langevin (ILL) in France and Helmholtz-Zentrum Berlin (HZB) in Germany are highly appreciated for allocating beam time for running the experiments of this PhD. I would like to thank once more my examiners, Dr Hannelore Derluyn and Dr Jingsheng Ma for their useful recommendations and comments that really improved the overall quality of the thesis.

I deeply thank my parents who have always been a great source of immense support and encouragement in my life. The sacrifices they have made for me are beyond any description. I am also extremely thankful to my parents-in-law for their continuous encouragement and positive energy in every step of this PhD. During my PhD years, I had the opportunity to share special moments with very nice friends in Edinburgh. I would like to thank you all, especially Hossein Doryani, Mohammad Yarali, Edris Joonaki, Mehrdad Vasheghani Farahani, Vahid Azari, Amir Heydari, Saleh Goodarzian, Omid Shahrokhi, Khosro Jarrahian, Benyamin Gorbanzadeh and Mostafa Tavana. You made my PhD life so joyful and an unforgettable experience. During my PhD, I also spent a pleasant time in my office thanks to my friendly and nice officemates, Saleh and Ilaria.

Finally, my countless appreciation goes to my wife, Parisa who have accompanied me in every single moment of this PhD adventure; from helping me in the most intensive experimental campaigns in Neutron facilities to being always happy to listen and discuss ideas related to my work. Without your endless devotion, patience and supports, I would not be able to complete this PhD. No success in the world is worth it unless I can share it with you.

HERIOT WATT UNIVERSITY

Research Thesis Submission

Please note this form should be bound into the submitted thesis.

Name:	Mohammad Madankan		
School:	School of Energy, Geoscience, Infrastructure and Society (EGIS)		
Version: *(i.e. First, Resubmission, Final)*	Final	Degree Sought:	PhD

Declaration

In accordance with the appropriate regulations I hereby submit my thesis and I declare that:

1. The thesis embodies the results of my own work and has been composed by myself
2. Where appropriate, I have made acknowledgement of the work of others
3. The thesis is the correct version for submission and is the same version as any electronic versions submitted*.
4. My thesis for the award referred to, deposited in the Heriot-Watt University Library, should be made available for loan or photocopying and be available via the Institutional Repository, subject to such conditions as the Librarian may require
5. I understand that as a student of the University I am required to abide by the Regulations of the University and to conform to its discipline.
6. I confirm that the thesis has been verified against plagiarism via an approved plagiarism detection application e.g. Turnitin.

ONLY for submissions including published works

Please note you are only required to complete the Inclusion of Published Works Form (page 2) if your thesis contains published works)

7. Where the thesis contains published outputs under Regulation 6 (9.1.2) or Regulation 43 (9) these are accompanied by a critical review which accurately describes my contribution to the research and, for multi-author outputs, a signed declaration indicating the contribution of each author (complete)
8. Inclusion of published outputs under Regulation 6 (9.1.2) or Regulation 43 (9) shall not constitute plagiarism.

* *Please note that it is the responsibility of the candidate to ensure that the correct version of the thesis is submitted.*

Signature of Candidate:		Date:	22/11/2021

Submission

Submitted By *(name in capitals)*:	MOHAMMAD MADANKAN
Signature of Individual Submitting:	
Date Submitted:	22/11/2021

For Completion in the Student Service Centre (SSC)

Limited Access	Requested	Yes		No		Approved	Yes		No	
E-thesis Submitted (***mandatory for final theses***)										
Received in the SSC by *(name in capitals)*:						Date:				

Inclusion of Published Works

Please note you are only required to complete the Inclusion of Published Works Form if your thesis contains published works under Regulation 6 (9.1.2)

Declaration

This thesis contains one or more multi-author published works. In accordance with Regulation 6 (9.1.2) I hereby declare that the contributions of each author to these publications is as follows:

Citation details	e. g. Author 1 and Author 2, Title of paper, Title of Journal, X, XX-XX (20XX)
Author 1	Contribution….
Author 2	Contribution….
Signature:	
Date:	

Citation details	e. g. Author 1 and Author 2, Title of paper, Title of Journal, X, XX-XX (20XX)
Author 1	Contribution….
Author 2	Contribution….
Signature:	
Date:	

Citation details	e. g. Author 1 and Author 2, Title of paper, Title of Journal, X, XX-XX (20XX)
Author 1	Contribution….
Author 2	Contribution….
Signature:	
Date:	

Please included additional citations as required.

Table of Contents

Chapter 1

Introduction

1.1 Background

A significant proportion of the world oil and gas and groundwater resources are found in carbonate reservoirs and aquifers. Carbonate reservoir rocks are characterised by heterogeneous texture caused by various processes involved in deposition, deformation and diagenesis occurring through chemical dissolution, reprecipitation, dolomitization, fracturing etc. The heterogeneous texture due to deposition and diagenesis plus the presence of mechanical deformation expressed via fractures and/or deformation bands add significant complexities to the void space of these rocks by introducing a wide range of pore sizes, complex pore geometry and spatial distribution of pores with different properties that control the connectivity of the pore system. These complexities may affect the determination of the transport properties of these rocks and bring many uncertainties to the estimation and simulation of their hydraulic behaviour. Thus, a good understanding of the influence of carbonate rocks pore system complexities on different fluid transport processes is crucial for an effective reservoir rock characterization.

The use of three-dimensional (3D) imaging techniques such as X-ray micro-Computed Tomography (micro-CT) and Neutron imaging has provided a great opportunity to characterise the complex structures and microstructures of the reservoir rocks and quantify the properties of their pore system in a non-destructive way. The advances in these techniques have also allowed four-dimensional (4D) imaging in which high temporal resolution is achieved to capture the dynamic processes. This provides the possibility of real time imaging of fluid transport within natural porous rocks and allows studying the interplay of the physical processes involved in fluid transport with the complex structures of carbonate rocks pore system. Most of the studies employing these techniques have focused on resolving phenomena occurring at the pore-scale during fluid flow within a few millimetre size samples. However, due to the multi-scale and heterogeneous pore structure of carbonate rocks (pore size distribution varying several orders of magnitude), obtaining representative data of the transport properties of these rocks from a small size sample is very challenging. In addition, exploring the impact of larger scale features like fractures, lamination or layering and other rock textural heterogeneity features on fluid transport is via a direct observation method requires scanning larger samples. Direct observation at the larger scale may have some limitations in terms of achieving desired temporal and spatial resolution. In order for a larger sample to be scanned, a sufficiently strong signal from the beam after it has been attenuated by passage though the object is required. Imaging with high temporal resolution that requires a shorter image acquisition time can adversely affect the image quality by reducing the signal to noise ratio. This means that the image quality is expected to be adversely affected by the lower signal to noise ratio when scanning larger samples in high temporal resolutions. Thus, the acquired images may not provide reliable data for investigating the fluid flow processes associated with the larger scale features.

The sensitivity of Neutrons to Hydrogen and its isotope, Deuterium, the very low neutron attenuation coefficient of geological materials, and the high fluxes of Neutrons available for imaging at Neutron beamline facilities, can make the Neutron imaging an ideal tool for visualising multiphase flow (of Hydrogen and Deuterium rich fluids) within rock samples of a larger size (e.g. 38mm diameter core samples in this PhD work) at a useful spatial and temporal resolution. In Neutron imaging, displacement of a Hydrogen-rich fluid like water (H_2O) or most hydrocarbon-based oils by a Deuterium-rich fluid like heavy water, D_2O (or vice versa) can be visualised thanks to the sufficient contrast between the Neutron attenuation coefficients of these two isotopes (Hydrogen and Deuterium) and liquids containing them.

The possibility of 4D Neutron tomography of miscible fluid flow in sandstone with spatial and temporal resolutions of about 200 µm and 60 second respectively, are previously presented by (Etxgarai, 2019, Tudisco et al., 2019). The obtained resolutions are lower than the few µms and few seconds of temporal resolution gained by 4D high resolution X-ray micro-CT (Van Offenwert et al., 2019; Hasan et al., 2020). However, the 4D Neutron imaging has provided the capability of scanning much larger sample (38 mm diameter core sample compared to a few mm size samples captured by X-ray micro-CT). The larger size of a scanned sample can provide a great opportunity for studying the interplay between the core-scale features (mm to cm scale features like layering and fracture) and fluid flow processes that is not possible to be investigated in a small sample using high resolution X-ray micro-CT. The trade-off between the sample size and the spatial and temporal resolution suggests the potential of complimentary use of Neutron tomography and high resolution X-ray micro-CT to better understand the transport properties of carbonate rocks with multi-scale pore system.

In this study, advantages of the complimentary capabilities of X-ray and Neutron imaging along with quantitative image analysis are taken to characterise carbonate rock samples and study the fluid transport processes. Different types of core-scale textural variation due to depositional and mechanical deformational features within the selected carbonate rocks will be first characterised by analysing the X-ray micro-CT images acquired from the dry samples. The High Speed Neutron Tomographies (HSNT) acquired during the flow experiments in carbonate rock samples (38mm diameter core samples) will be then analysed to investigate different ongoing fluid transport processes associated with the characterised core-scale features. In this study, employing the existing image analysis methods for new applications and developing new image analysis procedures offers the possibility to extract extra quantitative information of the fluid transport processes and properties from large datasets of HSNT images. Employing HSNT along with developed image analysis procedures in this study opens a new window for full-field examination of miscible and immiscible fluid displacement processes at core-scale in natural heterogeneous carbonate rocks. This allowes a quantitative investigation of the interplay between core-scale features (e.g. layering, layering orientation, fractures and anomalous textural variations) and fluid transport processes and properties including morphology of the flow patterns, irregularity (instability) in fluid front, hydrodynamic dispersion, saturation/relative concentration distribution of fluid phases, capillary heterogeneity trapping and fracture-matrix flow. The output from these analysis is combined with pore-scale characterisation of the tested samples (extracted from X-ray micro CT) to bridge the existing knowledge in pore-scale processes to macroscopic

transport observations and offer explanation for anomalous flow behaviours. The output of this study highlights the great potential of combining the pore-scale data extracted from X-ray micro-CT and full-field examination of fluid flow at core-scale (obtained from HSNT) to enhance our understanding of hydraulic behaviour of carbonates as rocks with multi-scale pore system.

1.2 Objectives

The main objective of this work is to deepen understanding of the influence of core-scale complexities of a carbonate rocks pore system on fluid transport properties and processes by means of direct and real time observation using full field techniques. This includes exploring the capability of Neutron imaging for temporally and spatially resolving the fluid transport processes at the core-scale within the carbonate rocks as well as developing new image analysis procedures to allow further quantitative data extraction from the HSNT datasets. This study aims to:

1) Characterise the carbonate rock samples in terms of textural variations due to depositional and lab-induced mechanical deformational features and their impact on pore network properties. This will be done using X-ray micro-CT and image analysis on four types of carbonate rocks including Coquina limestone, Biolithite, Travertine and Oolitic limestone. Samples with most interesting features will be chosen for flow experiments. The influence of features like fractures, layers or lamina and textural variations on the pore network properties such as porosity, porosity distribution, absolute permeability, specific surface area, pore connectivity and pore network tortuosity will be examined.

2) Capture the dynamics of fluids within the selected samples by means of HSNT during the flow experiments. The flow experiments will be performed with both miscible (water and heavy water) and immiscible (heavy water and oil) fluids. The capability of HSNT in capturing the movement of hydrogen-rich fluids (e.g. water flow in both dry and D_2O-saturated samples) in porous rocks at core-scale is shown by (Etxegarai., 2019; Tudisco et al., 2019; Tengattini et al., 2021). However, this study explores for the first time, the capability of this technique to capture oil (as a hydrogen-rich fluid) displacement by water in porous carbonate rocks at core-scale.

3) Provide quantitative measures of the fluid transport processes and their interplay with characterised core-scale features in the samples. For this purpose, quantitative image analysis will be employed and new image analysis procedures will be developed to extract information about ongoing processes captured in HSNTs. The abovementioned studies on water – heavy

water (as miscible fluids) displacement (Etxegarai., 2019; Tudisco et al., 2019) provide mainly an observation of flow patterns and quantification of fluid speed while lacking a quantification of miscible displacement processes. This thesis however, provides new image analysis procedures that allows quantitative analysis of these processes like the irregularity (instability) of the fluid front and hydrodynamic dispersion. Despite the considerable interest in miscible fluid displacement in layered porous media, the experimental studies in this fields are limited to employing conventional methods (Starr et al., 1985; Swami et al., 2013) that provide a global measurement and breakthrough curves and lack the information on local processes within the samples. However, this thesis presents, for the first time, the experimental results that reveal the processes involved in miscible fluid transport across layers of contrasting pore network properties and how they impact the longitudinal dispersion and morphology (stability) of the fluid front.

Our understanding of immiscible fluid displacement mechanisms associated with pore-scale complexities in carbonate rocks have been developed by recent uses of 3D and 4D imaging techniques (Andrew et al., 2015; S Schlüter et al., 2016; Pak, et al., 2015) however, full-field experimental studies on the influence of core-scale features on these mechanisms are lacking in the literature. In this thesis, the processes like fracture-matrix flow and residual trapping of the non-wetting phase as well as the saturation distribution of different phases at different times have been resolved with regards to characterised core-scale features. In addition, many of pore-scale experimental studies aim to improve the existing fluid flow models to better estimate the macroscopic flow anomalies in carbonate rocks (Mehmani et al., 2020). However, the full-field experimental data of macroscopic flow anomalies that can be used for evaluating the performance of these models are rare and limited to simplified 2D macro-models that does not work for correlating with modelling outputs of more complex rocks like carbonates (Zhao et al., 2019). The results from this thesis explores the capability of the HSNT for providing full-field experimental data of flow patterns in carbonate rocks that can be used for qualitative and quantitative evaluation of performance of relevant modelling methods.

1.3 Outline of the thesis

This thesis is organised into seven chapters, including the present chapter which provides a brief background and mainly introduces the scope of this work, and the next six chapters:

Chapter 2 provides a literature review. In this chapter, previous studies that have investigated carbonate rocks from the viewpoints of mechanical behaviour, their pore system

characterisation and their fluid transport properties are reviewed. Particular focus is on studies that have employed imaging techniques to study the fluid transport processes associated with different types of rock heterogeneity at pore-scale and core-scale.

Chapter 3 presents the experimental methods that have been employed to get the required data for this study focusing on the X-ray and Neutron imaging methods, their general description, advantages, limitations and the specific configuration adopted for our application. Then image processing and analysis methods used in this study to analyse the data are also described.

Chapter 4 describes the experimental procedures including the general workflow, sample preparation, mechanical testing and flow experiments. This is followed by a detailed characterisation of the material used in this work including four types of carbonate rocks. Their geological description, the textural characteristics due to depositional processes and lab-induced mechanical deformation features, their mechanical behaviour and a quantitative analysis of their pore system properties are presented.

Chapter 5 focuses on miscible fluid transport processes associated with textural variations due to depositional and mechanical deformation features at the millimetres scale (within a 38mm diameter core samples). The morphology of the flow patterns, irregularity in the advancing fluid front, fluid speed distribution, hydrodynamic dispersion and fracture-matrix flow within the sample have been examined.

Chapter 6 presents the results from immiscible fluid flow experiments carried out on intact and on mechanically deformed carbonate samples. The morphology of the flow patterns, fluid speed distribution, capillary heterogeneity trapping and saturation distribution of phases with regards to the features like layering, orientation of layering and existence of fractures are examined.

Chapter 7 includes a summary of the work carried out in this study, the key conclusions that have been made and some recommendations to be considered for further works.

Chapter 2

Literature review

Assessing the transport properties in carbonate rocks that host considerable water and hydrocarbon reservoirs is of crucial importance. The fluid flow within carbonate rocks is profoundly affected by their heterogeneous nature. In particular, their complex texture (due to depositional, burial, diagenetic and tectonic process involved) results in different textural heterogeneity characteristics at different length scales, which dramatically change the petrophysical properties of carbonates and bring many uncertainties to the simulation of their hydraulic behaviour. Characterising the impact of these complexities on fluid transport in carbonates has triggered the interest of the scientific community (Rowland., 2010; Pak et al., 2016; Menke et al., 2018). These studies can be grouped based on the length scale of the heterogeneity features that have been investigated. For example, at reservoir scale, the heterogeneity in distribution of petrophysical properties at a range of scales, from sub-metre

to 100s of metres, is focusing on assessing the reservoir quality [Rowland., 2010]. Nevertheless, a considerable proportion of studies focuses on smaller scales (core-scale and pore-scale) observations to understand the processes and mechanisms involved in flow of fluids within complex pore system of carbonate rocks aiming to further evolve existing models. In this chapter, the studies that have been carried out to characterise the complex pore system of carbonate rocks and investigate the interplay between these complexities and flow of miscible and immiscible fluids have been reviewed. A variety of experimental and numerical approaches have been employed in these studies. The particular focus will be on studies in which visualisation techniques, including X-ray and Neutron imaging, have been employed. Since fluid transport within most of the carbonate reservoirs are extremely affected by their tectonic history, studying mechanical behaviour of these rocks and how it can be linked by their flow properties is also of great importance. Therefore, some studies on hydro-mechanical behaviour of carbonate reservoir rocks are also reviewed.

A glossary of some basic terms has been included in this Chapter. These terms are used during the literature review that follows. The information in the glossary are based on the website: (https://glossary.oilfield.slb.com) (*The Schlumberger Oilfield Glossary | Oilfield Glossary*, n.d.).

2.1 Glossary of terms

- ***Wettability***: The preference of a solid to contact one liquid or gas, known as the wetting phase, rather than another.
- ***Oil-wet***: Pertaining to the preference of a solid to be in contact with an oil phase rather than a water or gas phase.
- ***Water-wet***: Describing the preference of a solid to be in contact with a water phase rather than an oil or gas phase.
- ***Wetting-phase***: The preferred liquid for a solid to contact with in presence of other liquids.
- ***Non-wetting phase***: The non-preferred liquids for a solid to contact with in presence of other liquids.
- ***Multi-phase flow***: The simultaneous flow of more than one fluid phase through a porous medium.
- ***Miscible***: Pertaining to a condition in which two or more fluids can mix in all proportions and form a single homogeneous phase.

- ***Immiscible fluids***: Pertaining to a condition in which two fluids are incapable of forming molecularly distributed mixtures or attaining homogeneity at that scale.
- ***Imbibition***: The process of absorbing a wetting phase into a porous rock.
- ***Drainage***: The process of forcing a non-wetting phase into a porous rock.
- ***Spontaneous imbibition***: Spontaneous imbibition refers to the process of absorption with no pressure driving the phase into the rock.
- ***Waterflooding***: A method of secondary recovery in which water is injected into the reservoir formation to displace residual oil.
- ***Pressure drop***: Pressure drop is defined as the difference in total pressure between two points of a fluid carrying network.
- ***Capillary pressure***: capillary pressure is defined as the pressure between two immiscible fluids occupying the same pore caused by the interactions of forces between the fluids and solid walls of the pore.
- ***Hydrodynamic Dispersion***: Hydrodynamic dispersion refers to the stretching of a solute plume in the general flow direction during its transport by an advecting fluid.
- ***Residual oil saturation***: Fraction of pore volume occupied by oil at the end of oil displacement that used a specific fluid.
- ***Relative permeability***: The relative permeability of a particular phase during multiphase flow is defined as a dimensionless measure of the effective permeability of that phase.
- ***Interfacial energy***: A property of the interface between two immiscible phases. When the phases are both liquid, it is termed interfacial tension that is the Gibbs free energy per unit area of interface at fixed temperature and pressure.
- ***Capillary number***: A dimensionless group used in analysis of fluid flow that characterizes the ratio of viscous forces to surface or interfacial tension forces.
- ***Viscous fingering***: A condition whereby the interface of two fluids, such as oil and water, bypasses sections of reservoir as it moves along, creating an uneven, or fingered, profile.

2.2 Mechanical behaviour of carbonate reservoir rocks

Mechanical deformation (natural) as a post-depositional process adds to the complexity of carbonate reservoir rocks pore system, and thus, may strongly affect the fluid flow properties within these rocks. Mechanical deformation itself can be seriously influenced by the rock heterogeneity features like different distribution of grain size, shape and arrangement as well as degree and type of cementation. Thus, a good understanding of the hydro-mechanical behaviour of carbonate rocks requires characterisation of all textural variations resulted from both depositional and diagenetic processes and any occurring deformation processes. In this section, the studies on mechanical behaviour of carbonate rocks (specially, the laboratory based mechanical deformation analysis) are reviewed. The studies on hydraulic behaviour of mechanically deformed carbonate rocks are presented in following sections.

Among the laboratory based mechanical deformation studies on carbonate rocks, those that are more relevant to our study (material and parameters under investigation) are reviewed including the studies that investigated the effect of different confining pressures (Vajdova et al., 2004; Baxevanis et al., 2006; Baud et al., 2009; Cilona et al., 2012), porosity, pore size/type (Vajdova et al., 2004; Zhu et al., 2010) and rock heterogeneity and bedding orientation (Cilona et al., 2014; X. Chen et al., 2020) on mechanical deformation in porous carbonate rocks.

The studies on the impact of confining pressure showed that by increasing confining pressure in triaxial experiments, the mechanical deformations tend to move from shear failure to compaction localisation and finally to homogeneous cataclastic flow (Renner & Rummel, 1996; Baud et al., 2009a; Cilona et al., 2014). For example in carbonate grainstone, at low confining pressures, damage in the form of cracks at grain contacts is primarily observed within the slip surface, while at high confining pressures, crack and generally grain damage diffuses along the whole volume of the sample (Cilona et al., 2012). It is also observed that at low confining pressures (5MPa) in carbonate grainstone samples, the intergranular pores within the deformation bands are filled by fine-grained material product by grain crushing and sliding while, at the highest confining pressures, intergranular pores tend to collapse by elongating themselves in the direction parallel to σ_3 (Cilona et al., 2012).

Another parameter that affects the type and mechanisms of strain localisation in carbonate rocks is rock porosity. As discussed in (Vajdova et al., 2004; Renner & Rummel, 1996) porosity exerts significant influence over the elastic, inelastic and failure properties of the carbonate rocks. It is observed that compressibility and porosity are positively correlated and brittle strength decreases with increasing porosity (Renner & Rummel, 1996). The authors in (Vajdova et al., 2004) added that the critical stresses for the onset of pore collapse under

hydrostatic and non-hydrostatic loadings also decrease with increasing porosity. They infer that mechanical twinning dominates in the more porous limestones and chalk, while dislocation slip is activated in the more compact limestones (porosities <15%). Although, deformation bands are usually expected to occur in highly porous carbonates, example of these strain localization features have been documented in a low porous platform limestone (Antonellini et al., 2014).

Apart from different porosity ranges, the question of how different porosity types can influence the development of mechanical failure in a carbonate rock has not been investigated systematically in rock mechanics (Cilona et al., 2012). In fact, different depositional environments and diagenetic processes can create complex textures and heterogeneous pore systems that can control mechanical behaviour of these rocks.

A few studies have examined the effect of cementation (Rath et al., 2011; Cilona et al., 2014; Patrick Baud et al., 2017) on mechanisms of lab-induced mechanical deformation in carbonates. Patrick Baud et al., (2017) have observed deformation bands in the less cemented samples of Leitha limestone (31% porosity) but not in more cemented ones (of 21% porosity). They suggest that increasing cementation created a more heterogeneous structure, in which compaction localization could not develop extensively. As presented in (Rath et al., 2011), the degree of cementation can significantly influence the deformation mechanism. The authors have observed that two generations of deformation bands formed before and after the main cementation of the bioclastic grainstone can be distinguished by their different deformation mechanisms, that is, dominantly grain rotation, translation, and porosity reduction for the first generation and cataclasis for the second generation of deformation bands. The authors in (Rustichelli et al., 2012) investigated the effect of sedimentological and pore network characteristics on the bed-parallel compaction localization in porous carbonate rocks (relatively shallow-water skeletal grainstones). Their results show strong influence of these features on both orientation and kinematics of deformation bands in the studied carbonates. Compaction banding may be more likely to happen in well-sorted carbonates with spherical grains. The authors also suggested a link between the depositional paleoenvironments and the sedimentological and pore network characteristics so that carbonates deposited in high-energy environments that form well-sorted, coarser-grained rocks (characterized by high intergranular macroporosity) are more prone to undergo compaction banding.

Cilona et al., (2014) have investigated the effects of rock heterogeneity and bedding orientation on compaction localization in porous carbonates. For this purpose, they conducted

series of triaxial compression experiments under a range of confining pressures (5-35 MPa) on samples cored in different orientations with respect to the bedding (i.e., perpendicular, parallel and at 45 degree). They suggest that under the same stress conditions, existence of strata (oriented oblique or perpendicular) can nucleate both compaction bands and bed-parallel compactive shear bands while in homogeneous porous carbonates, the absence of significant bedding-parallel heterogeneity can prevent the systematic development of compaction bands and result in diffuse deformation. Their experimental results also showed the strain localization tends to occur within laminae characterized by higher porosity and better sorting. From the reservoir production point of view, the authors postulated that, due to the sedimentary architecture, connectivity could increase in some portions of a reservoir if a higher effective stress would cause the formation of compactive shear band.

In other study (X. Chen et al., 2020) on the carbonate rock with heterogeneous porosity distribution, its observed that nucleation of compaction bands occurs in the highest porosity zones. As presented in this experimental study, local zones with higher porosity values trigger the initial pore collapse that is continued by a diffuse extension of compaction bands caused by loss of mechanical strength within this initially higher porosity zone. The authors have also identified a second phase transition from macroscopic solid behavior to macroscopic fluid-like behavior when the majority of macropores have collapsed.

2.3 Pore system characterisation using a range of techniques

Characterisation of a pore system has been a common tool for better understanding the hydraulic behaviour of reservoir rocks for many years. Many researchers have investigated pore network properties and how they can be linked with rocks petrophysical properties. The complexity of the pore network in carbonate rocks, resulted from their textural variation, raises the necessity of these analysis and makes this characterisation more and more difficult. A variety of techniques have been used to investigate rocks pore network properties such as mercury injection porosimetry (MIP), thin sections observed by optical microscopes and scanning electron microscopy (SEM) image analysis. In recent years, imaging techniques such as X-ray micro tomography has been commonly used to resolve the pore network complexities by imaging the 3D pore structure of the rocks down to micron and sub-micron scale. Prior to availability of this technique, 3D pore characterisation mostly relied on subjective interpretation of 2D sections of the 3D pore network (Cnudde & Boone, 2013) or, in some cases, 3D pore structure was reconstructed using statistical models from 2D thin section images (Keehm, 2004). In this section, previous studies on pore network

characterisation of sedimentary and in particularly carbonate rocks using different techniques are reviewed.

The size and size distributions of pores and pore throats are fundamental in pore network characterisation of reservoir rocks. The output of these analysis is used to interpret the transport properties of rocks (Aliakbardoust & Rahimpour-Bonab, 2013). The relation between pore throat size and permeability in carbonate rocks have been investigated, e.g., in (Rezaee et al., 2006; Gao & Hu, 2013 and references therein). In most of these studies, mercury injection porosimetry (MIP) is used to measure pore throat size distribution in the core samples. The output of MIP is a mercury injection curve in which incremental saturation of mercury is plotted as a function of injection pressure increases. As a non-wetting phase, mercury is forced to enter the pores so that pores with larger throats are penetrated by mercury earlier whereas pore with smaller throats are penetrated by mercury later (i.e., under higher hydrostatic pressures). Accordingly, the amount of porosity connected through different ranges of pore throat sizes can be determined based on mercury injection curves (Purcell, 1949). In addition to be a quick and relatively low-cost method to determine the pore/throat size distribution, the main advantage of MIP is that it can measure pores with very small size down to a few nanometers.

Thin section images analysis using an optical microscope is another method that has been extensively used by many researchers for pore network characterisation of rocks including carbonates (Ortenzi & Dichicco, 2014). This method is also used to investigate pore and throat size distributions (Wardlaw et al., 1988; Etris et al., 1988). Extracting the 2D digital image of pore spaces from the petrographic thin section allows further analysis of pore/throats size and size distribution in 2D. Wardlaw et al., (1988) have compared the pore size distribution extracted from MIP experiments and direct observation of thin section images. Their results showed that pore-size distributions obtained by porosimetry are partial distributions that do not include the larger pores in which mercury is trapped. Moreover, in this study, a larger volume fraction of smaller pores is determined by MIP than by direct observation of thin sections. Limitation of optical resolution in optical thin section analysis (to detect smaller pores) and partial withdrawal of mercury from the surface of larger pores in carbonates are considered the reasons for these differences.

X-ray tomography and image processing tools have also been used as a powerful method to determine the pore/throat size and size distribution (Arns, 2004; Shin et al., 2013). This method overcome the main limitations of MIP (lack of information on spatial distribution of pores/throats with different size) and thin section analysis (destructive method) by providing

3D investigation of pores/throats size, geometry and topology properties and their local variation within the samples in a non-destructive way. However, there are some limitations: the method is not enough to fully characterize the pore systems in low-permeability and tight rocks due to the sub-resolution pores that cannot be captured (Wu et al., 2019). Reducing the sample size as a solution to obtain higher resolution it is not always practical in carbonate rocks since it may not allow the pore network heterogeneity to be captured and it, therefore, affects the representativeness of the analysis.

To have a better understanding of the pore system from the nano-pores to macro-pores scale, higher resolution imaging techniques like scanning electron microscopy (SEM) can be a solution as they can provide information of the macro-pores and nano-pores which are not resolved in X-ray tomography images. An important issue in the 2D analysis, however, is the very small field of view (FOV) that each image can cover. Recently, thanks to improvements in technology, acquiring high-resolution images over increasingly larger areas of several square centimeters has become possible using automated image acquisition and analysis tools (James Buckman, 2014; Jim Buckman et al., 2017).

Using this technique and batch image processing, backscattered electron (BSE) images, collected from polished thin sections of carbonate samples have been employed to extract numerical quantitative data on porosity distribution at (Jim Buckman et al., 2017). The authors believe that in addition to porosity, the technique has potential for mapping other features such as pore size and geometry and the overall distribution of pore systems.

Another important pore network property that directly controls transport properties in sedimentary rocks, and in particular herein carbonate rocks, is connectivity of pores. Different approaches exist for examining pore connectivity such as determination of isolated and connected porosity, pore coordination number and connectivity density (Zambrano et al., 2017). Quantifying these parameters along with other pore network properties like specific surface area and tortuosity has been used (Zambrano et al., 2017) to understand the complexities of carbonate rock pore system and to have better estimation of their flow properties.

Variations in pores structure caused by natural deformation band have been investigated by quantifying pore network properties like porosity (connected and isolated), pore connectivity and specific surface area in carbonate grainstones by Zambrano et al., (2017) and the relation between these properties and permeability variation inside deformed zone and host rock has been explored. In their study, quantitative analysis of X-ray micro-CT images of representative volumes of rocks encompassing compaction bands provided information on

how pore network properties variation can influence the permeability variation in the sample. While the structure of the pores in the host rock depends on the morphology and size distribution of grains, in deformation bands it is controlled by cementation, dissolution, compaction and cataclastic processes. In the host rocks, direct relation between pore connectivity and permeability was observed, whereas specific surface area was inversely correlated with permeability. Within the deformed zone, significant reduction of connected porosity and pore connectivity due to the collapse or occlusion of pores creates local buffer zones or barriers to fluid flow. In the contrary direction, solution-enlarged stylolites and slip surfaces introduced connected pore networks within the deformed zone that are distributed parallel to the fault cores strike direction. These preferential conduits in one direction and the barrier role of deformed zone in perpendicular direction on the other hand may cause anisotropy in the permeability tensor within the fault zone.

Other study on the same materials (Zambrano et al., 2018) have been carried out in which fluid flow simulation based on lattice-Boltzmann method (LBM) is used to compute the permeability in different zones of the samples including host rock and deformation band. The same X-ray micro-CT images were used to extract the pore structure to be used as the input of simulation. The output of simulation is the 3D image of the flow velocity field that is used to compute the permeability. In addition to permeability calculation, effective pore network properties including effective porosity, specific surface area and geometrical tortuosity were calculated in three simulated flow directions (x, y and z) using the segmented velocity field by considering a threshold velocity value higher than zero. The effective pore network properties calculated in this way are more representative than those reported in (Zambrano et al., 2017) since they consider only the pore network that contributes to fluid flow in each flow direction x, y and z. Based on the correlative results of each pore network property and calculated permeability, the authors claimed that: permeability is controlled by the combined action of the effective porosity, the specific surface area and the tortuosity of the pore-network in the studied samples; permeability is directly related to the effective porosity, and inversely related to the specific surface area and the tortuosity.

Corbett et al., (2017) have employed porosity exponent (m) and pore-scale resistivity modelling to understand pore fabric types in Coquinas of the Morro do Chaves Formation, NE Brazil. The coquinas from this region revealed a wide range of pore sizes, pore types and pore geometry and as a result, variable pore connectivity which insert significant variation to their porosity, permeability and resulting electrical resistivity. The authors have used X-ray micro-CT to obtain information on characteristics of the pore system and to extract the pore

network of rock for 3D pore-scale resistivity modelling. Three different dominant pore types were characterized in the samples including intergranular pore, fracture-like pore that resulted in reduced porosity exponent and moldic or vuggy pore that resulted in increased porosity exponent. Also, it is found that the pore space shows a strong directional control on porosity exponent that indicates anisotropy in pore network of all tested Coquina rocks. The variation in petrophysical properties in these rocks are found to be controlled by a mutual effect of depositional fabric and diagenetic alteration.

In other studies, researchers have tried to find correlations between pore network parameters extracted from thin section images and flow properties like permeability (measured in lab before preparing of thin sections) by examining huge number of thin section images of different carbonate rocks and using artificial neural network analysis (Rabbani et al., 2017; Hossain, 2011). Developing automated image analysis tools makes it possible to extract quantitative data on pore size and shape parameters in a relatively short time. Again, the main limitation is the 2D nature of the results that cannot properly represent properties like pore connection and pore throats geometry for the 3D volume of the sample. By investigating 200 heterogeneous carbonate rocks thin section, authors in (Rabbani et al., 2017), found that permeability of carbonate rocks are acceptably predictable using pore network properties extracted from thin section images. The result of their artificial neural network analysis for estimating permeability from pore network properties showed that the average coordination number (average number of throats connected to a single pore) calculated from 2D thin section images is suitable pore network property that along with other parameters like porosity and average pore throat size can predict permeability.

A single 2D thin section image may also be used to reconstruct a 3D image of a rock sample and its pore network (Tahmasebi & Sahimi, 2012). In (Yao et al., 2015) SEM images of carbonate at three different resolutions were collected for inter-pore, intra-pore and vug (small to medium-sized cavity inside rock that usually forms isolated pore spaces) characterization. A Markov chain Monte Carlo method is used to reconstruct the digital rock in each resolution. Then, a carbonate multi-scale digital rock model was constructed based on superposition and integration of images in three different resolutions. The created model showed that this method could capture the pore size distribution, connectivity and pore topology characteristics of different scales. The authors believe that using this method allows to recognize the contributions of pores of different scale in flow properties.

The same approach (multi-scale digital rock model) is used in (Knackstedt et al., 2006) to measure the contribution of micro-porosity to the overall permeability. In this study, two

groups of carbonate rock with well connected and poorly connected macro-porous were imaged using X-ray micro CT. The results show that exploring the connectivity of the pores in different scales is crucially important when investigating the flow properties in carbonate rocks.

In another study (Pak et al., 2016), X-ray tomographies with different resolution acquired from carbonate rocks were integrated to produce a pore network model. Representativeness of different models created by combination of images at different length scale (single-scale, two-scale and three-scale) have been evaluated by comparing the simulated capillary pressure curves with experimental measurements. The results indicate that for carbonate rocks with a wide range of pore size distributions, pore network extracted from integration of two or three discrete tomographic data sets may be required in order to have reliable macroscopic flow parameters simulation.

Carbonate rock porosity is measured by multi-scale X-ray tomography analysis in (Hebert et al., 2014). X-ray images with voxel size resolutions ranging from 0.42 to 190.0 µm on sample volumes of less than 1 μm^3 to few cm^3 have been used for porosity calculation in this study. While high resolution images captured micro-porous material, lower resolution images of larger samples are used to identify vugs and millimetre-scale pore structures. The results indicate that multi-resolution X-ray tomography is a useful method for characterizing the multi-scale pore system in carbonate rocks and exploring how it can control petrophysical parameters like porosity and permeability.

2.4 Image based fluid flow analysis in carbonate rocks

Quantifying flow and transport properties through reservoir rocks which is necessary for reservoir quality evaluation requires a good understanding of the main rock and rock-fluid properties like porosity, permeability, relative permeability, capillary pressure and wettability. These properties are controlled by rock-fluid interactions that occur at the scale of individual pores of reservoir rock. Global measurements methods like gas porosimetry and permeametry, coreflooding and mercury injection capillary pressure experiments that quantify these properties, actually average all these interactions that occur at thousands of pores of the reservoir rock. In carbonate reservoirs rocks, where these interactions are controlled by the local variation of pore structures caused by the textural heterogeneity due to depositional and diagenetic processes and mechanical deformation features, a global value of rock and rock-fluid properties cannot represent and quantify the impact of these local variations and heterogeneities. As reviewed in previous section, advances in imaging and

image processing techniques have enabled us to resolve the complex pore system in carbonate rocks and quantify its properties. These techniques have also been combined with flow experiments to capture and analyse fluid flow processes within the heterogeneous carbonate rock in different length scale. This includes studies in sub-micron (pore-scale) to investigate fluid displacement mechanism involved in single and multiphase flow and in core-scale (a few cm scale) for investigating the impact of core-scale features (fractures / core-scale heterogeneity) on fluid flow.

The image-based fluid flow analysis can be divided to two groups: static and dynamic. In static analysis, images are acquired in static flow end points i.e., when displacement processes in the samples are finished. The dynamic analysis on the other hand employs real time (or syn-flow) acquisition of tomography and micro-tomography images of flow dynamic and displacement processes in pore and core-scale. In addition to the image based experimental approaches of fluid flow analysis, there are numerical methods that use the extracted pore structure image of the sample to simulate or quantify the fluid flow processes at pore-scale in complex sedimentary rocks such as carbonates. In this section, most important studies on image-based fluid flow analysis in carbonate rocks in pore-scale and core-scale have been reviewed. Due to the particular focus on neutron imaging in this thesis, studies that have employed this method are presented in an individual section.

2.4.1 Effect of core-scale features (fractures / core-scale heterogeneity)

This subsection discusses experimental studies in sedimentary rocks containing fractures (natural and artificial), presence of layering within the cores and the existence of vugs within the tested material. All above features add some extra complexity to the studied materials.

Fluid flow from fractures into matrix and in the fractures themselves, in reservoir rocks with different wettability, have been previously studied using magnetic resonance imaging, MRI (E. Aspenes et al., 2002; Ferno et al., 2007; Eirik Aspenes et al., 2008; Ersland et al., 2010). In these studies, the tested samples were designed to have an artificial fracture expressed via a gap/opening within the sample. Different orthogonal 2D cross sections of the sample (containing the artificial fracture) were produced to study the saturation evolution of different fluid phases as well as fluid flow from matrix to fracture and vice versa using MRI. This work aimed to understand mechanisms behind flow into and from fracture as a function of rocks wettability. In one of these studies, oil-wet limestone stacked cores with a 1mm artificial fracture were used (Ferno et al., 2007). A series of oil-water and water-oil flow experiments in core samples at strongly water-wet and moderately oil-wet conditions were carried out. Heavy water-brine and Decane were used as the water and oil phase, respectively, to provide

good contrast between oil and water in the MRI images (E. Aspenes et al., 2002). The results showed that during waterflooding at a strongly water-wet condition, water hydraulically displaced oil in the fracture, while no transport of oil was observed at moderately oil-wet condition and droplet of oil formed on the entire cross-sectional area of the fracture. At less water-wet condition, capillary continuity led the droplet to grow and reached to the other face of fracture in form of liquid bridges and transport the water across open fracture as depicted in figure 2.1 (E. Aspenes et al., 2002).

Presence of fractures even in the micrometer scale width has been found to be influential on waterflooding in carbonate rock by (Looyestijn et al., 2009). Waterflooding of an oil-wet carbonate rock having micro-fractures as small as 10-micron width have been investigated by means of X-ray CT scanning. Two subsequent CT-scans, which were acquired during waterflooding using NaCl and NaI brines, were subtracted to show the replaced fluid. The differential image made the fractures visible, and thus, the technique was powerful in visualising the narrow fracture network in this rock. The output 3D subtracted image revealed that water was displaced only through fractures and no fluid displacement in the rocks matrix was observed. This resulted in early breakthrough of waterflooding without any significant oil production.

The effect of core-scale heterogeneity on foam (nitrogen, N2, foam stabilized using sodium dodecyl sulfonate, SDS) flow has been investigated by (Zitha et al., 2003). In this study, core plugs of Berea Sandstone having layering parallel and perpendicular to the flow direction were flooded to investigate the impact of layering on foam displacement in samples. X-ray computed tomography captured the fluid phase saturation in different time steps after coreflooding.

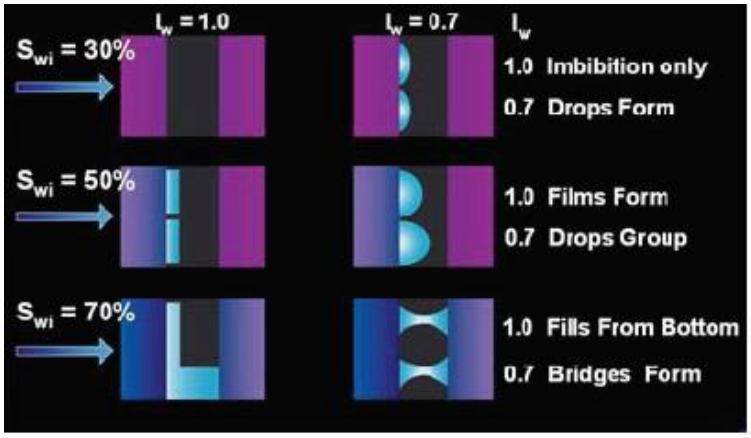

Figure 2-1 Proposed mechanism for matrix-fracture flow in different wettability condition (Aspenes et al. 2008) left: strongly water wet state where fracture starts getting saturated hydraulically when water saturation in the inlet block reaches its spontaneous imbibition endpoint (Swi=70%); right: in moderately water wet condition, liquid bridges form by water droplet growth between two blocks.

Analysis of images showed that fluid distribution patterns are completely different with regards to layering orientation. In sample with layering parallel to flow direction, faster displacing of the foam in the layers with higher permeability resulted in strong fingering pattern while in the sample with layering perpendicular to the flow direction, singular fluid distribution is observed due to capillary entrapment phenomenon. After foam breakthrough, pressure drop in the sample with perpendicular layering is much lower, which indicates lower effectiveness of foam as mobility reducer in this sample.

In another study (Olivier et al., 2005) the effects of small-scale heterogeneities (groups of vugs interbedded in a dense carbonate matrix) on waterflooding conventional methods in a vuggular carbonate rock have been investigated. X-ray CT scanning during the progression of miscible tracer front in a first-contact miscible flow has been used to image the porosity map. The permeability map was also derived from the porosity map based on a porosity-permeability correlation. The X-ray CT images acquired after injection of different pore volumes of displacing fluid show the fingering of the water front and heterogeneous saturation of different phases due to vuggular nature of pore system. The fluid saturation distribution extracted from CT images helped to understand how the water sweeps out within the heterogeneous pore system of this rock at the millimeter scale.

2.4.2 Displacement mechanisms

This subsection discusses different fluid displacement mechanisms that have been observed in carbonate rocks by employing X-ray micro-CT.

S Schlüter et al., (2016) have introduced the fluid topology, defined as the Euler characteristic of the non-wetting phase to investigate the front displacement mechanisms. High resolution images of fluid displacement obtained by fast (dynamic) X-ray tomography have been used for topology analysis and identifying the underlying displacement patterns. The results demonstrated the closing link between a topological characterization and underlying displacement pattern of two-phase immiscible fluid displacement in porous rock. Moreover, correlation between fluid topology and percolation properties can be found that helps understanding of hysteresis effects that are usually observed for the constitutive relationships between macroscopic state variables.

In another study (Pak, Butler, Geiger, Van Dijke, et al., 2015), qualitative and quantitative analysis of X-ray micro-CT images of trapped non-wetting phase (oil) in heterogeneous carbonate rock after steps of brine injection at high and low capillary numbers, has led to the identification of a previously unidentified pore-scale event. This event that has been named

"droplet fragmentation of the non-wetting phase" by the authors occurs in large pores during capillary desaturation and results in increasing volumetric production of the non-wetting phase as well as fluid-fluid interface. Multiple CT scans captured the 12.5 mm diameter carbonate core in the flow cell in static conditions after each step of injection including drainage (oil injection into the brine-saturated sample) and imbibition (brine injection into oil and brine saturated sample) with two slow and fast flow rates (10 and 700 μL/min). Cluster size distribution curves calculated based on these images show continuous increase in number of clusters while the cluster volumes decrease. This indicates that oil clusters structure changes during the drainage and imbibition processes. Small changes in the interfacial energy caused by increasing the viscous forces is identified as the reason for fragmentation of larger trapped oil droplets in large pores with higher capillary numbers that leads to this evolution of cluster size distribution.

2.4.3 Relative permeability in multiphase (immiscible) flow

This section presents some experimental studies discussing relative permeability in multiphase flow. These studies employ X-ray tomography in carbonate rocks.

Pore occupancy and relative permeability for a two-phase brine-oil steady state flow within a micro-porous carbonate rock have been investigated by(Y. Gao et al., 2019) using X-ray micro-tomography. Due to high fraction micro-porosity of this rock that are not directly resolvable in available X-ray resolution, differential imaging technique have been used to capture these pores and determine fluid pore occupancy and relative permeability. Observation of fluid occupancy in micro-porosity reveals that in addition to brine and oil occupied micro-pores, a fraction of these pores contains an intermittent phase, which is occupied either by brine or oil during the flow. The relative permeabilities of the two fluids were calculated based on measurements of the pressure differential across the sample and the saturation calculated from the images. The results indicate that the better connectivity of the pore space provided by micro-porosity in this carbonate sample resulted in a higher end-point water relative permeability and a lower residual oil saturation in comparison to a sandstone under similar conditions. In this method, relatively higher recovery (of the non-wetting phase) is observed from micro-porosity at the beginning of the waterflooding. In the macro-pore space, the intermittent phase was observed mostly in the smaller and intermediate sized pores. This experimental technique is useful in investigating multiphase flow in rocks where micro-porosity plays a crucial role in flow properties like in many carbonate rocks.

Using the same technique, a recent study on steady state brine-crude oil flow in a mixed-wet carbonate rock has been carried out(Alhammadi et al., 2020). It is observed in this study that,

at the beginning of flooding with brine (where brine was the wetting phase), brine started to flow through micro-porosity and water-wet pores. The brine relative permeability remained low at this stage. In larger macro-pores, the brine phase connectivity was poor until a high brine saturation was reached that resulted in increasing of brine relative permeability. In macro-pores scale, this can be seen as developing the connectivity of discrete clusters of the brine phase during the incremental fractional flow.

Morphological characterization of two phase flow in pore-scale as other fundamental tool for understanding the relative permeability has been presented in(Liu et al., 2017). By visualising multiphase flow during core flooding experiments using X-ray micro-computed tomography, and employing image processing tools afterwards, different fluid phase morphologies are quantified using Minkowski Functionals. In a 3D reconstructed pore network image, the Minkowski functionals can be used to describe the basic morphological properties including volume, surface area, mean curvature and Euler characteristic. Relative permeability is computed using lattice Boltzmann simulations based on the extracted pore network image of the connected phases. A Pearson product-moment correlation has been employed to evaluate the interrelationships between quantified morphological properties and computed relative permeability. The strongest correlation found is between phase volume (saturation) and relative permeability for both wetting and non-wetting phases as expected. Moreover, relative permeability of the non-wetting phase and the Euler characteristic show strong correlation.

The impact of pore size disorder on immiscible fluid flow as a function of flow rates and wettability has been investigated (Holtzman, 2016). This study presents results of time lapse images from 2D micro-model (see reference article for details) as well as corresponding numerical simulation for immiscible fluid displacement. Flow efficiency has been described based on displacement patterns (capillary fingering and front compactness) in 3 cases with different pore size disorder and in 3 different flow rate and wettability condition. The results indicate that displacement efficiency is promoted and more compactness is observed in the displacement pattern when reducing the pore size disorder that resulted in reduced fluid-fluid interfacial area. When the invading fluid is more wetting, the impact of disorder is minimized by stabilizing the invasion patterns and smoothening the interface, while increasing the flow rate led to transition from a compact front pattern to dendritic fingers.

2.4.4 Residual (trapped) non-wetting phase during immiscible fluid flow

The effect of flow rate on trapping of the non-wetting phase has been investigated at the micro-scale by means of X-ray micro-tomography (Khishvand et al., 2016). Saturation of residual oil as well as size and distribution of its disconnected globules in two rock types

(Bentheim sandstone and Gambier limestone) as a function of capillary number are investigated and presented in this study. Increase in capillary number has resulted in decreasing the residual oil saturation at the end of the imbibition and significantly altered the fluid phases distribution and also reduced the size of trapped globules. Images of pore occupancy indicate that brine imbibes into small pores when capillary number is low while increasing the brine flow rate results in some oil displacements in larger pores and reduction of residual oil saturation. However, those trapped oil clusters in the large pores that are surrounded by brine remain immobile even in higher capillary numbers. Incremental flow rate in three course of imbibition tests leads to lower saturation of residual oil but the uniform saturation distribution is only changed when the brine flow rate is very high. Actually, viscous pressure drop of the wetting phase in this test alters the order by which brine-to-oil displacements take place.

The same concept can be found in another study (Datta et al., 2014) where it is observed that the configuration of the non-wetting phase ganglia in immiscible two-phase flow dose varies for small changes of capillary numbers while increasing the capillary number to above a threshold value can mobilize large ganglia and produce it.

2.4.5 Fluid flow dynamic captured by real time X-ray tomography

Temporal resolution in imaging techniques can be a restricting factor when one wants to capture the dynamics of a process. Capturing the fluid flow processes at the pore-scale is not possible if the acquisition time for the imaging technique is longer than these processes time-scale. This is why most of the mentioned studies were limited to investigating static flow end points, when displacement processes in the samples are finished. However, thanks to high intensity synchrotron light or neutron sources, imaging with a high temporal resolution have been possible in recent years allowing real time acquisition of tomography and micro-tomography images of flow dynamic and displacement processes in pore and core-scale.

Fast X-ray micro-tomography, with temporal and spatial resolution of 30 s and a 2.2 μm/pixel, respectively, has been employed to image non-wetting cluster distribution in pore-scale during desaturation experiments in small samples (4 mm diameter and 10mm length) of sintered glass (Armstrong et al., 2014). Continuous imaging is carried out for 46 minutes during the flow with incremental flow rates. The output images were used to assess the critical capillary number by linking desaturation and pore-scale fluid topology.

In another study (Andrew et al., 2015), fast synchrotron-based X-ray micro-tomography has been used to image the injection of super-critical CO_2 into brine saturated carbonate rock

under reservoir conditions. The imaging with spatial and temporal resolution of 1.82 μm and 45 sec respectively and a field of view 4 mm x 4 mm x4 mm have been carried out in this study. Dynamic drainage events including interface recession, local and nonlocal snap-off were analysed based on output images. Changes of capillary pressure during the injection were calculated from images based on the curvature of CO_2 clusters terminal menisci. The results indicate that disconnected fluid clusters produced by local snap-off (roof snap-off) were quickly reconnected to the connected CO_2 body whereas disconnected clusters produced by nonlocal snap-off preserved their configuration.

High speed X-ray micro-tomography is capable to study reactive flow as presented in (Menke et al., 2018). In this study, impact of flow pattern heterogeneity on the limestone rocks dissolution caused by injected CO_2 saturated brine have been investigated by real time micro-tomography scanning. The same reactive flow experiments have been carried out on two size sample of each rock type. Small (1 cm length and 4mm in diameter) core samples were dynamically x-ray scanned (4 μm voxel size, 45 sec for each scan) during 90 min of reactive flow. Moreover, bigger samples (38mm in diameter) were scanned about 13 times at a coarser voxel size (27 μm) during the same reactive flow condition. The evolution of porosity caused by dissolution is captured in the output images at core-scale. Analysis of these images provides insight into the local reaction rate and its interplay with local heterogeneity as well as controlling mechanisms in millimetre and centimetre scale. Channel widening was observed at the mm scale whereas evolution of high porosity pathways due to dissolution is captured at core-scale images.

2.4.6 Solute transport in porous rock

Studying solute transport in porous rock is important for different application such as contaminant groundwater remediation. The processes and mechanisms involved in solute transport like spreading and mixing have been experimentally investigated at the centimeter scale and even at the pore-scale in natural porous rock using X-ray micro CT imaging. Van Offenwert et al., (2019) developed a new methodology to quantify transient solute concentration fields at pore-scale by employing fast laboratory-based X-ray micro CT. In this study, continuous tomography acquisition with spatial and temporal resolutions of 13.4 μm and 15 second respectively were carried out during tracer (CsCl 10 wt%) injection experiments into the samples (6 mm diameter and 20 mm length) with different degrees of pore-scale heterogeneity (porous sintered glass and Bentheimer sandstone). Tracer concentrations evolution in each individual pore that was calculated based on grey-scale evolution was used to characterise the transport by calculating the solutes arrival time and

transient (filling) time in each pore. Finally, the pore-based transient filling times and further quantifications based on experimental results, showed higher dispersion in the sandstone sample compared to the more homogeneous sintered glass sample. To reduce the impact of random noises due to the short acquisition time and using laboratory-based micro-CT scanner, Van Offenwert et al., (2019) proposed a method to average the grey-scale value of voxels over each individual pore body and calculated the averaged solute concentration for each pore rather than each voxel. They showed that coarse gridding these values per individual pore significantly lowers the uncertainty in the solute concentration data and allows using laboratory-based micro-CT scanners for high-speed imaging application.

Boon et al., (2017) have investigated the impact of rock heterogeneity on solute spreading and mixing in 76mm diameter core sample with 20cm length. They have employed X-ray CT imaging using a medical CT-scanner to spatially resolve the steady state concentration of a sodium iodide solute while flowing brine through cylindrical rock cores with increasing level of heterogeneity including Berea sandstone, Ketton and Indiana carbonates. Each scan takes approximately 10 minutes and provide a spatial resolution of 1mm (voxel size). Visualising and analysing flow structures using isoconcentration contour maps extracted from the acquired tomography images provided insight into the impact of heterogeneity on solute transport. To avoid the uncertainty in the spatially resolved concentration calculation due to the random noise in the CT-numbers produced by a given scan, Boon et al., (2016) suggested a multiple repeated scans to be performed and averaged CT-numbers to be used.

Synchrotron-based X-ray computed microtomography has been recently employed for detailed study of solute transport mechanisms at pore-scale. This method is used by Hasan et al., (2020) to characterises the transport through an unsaturated porous medium in 3D with spatial and temporal resolutions of 3.25 µm and 6 second, respectively. The very high temporal resolution allowed monitoring of fluid concentration distribution within single pores during injection of several pore volumes of fluid. Their results showed that the concentration distribution across a pore was not uniform even after injection of 17 pore volumes meaning that the common assumption of full mixing at pore bodies cannot be valid. The used experimental method shows a great capability to obtain time-variable characterization of transport in porous media.

The miscible displacement in layered porous media have been also the interest of many studies with implication to solute and contaminant transport. Experimental studies on solute transport in layered porous media are limited to those that use conventional methods to investigate the breakthrough curves of solute that provides a global measurement for the

whole sample (Starr et al., 1985; Swami et al., 2013). In addition to experimental studies, there are also numerical and analytical studies that use for instance advection-diffusion equation and consider the layered aquifer as an aquifer-aquitard system to study the solute transport in layered porous media (Tang & Aral, 1992). These measurements lack the information of local processes in the layered samples and at layers boundaries. A numerical study has also carried out to model dispersion in pore-scale by solving the point equation of flow and transport in two-dimensional pore-scale model of granular porous media with different layering configurations (Afshari et al., 2018). This study provides a 2D data of concentration distribution within sample. Despite the advances in 3D and 4D imaging techniques as reviewed in this section, employing them for investigation of miscible displacement in natural layered rocks are not reported in literature yet.

Pore-scale modelling

In addition to the image based experimental approaches for analysing fluid flow in carbonates that have been reviewed so far, there are numerical methods that use the extracted pore structure image of the sample to simulate or quantify the fluid flow processes at pore-scale in porous rocks including carbonates. A brief description of the pore-scale imaging method, underlying technologies and different numerical techniques that use these images as input to simulating single and multiphase flow have been presented in (Blunt et al., 2013). In this study, three imaging techniques used for pore-scale modeling; X-ray micro computed tomography, scanning electron microscopy and statistical reconstruction of the pore network based on high resolution 2D images and two main modeling techniques including direct modeling and network modeling have been presented. In direct modeling methods that are mostly particle-based techniques like lattice Boltzmann method (Boek & Venturoli, 2010) flow is computed directly on the pore-space image by simulating the motion and collision of particles on a grid. In pore network models, pores and throats of the rock are extracted from the pore-space image by different techniques like grain-based approaches, skeletonization (by erosion-dilation technique) and maximal ball techniques (Silin & Patzek, 2006). By assigning effective properties of size, radius, shape and connectivity to pores and throats, characterisation of flow in the extracted pore network model is possible.

A comprehensive review of the pore-scale modelling of carbonates can be found in (Mehmani et al., 2020). In this study, several methods for generating pore-scale models of carbonate rocks are described and fluid flow and solute transport simulation approaches along with advantages and limitations of each method are discussed. In another study (Zhao et al., 2019) a comprehensive comparison of pore-scale models for multiphase flow in porous media is

carried out. The authors in this study have compared the performance of different pore-scale modelling methods with the experimental data from 2D micromodels.

2.4.7 Neutron imaging

Along with development of abovementioned visualisation methods and their application in studying fluid flow in porous rocks, Neutron imaging has been evolving and matured sufficiently to be used as suitable technique for capturing hydrogen-rich fluids flow in geomaterials. Advantages of this technique over previous techniques like MRI and X-ray imaging stem from the neutrons strong attenuation by hydrogen and their relative insensitivity to metals and most of the common rock-forming elements. This allows the visualisation of transport of hydrogen-rich fluid phases in rock samples. Also, it should be noted that the Neutrons are sensitive to the isotopes of Hydrogen (e.g. Hydrogen and Deuterium) so that fluids containing these isotopes such as water (H_2O) and heavy water (D_2O) can be distinguished from each other in neutron tomography images. This allows visualising the immiscible fluid flow without needing to add dopants to the fluid phases (which are required in X-ray tomography to obtain adequate contrast). Here, we review some of most important studies in which fluid flow in porous rocks have been investigated using this technique.

One of the first application of neutron imaging of flow phenomena dates back to 1992 when Jasti & Fogler, employed neutron transmission imaging (radiography) to study dissolution, precipitation and miscible tracer dispersion in porous media. At that time, porous patterns produced by dissolution in limestone was experimentally extracted by injecting molten wood metal into the acidized porous matrix that had some limitations in preserving the delicate branches of porosity (Jasti & Fogler, 1992). High contrast that Cadmium in Wood metal could provide in neutron radiography allowed the visualisation of wood metal-filled porous media quickly and precisely. This technique allowed the fine structure of the acid etched pathways to be imaged in the limestone and showed for the first time that they can propagate against the bulk direction of flow. Advancement of miscible tracer in Berea sandstone slab with dimensions of 1.9 cm x 7.6 cm x 20.3 cm during the injection of solvent at a flow rate of 360 mL/h was also investigated using real time thermal neutron imaging. In this way, capabilities of real-time neutron imaging of flow processes with a time resolution of seconds was demonstrated. However, the analysis on the output images was limited to direct observation and some basic quantitative analysis.

Application of high-resolution neutron tomography in studying fluid distribution inside porous media has been presented in (Murison et al., 2015). In this study, neutron tomography is shown to provide sufficient resolution to allow an analysis at pore-scale level. A 6 mm

diameter pack of glass beads (365 μm diameter) with pore spaces occupied by heavy water, oil (n-hexadecane) and air was imaged at resolution of 11.8 μm voxel size. An X-ray micro-tomography of the same sample was acquired to compare with neutron tomography. The results show enough contrast between air and glass beads in X-ray image but fluid phases of heavy water and the hexadecane cannot be distinguished due to lack of contrast. On the other hand, oil and water phases can be clearly distinguished in the neutron tomography image thanks to the considerable difference between their mean grey-scale levels that is approximately 30% of the total dynamic range. The authors pointed out that the complementary information that neutron and X-ray tomography can provide, calls attention to the potential for enhanced sample characterization by employing both techniques on the same sample. However, despite the X-ray tomography being a more convenient way of imaging with high resolution in these types of application, neutron tomography is proposed as a preferable and useful tool where the multiphase flow phenomenon are known to be sensitive to the salinity and species of ions present, such as low salinity water, surfactant, and polymer flooding.

By taking advantage of neutrons ability in passing through metals (some metals are transparent to neutron beam due to their low neutron attenuation), Yehya et al., (2018) investigated the fluid flow under high pressure gradients within low-permeability concrete. Using a titanium Hassler cell that was transparent to the neutron, a high confining pressure of 50 MPa was applied and neutron radiographies and tomographies were acquired from a 7cm diameter concrete sample during the injection of water into the heavy water saturated low permeability concrete at high pressures. A series of radiographies with an exposure time of 10 s were acquired 100 minutes of the injection of H2O phase. In addition, 2-hour long neutron tomographies with 720 projections and 10 second exposure time for each radiography were acquired in some time steps while the injection was paused. To reduce the overall attenuation of the apparatus, the confining volume was minimised and heavy water was used as confining fluid inside the cell because of its significantly low neutron attenuation. For the same reason, heavy water was used as the initial pore fluid that allowed the imaging of the initial state and microstructure of the sample. After reaching the desired confining pressure, normal water injection started at 20MP, the pressure was than optimised based on the available imaging speed at the instrument. The study proved the possibility of using high neutron flux instruments to study fluid flow in low-permeability materials in reasonable time. The results obtained from concrete indicated that the waterfront surface is not homogeneous contrary to expectations.

In a recent study (Zambrano et al., 2019), the complementary properties of neutrons and X-ray experiments have been assessed to investigate the hydraulic behaviour of porous carbonates. Different techniques including dynamic neutron radiography, X-ray and neutron tomography and computational fluid dynamics simulations based on lattice-Boltzmann method have been employed to assess the water flow in two carbonate rock cores of 10mm diameter. Combination of these complementary technique provided useful results. While X-ray tomography and the lattice-Boltzmann method made the 3D analysis of pore spaces and permeability computation possible, time-lapsed neutron radiography obtained at time intervals of 90 seconds show the flow front progression during water injection into the dry sample. Images acquired from both methods were aligned and presented with the same nominal resolution (pixel size equal to 13.5 µm). Differential images obtained by subtracting neutron tomographies acquired in samples dry and saturated states shows the pores filled by water. This image is somewhat different from the pore network image extracted from the X-ray tomography of the same sample at same resolution. While some pores that are visualised in X-ray tomography are not filled with water or are partially filled in differential neutron image (indicating isolated pores), some zones show water saturation that do not correspond to the location of extracted pores from X-ray tomography. This probably reveals the existence of connected sub-resolution micro-pores contributing to the flow that are not resolved in the X-ray tomography. Although differential neutron tomography can image the water presence in these micro-pores, the structure of these pores is not clearly resolved.

Neutron imaging has been also employed to study sorption and transport of cadmium as a pollutant in porous rock (Cordonnier et al., 2019). Sensitivity of neutrons to heavy metals like cadmium, makes it ideal for this purpose. In this study, the process of primary heavy water injection into limestone and sandstone samples (5 by 5 cm cylindrical sample) followed by injection of heavy water and the cadmium tracer and finally a washing process (second injection of heavy water) was imaged by neutron tomographies. Neutron tomographies (250 µm resolution) with 650 and 900 projections were acquired resulting in a total acquisition time of 60 and 80 second respectively. Results demonstrated existence of some unwashed cadmium in most of the samples however in some zones the unwashed cadmium was maximum. It was observed that cadmium transport followed preferential pathways and locally interacted with the limestone.

The application of neutron radiography in investigating fluid flow in the rock fracture for geothermal purposes has been presented in (Bingham et al., 2015) . In this work, an engineered rectangular fracture with 1.5 mm opening was produced in a 35 mm diameter core

sample of rock (along the core sample) to simply resemble a fracture in enhanced geothermal system. Neutron radiographies (145.5 μm pixels) were acquired where the neutron direction was perpendicular to the fracture surface allowing the transmission through the fracture face and visualising water flow within this fracture. To track a single-phase water flow in the fracture, Fluorinert bubbles in water have been used and a tracked using an algorithm capable of isolating and tracking individual bubbles. Using the bubbles as tracer allows the tracking of fluid motion in the fracture. The advantage of using neutron imaging for this application is noted by the authors; Compared to X-rays, neutrons provide a higher contrast between hydrogen-rich fluids in a geothermal system and the high-density elements found in the geomaterials and in the metallic surrounding sample environment.

Water imbibition into intact and mechanically deformed sandstone samples (cylindrical sample with 40 mm diameter) captured by time-lapse neutron radiography with 5-15 second interval has been presented in (S. A. Hall et al., 2010). The radiography images that monitor the water advancement through samples are used to investigate the impact of localised deformation features in fluid flow. Direct observation of these radiographies reveals different flow advancement pattern in three sandstone including intact sample and samples deformed at 20 and 50 MPa confinement. While water advancement in the intact sample has a simple and almost planar piston-like shape, water front have been affected by shear bands in the deformed sample. In the sample with an open shear band (20 MPa confinement) water instantaneously enters into the band and quickly advance through the band and from the band into the matrix. The closed shear band in the other sample (50 MPa confinement) also gets imbibed faster than the matrix but the water front advancement within the band is slower. In this study, as a first step to further analysis of the radiographies in a quantitative way, flow front has been identified at consecutive steps of flow based on Akaikes Information Criterion, which is a technique used in seismology for picking seismic wave arrivals in seismograms. Although this technique seems to provide successful results, it was problematic to pick the more complex fronts. An attempt of performing 3D imaging of flow by acquiring radiography at different rotation angles was not successful because the fast imbibition of water made the tomographic reconstruction impossible. In fact, each radio-graph of a tomography has to be taken as fast as possible to avoid the reconstruction artefacts caused by the considerable progress of injected fluid in the sample during a single tomography but also it should be as long as it is needed for acquiring high quality signals. However, the acquired radiographies in that study were used to provide information about 3D aspects of fluid flow. It should be noted that the mentioned work is precedent to the (neutron imaging) works presented so far in this chapter in which neutron tomography with high temporal resolution was possible. It is

observed that in a capillary dominant regime, water flows faster in the shear band at outer part of the sample than in the centre. The authors have mentioned that this is probably due to a more dilatant feature of deformation close to the edges of the sample that resulted in shear bands with wider opening.

A new approach for tracking the fluid flow in deformed sandstone sample was presented later in 2013 (Stephen A. Hall, 2013). This work shows how velocity fields that provide local measurements of flow throughout the sample can be obtained based on time-lapse neutron radiographies and digital image processing. In this technique, identifying the advancement of fluid front at every time step and tracking every point along the front from one step to the next provides the time-lapse traces of the front position and streamlines connecting the points between two consecutive front positions. This technique is able to handle the highly convex and concave regions of advancing fronts. Knowing the time interval between two consecutive radiographies (time step), flow velocity is calculated and velocity field over the whole sample can be computed. Obtained velocity field based on time-lapse neutron radiographies of water imbibition in sandstone sample having a shear band demonstrated that spontaneous imbibition is faster at the bottom of the sample and decreases with height as is expected. Moreover, obvious higher flow velocity in the shear band is associated with increased micro-crack density caused by localised damage that resulted in higher capillary effect and faster imbibition. Creation of new pathways by breakdown of cements due to the localized damage is also known to be another potential reason for higher flow velocity within the shear band.

The idea of using neutron tomography coupled with 3D digital volume correlation (3D-DVC) to analyse the internal deformation field of rock samples have been presented in (Tudisco et al., 2015). The basic requirement of tomography images for using as input for 3D-DVC is having sufficient traceable internal characters. As the first important result, this work showed that neutron tomography images in the tested Bentheim sandstone can meet this requirement and 3D-DVC analysis was successfully carried out on these images. Although this analysis was previously proven to be successful using X-ray tomography images, the advantage of using neutron tomography is the neutrons capability to pass through denser material like the metals used for high pressure confining cells allowing in-situ imaging of mechanical deformation . In addition to strain localisation analysis, neutron radiography was used to capture the fluid flow (water injection into dry sample) through the same deformed sample. Results show that water flow is accelerated inside the localised deformation band that is in agreement with the observation of dilation inside the band based on strain field obtained from 3D-DVC.

In another study (Lewis et al., 2017), neutron radiography and tomography have been employed to image the flow and sequential positions of the flow within a very fine grained, low-permeability laminated carbonate rocks having a series of shear and extensional lab-induced fractures. The output images allowed the tracking of the movement of two different fluids (distilled and heavy water) through the samples complex fractures array and the mm-scale layering (laminites). By injecting the fluids from the sample base under pressure control, progression of heavy water into air-filled sample was visualized followed by the injection of distilled water. It is observed that fluid front progresses stepwise from one lamina to the next where the fracture network does not exist. On the other hand, in the fractured laminate zones, fluid enters the connected fracture network and progresses both upwards and across the sample and also moves into most of the laminae that are connected to the fracture network. The progression of heavy water is slowed down in some parts where fractures network are less well developed. It is observed that when the distilled water was injected afterward, it mainly flowed in the facture network with slight diffusion and mixing with the heavy water that previously occupied the pores.

A comprehensive review of applications of neutron imaging in the field of geomechanics can also be found in (Tengattini et al., 2021). Neutron tomography is also used for hydro-mechanical characterisation of deformed sandstone sample in (Etxegarai., 2019; Tudisco et al., 2019). Multiple experimental campaigns performed to investigate in-situ hydro-mechanical process in sandstone samples by means of neutron tomography are presented in (Etxegarai., 2019). In this work, a new image analysis tool was developed to compute the fluid flow speed field using high-speed neutron tomographies acquired during the flow experiments. This method uses a series of high-speed neutron tomography images as input and calculating the arrival time of injected fluid at every voxel of the 3D volume of sample by plotting the grey-scale evolution of that voxel during the flow experiment. In this way, front position in 3D volume at different time steps can be easily extracted and by calculating the distance between consecutive fronts and given the time elapsed between two tomography, the flow speed field is computed. This tool provided a robust way of tracking the propagating fluid front in both dry and saturated samples and calculating the corresponding 3D flow speed field. As concluded in this work, where the imbibition of water in dry sample was the key flow driving force, the higher fluid flow speed observed in the localised deformation bands can be interpreted as a consequence of smaller pore sizes in the band (higher air-water capillary pressure). On the samples with compactive shear bands and during pressure driven flow in saturated samples, it was observed that compaction features play obstacles role in the

flow, resulting in lower flow speed. This confirms the expectation of lower permeability in a compactant shear band, caused by the reduction in porosity.

Fluid front speed field obtained based on similar method for a sandstone samples having shear band was compared with the full-field strain measurements based on digital volume correlation (DVC) analysis of X-ray tomography images of the same sample acquired before and after the laboratory triaxial loading c. As concluded in this work, the localization of fluid front speed correlates well with localization of deformation meaning that the fluid front speed is higher where more deformation is observed (i.e., in the shear bands). This can likely be related to increased capillary drive due to reduced pore sizes in the band, which is consistent with the general compactant nature of the localized shear features.

High-speed neutron tomography has been also successfully used to capture the 4D evolution of water front during spontaneous imbibition tests in sandstone samples containing lab-induced shear-enhanced compaction bands (E. M. Charalampidou et al., 2017). The formation and evolution of these deformation features together with the micro-crack type mechanisms have been previously identified by means of syn-deformation Acoustic Emission locations; digital volume correlation (using pre- and post-deformation x-ray CT images) was applied to get the shear and volumetric strain fields within the tested samples (E.-M. Charalampidou et al., 2014). Shear-enhanced compaction bands appear to rapidly imbibe the water, but the frontal advancement is retarded as it was revealed by the high-speed neutron tomography images.

2.5 Summary of the existing knowledge and research gaps

The review of the previous studies in this chapter shows a good capability of the 3D and 4D imaging techniques to deepen our understanding from the internal structure of reservoir rocks and processes involved in fluid transport within them. X-ray tomography technique has been widely used to characterise the textural properties of rocks, extract and study their pore network and explore fluid transport properties of different reservoir rocks for several applications including solute transport in porous rock, enhanced oil recovery and transport/displacement of dissolved CO2. Using 4D X-ray tomography has also been more frequent in recent years that allows visualisation and quantitative analysis of the fluid displacement processes in porous rocks including carbonate rocks. However, most of studies employing this technique focus on pore-scale investigations on very small sizes samples (few mm size). In this scale, tomographs can be obtained at high temporal and spatial resolutions to achieve a good understanding of pore-scale complexities in heterogeneous rocks and how

they affect different transport processes (Andrew et al., 2015; S Schlüter et al., 2016; Pak, et al., 2015; Van Offenwert et al., 2019; Hasan et al., 2020). However, there is a trade-off between the sample size and spatial resolution of image meaning that a high resolution image that resolves pore-scale details can not reveal details of large-scale features in a larger sample. Due to a multi-scale and heterogeneous pore structure of carbonate rocks (pore size distribution varying several orders of magnitude), obtaining a representative data of the transport properties of these rocks from only pore-scale data of a small size sample is not possible. In addition, the effect of relatively larger scale anisotropic features like fractures, layering or lamina in rocks and their interplay with fluid transport processes are less investigated using 3D and 4D X-ray imaging techniques. These techniques are expected to have potential for obtaining an insight into the effects of heterogeneous and anisotropic features on spatial and temporal patterns of miscible and immiscible fluid displacement during multiphase flow in heterogeneous carbonate rocks. But, they requires scanning larger size samples that can be challenging particularly for 4D X-ray imaging technique; because a stronger beam (source) is required to achieve a high signal to noise ratio (for a good quality image) when it passes through a thicker cross section (of a larger size sample) and in a very short acquisition time. On the other hand, low Neutron attenuation of geomaterials allows Neutron beam to better pass through thicker cross section of a larger size samples.

While the early use of Neutron imaging was limited to neutron transmission imaging, in recent years Neutron Tomography and even 4D HSNT become available. Also, the advances in image processing tools for HSNT data in particular the new development of image analysis methods by Etxegarai (2019) allows quantitative analysis of HSNT data. Despite the successful use of these techniques for analysing the more homogeneous rocks like sandstones (Tudisco et al., 2019; Etxegarai., 2019) the use of these techniques to study fluid flow in more heterogeneous rocks like carbonates is rare. Also, exploring the capability of HSNT to capture oil (as another hydrogen-rich fluid) displacement in porous rocks at core-scale is not reported in literature. Therefore, the focus of this study is on using HSNT to provide a full-field examination of miscible and immiscible fluid displacement processes associated with core-scale features in natural heterogeneous carbonate rocks. This includes exploring the capability of Neutron imaging for temporally and spatially resolving the fluid transport processes at the core-scale within the carbonate rocks. The abovementioned studies on miscible fluid flow within sandstone (Etxegarai., 2019; Tudisco et al., 2019) provide mainly an observation of flow patterns and quantification of fluid speed while lacking a quantification of miscible displacement processes. This thesis however, provides new image analysis procedures that

allows quantitative analysis of these processes like the irregularity (instability) of the fluid front and hydrodynamic dispersion with regards to the core-scale features like layering.

In this thesis, the output from full-field analysis of transport processes at core scale, will be combined with pore-scale characterisation of the tested samples (extracted from X-ray micro CT) in order to bridge the existing knowledge in pore-scale processes to macroscopic transport observations and to offer explanation for anomalous flow behaviours. In fact, combination of these methods aims to enhance our understanding of hydraulic behaviour of carbonates as rocks with multi-scale heterogeneous pore system.

Chapter 3

Methods

This chapter discusses the experimental methods employed in this work to better characterise the textural features, lab-induced mechanical deformation features and fluid migration within tested carbonate rock samples at the laboratory-scale. In particular, X-ray and Neutron imaging methods are presented focusing on the general concept behind these methods, their general description, advantages, limitations and specific configuration adopted in this work. Both methods provide users with digital images, thus, image processing used in this study to analyse the acquired data is also described. For example, reconstruction and segmentation methods are presented. Image analysis aims to: a) visualise regions of interest (qualitative analysis); and b) measure and/or calculate quantities of interest (quantitative analysis). In the latter case, the concept of representative volume is discussed. Moreover, the methodology for the calculated fluid arrival time fields and fluid speed fields is presented. Finally, this chapter presents briefly the fluid flow simulations performed in parallel with the experimental data to calculate the permeability variation along a sample.

3.1 X-ray imaging

3.1.1 X-rays and their interaction with matter

X-rays are electromagnetic radiations whose wavelengths (raging between 10 and 0.01 Nm) are shorter than visible light so that they are not visible for human eye but they can pass through many materials that are opaque to light. X-rays that are discovered by Wilhelm Conrad Röntgen in 1895, are produced by sudden deceleration of fast-moving electrons due to the collision and interaction with the target anode where most energy of electrons is converted to heat and slight portion of their energy is converted to x-rays. X-rays were initially used for diagnostic medical purposes but their capability as a non-destructive method to explore the internal structure of a variety of objects opened new venues into other application such as for industrial and scientific purposes. Thus, X-rays become a common method in various research fields including Material Science (Baruchel et al., 2000), and Geosciences (recent use of X-ray tomography were reviewed in chapter 2).

When an X-ray beam interacts with matter its intensity decreases, a process named attenuation. Four dominant physical processes underlay in this attenuation of an X-ray signal: photoelectric absorption, Compton scattering, coherent (Rayleigh) scattering and pair production (Cnudde & Boone, 2013). The degree of attenuation is controlled mainly by two parameters: 1) A materials property called "linear attenuation coefficient" (μ) that is closely related to atomic number of atoms forming that material and as a result, to the materials density and 2) the distance travelled by the X-ray photons in the matter (x). The basic relationship between X-ray absorption for a monochromatic beam and these two parameter for a homogeneous material can be mathematically formulated by Beer-Lamberts law (equation 3.1) in which I_0 is the initial X-ray intensity.

Equation 3.1 $$I = I_0 \, e^{-\int \mu \, dx}$$

In cases the X-ray pass through an object that is composed of different materials, the Beer-Lambert law (equation 3.2) is used in which μ_i is the attenuation coefficient of each material i over a linear distance X_i.

Equation 3.2 $$I = I_0 \, e^{-\sum_i \mu_i x_i}$$

The probability of a photoelectric absorption is proportional to the cube of the atomic number of each element, Z. The relation between attenuation coefficient and this probability that is known as absorption cross section (σ_{pa}) can be expressed as:

Equation 3.3

$$\mu = \left(\frac{\rho_m N_A}{M}\right) \sigma_{pa}^{0}$$

where ρm is the density, N_A is Avogadros number and M is the molar mass. In an X-ray image, variation of X-ray attenuation coefficient corresponding to the scanned object is mapped. Given the direct relation between attenuation coefficient and density of materials, the map shows density variation in the material. This means that materials with different density can be distinguished in the X-ray image of an object.

3.1.2 Image acquisition

To capture an image using X-rays, a beam of X-rays that is produced by an X-ray source is projected toward the object to be scanned. The projected X-rays that pass through the object are captured behind the object using a detector. Figure 3.1 shows the schematic representation of a typical lab-based X-ray imaging setup. Depending on the objects density and thickness, a certain amount of the X-rays energy (intensity) is absorbed by the object. Given the initial intensity of the projected X-rays beam and the captured intensity of passed X-rays in the detector, the amount of X-ray signal attenuated by the object is measured and the variation of X-ray attenuation coefficient corresponding to the scanned object is mapped as a two dimensional image. This process is called projectional radiography.

Usually, some dark field and flat field radiographies are also acquired before scanning the object for further corrections on the scanned objects image. Dark fields are radiographies taken while the beam is off and flat fields are radiographies acquired when the beam is on but there is no sample in between beam and detector. The non-uniformity in the resulting dark field includes effects of non-uniformities in detector while in the flat field non-uniformity of the incident beam is also included. The acquired radiographies from the object are then subtracted from the dark and flat field images to eliminate these non-uniformities.

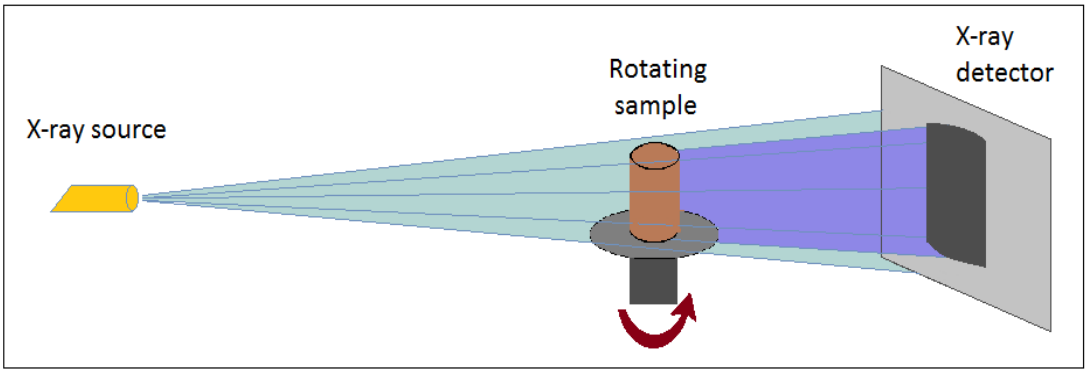

Figure 3-1 Schematic of the cone beam X-ray tomography setup

Two main X-rays sources that are commonly used for imaging purposes are Synchrotron radiation (SR) and X-ray tubes. In Synchrotron radiation sources, the electrons are accelerated in an evacuated rings of several tens of meters diameter and are steered and manipulated in a controlled way by magnets in order to produce intense beams of X-rays. X-ray tubes, as most compact X-ray sources used in lab-based imaging setups, generates X-rays beam by accelerating electrons through a potential difference (a voltage drop) and guiding them toward a target material (i.e. tungsten). The X-rays are released due to the slowdown of the incoming electrons at the target material.

In lab-based imaging setups (which are used to scan the samples in this study), X-ray tube projects the object by a fan shape beam as shown in figure 3.1 which allows geometrical magnification that is defined as the ratio between the source to detector distance and the source to object distance. By moving the sample closer to the source, higher geometrical magnification is resulted but on the other hand, the field of view becomes smaller meaning that the smaller area of the object can be covered in the detector and be captured in the image as a result. By keeping the same detector parameters (number of voxels and the distance between the centre of two neighbouring pixels in the detector) and the source to detector distance, higher geometrical magnification (smaller source to object distance) results in smaller pixel/voxel size (higher resolution) in the captured image.

Two-dimensional X-ray detectors commonly used in X-ray tomography can be divided into two main classes. In detectors with direct detection technology, the X-ray photons are directly converted to an electrical signal while in indirect detection based detectors, the X-ray photons are first converted to a visible light (using a scintillator) and then recorded using sensors like charge coupled devices (CCD). More details about common types of detectors and their elements can be found in (Graafsma & Martin, 2008).

3.1.3 X-ray Computed Tomography (CT)

As described in previous section, the projectional radiography technique projects a 3D object on a 2D detector plane, losing the information of one direction (depth). This prevent the analysis of composite object where the X-ray beam passes several different materials with variable attenuation coefficient and thicknesses. In fact, it provides a single value of attenuation of the whole path of an X-ray beam, averaging the contribution of attenuation of all materials. This problem was overcome by developing a new method called Computed Tomography (CT) in 1970s (Hounsfield, 1973; Ambrose, 1973). CT as a non-destructive technique, which allows visualization and characterization of a scanned object in three

dimensions. In this technique, by acquiring radiography images from different directions of an object, a 3D X-ray attenuation field is reconstructed using computer algorithms that corresponds to the density variation within the scanned object. In X-ray CT scanners, several radiographies are acquired during the rotational movement of either sample itself (X-ray source and detector are fixed) or the whole assembly of the X-ray source and detector (sample is fixed) over 180 or 360 degree. Improvement of CT scanners over the years has enabled us to acquire X-ray tomographies of high spatial resolution (sub-micron voxel size) commonly called micro-CT. In addition to the spatial resolution, improvement of temporal resolution in CT has provided the opportunity of 4D (3D+time) X-ray tomography as a very powerful method to investigate dynamic phenomenon at the micro-scales.

Tomographic reconstruction is the process of reconstructing 3D volumetric image of an object based on a series of 2D projection images acquired at different angles. In our application, raw X-ray intensity values are converted to the value proportional to the X-ray attenuation coefficient of the material that correspond to the grey-scale value in the generated image. Many algorithms have historically been developed for tomographic reconstruction. Among these, the back-projection is one of the most common algorithm. In this technique, the reconstruction starts with first radiography when the measured attenuation in the radiography is equally distributed along the path of the X-ray beam within the object. The model is then refined by including other radiographies in the calculations (G.-H. Chen et al., 2006). In order to fix the blurring problem that is created by standard back projection, a filtered back-projection method is commonly used. In this approach, the data are first convolved with a filter and each view is successively superimposed over a square grid at an angle corresponding to its acquisition angle (Ketcham & Carlson, 2001). Filtering refers to modifying the projection data before the back-projections process starts. A high-pass filter is particularly used for this purpose to increase the sharpness within the projections to compensate for the extra blurring caused by back-projection process (Wei et al., 2005).

The other group of algorithms are iterative reconstruction (IR) such as algebraic reconstruction technique and maximum likelihood expectation maximization (Shepp & Vardi, 1982; Gordon et al., 1970). In IR algorithms an approximated initial solution is calculated first and it is refined in multiple iteration steps that results in higher quality of reconstructed image and mitigate reconstruction artefacts at the cost of higher computation time.

The output of computed tomography might have some imperfection called artefacts that can be problematic in the data interpretation process. Many factors can cause these artefacts

including erroneous assumptions about the alignment of source, detector and rotation axis, as well as by the type of X-ray beam type (notably its polychromacity), defective detectors and high density material in the scanned object. Some artefacts can be reduced by optimising acquisition condition whereas some of them need to be corrected using various algorithms during the reconstruction. Most frequent artefacts in X-ray computed tomography for Geoscience applications including beam hardening and ring artefacts can be found in Ketcham & Carlson (2001).

Sometimes, a permanent or even temporary failure in one or more detector element (such as the disparity in efficiency of some pixels of the detector) can cause error in particular pixels of radiographies. The consistent error during a tomography results in ring shaped distribution of erroneous voxels in the reconstructed volume that is called ring artefacts. As spurious concentric rings, they are overlapped to the structure of the scanned samples and its effect on the images grey- scale makes the quantitative analysis problematic. A possible approach to reduce ring artifacts in is dark and flat field correction. Dark fields are radiographies taken while the beam is off and flat fields are radiographies acquired when the beam is on but there is no sample in between beam and detector. The non-uniformity in the resulting dark field includes effects of non-uniformities in both scintillator and CCD detector while in the flat field non-uniformity of the incident beam is also included. However, if different detector elements will have different response functions, ring artifacts will not completely be removed by the flat-field correction (Sijbers and Postnov, 2004). Moving the detector array during the acquisition is alternative solution for ring artefacts reduction (Davis & Elliott 1997) that requires special hardware.

Beam hardening is another most common artefacts that happens when scanning an object with a polychromatic beam which is the case in used X-ray CT scanners in this study. In most materials, low energy X-rays are more pronouncedly absorbed by than high energy ones. When a polychromatic X-ray beam passes the object of varying cross sectional thickness, there is higher likelihood that lower energy beams be absorbed when passing thicker part of the object due to higher interaction with the object. Thus, the beam travelled through the thicker parts of an object (like the central part of a cylindrical sample) will have higher proportion of high-energy beams (or called harder beam) compared to the beam passed through thinner parts of the object (like the edges of the cylindrical sample). In this way, higher proportion of low-energy beams detected by detector at the edges of the sample will result in higher attenuation coefficient to be calculated for this regions. Some post-processing algorithms have been developed to reduce this arteffect for different applications.

3.1.4 Facilities used

In this study, X-ray tomography of the samples were performed using lab-based cone beam X-ray tomography facilities with polychromatic beam at the Institut Laue–Langev (ILL, France), Helmholtz Zentrum Berlin (HZB, Germany), Lund University (Sweden) and Institute of GeoEnergy engineering, Heriot-Watt University (UK). List of the scanned samples in abovementioned facilities with some scanning specification are presented in table 3.1.

All these different facilities were used because of time constrain/access issues as alternative sources. However, when samples are compared before and after a process, the scanning parameters are kept constant.

3.2 Neutron imaging

3.2.1 Neutrons and their interaction with matter

The neutron is a non-charged subatomic particle discovered by J. Chadwick, (1932). Neutrons mainly interact with the nuclei of an atom rather than its electron cloud. In this interaction, neutrons can be attenuated either by being scattered or absorbed. Depending of the scattering type, coherent or incoherent, Neutron scattering data can be used for different applications. Coherent scattering in which interference between scattered Neutron waves

Table 3-1 X-ray tomography facilities and acquisition parameters for scanned samples

Rock	Sample*	facility	Voxel size (µm)	Projection numbers
Coquina	C11	ILL	42	800
	C12	ILL	42	800
	C13	ILL	52	800
	C16	Lund	50	800
	C21	ILL	47	800
	C22	Heriot-Watt	54	800
	C23	Lund	50	800
	C24	Heriot-Watt	54	800
	I	Heriot-Watt	5.5	800
	II	Heriot-Watt	5.5	800
Travertine	T11	Lund	50	800
	T21	Lund	50	800
Oolitic limestone	O15	Lund	50	800
	O27	Lund	50	800
Biolithite	B11	Lund	50	800
	B13	HZB	50	700
	B23	Lund	50	800
	B33	Lund	50	800

*All the samples and rock types will be described in chapter 4.

from different scattering centers (different atoms) provide information on the relative positions of these atoms, can be used to study structural properties of materials whereas incoherent scattering with lack of interfered scattered Neutron waves give information on the movement of the same atom in time that can be useful to trace single atom dynamics. Absorption of incident neutrons by nuclei of an atom makes the nuclei heavier put it in excited states. This can result in the creation of radioactive and unstable isotopes that starts decaying immediately by emitting a variety of secondary radiations. Such radioactive nuclei may have half-lives ranging from small fractions of a second to many years. For imaging application, similarly to X-ray imaging, the attenuation of the Neutron beam caused by absorption or scattering by the scanned object is important. Unlike X-rays, Neutrons attenuation is not dependent on the atomic number of the element, but instead varies based on particular isotope of the element (Anderson et al., 2009). For example, isotopes such as Hydrogen ($_{1}$H) and Boron ($_{10}$B) highly scatter and absorb Neutrons respectively while isotopes such as Deuterium ($_{2}$D) and Aluminum ($_{26}$Al) allow most Neutrons to pass through them. In fact, the Neutron attenuation is dependent on the probability of its interaction with atoms nuclei that is itself controlled by the total microscopic attenuation cross section of atom.

For a monochromatic beam passing through a homogeneous object, the Beer law (equation 3.1) is valid for measured Neutron intensity. The Neutron linear attenuation coefficient of material (μ) is controlled by the microscopic attenuation cross section (σ), a parameter that indicate the probability of Neutron interaction with the nuclei of atom. This parameter (σ) and as a result Neutron linear attenuation coefficient (μ) are dependent on the wavelength of incident Neutron beam (λ). Thus, for a polychromatic Neutron beam traversing a heterogeneous object with thickness τ, equation 3.1 becomes:

Equation 3.4

$$\boldsymbol{I(\lambda) = \int_{\lambda min}^{\lambda max} I_0\,(\lambda)\ \exp\left[-\sum_i \mu_i \tau_i\right] d\lambda}$$

The range of neutron wavelength available in the beamline or Neutron beam energy which depends on radiation source controls the output images contrast. The microscopic attenuation coefficient of some elements and isotopes that have been used in this study is given in table 3.2. These values are for cold neutron beam (with energy ranging from 0.0–0.025 electron Volts, eV) that is the case for our experiments.

As seen in this table, coherent and incoherent scattering are the main responsible for neutron attenuation of these elements. Based on table 3.2, in our study, the carbonate rock samples that are mainly composed of calcite ($CaCO_3$), are almost transparent to the Neutron beam due

Table 3.2 Microscopic cross section of some of the element and isotopes used in the experiments in this study for cold neutrons (E = 12.3 meV, wavelength = 3 Å). The table is from (Etxegarai, 2019)

Element/Isotope	Coherent Scattering (barn)	Incoherent Scattering (barn)	Absorption (barn)
H	1.757	80.26	0.555
D	5.592	2.050	0.001
O	4.232	0.001	0.000
Al	1.495	0.008	0.385
Ca	2.780	0.050	0.717

to their very low Neutron attenuation. On the other hand, hydrogen-rich fluids flowing through the pore spaces of our sample will strongly attenuate the Neutron beam so that contrast between these phases can be obtained. Due to the low Neutron attenuation of Deuterium, heavy water (D_2O) is used for miscible and immiscible fluid flow experiments to provide contrast against water and oil phases. Due to the low Neutron attenuation of Aluminium, it can be used to construct flow cells in experiments. Also, Aluminium does not get seriously activated while exposed to the Neutron beam. In this study, Aluminium is used to make the end caps of the flow setup to make handling (removing them from a tested sample and using them for a new sample) of the flow setup safer while being exposed to the neutron beam and to avoid scattered Neutrons from the flow setup.

3.2.2 Image acquisition

Neutron imaging have much in common with X-ray imaging in terms of fundamental acquisition process. The difference is in use of Neutron beam instead of X-ray and its different interaction with matter. Neutron attenuation is the main concept behind the neutron imaging like X-ray attenuation in X-ray imaging. Neutrons are capable to detect Hydrogen and any material containing it like Hydrogen rich fluids. On the other hand, Neutrons are able to pass through many commonly used metals like aluminium. These make the Neutrons ideal for wide range of imaging applications such as capturing Hydrogen rich fluids flow like water and oil in porous rock inside the metallic flow vessel. However, due to the difficult process of producing Neutron in enough flux required for imaging or other Neutron scattering applications, use of them is limited in the world.

Neutrons can be generated with two approaches: accelerating protons against heavy metal targets or through nuclear fission (*i.e.*, with a Nuclear Reactor). Since the energy and speed of produced Neutrons in the reactor is too high for most imaging (and other probing) purposes, the neutron beam pass through moderators. These are a medium containing light elements with high attenuation, like H2O, which are used to reduce the energy to the level

that is suitable for imaging application. This neutrons are then transported to the instruments by means of neutron guides. As shown in figure 3.2, to increase the parallelism of neutron beam, some collimation elements (a pinhole and a flight tube) are placed before the imaging instrument. The beam traverses the sample and reaches to the detector. The indirect detection based detectors are commonly used in Neutron imaging. In this system, first, the Neutron beams received at a scintillator plate are converted to visible light.

Scintillator is luminescent materials that, when excited by an incident ionising radiation, re-emit the absorbed energy in the form of visible light (Tengattini et al., 2021). Next, the resulted luminescent image in the sintilator is projected toward a CCD sensor (camera) using proper visible light optics. To avoid any damage to the camera caused by the direct exposure to the beam path, a visible light mirror is embedded in these detector system (figure 3.2) that reflect the image to the camera while protecting it from high-energy γ radiation and highly penetrating neutrons, as well as decreasing noise in the recorded images (Williams et al., 2012).

For different applications, various combination of resolution, scanning time and field of view may be desired that can be achieved by adjusting parameters like distance of the sample from the detector (l), distance between the beam and the detector (L) and the pinhole aperture diameter (D). However, not all the above-mentioned parameters may be adjustable in different beamlines. Moving the sample closer to the detector can help to gain higher spatial resolution by reducing the so-called Geometric Unsharpness, but on the other hand can increase the scattering artefacts.

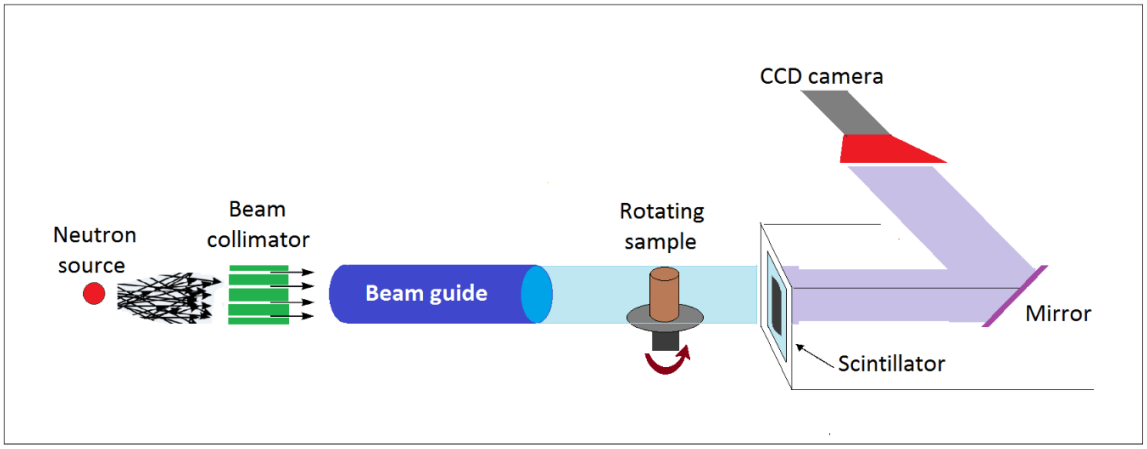

Figure 3-2 Schematic representation of a typical neutron imaging instrument

Equation 3.5 shows the relationship between these parameters and loss of spatial resolution that is quantified by Geometric Unsharpness, U_g (ASTM, 2012: E94-04, E2698).

Equation 3.5

$$U_g = l \Big/ \frac{L}{D}$$

Figure 3.3 demonstrate how decreasing the distance between the sample and the pinhole aperture cause loss of the spatial resolution by increasing Geometrical Unsharpness. Based on the equation 3.5, larger pinhole aperture diameter also cause a loss of spatial resolution. Similar to the X-ray image acquisition, some dark field and flat field radiographies are also acquired before scanning the object for further corrections on the scanned objects image.

3.2.3 Neutron Tomography and High Speed Neutron Tomography

Neutron tomography relies on similar principles as X-ray tomography, described in section (3.1.3). A series of 2D radiographs acquired at different angles during the rotation of sample is used to reconstruct the 3D volume of the scanned object. The difference is that reconstruction of Neutron imaging is done considering parallel beam geometry unlike the reconstruction of the lab-based X-ray tomography data that is based on cone beam geometry. The final output of the reconstruction, is a 3D image in which each voxel has a grey-scale value that is proportional to the Neutron attenuation at that voxel. So, voxels of pore spaces saturated with high-Neutron-attenuated water will have higher grey-scale values while voxels saturated with low-Neutron-attenuated heavy water will have low grey-scale values.

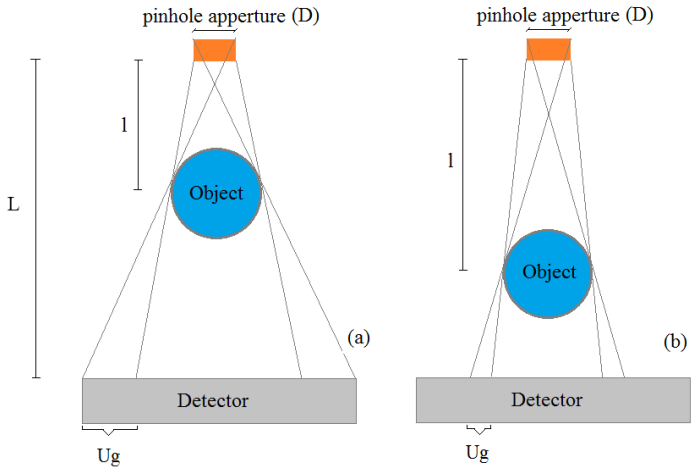

Figure 3-3 Geometrical Unsharpness; Given the constant sample size, pinhole to detector distance (L) and pinhole aperture (D), the Geometrical Unsharpness (Ug) increases by decreasing the distance between the object and pinhole (l)

Along with the image acquisition parameters (pinhole aperture, beam to detector distance and sample to detector distance) described in previous section, number of projection and exposure time are important factors in Neutron tomography that control the total time required for tomography acquisition, signal to noise ratio and quality of the reconstructed tomography images. These parameters varies for our experiments based on different test scenarios and objectives and will be presented in detail in chapter 4. In brief, two main experiment configurations were used: middle resolution Neutron tomography (MRNT) and high speed Neutron tomography (HSNT). The HSNT coupled with the flow experiments aimed to capture fluid flow in` real-time whereas MRNT is used to more carefully characterise the distribution of different fluid phases within the sample once the imposed flow is stopped and the process has stabilised, as a compromise between resolution for quantitative analysis and the stability of the process.

Defining the spatial and temporal resolution for Neutron tomography is dependent on the purpose of the study and the features and processes that need to be resolved. The spatial resolution should be high enough to provide the desired details of a feature. In fact the voxel size of the image should be adequately smaller than the size of that feature. For instance, if calculation of the volume of a sphere-shaped feature is needed, the voxels size of the image should be at least a few times smaller than the size of the sphere. The smaller the voxel size, the better the boundaries of the sphere to be resolved that result in more accurate calculation of its volume. But, there is always a trade-off between the spatial resolution and the size of the sample that can be scanned. This means that higher spatial resolutions can be achieved in a cost of reducing the sample size that might not be always a solution given the limitation imposed by the Representative Elementary Volume (REV). On the other hand, larger samples can be scanned (to allows studying larger REVs) in a cost of loosing spatial resolution. Thus, the scale (size) of the feature that needs to be resolved determines the proper spatial resolution. For a given sample size and field of view, the maximum spatial resolution can be achieved is determined by the spatial resolution (pixel size) of the detector system, distance of the sample from the detector, distance between the beam and the detector, and the pinhole aperture diameter as described before.

The similar logic applies to the temporal resolution of Neutron tomography with regards to resolving a dynamic process. The number of tomographies need to be acquired in a unit of time to resolve a given process is controlled by the speed of changes in that process. In fact, the delay between two consecutive tomographies should be less than the time at which the change in a studied parameter happens. The higher the temporal resolution, the faster the

dynamic processes that can be resolved. The maximum temporal resolution that can be achieved depends on the minimum duration that is needed for acquisition of a single tomography. There is a trade-off between the tomography acquisition time, size of the sample and the quality of the image. First, the image quality is directly controlled by the signal to noise ratio. Accordingly, the better quality image can be obtained by longer exposure time for each radiography that increases the tomography acquisition time and decreases the temporal resolution. Second, in order for a larger sample to be scanned, a sufficiently strong signal of the beam after it has been attenuated by passage though the object is required that itself needs an increased exposure time that reduces the temporal resolution accordingly. Therefore, the optimum temporal resolution is mainly determined based on the speed of the process that need to be resolved. However, the sample size and the nature of analysis that defines the required quality of the image are also other parameters that are considered in choosing the optimum temporal resolution.

Thanks to the instrumental advancement in Neutron imaging facilities in recent years including the higher resolution detectors and high speed and high quality sensors in the used cameras as well as the high flux of Neutron beam in the mentioned facilities, High Speed Neutron Tomography acquisition was possible in these facilities. This provided the opportunity of capturing the dynamic processes in 4D (3D + time) within relatively large sample (38mm diameter core sample). Compared to the Neutron imaging in the past decades that was only limited to 2D Neutron radiography (Jasti & Fogler 1992; Hall et al., 2010), 3D visualisation provide more accurate insight into internal features of the scanned sample. In a 2D radiography, the intensity value at each pixel is attributed to the average attenuation of the whole cross-sectional path that neutron beam has travelled through while, in 3D Neutron tomography every voxel in a 3D volume has a grey-scale value that represents the attenuation properties of that specific voxel (point) in the sample. Unlike the time laps Neutron radiography (Hall et al., 2010) that capture the intensity evolution over a sinlge projection (provide a series of 2D images of same projection with time), 4D Neutron imaging in this study enables us to capture the 3D morphology of flow patterns with time during the flow experiments. This allows further quantitative analysis of the fluid speed. This is crucially important in this PhD since the irregular morphology of the flow patterns in heterogeneous carbonate rocks can be investigated in 3D and with time.

In HSNT of this thesis, about 200 to 400 tomographies are acquired during the injection of fluid into sample to cover the full span of fluid entrance from inlet and its travel through the sample to reach to the outlet. In each single tomography, radiographies are acquired at

different angles while the sample is rotating over 180º. The sample actually rotates by 190˚ and only projections acquired during 180˚ rotation are used for tomography reconstruction to avoid any issues with the inhomogeneous rotation acceleration at the beginning and the end of rotation. The number of projections and the exposure time for each radiography are reduced in this configuration. Specifically, tomography acquisition has to be as fast as possible to avoid the reconstruction artefacts caused by the considerable progress of injected fluid in the sample during a single tomography. In addition, intermittent occupancy of pores with different immiscible fluid phases during a single scan, as observed by Y. Gao et al., (2019), may result in erroneous interpretation of occupying fluid in the image. The higher the speed of tomography acquisition, the lower the effect of intermittent occupancy of pores with different fluids. In our case, usually around 500 projections with 0.12 second exposure time were set for the HSNTs that results in 60 second exposure for each tomography. In such a short time, applying pixel binning on the camera is essential to improve the signal-to-noise ratio for a given frame rate of the detector. Pixel binning is the process of combining the values of adjacent CCD sensors pixels into one pixel, to reduce noise by increasing the signal-to-noise ratio in these sensors. For example, a binning 2x2 means combining the values of 4 adjacent pixels to one pixel. Obviously, this results in reducing the spatial resolution of the image by 2. At given Neutron flux and L/D ratio, samples were placed as close as approximately 3cm to the scintillator to improve the resolution but also minimize the scattered Neutrons effect. Field of view were optimised to cover whole size of the sample. By having above configuration, HSNTs with maximum spatial (voxel size) and temporal resolutions of 170 µm and 60 sec were achieved. While the spatial resolution was slightly improved compared to recent studies employing HSNT, including Cordonnier et al., 2019 (250 µm on 50 mm diameter sample) and Etxegarai, 2019 (200-220 µm for 38 mm diameter sample) the temporal resolution was similar to these studies.

MRNTs are acquired instead when there is no dynamic flow in the sample to obtain image with higher spatial resolution. While the Neutron flux, field of view and samples position was similar to the HSNT configuration, longer exposure time (2-3 sec) in MRNT allowed imaging with no binning that result in improving image quality by increasing signal to noise ratio. Number of projections in MRNT was also more than twice than in the HSNT (600 to 800 projections).

In finding the best possible configuration of the Neutron image acquisition parameters for different application, occurrence of possible artefacts should also be taken into account to have the optimal configuration for Neutron tomography. Beam hardening is one of the most

common artefacts when imaging a thick sample with a polychromatic neutron beam (R. K. V. Hassanein, 2006). Ring artefact can also happen in Neutron tomography. The mechanism of these artefact as well as ring artifact are same to ones in the X-ray tomography as described in section (3.1.3).

As presented in table 3.2, scattering of Neutrons are the main responsible for the attenuation of Neutron beam given the tested materials in our experiments. Scattered Neutrons can cause important artefact if they reach to the detector. In this case, they are counted as transmitted Neutron and result an extra intensity to be detected at the position where the scattered Neutron hits the detector. This means lower attenuation to be acquired for that position in the Neutron radiograph. When the sample has material with strong scattering cross section or located very close to the detector, there is more chance for scattered Neutrons to hit the detector. Although, different techniques have been proposed to reduce these artefacts such as reducing the water content in sample (Kim. et al., 2012), Monte Carlo modeling of point scattering functions (R. Hassanein et al., 2005) or increasing distance between the sample and detector for few centimeters (Kardjilov et al., 2005), none of them have provided a universal solution and alternative. It means that the practices for reduction of scattering artefact have to be taken into account for each particular application/beam line configuration. In our experiments, it was tried to keep approximately 3 cm distance between the sample and the detector to minimize the impact of scattered Neutrons.

3.2.4 Facilities

Neutron imaging experiments of this PhD project were carried out in European Neutron facilities including Helmholtz Zentrum Berlin, HZB (CONRAD-2 instrument) and Institute Laue-Langevin, Grenoble, ILL (NeXT-Grenoble instrument). In these facilities, Neutrons are produced in reactors BER-II and HFR, respectively, by means of fission. These are pool-typed reactors in which generated Neutrons are moderated using water and heavy water. The Neutron beam used in these imaging instruments have energies in range of cold Neutrons as shown by the spectra in figure 3.4. Comprehensive characteristics of Neutron imaging instruments and beam lines at ILL and HZB can be found in:(Tengattini et al., 2020; Kardjilov et al., 2016) respectively. Table 3.3 also presents a summary of these characteristics.

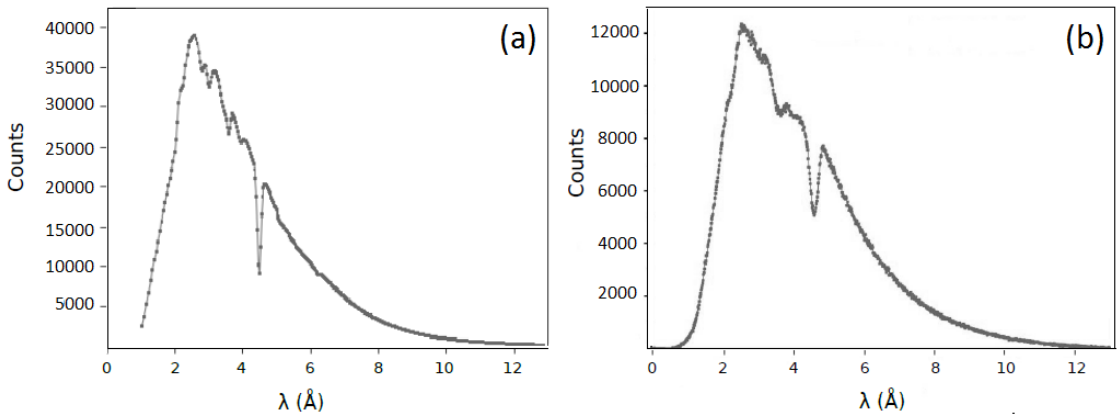

Figure 3-4 Neutron beam spectrum in NeXT Grenoble, ILL (a) and CONRAD-2, HZB (b) instruments

3.3 Image processing and image analysis

In this section we introduce the image processing and image analysis techniques employed in this work to extract qualitative (visualisation) and quantitative (metrics) information from the acquired X-ray and Neutron tomography data. These include some techniques that are commonly used in wide range of applications as well as more specific techniques used to analyse 4D Neutron tomography data.

3.3.1 Tomography reconstruction (pre-processing)

Tomographic reconstruction is the process of reconstructing 3D volumetric image of an object based on a series of 2D projection images acquired at different angles. The fundamental of tomography reconstruction is presented in section (3.1.3), but some technical details about the tools used for reconstruction of the tomographic data in this study is provided here.

In this study, X-rays tomography data were reconstructed with commercial software Octopus (at HZB) and X-act software (at ILL and Heriot-Watt). MRNTs were also reconstructed using XAct software. In both tools it is essential to input the correct horizontal (X) and vertical (Y) offsets and vertical axis tilt of the rotation axis. Multiple slices can be reconstructed varying these parameters to find the optimal parameter set. One by one reconstruction of HSNTs were

Table 3.3 Neutron imaging instruments and their beam lines specifications

Facility/ instrument	Reactor Power (MW)	Flux "on sample" (n cm−2 s−1)	L/D	Voxel size (μm)	Field of view (cm x cm)
ILL	58.3	3×10^8	167	85	60 x 73
HZB	10	2.4×10^7	330	85	50 x 50

time-consuming due to the large numbers of tomographies acquired for each sample (200 to 400 tomographies).

The HSNTs acquired at ILL were reconstructed using XAct. For reconstruction of HSNTs acquired at HZB, an in house code written by (Etxegarai, 2019), and based on the open source code reconstruction software Astra (van Aarle et al., 2015) were used. In this code, first, all rariographies are corrected by dark and flat field images that were acquired at the beginning of HSNT of each sample. Then attenuation coefficient is computed for radiographies and used as input of Asrta toolbox. Finally, the values of the X and Y offsets well as tilt of the rotation axis are iteratively optimised before completing the reconstruction. More details on the code workflow can be found in (Etxegarai, 2019).

3.3.2 Qualitative analysis, 2D and 3D Visualisation

Direct observation of the reconstructed image is a simple way of sample characterization and even powerful analysis tool still for some application. In this study, reconstructed X-ray tomographies and some Neutron tomographies are visualized in 3D and 2D vertical and horizontal slices in different orientation using volume rendering and ortho-slice modules of commercial Avizo software to directly observe and display properties of interest in different regions of the samples. A general idea of textural features like approximate grain size, shape and arrangement and spatial variation of these parameters in the studied sample are of some useful information that can be obtained from direct observation of X-ray tomography data. In addition, distribution of void spaces in 3D can be qualitatively investigated. Visualisation of Neutron tomography data acquired in different time steps during flow experiments also can provide a general insight of the distribution of different fluid phases in the samples. Visual correlation between some features observed in the X-ray tomography images such as sedimentary structures (layers) or lab induced mechanical deformation features (fracture) and the captured fluid flow patterns in the HSNT data is the first step in interpretation of observations.

3.3.3 Pore system characterisation

In addition to the qualitative analysis, quantitative analysis is required for accurate and detailed characterisation of the pore system in tested samples. Quantitative analysis on the X-ray tomography data starts from extracting the pore network image (performed after the segmentation process) and employs different methods to calculate the properties of interest. In this section, a detailed description of methods used for image segmentation is provided along with comparing different methods, their advantages and limitations. Then, different

methods and algorithms used to compute pore network properties including porosity, specific surface area, pores connectivity and tortuosity are presented in this section together with the underlying logic of using them and their limitation.

3.3.3.1 Image segmentation

Reconstructed X-ray tomographies are used for qualitative and quantitative characterisation of samples texture, deformation and pore system. As first step for further quantitative analysis on the samples pore system, the 3D pore network image needs to be extracted from the tomographies by image segmentation. Segmentation that is defined as process of classifying pixels into different classes is a fundamental and crucial step in image processing as it controls the accuracy and reliability of the quantitative image analysis. There are several methods and techniques for image segmentation. A review of these methods and algorithms can be found in Kang et al. (2009). Each method applies to some types of materials and images and may have limits in other cases. Iassonov et al., (2009) reviewed the methods applied for segmentation of X-ray computed tomography images of porous materials.

First group of methods rely on global thresholding meaning that they segment the whole image by identifying a threshold value. This threshold value is determined in different way in various methods of this group. For example, histogram shape based thresholding method determine the threshold by geometrical analysis of the histogram shape (Zack et al., 1977). The Otsu method (Otsu, 1979) as a commonly used clustering based thresholding methods uses combination of statistical approaches to finds the threshold value that maximise the variance between the means of two groups of separated voxels while minimizes the variance within each group. The threshold value can also be determined manually based on the subjective visual examination of the grey-scale image.

The other group of segmentation methods that has been commonly used to segment the porous material particularly for geoscience application is watershed segmentation (Andrew et al., 2014; Alhosani et al., 2019; Garfi et al., 2020). The watershed algorithm treats the grey-scale value of each pixel or voxel as a magnitude, usually referred to height value in topographic maps (Beucher & Meyer, 1993). The algorithm then finds the watershed lines that run along the tops of ridges by connecting the pixels or voxels of largest values. It start expanding the classes (phases) from pre-defined markers (seeds) by flooding these seeds until the expanding boundary of each phase reaches to the watershed lines. The process resemble the condition that water filling basins during flooding. The watershed segmentation can be used for segmentation of multiple phases by defining multiple seeds.

Another group of image segmentation methods that has been recently emerged as powerful tools to include part of human knowledge in the segmentation process and improve the accuracy of the labeled regions are those using machine learning algorithms. Trainable Weka segmentation (TWS) method (Arganda-Carreras et al., 2017) is one of the most recent example that has outperformed other traditional segmentation methods particularly in the case of high noise levels of images (Berg et al., 2018). The concept behind this method is the generation of multiple modalities of the original image by applying nonlinear filters(Garfi et al., 2020). In this method, classifiers are trained based on user generated training data. The training of classifiers are on the basis of combination of selected features. Trained classifiers are then applied on whole image automatically to create segmented image.

In this study, we examined the performance of four different method for segmenting X-ray tomography images of the Coquina rock. The aim was to choose the segmentation method that provides the best quality of segmented image and retain as much detail as possible while be robust enough to the image noises. The methods used were Otsu global thresholding, manual global thresholding, watershed segmentation and trainable Weka segmentation. The X-ray tomography images were filtered before applying segmentation algorithms, unless for trainable Weka segmentation, as it was found by (Berg et al., 2018) that this method is more robust to image noises and artefacts compared to other segmentation methods. Among the variety of available filters, non-local means filtering algorithm was applied to the images prior to the use of Otsu thresholding, manual thresholding and watershed segmentation as this filter has shown the capability of reducing image noise without sacrificing the sharpness of phase boundaries (Steffen Schlüter et al., 2014). For this purpose, the available filtering module in Thermofisher Avizo Fire 9.1 was employed while a small similarity value (0.3) was chosen to avoid over-smoothening of the image.

The Trainable Weka Segmentation and Otsu global thresholding were carried out using the available plugins in ImageJ software. In TWS, classifiers were trained based on the input provided by drawing lines on different phases like pores and grains and by choosing the mean and variance of each voxel as training features. After applying the trained classifiers to the whole image, the quality of the segmented image was regularly checked and improved by overlaying transparent segmented and original image and amending the input data. The Otsu global thresholding was performed automatically without any manual input. Watershed segmentation and manual global thresholding were performed using watershed segmentation and interactive thresholding modules of Thermofisher Avizo Fire 9.1 software respectively. In manual thresholding, the threshold was found by applying different threshold values on

the histogram of the image while interactively checking the quality of the result (segmented image) by visual inspection. In watershed segmentation, three input values including the number of the phases and the threshold values defining the seeds for each phase were provided to the software while the gradient magnitude defining phase boundaries was automatically calculated by the software.

Here, the results from applying the four segmentation methods on a 2D slice of X-ray tomography image (5 µm voxel size) are provided. Figure 3.5 shows the original grey-scale image and the segmented images using different methods. As seen in these images (and the images from a zoomed area), the output of watershed segmentation method is lacking some details of the pore spaces (for example the micro-fracture within grain) while the output of

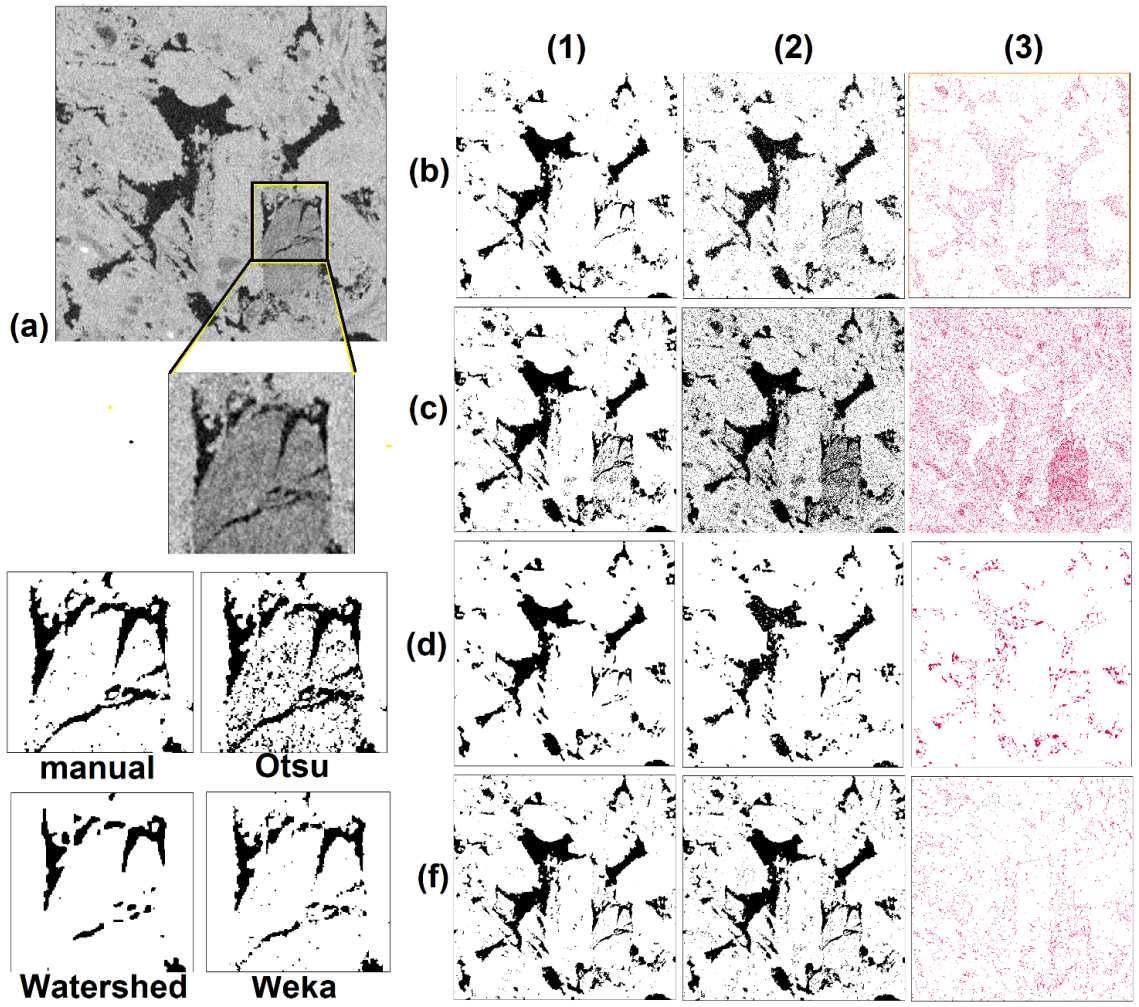

Figure 3-5 2D slice of X-ray tomography image of a Coquina sample (5 µm voxel size) showing pore (darkest colours) and grains (lighter colours) (a). The segmented images using Manual thresholding (a), Otsu (b), Watershed (c) and trainable Weka segmentation (d) methods. Column 1 and 2 correspond to the segmented images of the original X-ray image and the image with noise standard deviation of 40 respectively while column 3 show the difference between images of column 2 and 1 representing the misclassified voxels.

the Otsu method seems very noisy. On the other hand, the segmented images based on both manual thresholding and Weka show better quality of details in visual examination. It should be noted that Weka segmentation has been applied on the non-filtered image.

To investigate the robustness of methods to image noises, four grey-scale images with incremental levels of noises were produced by adding specified noises to the original grey-scale image. To do this, Gaussian noises with standard deviations of 10, 20, 30 and 40 grey-scale unit were added to the image. A non-local means filter with similarity value of (0.3) was then applied to all images prior to the use of Otsu thresholding, manual thresholding and watershed segmentation. After applying the four methods on the images of different noise levels, the segmented images was subtracted from the original segmented image (of the image without noise) to identify the misclassified pixels (See column 3 in figure 3.5). These pixels are those that has been assigned to the class different from one in the original segmented image. The percentage of misclassified pixels (proportional to the total pixels in the 2D image) was calculated and plotted versus the noise standard deviation of images for four different methods (figure 3.6). Based on these results, the number of misclassified pixels increases by the noise standard deviation of images for all methods. The output of Otsu method show significantly

higher misclassified pixels compared to other methods. The Weka segmentation method shows the best performance by very low percentage of misclassified pixels (<4%) even in high levels of noises. The distribution of the misclassified pixels also shows differences for different methods. For example, the misclassified pixels are distributed as lager areas of connected pixels (See column 3 in figure 3.5) in watershed methods while in the output of Weka segmentation method, the misclassified pixels are distributed as single (or areas containing only a few connected pixels) that can be easily removed (as outlier pixels) by filtering the segmented image.

Based on visual examination as well as comparing the performance of different methods in segmenting the images with different levels of noise, the trainable Weka segmentation was chosen as the best method for image segmentation in this study. This method provide the very good quality of segmented images. After training the classifiers, automated process of this method makes it easy to use for segmentation of large dataset and particularly in multiphase segmentation. No need for image pre-processing (filtering) in this method helps to save time and retain the details of the features in the images.

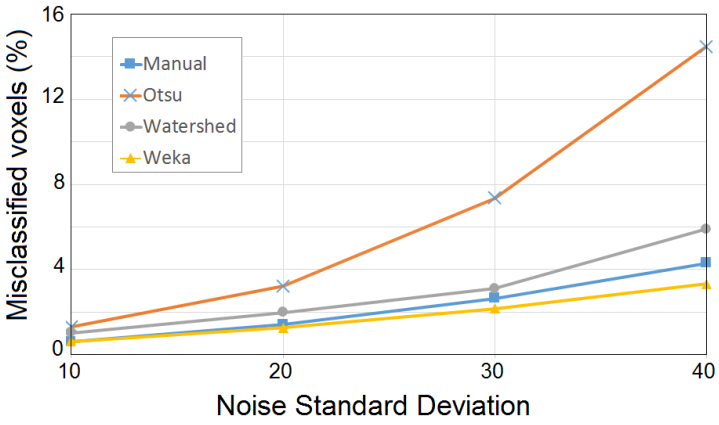

Figure 3-6 Relationship between the noise standard deviation in images and misclassified voxels for four segmentation methods.

It should be noted that the capability of this method for image segmentation without using filters is in context of its robustness to image noises. This capability may vary when filtering is needed for enhancing the contrast between phases which is not the case in this thesis. The robustness of method to the image noises makes it powerful tool for segmenting the Neutron tomography images which have relatively higher noises (due to the shorter acquisition time) to the X-ray tomography images.

3.3.3.2 Porosity and mean pore size

The total porosity is calculated by dividing the volume of pores by the sample volume. Not all the pores contribute equally to fluid flow within the sample since some are not connected to rest of the pore network. To find the connected and isolated pore network, the segmented images were labelled using labelling module of Avizo software, in which each connected pore network within the samples binary volume is assigned with a unique value. For two individual pore spaces to be considered connected, they need to share at least a common voxel face, voxel edge or voxel vertex (figure3.7). Here, connected porosity is defined as the pore network volume through which fluid can flow between the bottom and top (inlet and outlet of fluid flow) of the sample divided by the samples volume. Isolated porosity represents the pores that are not connected to the main pore network even though some of these might be inter-connected over a small network. This calculation are significantly dependant of the resolution of image and nature of rocks pore system. The connected porosity may be underestimated when considerable proportion of pores are not resolved (sub-resolution pores). The calculation of porosity provides a global value for the whole studied volume, but the pore spaces are not evenly distributed throughout the sample due to the heterogeneous nature of pore system in carbonate rocks. To explore the variation of porosity in the samples, the porosity profiles indicating the porosity variation along the length of the samples are

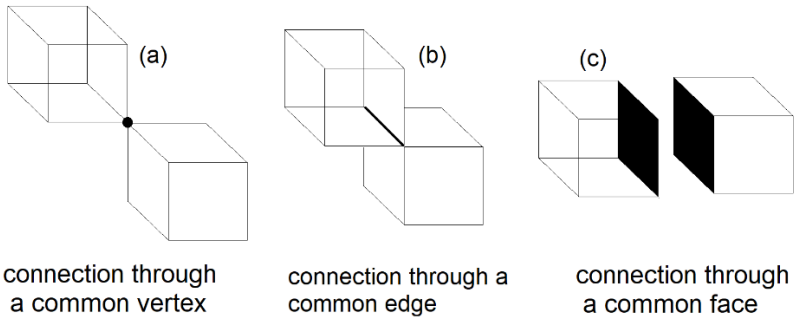

Figure 3-7 Voxel connections through a common vertex (a), common edge (b) and a common face (c)

generated. For this purpose, the porosity is calculated for every single horizontal slice (2D) and the calculated porosity values were plotted versus the slice number. The standard deviation of these porosity values can be used to compare the variation of porosity in different samples.

The mean pore size is also calculated from the segmented void space image. For this purpose, the pore sizes is calculated as the equivalent pore diameter using Avizo 9.1 software. For a given pore, the equivalent diameter measure computes the diameter of the spherical pore of same volume (ThermoFisher Scientific, 2018). The mean pore size is calculated as D_{50} that represent the volumetric mean pore diameter. First, a cumulative pore diameter (volumetric) distribution is plotted for the pore diameters and then the D_{50} is calculated as the pore diameter corresponding to 50 percent of the sample pore volume. In fact, for a given sample, half of the pore volume is consisted of pore spaces with diameter smaller than the D_{50} calculated for that sample.

3.3.3.3 Specific surface area

The Specific surface area calculated for each sample by dividing the surface of pores by the total pores volume (mm^{-1}). Both parameters are computed in Avizo given the voxel size of the used image. It is calculated for both the connected and the isolated pore network. Porosity, pores size, shape and roughness can control the specific surface area of a pore network. For same porosity, the specific surface area increases by decreasing pore sizes, increasing the pore surface roughness and existence of pores of irregular shapes. Higher values of the specific surface area may put a larger surface per volume in contact with hypothetical fluids which may exert a higher friction on fluid flow and therefore lower permeability of the rock (Zambrano et al., 2017). The calculated specific surface area is very sensitive to the image resolution. The higher details of the pore surface roughness that is resolved, the more reliable specific surface area value is achieved.

3.3.3.4 Connectivity Density

The connectivity of the pore network is examined in this work by studying the structure of the pore skeleton extracted from the segmented pore network image. As represented by (Zambrano et al., 2018), this is a useful approach to analyse the connectivity of a heterogeneous pore network (deformed carbonate grainstone). Skeleton image is interpreted as a set of nodes representing pore spaces and centrelines that represent the connection between pores. Using skeletonization module in Avizo 9.1 software, thinning algorithm is employed to generate the skeleton model. In this method, the aim is to remove as many voxel as possible from the pore spaces binary image and retain only a string of connected voxels in the centre of pore spaces as centrelines. The thinning process itself uses a distance field as an input. This is a 3D distance field of the 3D pore spaces in which each voxel is assigned a value depending on the distance to the nearest pores boundary. The boundary voxels of the pores are assigned a value of zero whereas the assigned value increases as the distance from boundary increases. A centreline between two nodes that represents connection between two pores is called segment.

A connectivity density (CD) parameter is used here to describe the degree of connectivity of the pore network. It is a scalar value that represents number of redundant connections between pores per unit volume of the analysed sample. CD (mm^{-3}) is calculated using equation 3.6;

Equation 3.6

$$CD = \frac{\mathbf{1} - (\boldsymbol{a} - \boldsymbol{b})}{\boldsymbol{V}}$$

where a and b are the number of nodes and segments available in the connected pore network, respectively and V is the analysed volume (mm^{-3}). CD is higher for highly connected pore networks and can be negative or close to zero for isolated pores.

3.3.3.5 Coordination number

The coordination number describes another aspect of the interconnectivity of the pores. The coordination number of each pore is defined as the number of throats connected to that pore. The pore throat is the small pore space which connects two larger pore volumes. The coordination number is usually presented as average coordination number of the pore network or as distribution of coordination number of pores in a porous media. In this study, the average pore coordination number is calculated for regions of interest using skeleton model extracted from pore network in the Avizo software. The skeleton model is extracted as described in previous section (3.3.3.4) and the number of segments connected to a pore is considered as the pores coordination number.

3.3.3.6 Tortuosity

Pore space in carbonate rocks is highly chaotic, with variable pore sizes and shapes. But what makes carbonates pore network particularly complex is that the available paths for fluid movement can be extremely tortuous and meandering. Tortuosity (T) is a scalar value used to measure the hydraulic conductivity, fluid travel time and diffusion in porous media can be affected by textural heterogeneity in rocks. Among several methods to calculate tortuosity (Ghanbarian et al., 2013), here, T is calculated based on two methods. First, the min tortuosity ($T_{\min}$) as the ratio of the shortest pathway (L_{min}) to the straight-line length (Ls) across the medium (Scriven, 1994). The second method provide the geometric tortuosity or mean tortuosity (T_{mean}) that is more general definition of tortuosity and is calculated as the ration of the average length (L_{ave}) of the flow paths to the straight-line length (Ls) across the medium. The higher tortuosity value, the more chaotic a pore network is. In this study, L_{min} and L_{ave} values were obtained from the 3D distance field computed for the pore networks binary image using Avizo software. In the distance field, each voxel has a value that represents its shortest distance from defined boundary of an object. Figure (3.8) shows the 3D distance field extracted for pore network of shown sample volume.

3.3.4 Representative Elementary Volume (REV)

Representativeness of the measured or calculated properties for the samples were evaluated by analysing representative elementary volume (REV). REV is defined as the smallest volume of a system over which a measured or calculated property can be considered as representative of the whole system. In other words, REV is the volume in which the variability of a property approaches a constant level, by covering a representative amount of the sample heterogeneity (Zhang et al., 2000; Zambrano et al., 2018). In order to have meaningful statistical average of a pore system property in the case of heterogeneous samples, the REV

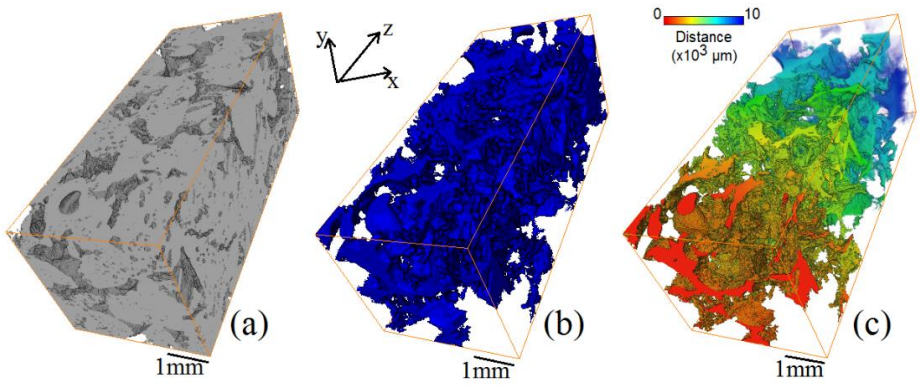

Figure 3-8 The 3D extracted volume of X-ray tomography (5µm voxel size) image of Coquina rock (a) and the extracted pore network image (b). The distance field calculated in Z direction of the 3D volume (c).

must be large enough to encompass as much pore types and sizes as possible from different parts of the sample, while still being small enough to allow us to investigate the fluctuation of the measured value of interest across the sample.

In this study, aforementioned pore network properties were calculated for concentric cubic volumes of increasing sizes extracted from the whole volume of the sample. Then, the variation of each property was plotted against the volume sizes. The representative elementary volume (REV) can be determined as the volume above which the variation of each properties by changing the volume size is trivial. This volume may vary for each property. To avoid inconsistency in REV values, the most representative volume that is largest one can be considered as REV for all properties. These analysis are crucial since they reveal the capability of each pore network property as a quantitative result to be used in supporting the local flow behaviour of our heterogeneous samples.

Figure 3.9 shows the plots of calculated pore network properties including porosity, specific surface area and tortuosity for different size on the studied volume. As seen in this plots, the variation of tortuosity and specific surface area values become trivial for studied volumes with cube side size of over 10mm. Variation of calculated porosity values however becomes almost constant for cube side size of over 12.5 mm. This means that the volumes with cube side size of 12.5mm is the smallest volume for which the calculated aforementioned properties can be representative.

3.3.5 Fluid arrival time field

In the grey-scale reconstructed HSNTs, progress of injected fluid during flow experiments can be followed thank to the variation of the grey-scale induced by the variation of neutron attenuation following the invasion of hydrogen-rich fluids in the pores. In fact, a qualitative observation of the flow patterns of the advancing fluid is possible from the grey-scale HSNT

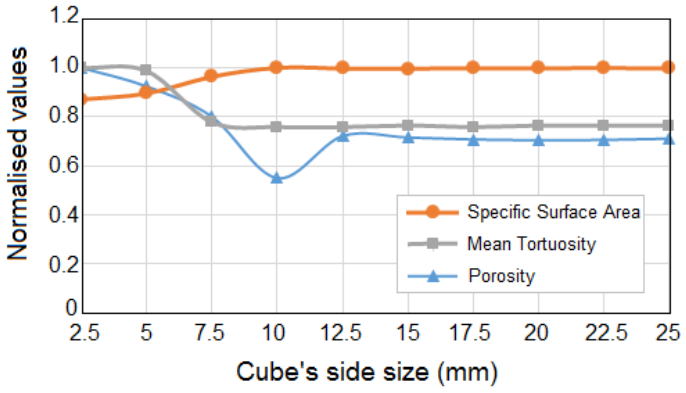

Figure 3-9 Variation of calculated Porosity, Tortuosity and Specific Surface Area values for cubes of different sizes extracted from X-ray tomography image of Coquina sample.

images due to the resulted contrast between the initial fluid phase and injected fluid. However, a quantitative analysis of the flow patterns, fluid speed and fluid flow processes needs further image analysis on the grey-scale HSNT images in more rigorous approaches that will be described here and the following sections.

The first necessary step is to use the reconstructed HSNTs to calculate the arrival time of the fluid for each voxel of tested sample. Each voxel of the reconstructed High-Speed Neutron tomography images represents in fact the neutron attenuation coefficient of a region of space, which changes significantly when injected fluid with distinct attenuation coefficient arrives at that voxel. For this purpose, we have used a code written by (Etxegarai, 2019). This code follows the attenuation value of each pixel along time throughout the test. This allows to trace a history of the attenuation of a voxel in 3D space, without taking into account the behaviour of the voxels around (Etxegarai, 2019). This is important to avoid the effect of beam hardening on calculations. It should be noted that the grey-scale evolution of each voxel and the extent to which its grey-scale changes can depends on the location of that voxel with regards to the pore space. For instance, a voxel that is located in the centre of a large pore space may show higher range of grey-scale change due to fluid displacement in the pore space. But, a voxel in the border of pore space may show lower range of grey-scale change as it partially resolve the pore space and the solid component of the rock. This is controlled by the spatial resolution of the image meaning that the higher spatial resolution will better resolve the small pore spaces and minimise the effect of partially spatial resolved voxels.

Figure 3.10, shows the grey-scale value evolution of a randomly selected voxel within the scanned samples volume over time. As can observed in this plot, the voxel has a constant intensity value at the beginning of the experiment, but when the injected fluid (water in this case) reaches that voxel, its intensity starts increasing until it finally reaches a new plateau in its saturated state. This intensity evolution can be fitted by a sigmoidal function, defined as bellow:

Equation 3.7

$$y = A + \frac{B-A}{1+(\frac{C}{x})^D}$$

where A and B are the constant grey-scale values at the beginning and the end of evolution, respectively. C is instead the time at which the grey-scale value is halfway between A and B, and D is the parameter proportional to the slope of the curve indicating the speed of variation of the grey-scale changes due to the arrival of new fluid.

In this method, C is considered as the fluids arrival time. Each of these parameters are calculated for each voxel that can be plotted as multiple 3D fields for the whole volume of

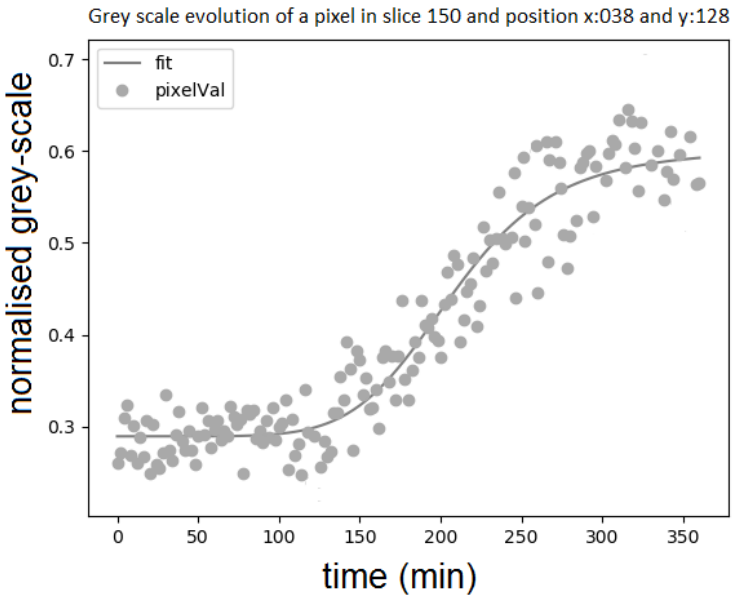

Figure 3-10 Example of a sigmoidal fitting of the evolution of grey-scale value of a voxel in time.

sample. In addition to these parameters, an error parameter can be calculated to measure the error between the real data the fitted sigmoidal. The distribution of C parameter is in this case a key output as it represents the 3D of arrival time of injected fluid to that point. Given the fact that the C-parameter for each voxel is calculated only based on the grey-scale evolution of that voxel (not dependent of other voxels), the effect of partially spatial resolved voxels (controlled by the spatial resolution) on estimation of fluid arrival time is expected to be minimised.

Employing a sigmoidal fitting on the grey-scale evolution of each voxel with time provides the possibility of an effective tracking of the fluid front advancement in the case of low contrast to noise ratio caused by the short acquisition time in HSNTs. The sigmoidal fitting also makes it possible to gain a temporal resolution below the HSNTs acquisition time in fluid arrival time field.

Further processing on the computed fluid arrival time fields can provide useful information of fluid front shape, position and propagation speed throughout the sample (3D). The position and shape of the advancing fluids front in 3D and with time can be extracted by segmenting the fluid arrival time field. For example, for extracting the 3D front position at a given time (t) after the onset of the flow experiment, the fluid arrival time field is segmented by applying the threshold value of (t) so that only voxels with value equal or smaller than (t) are retained and visualised.

By further processing of the extracted 3D front positions, a quantitative measure of the extent of the irregularity of the fluid front can be obtained. For this purpose, the surface area of the segmented (using interactive thresholding module of the Avizo software) 3D fluid front is calculated using the Label Analysis module in Avizo software. Higher surface area of the fluid front represents the existence of more protrusthe ions or existence of protrusions with more complex morphology at the leading face of fluid front. The surface area of the fluid front also indicates the reactive interface available between miscible fluids for mixing in miscible fluid displacement analysis. In addition, by calculating the surface area of the leading front in a sample at different times, the variation in morphology (irregularity) of the fluid front with time can also be understood.

This procedure that is proposed for the first time in this thesis, provide a new way to further exploit the HSNT data. In fact, the fluid arrival time field (as an output of sigmoidal fitting method) was mainly used as an input for computing fluid speed field before (Etxegarai, 2019) while, in this PhD, it has also been used for quantitative analysis of irregularity (instability) in the flow patterns.

3.3.6 D-parameter field

From the sigmoidal curves fitted to the grey-scale evolution of every voxels, and based on the sigmoidal function (Equation 3.7), the D-parameter that is proportional to the steepness of the fitted sigmoidal curve, was calculated and assigned to each voxel to generate the D-parameter field. This parameter indicates how fast the transition in miscible displacement has taken place at that voxel that can be linked to the local fluid speed. Higher values of D-parameter indicate a steeper sigmoidal slope that is related to a relatively faster fluid displacement or miscible mixing in the voxel while the smaller D-parameter is linked to a gentle sigmoidal slope that is a result of fluid displacement or miscible mixing of fluids over a longer period of time. In this study, the D-parameter fields are used to investigate the variance of local fluid speed in the sample that can be linked to the hydrodynamic dispersion during miscible displacement. The higher variance in D-parameter is expected to increase the potential for hydrodynamic dispersion because of the higher variance in the local fluid speed in the sample. The histograms of the D-parameter obtained for each D-parameter fields are used to compare the variation in D-parameter in different samples. Also, slice-averaged D-parameter is calculated by averaging the D-parameter values of voxels in each horizontal slice and plotting the values versus the slice number along the length of samples. The trends of variation in D-parameter along the length of the sample (along the flow direction) is used to get insight into longitudinal dispersion during miscible displacement experiments.

The procedure of using D-parameter for the hydrodynamic dispersion analysis during miscible fluid displacement is introduced for the first time in this thesis. This is a step forward in HSNT analysis using the sigmoidal fitting method developed by Etxegarai, 2019. In fact, in addition to the fluid arrival time output, the new potential of the sigmoidal fitting method has been employed in this PhD by using the steepness of the sigmoidal curve and its variance throughout the sample or along a given axis (e.g. the flow direction) as an indicator of hydrodynamic dispersion and longitudinal dispersion.

3.3.7 Fluid speed field

The fluid speed field represents in 3D the distribution of the injected fluid speed within the sample. The progress of the injected fluid front in the sample is captured by series of HSNTs. By calculating distance between fronts at two consecutive tomographies and given the knowledge of time elapsed between two tomographies, it is possible to deduce the front progression.

The following explanation of the procedure of calculating fluid speed field and the presented example are based on (Etxegarai, 2019). To compute fluid speed field, the code written by (Etxegarai, 2019) was used in this work. This code takes the 3D fluid arrival time as input to detect the front position in desired time steps (e.g. every one, five or n tomographies). First, a Gaussian filter with a standard deviation of 5 pixels is applied on the fluid arrival time field to reduce the noises. Then, parameters like voxel size, time step at which front needs to be picked (for example every 5 minutes) and the maximum time (the duration of the flow experiments) need to be defined. Fronts position at a given time steps are then detected based on the fluid arrival time value. For example, the front position in (t = 20min) is extracted by applying a threshold that keeps only voxels with arrival time value smaller than 20min. In next step, Euclidean distance of every voxel in the 3D from the two consecutive fronts below and above that voxel is calculated given the voxel size. Figure 3.11 shows the simplified 2D abstract example of front progress in sample. In this case, the front (position a) has moved up by 100 pixel in the vertical direction (position b), while its shape is retained. The hatched area (figure 3.11-c) shows the distance covered during the front progress from position a to position b. Euclidean distance of all pixels inside the hatched area from the fronts in position (a) and (b) and vice-versa is then calculated and is presented in the colour map in figure 3.11-d and 3.11-e respectively. These two distance value are calculated for each voxel are then summed together, giving the shortest-path distance that fluid crossing that point travels to reach the front in position (b) from the front position (a) (figure 3.11-f). Examples of the effect of this procedure with more complex geometries can be found in (Etxegarai, 2019).

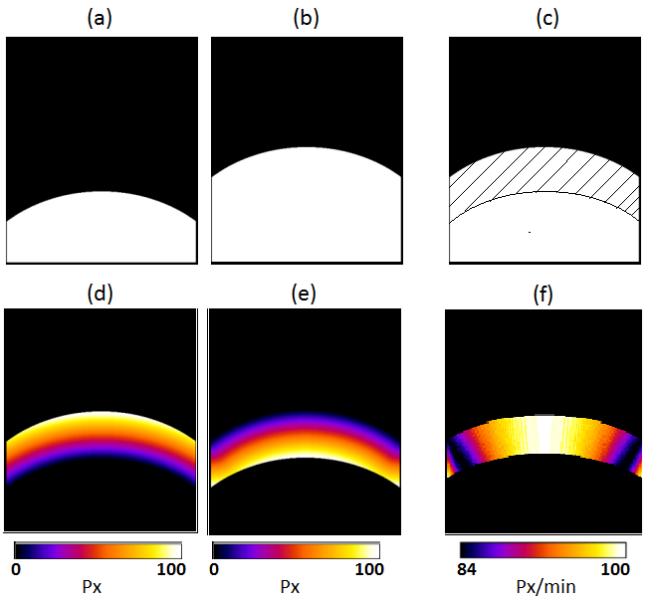

Figure 3-11 Simplified 2D front in first position (a) and moved 100 pixel in vertical direction (b); distance between front in position a and b, represented as hatched space (c); Euclidean distance of all pixels inside the hatched area from the fronts in position a (d) and position b (e); final distance field between fronts a and b (f), resulting from the sum of (d) and (e). (Etxegarai, 2019)

The same procedure is applied to all voxels of the 3D volume, resulting in a 3D distance field showing the vertical distance between every two consecutive fronts that is directly related to fluid speed. Given the time elapsed between acquisition of tomographies (time step), fluid speed in each voxel can be calculated based on its distance value and generate a 3D fluid speed field. The main limitation of the method is that it only provides the shortest path distance for the fluid while the fluid does not necessarily flow through the shortest pass in real case (flow in porous rock). In fact, the fluid speed calculated in this method may be underestimated.

The frequency of HSNT acquisition and spatial resolution of the reconstructed tomographies control the resolution of fluid speed field. Depending on the injecting flow rate and samples flow properties, front can progress with different speeds. This have to be taken into account in defining the time step. For optimal results, the time step should be large enough so that the movement between two fronts becomes larger than the front roughness. When the advancement of front is very slow between two consecutive tomographies, time step needs to be increased.

3.3.8 Differential imaging

To assess the distribution of phases concentration (during miscible fluid displacement) and phases saturation (during immiscible fluid displacement) in samples and its evolution with time, a procedure has been introduced in this thesis called differential imaging. In this procedure, the HSNTs taken at different times after the onset of flow experiments are

subtracted from the first HSNT where the sample is fully saturated by the initial fluid. The resulted images show the difference in grey scale value of each voxel due to the displacing or mixing of the initial fluid with the injected fluid. For miscible fluid experiments, the resulted differential images are normalized against the maximum grey scale differences observed within the sample when subtracting the initial and the last HSNTs. This maximum grey scale difference is observed in pore spaces in which almost a full displacement of the initial fluid by the injected fluid is expected based on the visual examination of HSNTs and differential images. The normalised differential grey scale values can be directly linked to the relative concentration of the injected fluid.

For immiscible fluid displacement, the differential grey-scale images are used to detect the pore spaces in which immiscible displacement has happened and to investigate the proportion of pore spaces to the total porosity of the rock. The results of differential images is a 3D image for each sample in which the voxel values correspond to the grey-scale value change due to the displacement of fluids (oil and heavy water). Figure 3.12 shows the cross sectional slices of the neutron tomographies before and after the flooding and the corresponding differential image. As seen in the differential images, the regions with high differential value correspond to regions in the neutron tomography images where the oil (voxels with lighter colour) is replaced by heavy water (voxels with darker colour). The regions with lower differential values correspond to regions where the oil is only partially displaced by the injected heavy water. Accordingly, the differential values can be a representative of the contribution of the pore spaces of two phase immiscible displacement. The regions with zero or low differential values can be attributed to the solid components of rock or those proportion of pore system that does not contribute anymore to immiscible displacement such as isolated pores, stagnant zones and pores occupied by non-mobile/entrapped oil ganglia.

By segmenting the differential grey-scale image, a 3D image of the distribution of regions with differential grey-scale value over a defined threshld (grey-scale unit) can be extracted. The regions with differential grey-scale values over this threshold are considered as pore spaces in which significant fluid displacement has been happened. In this study, the proportion of these pore spaces to the volume of the sample is defined as contributing porosity.

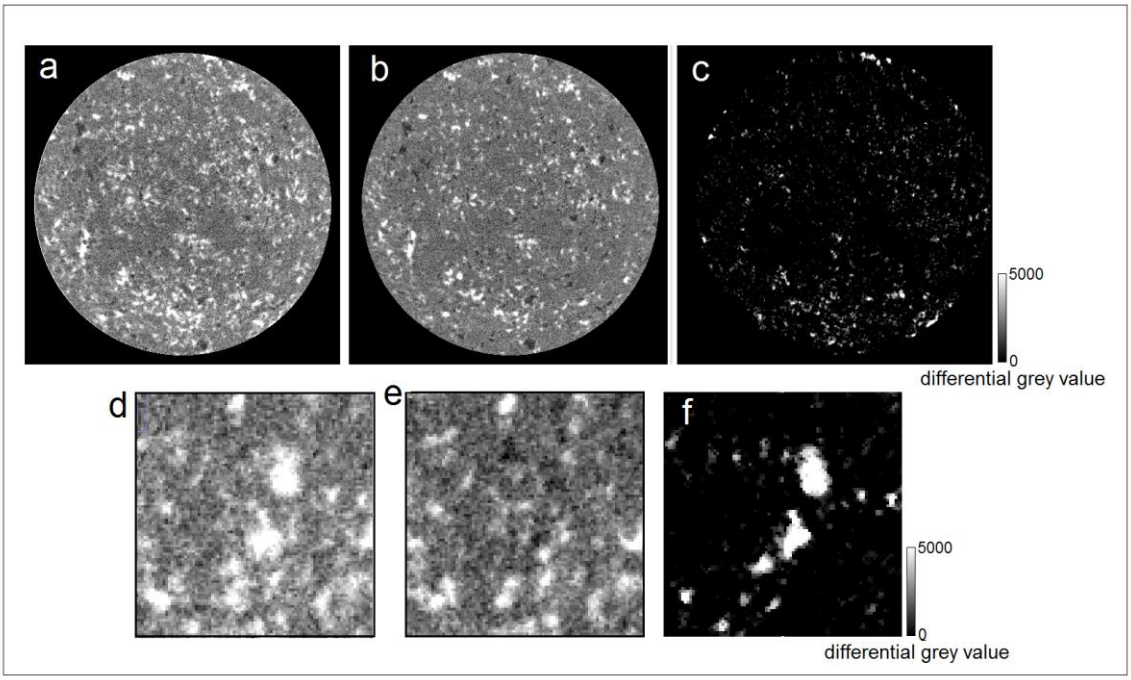

Figure 3-12 Cross sectional slice of neutron tomography image of a coquina sample (C16) acquired at initial mixed saturated (heavy water and Decane) condition (a,d) and after flooding the sample by one pore volume of heavy water (b,e) and the resulting differential image (c,f). In grey scale images (a,b,d and e) the brighter and darker colours represent higher saturation of Decane and heavy water respectively while the grey colours represent the solid components of the rock. In resulted differential images (c and f) the brighter colour represent pore spaces in which more fluid displacement has occurred while the black colour represent no fluid displacment.

3.4 Robustness and reliability of the image analysis on HSNTs

In this section, the robustness of the image analysis methods used for quantitative analysis of HSNTs and its potential errors are investigated. First, the errors in the sigmoidal fitting and the 3D distribution of errors in the sample are investigated by analysing the sigmoidal fitting error fields obtained from HSNTs taken during flow experiments in a Coquina sample. Next, the sensitivity of the image analysis methods to the chosen parameters is investigated. For the sigmoidal fitting method, the effect of temporal resolution on the error of the sigmoidal fitting is investigated by running the sigmoidal fitting analysis using 4 different frequency of HSNTs (as a representative of 4 different temporal resolutions) as input data. The sensitivity of the resulted fluid arrival time and D-parameter values to temporal resolution are also investigated. For the fluid speed fields, the effect of chosen parameters like used filters (on the input fluid arrival time field) and time intervals for front picking on the resulted 3D distribution of fluid speed is examined. The sigmoidal fitting method as a fundamental of image analysis methods used here for analysing the HSNT data, is developed by Etxegarai (2019) and the successful performance of this method is shown by Etxegarai (2019) for

calculating fluid speed field for sandstone samples. The reliability of the method to be used for more complex and heterogeneous carbonate sample in this study is also evaluated.

3.4.1 Sigmoidal fitting error and sensitivity of calculated C and D parameters

As shown in figure (3.10), a sigmoidal curve is fitted to the evolution of grey-scale values (Y axis) in time (X axis) for a given voxel. The errors in sigmoidal fitting process is calculated for each fitted sigmoidal (using the code written by Etxegarai (2019). This is the error between the real grey-scale data and the fitted sigmoidal that shows how close are the fitted data to the grey scale values. The error is calculated as the mean of the absolute deviation of the grey-scale values from the fitted sigmoidal at every point. The calculated error values for each voxel is then normalised against the maximum range of the grey-scale change in that voxel and is presented in percentage. By assigning the calculated error of each voxel, the sigmoidal fitting error field is generated for the tested sample. The higher error value shows the high discrepancy between the grey-scale values and the fitted sigmoidal that reduce the reliability of the parameters calculated form the sigmoidal function such as fluid arrival time and D-parameter. Different parameters may affect this error value such as signal to noise ratio during image acquisition, temporal resolution, and some parameters related to the flow experiments and the features in the sample.

The robustness of the sigmoidal fitting method for tracking the fluid front to the random noises in the images is investigated by Etxegarai (2019) that shows the method is more robust to image noises compared to other method (image binarisation). This is a major advantage of the sigmoidal fitting for analysing HSNTs where image noises are expected due to the short acquisition time.

Temporal resolution is expected to have significant effect on the error of sigmoidal fitting. The number of the HSNTs used in sigmoidal fitting process and the time elapsed between two consecutive tomographies define the number of available data points on which sigmoidal curve is fitted and the changes in grey-scale between the two consecutive tomography. Here, the effect of temporal resolution of HSNTs on the sigmoidal fitting error is investigated. Also, the sensitivity of the resulted fluid arrival time field and D-parameter fields to the temporal resolution of used HSNTs is examined. For this purpose, five sets of HSNT data are extracted from a series of 360 HSNTs captured during water-heavy water displacement experiments in a Coquina sample (C13). The first set encompasses all the 360 tomographies while the second, third, fourth and fifth sets have 180, 120, 90 and 72 HSNTs respectively that are picked from the same sets but in every two, three, four and five tomography intervals

respectively. The sigmoidal fitting process was carried out for each set of HSNTs and the outputs including the error fields, fluid arrival time field and D-parameter fields were obtained. Figure 3.13 show the cross-sectional slices of the error fields for five mentioned datasets. As shown in this figure, the error increases by decreasing the temporal resolution and number of HSNTs used for the sigmoidal fitting. This is also obvious in figure 3.14 that shows the cumulative distribution of the sigmoidal fitting error for 5 different temporal resolution. By decreasing the temporal resolution from 1 to 2 minute, the proportion of voxels with higher errors slightly increases. However, by further reduction of temporal resolution to 3, 4 and 5 minute, the number of voxels with high errors significantly increases. For instance, the proportion of the sample voxels with error values below the 5 % is equal to 90 %, 86 %, 77 % 64 % and 40 % for the temporal resolutions of 1, 2, 3, 4 and 5 respectively. Its also observed in the error fields that the distribution of errors is not homogeneous throughout the sample. The error is generally higher in the central part of the sample compared to the periphery of the sample. This is consistent with observation by Etxegarai (2019). Lower signal to noise ratio in the central parts of the sample due to the passage of beam through thicker part of the sample (higher cross-sectional distance and higher attenuation of the beam) is expected to cause higher error in the central part. The high errors in the bottom part of the

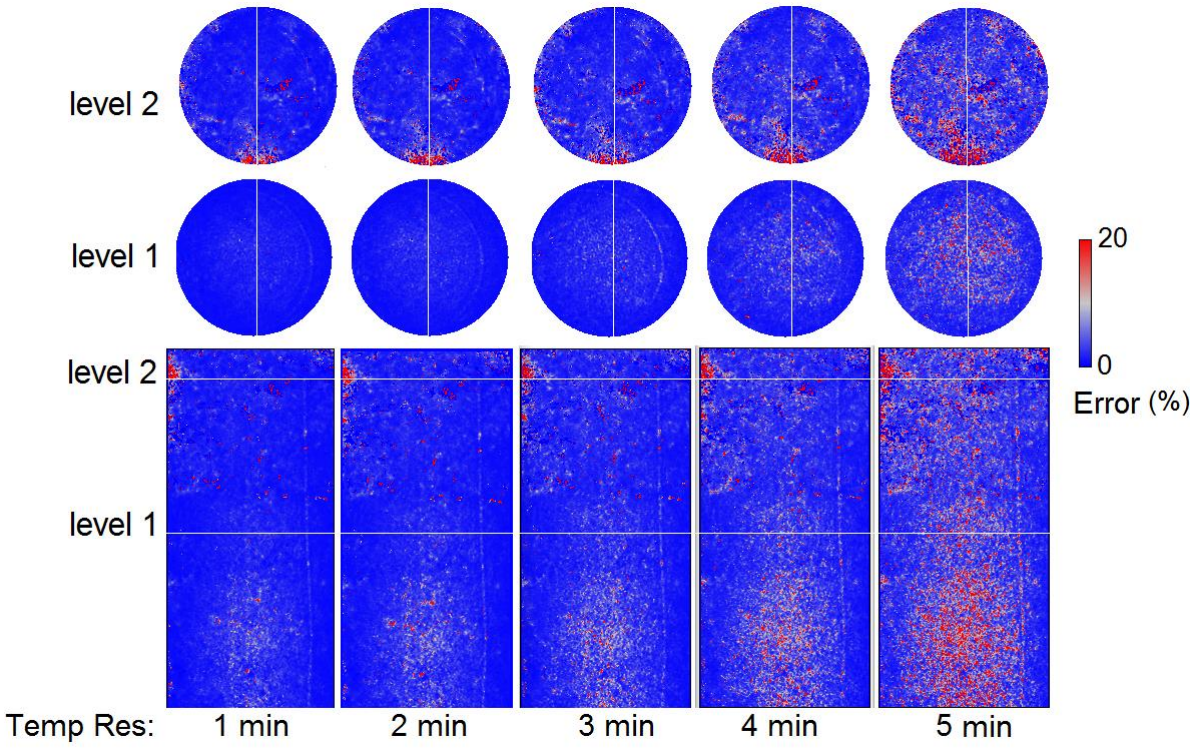

Figure 3-13 Vertical and horizontal slices of error fields representing the distribution of error of sigmoidal fitting on five sets of HSNTs of a same Coquina sample (C13) sample with different temporal resolutions of 1, 2, 3,4 and 5 minute. HSNTs are acquired during injection of one pore volume of water into previously heavy water saturated sample. The flow direction is from bottom to the top end of core sample.

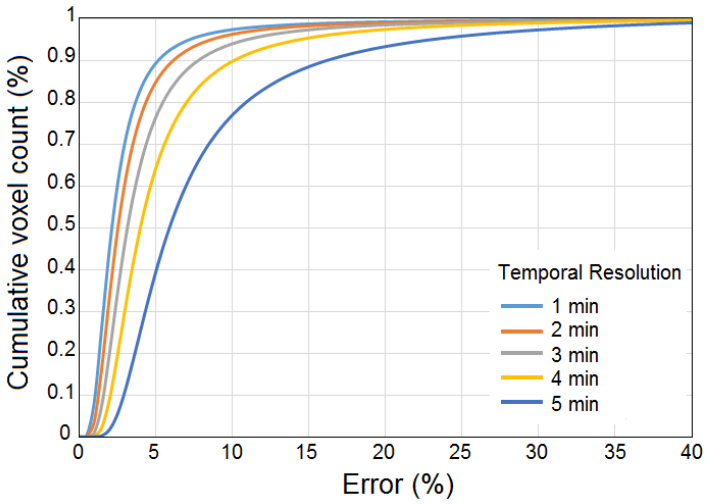

Figure 3-14 Cumulative distribution of the sigmoidal fitting error for five different temporal resolutions of 1, 2, 3,4 and 5 minute. The cumulative distributions are extracted from the histograms of the error fields of the Coquina sample (C13).

sample (near the fluid inlet) seems to be related to the relatively quick displacement of fluids and grey-scale change while some locally distributed voxels with high error in the top part of the sample is expected to be due to lack of a full fluid displacement in that parts. Nevertheless, the error is generally very low when the temporal resolutions are high such as 1 min and 2 min.

Figure 3.15 presents the cross-sectional slices of the fluid arrival time field and D-parameter fields obtained from sigmoidal fitting method using the five sets of HSNTs with temporal resolution of 1 min to 5 min. As observed in these results, by decreasing the temporal resolution from 1min to 5 min, more voxels with significantly different value appear in the image that can be treated as outliers. By comparison of figure 3.15 with corresponding slices of error field in figure 3.13, its found that the general distribution (pattern) of fluid arrival time does not seem to be dependant on the distribution of errors. However, general pattern of D-parameter distribution correlates with distribution of errors so that the regions with higher error (for instance the central parts in the bottom half of the sample) have higher D-parameter as well. It seems that the quick displacement of the fluid can result in sudden change in grey value of the voxel and result in steeper slope and higher error of the fitted sigmoidal curve.

In order to better evaluate the sensitivity of the resulted fluid arrival time and D-parameter values to the temporal resolutions, the resulted fluid arrival time and D-parameter fields for each reduced temporal resolutions (2 min, 3 min, 4 min and 5 min) is subtracted from the first fluid arrival time and D-parameter fields (as reference values calculated at temporal resolution of 1 min) to find the miscalculated fluid arrival time and D-parameter values. Based on the histograms of the resulted subtracted images, cumulative distribution of the

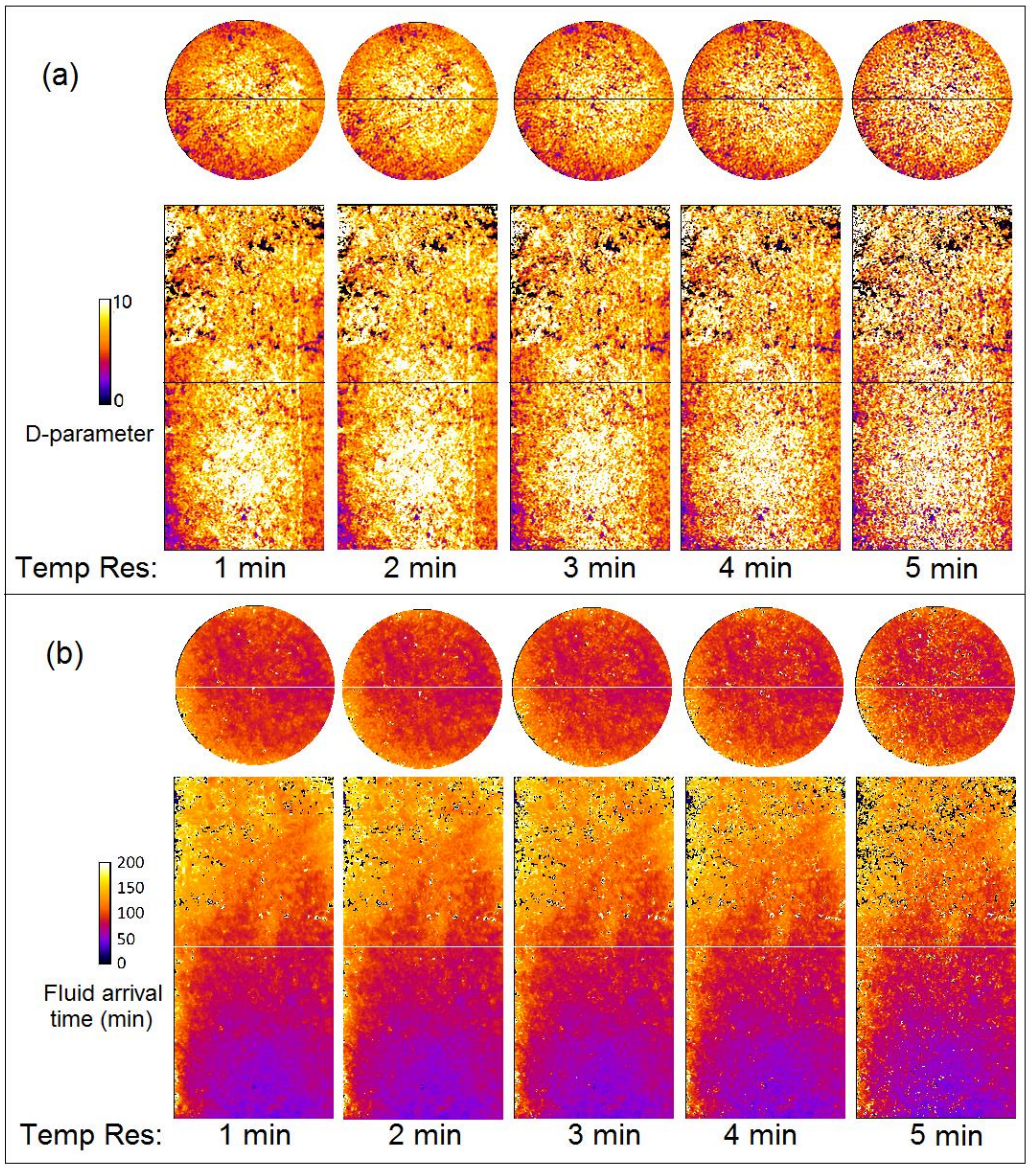

Figure 3-15 Vertical and horizontal slices of D-parameter fields (a) and fluid arrival time field (b) calculated using five sets of HSNTs of a same Coquina sample (C13) with different temporal resolutions of 1, 2, 3,4 and 5 minute. HSNTs are acquired during injection of one pore volume of water into previously heavy water saturated sample. The flow direction is from bottom to the top end of core sample.

miscalculated voxels are obtained (figure 3.16) that shows the proportion of voxels with different range of D-parameter and fluid arrival time difference values at reduced temporal resolutions (2 min, 3 min, 4 min and 5 min). As seen on these plots, by decreasing the temporal resolution (from 2min to 5 min), the proportion of voxels with lower differences in D-parameter and fluid arrival time values decreases and proportion of voxels with high differences increases. For instance, in temporal resolution of 2 min, only 11% of voxels have arrival time value differences over 4 minute while, over 40% of voxels in temporal resolution of 5 min have difference values over 4 minute. For D-parameter fields, the proportion of

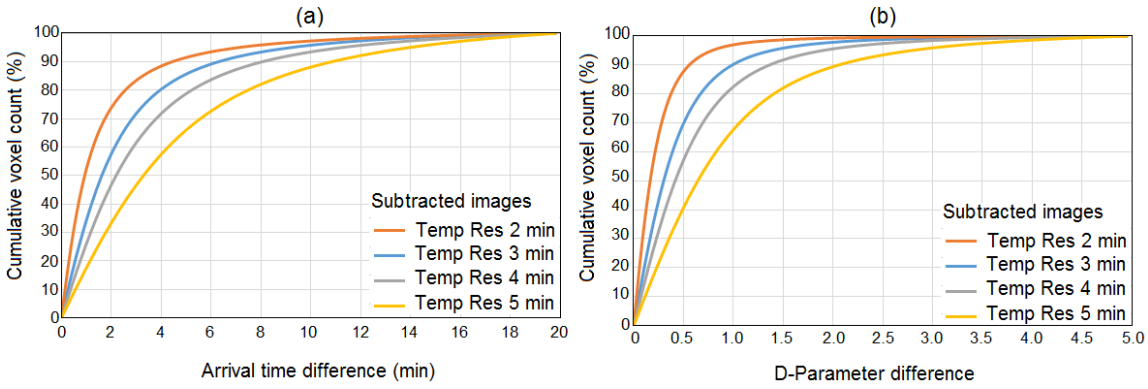

Figure 3-16 Cumulative distribution of voxels with fluid arrival time (a) and D-parameter values (b) representing the proportion of voxels with different differences in the D-parameter and fluid arrival time values at different reduced temporal resolutions (2 min, 3 min, 4 min and 5 min) compared to the D-parameter and fluid arrival time values of temporal resolution of 1 min.

voxels with D-parameter difference of over 0.5 increases from 12% to 60% in temporal resolutions of 2 min and 5 min respectively.

3.4.2 Reliability of the used image analysis techniques for tested carbonate samples

This section investigates the reliability of the used image analysis techniques for analysing HSNT data of fluid flow experiments in heterogeneous carbonate samples studied in this PhD. The successful performance of the used image analysis tools including the sigmoidal fitting for fluid arrival time calculation as well as fluid speed calculation is presented in Etxegarai (2019) where the methods are used on synthetic images as well as to analyse the HSNT data of fluid flow in sandstone sample. In this study, however, fluid flow within the more complex pore system of our intact and mechanically deformed carbonate rocks (compared to the more homogeneous sandstone) may affect the reliability of the results of these image analysis techniques.

3.4.2.1 Fluid arrival time field based on sigmoidal fitting

As explained in the previous section, high error in the sigmoidal fitting on grey scale evolution of voxels can adversely affect the reliability of the calculated fluid arrival time and D-parameter. In addition to the image acquisition parameters like temporal resolution, parameters related to the fluid flow experiments and some features within the sample can also control the error in sigmoidal fitting and hence the calculated fluid arrival time and D-parameter values. One of the most important parameters that can control the sigmoidal fitting error is the range of grey scale change in each voxel. High error is expected in case of small grey-scale changes that can be resulted due to the lack of full fluid displacement. However, the porosity also affect this grey-scale change so that regions with lower porosity will have

lower differential grey-scale value even if the injected fluid completely displaces the initial (saturating) fluid in that region. This is expected to impact the reliability of the image analysis results in fractured samples in which flow is dominated by fracture resulting a negligible fluid displacement in some regions of the matrix. To better evaluate this, the sigmoidal fitting error field and the resulted fluid arrival time fields for a same Coquina sample before and after being mechanically deformed are compared. As presented in figure 3.17, the sigmoidal fitting error increases in the deformed sample (c) in which the mechanical deformation introduced an almost vertically oriented fracture (indicated by white line). As shown in this figure (3.17-c) high error values (red colour) are observed in regions with high distance from the fracture (particularly in the top half of sample) while the generally low error is observed in the intact sample. As observed in the fluid arrival time of the deformed sample (figure 3.17-d), fluid arrival time is smaller (earlier) in vicinity of the fracture and it gradually increases by distance from the fracture. However, in regions with high error in sigmoidal fitting (close to lateral boundary), an almost constant fluid arrival time is observed. The observation suggests that the lack of full fluid displacement in some parts of the matrix with high distance from the fracture increases the sigmoidal fitting error and adversely affect the reliability of the results for these regions. This means that care should be taken when interpreting the results in similar samples.

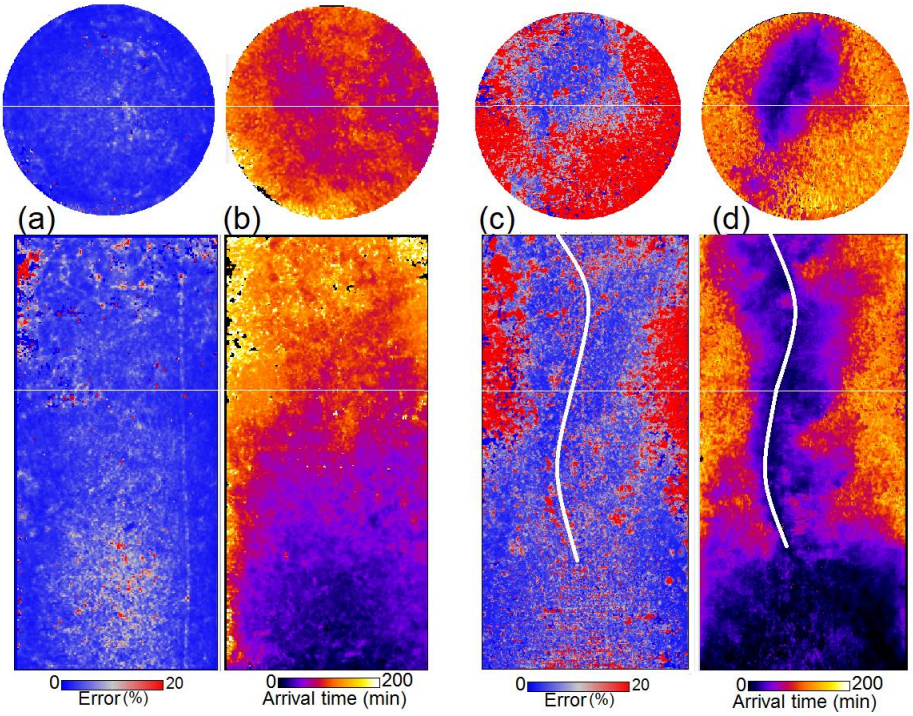

Figure 3-17 Vertical and horizontal slices of sigmoidal fitting error filed for same Coquina sample (C13) but before (a) and after being fractured (c) and the corresponding slices from resulted fluid arrival time field for intact (b) and fractured (d) samples. HSNTs are acquired during injection of one pore volume of water into previously heavy water saturated sample. The flow direction is from bottom to the top end of core sample.

3.4.2.2 Fluid speed fields and front picking

In addition to the fluid arrival time field and D-parameter fields, fluid speed calculation can also be affected by the complexities in carbonate rock studied in this PhD. As described in section 3.3.7, fluid speed calculation method relies on picking the fluid front in desired time steps and calculating the distance between two consecutive fronts. While the method is previously used by Etxegarai (2019) to calculate the fluid speed field in sandstone sample, increasing the rock heterogeneity is expected to significantly control the front picking process due to the more complex morphology of the front. Here, sensitivity and reliability of the resulted fluid speed fields to the time step chosen for front picking and filter chosen to smoothen the front is investigated.

To choose the optimum time step for fluid speed calculation, a same input data (fluid arrival time field of a Coquina sample, C13) was used to run the fluid speed code with four different time steps of 2 min, 3 min, 4 min and 5 min. Figure 3.18 shows the picked front levels in a horizontal slice and resulted fluid speed fields for each chosen time step. Smaller time steps are expected to better resolve the fluid speed variations however, as shown in figure 3.18,

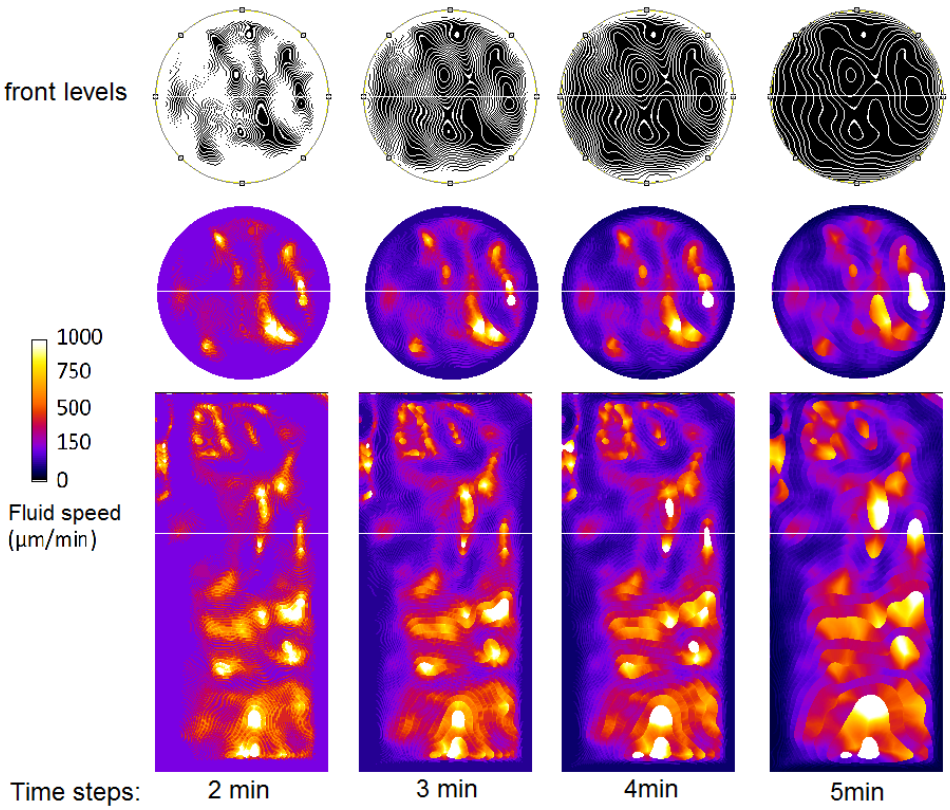

Figure 3-18 Cross sectional slices of front levels (white lines) and fluid speed fields for a same Coquina sample (C13) but calcualted using four different time-steps (as an input parameter) of 2 min, 3 min, 4 min and 5 min. For fluid speed fields presented in this figure, HSNTs acquired during injection of one pore volume of water into previously heavy water saturated sample is used. The flow direction is from bottom to the top end of core sample.

very small advancement of the front in reduced time steps (2 min and 3 min) resulted in considerable overlap of front lines that dose not allow speed calculation for these regions. On the other hand, the increased time step (5 min) resulted in over-smoothening of the calculated fluid speed. In fact, the speed at which fluid move across the distance between two fronts can be highly variable so that by increasing the distance between two consecutive front, the variation of fluid speed is being smoothened over the longer flow path. Based on these evaluation, the time step 4 min was chosen as an optimum time step since the distance between the consecutive fronts are the minimum possible distance that does not incur a significant overlap of the front lines.

The fluid arrival time field used as input for fluid speed field computation is filtered using Gaussian filter in order to reduce the noises and smooth the image for better front picking performance. The degree of smoothening varies depending on standard deviation (sigma) chosen for the Gaussian filter that can significantly control the resulted fluid speed fields. To choose a proper standard deviation, a series of fluid speed computation were carried out on the same input fluid arrival time field but using different standard deviations of 3, 4, 5, 6 and 7 for Gaussian filter. The front picking time step was kept constant (4 min) for all five series of computations. Figure 3.19 shows a vertical slice of binary image of a fluid arrival time (Coquina sample C13) at time: 80 min and the corresponding vertical slices after being filtered by different standard deviation values of 3, 4, 5, 6 and 7 of Gaussian filter. The vertical slices of the resulted fluid speed fields are also shown below each filtered image. As shown in this figure, when the low standard deviation values (3 and 4) are chosen, the complex morphology of the fluid front is better preserved while so many isolated clusters are remained in the segmented image that resulted in non-reliable fluid speed calculation. On the other hand, increased standard deviation values (6 and 7) are found to over-smooth the front and does not preserve the details of the front. The standard deviation of 5 for Gaussian filter is found to provide the best results for the tested sample since it avoids most of the isolated clusters in the binary image (that cause non-reliable fluid speed calculation) while retaining a good level of details in the morphology of front.

3.4.2.3 Differential imaging

As mentioned in section 3.3.8, the differential imaging is used to get an insight into the relative concentration of miscible phases and saturation of immiscible phases. Here, the reliability of this technique for these calculations is investigated. For calculating the

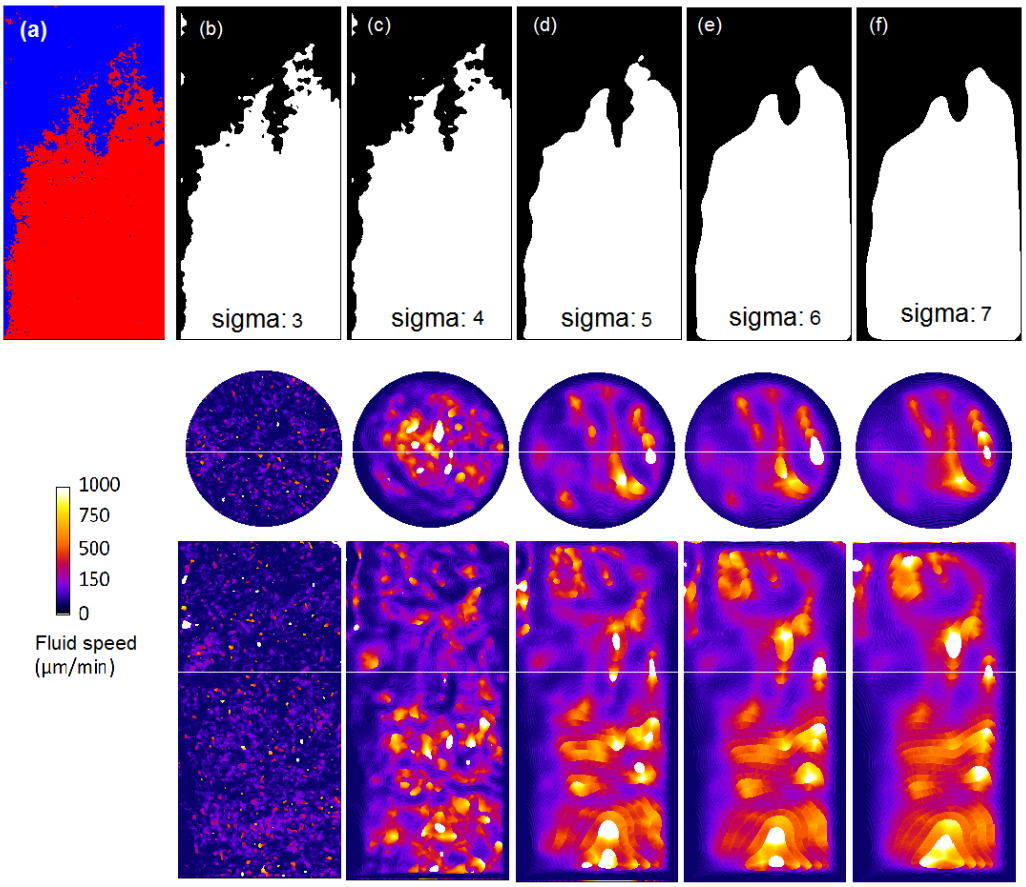

Figure 3-19 Vertical slices of binary fluid arrival time field (a) and corresponding filtered image by applying Gaussian filters with standard deviations of 3,4,5,6 and 7. The resulted fluid speed fileds are presented below each filtered image. For fluid speed fields presented in this figure, HSNTs acquired during injection of one pore volume of water into previously heavy water saturated sample is used. The flow direction is from bottom to the top end of core sample.

normalised relative concentration in each voxel, the grey-scale changes are divided by the maximum grey-scale changes observed in pore spaces of the sample. For this purpose, differential grey-scale values for some large and connected pores (explored using corresponding X-ray tomography image) in different parts of the sample in which the highest fluid displacement was expected was calculated and used for normalising. Here, the assumption was made that the full fluid displacement or mixing has happened in these pores. Although, the fluid displacement or mixing in these pores approaches a fully displaced or mixed condition, but more accurate data on this requires injection of more pore volumes of the injected fluid that was not possible due to the time restriction during Neutron experiments. Therefore, calculated normalised relative concentration and saturation may have some uncertainties that makes a reliable comparison of the results of different samples a bit challenging. Nevertheless, the way that these data have been used and interpreted in this study is still reliable as they are used for investigating the relative concentration/saturation

distribution of phases within each sample and not as an absolute value for comparing with other samples. In fact, the relative concentration values for each sample has been normalised by the maximum grey-scale difference of that specific sample and it should not be used as absolute value when comparing different samples.

The other parameter that should be noted when interpreting the results of differential imaging is the impact of beam hardening. As explained in section 3.1.3, the beam hardening artefact can result in erroneously high calculated beam attenuation in the lateral borders of sample and as a result, higher grey-scale values in these regions. This artefact is expected to be intensified when there are more hydrogen in the sample that attenuates low energy neutron beams in the thicker part of the sample. The erroneously higher grey-scale values at the lateral boundary of the sample can result in higher calculated differential value in these regions. Figure 3.20 shows the vertical slices of differential imaging (of a Coquina sample, C11) at different times after onset of flow experiments (here, injection of water in previously heavy water saturated sample). As its observed in this images, by increasing the time (e.g. 125 min) and increasing the amount of hydrogen reach fluid (water) in the sample as a result, higher differential values is obtained at the lateral boundary of the sample that can be due to the beam hardening artefact. This should be taken into account when interpreting the differential imaging for studying relative concentrations distribution of phases.

3.4.2.4 Surface area of the leading front

The surface area of the leading front, as described in section 3.3.5, can be used as a quantitative measure of the irregularity of the fluid front surface that is expected to be highly variable in carbonate rocks due to their heterogeneous pore system. Given that the surface area can represent the extent of roughness and unevenness of a surface, it is expected that the calculated surface area value to be highly sensitive to the capability of the imaging technique to resolve the surface roughness and unevenness of different scales. In fact, this is directly

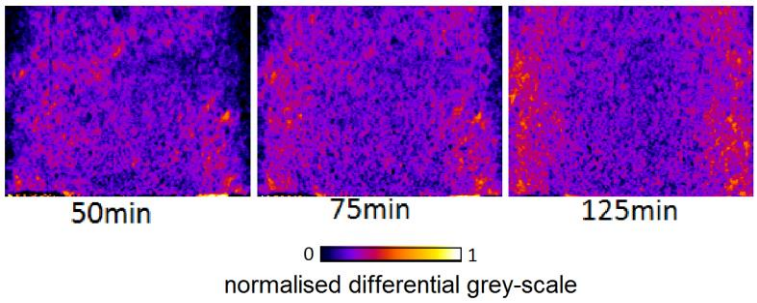

Figure 3-20 Vertical slices of differential image of a Coquina sample (C11) at different time during injection of one pore volume of water into heavy water saturated sample. Only the bottom half of the vertical slice in which the effect of beam hardening is obvious are shown in this figure. The higher normalised differential grey-scale in the lateral boundary of the sample is due to the beam hardening.

liked to the spatial resolution of the image used for calculation of the surface area. To investigate the sensitivity of the calculation of the front surface area, first, fluid arrival time field of a Coquina sample (C13) with spatial resolution of 170 µm was used from which two fluid arrival time fields with reduced spatial resolutions of 340 µm and 680 µm were extracted by applying 2x2 and 4x4 binning respectively on the original fluid arrival time field (170 µm voxel size). Then, surface area of the front at four different times were calculated for these fluid arrival time fields. Figure 3.21 shows the calculated surface area of the leading front. As seen in this figure, the calculated surface area values decreases with reducing the spatial resolution of the used fluid arrival time field. This is because that in the image with higher resolution, surface roughness can be better resolved compared to the lower spatial resolution images. It is also observed that the surface area of the front changes with time regardless of spatial resolution so that the trend of these changes are resolved even in reduced resolutions. It suggests that these changes are caused by larger-scale unevenness or irregularities in fluid front (like protrusions and finger like morphology of the front) that are resolvable even in lower spatial resolutions.

3.5 Fluid flow simulation and permeability computation

To explore permeability variation within the samples and how this can be affected by any local (due to textural variation) fluctuations of pore network properties, permeability values must be estimated for each sub volume of the sample. Laboratory measurement of

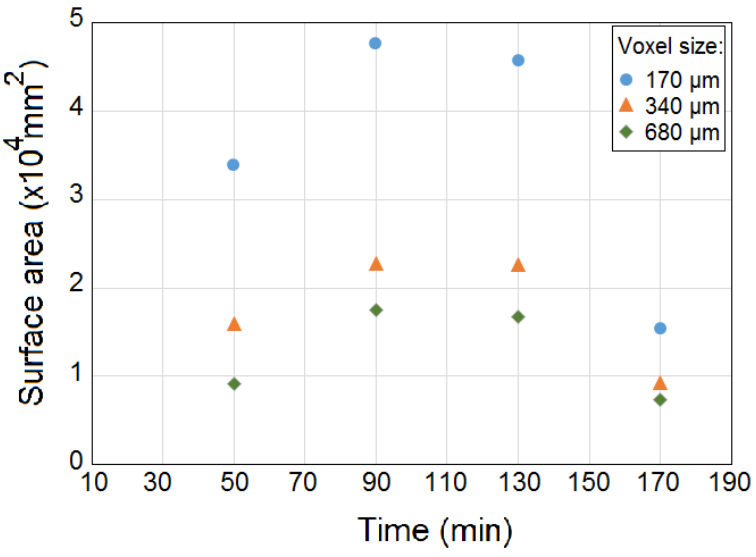

Figure 3-21 Surface area of the advancing fluid front at four different times calculated based on the fluid arrival time fields with different spatial resolutions (170 µm, 340 µm and 680 µm)

permeability (gas permeameter) give a *global* permeability value for the whole sample and does not provide any information of its local variations within the sample. On the other hand, computational fluid flow simulation allow us to compute the permeability of sub sections of the sample non-destructively. In this study, pressure-driven flow simulation using the lattice-Boltzmann method (LBM) was used to calculate permeability for subsections of a sample. The input of this method is the 3D pore network image extracted from the X-ray tomography of the sample by means of Weka trainable segmentation. The X-ray tomography image (53 µm voxel size) of the core sample was split to 29 disc shaped sections along its Z direction (with radius and thickness of 19000 and 2500 µm respectively) and LBM was used to calculate permeability for each section.

The 3D segmented image of pore spaces was exported from ImageJ with the *.obj format, converted to *.stl format using MeshLab software, a 3D mesh processing software system, and eventually imported to OpenLB package to find its absolute permeability. OpenLB provides a C++ package for the implementation of lattice Boltzmann methods (LBM), addressing a vast range of transport problems, e.g. in computational fluid dynamics.

The absolute permeability of the segmented 3D image of the sample was obtained by simulating flow of a single phase, incompressible, and Newtonian fluid through the pore space, where a fixed pressure gradient was imposed between the inlet and outlet, while considering the lateral faces considered sealed. A no-slip boundary condition was also considered to capture the rock-fluid interaction by using the standard bounce-back method. A zero velocity field was also considered to initialize the simulation. The simulation ended by reaching to a steady state, where the standard error of the velocities becomes less than 10^5.

At steady state, the computed average fluid velocity per unit of area (U) from the simulation results was used to calculate the permeability k in the direction of imposed flow for each section using Darcy law, $\frac{\partial \mathrm{P}}{\partial \mathrm{x}} = \frac{\mu}{K} U$ in which µ and $\frac{\partial \mathrm{P}}{\partial \mathrm{x}}$ are the fluid kinematic viscosity and flow pressure gradient, respectively. Since all the variables are in lattice units, the obtained permeability was transformed to SI units via multiplying it by the effective length of the voxel side in meters. To make sure that the Darcy law has been implemented, it was checked that the permeability is constant by using different pressure gradients and the Reynolds number satisfies the condition: Re <10.

3.6 Summary and discussion

This chapter described the methods used in this study including X-ray and Neutron imaging methods and various image processing and analysis methods employed to extract qualitative and quantitative results from the acquired images. Here, a summary of these methods are presented along with their advantages and limitations.

Both X-ray and Neutron tomography are non-destructive methods that provide information (of properties of interest) within the scanned material. Complementary capabilities of X-ray and Neutron tomography that comes from their different sensitivities to the different parts of the rock-fluid system were employed in this study. Sensitivity of X-rays to the materials atomic number, provides the possibility of mapping the density variation within the material that has been scanned with X-ray tomography. Considerable contract between the void spaces (air-filled) and solid component of the rock in the X-ray tomography images makes these images ideal for investigating internal structures in rock samples (like fractures) and extracting the pore network images of the samples.

Unlike X-rays, Neutrons attenuation is not dependent on the atomic number of the element, but instead varies based on particular isotope of the element. Sensitivity of Neutrons to Hydrogen ($_1H$) (that highly attenuates Neutrons) makes the Neutron imaging ideal for detecting hydrogen-rich fluids such as water and/or hydrocarbons. High fluxes of Neutrons allows for the application of the High Speed Neutron Tomography that is useful method to capture the dynamic of fluid flow within porous rocks. However, the use of Neutrons is limited in the world because of the difficult process of producing Neutron in enough flux required for imaging or other Neutron scattering applications. On the other hand, lab-based X-ray tomography equipment is widely accessible nowadays but require considerable density difference between fluid phases to achieve enough contrast between the fluids.

The principals of Neutron tomography provided in this chapter indicate that there is a trade-off between the image quality and temporal resolution when scanning a sample using this method. Another trade-off exist between the sample size and the spatial resolution that can be achieved. Choosing the proper parameters to achieve the right combination of spatial and temporal resolution mainly depends on the features and processes of interest that need to be studied. While a Neutron tomography with longer exposure time can results a high signal to noise ratio and provide a very good quality image (Yehya et al., 2018), scanning at high temporal resolution can cost in relatively lower quality and lower spatial resolution (Cordonnier et al., 2019). Although the temporal resolution does not directly control the spatial resolution, but to compensate for the low signal to noise ratio during scanning at higher temporal resolutions, a binning may be applied to the image that reduces the spatial

resolution. Sample size can also control the spatial resolution during Neutron tomography. While the small sample size (6 mm diameter) has allowed a high spatial resolution (11.8 µm voxel size) Neutron tomography (Murison et al., 2015), the maximum spatial resolution achieved in this thesis is 85 µm for a 38mm diameter size sample.

Depending on the physics to be resolved, the proper spatial and temporal resolutions needs to be defined. In this study, an attempt has been made to achieve the highest temporal resolution for HSNTs. This is because the quick processes like flow through fractures or capillary uptake of fluid during immiscible two-phase flow need to be studied in this thesis. To achieve this temporal resolution, the binning 2x2 was applied to the HSNT images resulting in reducing spatial resolution from 85 µm to 170 µm. This introduces limitations so that the micro pores smaller than 170 micron size and details of pore (fluid) occupancy and displacement processes at pore scale cannot be resolved. These limitation however, do not obstruct our work since the main focus of the HSNT analysis in this thesis is to resolve the fluid displacement processes associated with larger scale features (mm to cm scale) like fractures, layering and anomalous textural variation. The capability of the HSNT and the chosen temporal and spatial resolution to resolve different features and processes related to tested sample and fluid displacement within them will be discussed more specifically in chapters 5 and 6 where the results from miscible and immiscible fluid flow experiments are presented.

Different image processing and image analysis methods are employed to extract qualitative and quantitative data from the X-ray tomography images. The results from this analysis that mainly focuses on quantifying pore network properties (such as porosity, specific surface area, tortuosity, pores connectivity and pore) are very dependent on the used algorithm and are sensitive to the images spatial resolution. The image segmentation as the first step for quantitative analysis has crucial importance in the reliability of the results. After comparing the performance of different segmentation methods (including manual thresholding, Otsu, watershed and trainable Weka segmentation), X-ray and Neutron tomography images were segmented using the Weka segmentation method. This method provides the very good quality of segmented images without needing any pre-processing (filtering) on images that helps to save time and retain the details of the features in the images. In addition, this method was identified as most robust method against image noises among the tested methods.

Image analysis methods are also employed on HSNT data to better visualise the flow patterns, track the fluid front advancement and calculate fluid speed field. Due to the short acquisition time in HSNTs, the weak signal to noise ratio makes the analysis of these data a bit

challenging. Employing a sigmoidal fitting on the grey-scale evolution of each voxel with time can be used to quantify the fluid arrival time for every voxel of the 3D volume. This provides the possibility of an effective tracking of the fluid front advancement in the case of low contrast to noise ratio in these images. The goodness of the sigmoidal fitting to the evolution of grey-scale data is investigated based on the fitting error field extracted during the image analysis. The error in sigmoidal fitting that shows how close are the grey scale values to the fitted sigmoidal can control the reliability of the parameters calculated form the sigmoidal fitting method such as fluid arrival time and D-parameter. Different parameters may affect this error value such as signal to noise ratio during image acquisition, temporal resolution, and some parameters related to the flow experiments and the features in the sample. The observation from error analysis in this chapter suggest that the lack of full fluid displacement in some parts of the matrix (for instance in fractured sample in which flow is dominated through the fracture) with high distance from the fracture increases the sigmoidal fitting error and adversely affect the reliability of the results for these regions. However, the results are still useful as they provide robust values in most of the voxels, but care should be taken when interpreting the results in similar samples. It was also observed that the sigmoidal fitting error increases by decreasing the temporal resolution and number of HSNTs used for the sigmoidal fitting. By decreasing the temporal resolution from 1 to 2 minute error slightly increases. However, by further reduction of temporal resolution to 3, 4 and 5 minute, the error significantly increases that result in increasing the miscalculated fluid arrival time and D-parameters.

By having the position of fluid fronts at different times, the distance between every two consecutive fronts can be calculated and given the elapsed time, fluid speed in each voxel can be calculated. This method is able to provide a 3D field of fluid speed within the sample. However, the main limitation is that it only provides the shortest path distance for the fluid while the fluid does not necessarily flow through the shortest pass in real case (flow in porous rock). In fact, the fluid speed calculated in this method may be underestimated. It was also shown in this chapter that calculation of fluid speed is sensitive to input parameters including front picking interval and the standard deviation of the Gaussian filter applied on the fluid arrival time field. This is also another limitation of the technique that highlights the importance of choosing proper input parameters. To find the best combination of input parameters, the fluid speed calculations were carried out on a same sample using 4 different input for front picking interval and 5 different input for standard deviation of Gaussian filter and the proper input parameters were then chosen based on qualitative visual examination of

the resulted fluid speed fields. However, the results indicated that the computed fluid speed are highly sensitive to the chosen parameters.

Chapter 4

Materials and experimental procedure

This chapter presents the studied material and the experimental procedures followed during the sample preparation, the lab-induced mechanical deformation and the flow experiments. The tested materials in this study are from different types of carbonate rocks with distinct textural characteristics. Carbonates host considerable part of reservoirs which accommodate significant proportion of geofluid resources around the world. Thus, accurate evaluation of their hydraulic behaviour is of crucial importance. These rocks are characterised by challenging pore systems since the various process involved during deposition and diagenesis in these rocks result in spatial variation of their petrophysical properties and bring many uncertainties to the estimation of their flow properties. Thus, a successful evaluation of fluid flow in these rocks requires a deeper understanding of the impact of textural variations and mechanical deformation features (like fractures and/or deformation bands) on pore network properties of these rocks. For this purpose, four types of carbonate rocks from different textural classes were investigated including Coquina type Limestone, Oolitic limestone, Travertine and Biolithite. Samples characteristics have been investigated in different ways from visual examination of the hand specimens, to analysing petrographic thin section images (destructive) and qualitative and quantitative investigation of the X-ray Computed Tomography (CT) images (non-destructive) acquired from the samples. The focus, however, has been placed on the X-ray CT analysis. Impact of textural characteristics on both pore

network properties variations and mechanical behaviour (under triaxial compression) of the sample are investigated and presented in this chapter. Also, any alteration in pore network of samples caused by the lab-induced mechanical deformation has been investigated. Pore network properties including porosity, specific surface area, pores connectivity and tortuosity have been quantified for different samples. The variations of these properties along the length of one of Coquina samples and their correlation with the computed absolute permeability values was also investigated.

The experimental procedures employed in this study have also been presented in this chapter. First, a general workflow is provided and then a detailed description of sample preparation, mechanical deformation of the samples and the fluid flow experiments coupled with high speed neutron tomography have been presented.

4.1 Experimental procedure

4.1.1 General workflow

In this study, complementary capabilities of X-ray and Neutron imaging methods were used for pore network characterisation of heterogeneous and mechanically deformed carbonate rock samples and to study the fluid flow within them respectively. First, core samples were prepared from four types of carbonate rock and then porosity and permeability of these samples was measured at the laboratory. Next, using triaxial compression, selected samples of each rock type were mechanically deformed while the rest of samples remained intact. This was to induce mechanic deformational features like fracture and/or deformation bands and to investigate their impact on fluid flow in samples. From now on, the samples that were not subjected to the lab-induced mechanical deformation are called *intact*. X-ray tomography images acquired from selected samples enabled us to visualise the 3D structure of the samples, extract their pore network and analyse the pore system properties and their variations caused by the lab-induced mechanical deformation. The samples were then prepared and placed in a portable fluid flow set-up to run the flow experiments coupled by real time Neutron tomography. The coupled flow experiments with HSNT acquisition enabled us to capture 4D flow (3D + time) during flooding the samples with Hydrogen-rich fluids (water, heavy water and oil). In addition to fluid flow dynamics, normal Neutron tomographies with higher resolution were also acquired to examine the 3D distribution of different phases in the samples in different time steps after flooding. The flowchart of the experimental procedure followed in this study is presented in figure 4.1**.**

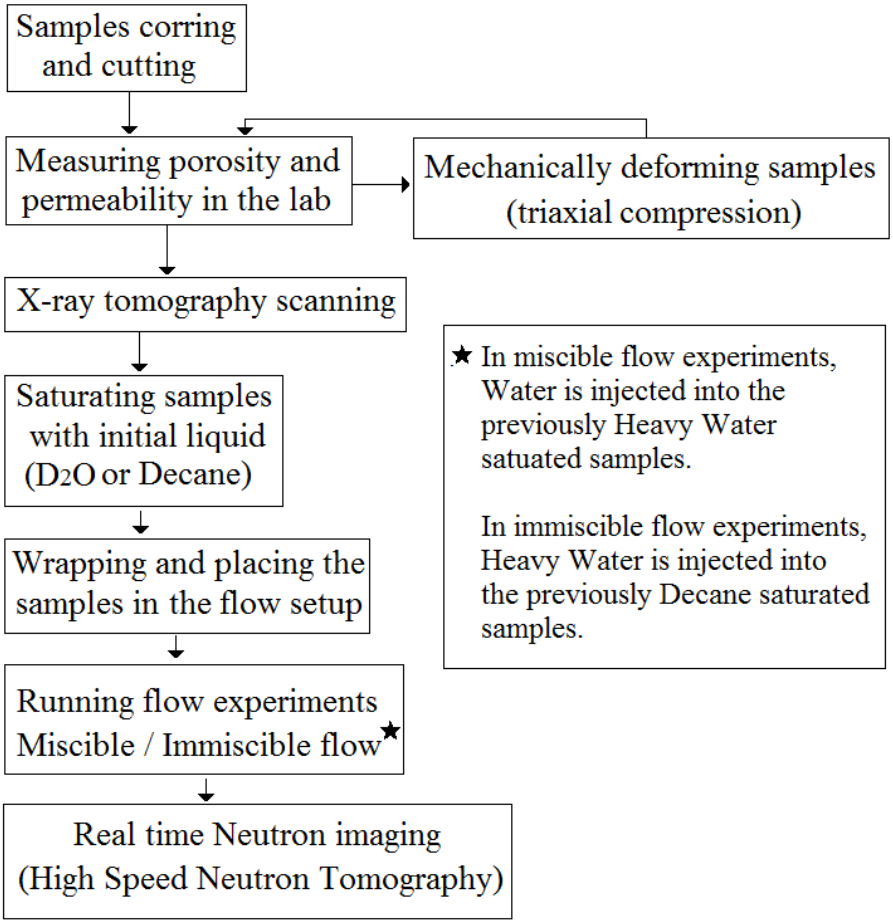

Figure 4-1 The flowchart of the experimental procedure followed in this study

4.1.2 Sample preparation

All the samples studied in this work, were cored from the rock blocks of each rock type using a rock coring machine at Heriot-Watt University and were then cut to the required length. The samples had a diameter of 38 mm and a length of 76mm. They were cored in two (or three for the Biolithite) orthogonal directions to capture any potential anisotropy in flow properties and mechanical deformation. The names of the samples were coded in the following way: the names begin with a letter indicating the rock type (C for Coquina, B for Biolithite, T for Travertine and O for Oolitic limestone) followed by a two digit numbers. The first digit defines the coring direction (1, 2 and 3) and the second digit is unique for each sample. For instance, C13 is the third Coquina sample that is cored in the first defined direction. The bottom and top edges of the core plugs were lightly sanded by sandpaper to remove the dust and scratch traces caused by the saw.

Those samples (deformed and intact) used for the flow experiments (at HZB or ILL) had been previously saturated in the fluids of interest. Depending on the scope of each experiment, samples were saturated in heavy water or in decane before the experiments. Two types of set-up were used, depending on where the saturation took place. In the first set-up, (figure 4.2 a) samples were placed in a beaker filled with saturating fluid; the beaker was put in a glass vessel connected to a vacuum pump. By applying the vacuum to the glass vessel, air in the sample pores started to be replaced by the fluid in the beaker. The samples were left under the vacuum about 12 hours until no bubbles could be seen at the sample surface meaning that the sample approached to its fully saturated condition. Also, the samples were weighted before and after initial saturation and the porosity of sample were calculated based on the weight of the saturating fluid to make sure that the value is very close to the measured porosity of the sample using Helium Porosimetry. For the first experimental round, this process was carried out at Heriot Watt University and the samples were wrapped in Teflon (PTFE) tape, packed and sealed in plastic bag to remain saturated during their transport to the experimental facility (ILL). The second set-up was used when the saturation took place in the beamline facility shortly before the flow experiments. This setup (figure 4.2 b,c) included a 50mm cylindrical core holder that had a valves, that is first connected to a vacuum pump. Once the sample placed inside the holder (without any fluid), vacuum was applied while the valve was open. After reaching the highest vacuum inside the core holder, the valve was closed and the setup is disconnected from the vacuum pump and connected to a funnel. After filling the funnel with desired fluid, the valve is gently opened until the fluid in funnel is sucked into the core holder due to a vacuum within the core holder and the sample got saturated in the fluid. Care should be taken that no air find its way into the core holder by maintaining enough level of fluid in the funnel when the valve is being open.

4.1.3 Porosity and permeability measurements

Porosity and permeability of the prepared core sample were measured using Helium porosimeter and Nitrogen gas permeameter at the rock mechanics laboratory of Heriot-Watt University. A brief description of the methods used for porosity and permeability calculation is presented below.

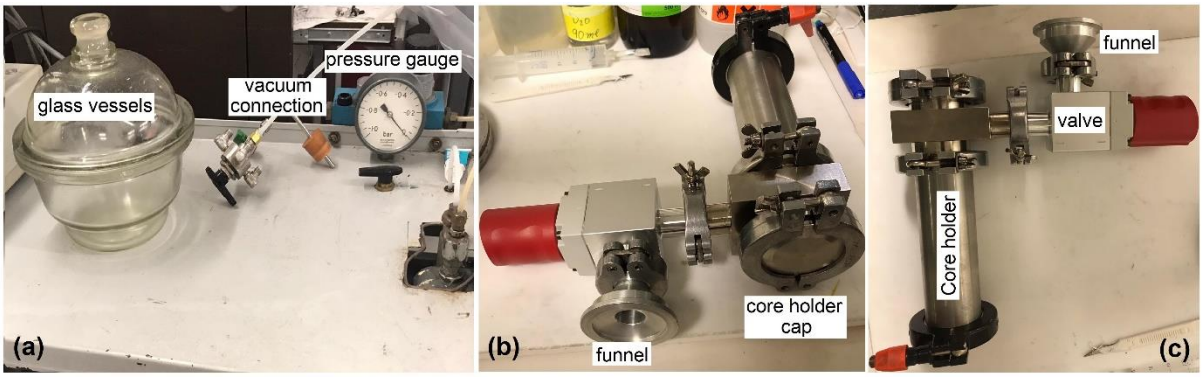

Figure 4-2 Photos of the vacuum vessels used for initial saturating of the samples with fluids (heavy water or decane) at Heriot Watt University (a) and at HZB neutron facility (b and c).

4.1.3.1 Helium porosimetry

A helium gas expansion porosimeter was used to determine the porosity of the 38mm diameter core samples. The porosimeter encompasses a steel sample container (cup) of known volume (Vc) connected to a reference cells of known volume (Vr) via a valve. First, the sample is placed in the chamber and the helium is filled in the cell while the chamber is isolated by the closed valve and the pressure in the reference cell is recorded (P1). Then helium is allowed to expand into the chamber containing the core sample by opening the valve. After reaching to an equilibrium pressure (P2), the volume of the solid components of the sample (Vs) can be calculated based on Boyle's law:

Equation 4.1 $$P_1\ Vr = P_2\ (Vr+Vc-Vs)$$

Then, by having the bulk volume of the core sample calculated based on the core plugs dimension, the porosity is calculated. Before measurements, calibration was carried out by using standard steel samples of different sizes with given weight and volume.

4.1.3.2 Nitrogen gas permeametry

Permeability of the dry core samples was measured by using Nitrogen gas (N_2) permeameter. In this method, the core sample is placed in a core holder that is designed for gas flow across the core plug (from inlet to outlet) while a confining pressure is applied to the sample lateral surface to avoid gas flow at the interface between samples cylindrical surface and the core holder wall. Then, an appropriate pressure gradient is adjusted across the core sample and the flow rate is recorded by measuring the volume of injected gas in a given unit of time. The same procedure is repeated for three different pressure gradients and flow rates. The measurement of the permeability should be carried out at the low flow rate to avoid turbulent flow within the sample.

To calculate the permeability, the ratio of flow rate to area (q/A) is plotted versus the pressure function (P1 - P2) / L (where P1 and P2 are upstream and downstream pressures and L is the length of core plug) for three different flow rates. Based on the Darcy law (equation 4.2), the slope of the linear part of the graph is equal to K/μ, where K is the permeability and μ is the viscosity of the flowing fluid.

Equation 4.2

$$Q = -\frac{KA}{\mu}\frac{dP}{dL}$$

The part of the graph that deviate from the straight line indicates the turbulent flow. Calculated gas permeability values were converted to the liquid permeability by considering the Klinkenberg effect [3].

4.1.4 Mechanical testing

4.1.4.1 Triaxial compression testing apparatus

The laboratory-induced deformation of the used material was carried out in the rock mechanics laboratory of Heriot-Watt University. Samples were deformed under triaxial compression loading using the Hoek Cell (Hoek & Franklin, 1968) and a loading frame. As shown in figure 4.3, the Hoek cell consists of a hollow steel cylinder with two removable ends. A rubber sleeve suitable for 38mm diameter core creates a pressurizing chamber for applying uniform hydraulic pressure to the curved surface of a cylindrical specimen. At bottom and top ends of the cell, there are 38mm diameter cylindrical platens that contact the samples flat ends. A spherical seat is used at the top platen to ensure axiality of loading by compensating for any initial misalignment of the specimen ends. To provide a confining pressure, the inlet of Hoek cell is connected to the confining pressure intensifier through a quick-connect fitting. The used apparatus is capable to apply a maximum of 50 MPa confining pressure.

Axial loading is applied using a servo-hydraulic loading frame from RDP Howden with a maximum loading of 1000 kN. The system controlling the triaxial apparatus allows both load/pressure and displacement control modes. The data from the Load cell (measuring the axial load), displacement

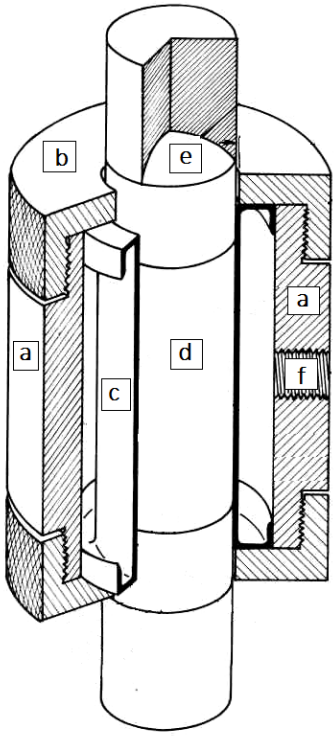

Figure 4-3 A schematic cutway view of the Hoek cell on the right (Hoek and Franklin, 1968). The steel cylindrical cell (a) with two removable ends (b) encompasses the rubber sleeve (c) and the sample (d). The hardened steel platen with spherical seat (e) and the hydraulic fluid inlet (f) are shown.

gauge (recording the axial displacement of the piston) and confining pressure transducers are all collected and recorded into computer using Instron controller and software. The whole procedure of triaxial loading is controlled by the Instron WaveMatrix software that enables us to define and control the test path for each experiment.

4.1.4.2 Testing procedure

After embedding the sample in the Hoek cell and placing the cell between pistons of the load frame, 4 main loading steps including isotropic compression loading, deviatoric compression loading, deviatoric compression unloading and isotropic compression unloading were carried out. In the first step, isotropic compression was applied to the sample by increasing the confining pressure with the rate of 2 MPa/min in the Hoek cell and its equivalent axial load at the same time until reaching to the confinement of interest. In the next step, the deviatoric loading was applied to the sample by moving the piston at the constant displacement rate of 20 µm/min while the confining pressure was kept constant. During the loading, the live load-displacement graph is regularly checked to have an idea of the yield point and the peak load to decide when to start unloading. Slightly after the peak load point and by reaching the desired axial strain, the unloading step started. First, the axial load was decreased down to the load equivalent to the isotropic load and then both axial load and confining pressure decreased to zero in same duration of time and at the same rate as the loading was applied.

As mentioned above, the programme of each test was defined in the software before starting the test.

To account for the loading frame stiffness, axial displacement correction was carried out for all samples. For this purpose, a uniaxial loading test was conducted without a sample in which a column of all metallic components used during the experiments (platen, spacers etc) were loaded up to 300 KN axial load. Based on the load-displacement curve of the calibration test, the measured displacement of the piston were corrected for every triaxial compression test.

4.1.5 Fluid flow experiments

For fluid flow experiments, performed in European Neutron Facilities, a portable flow set-up was needed to be transported to the neutron imaging facilities. This set-up should be designed in a way that allows for real time neutron imaging during the injection of fluids within the sample. Figure 4.4 shows a schematic representation of the flow set-up used in this study. The main components of this set-up [4, 5] are two aluminium caps, the shrinkable membrane, the syringe pump, air trappers, pressure transducer and tubing. A national instrument card and LabView software were also used to control the system from outside the imaging chamber and record the required

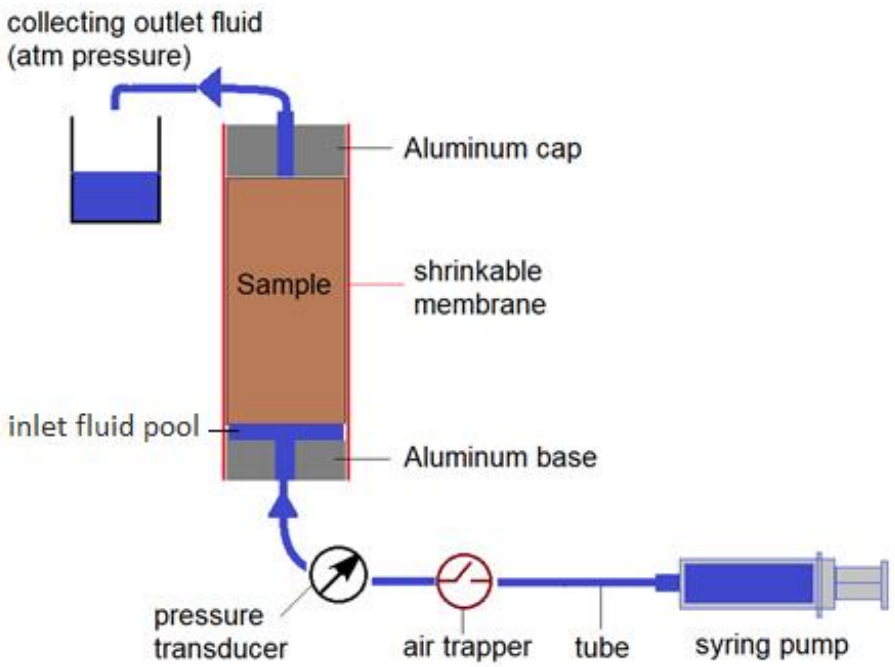

Figure 4-4 schematic representation of the used flow setup; blue arrows show the flow direction**.**

measurements. The aluminium used to build the caps is 7075 T6 aluminium alloy which has relatively low activation by neutrons.

In this set-up, core sample is placed vertically between two aluminium caps that have a 2 mm diameter hole in the centre connected to tubes for fluid inlet and outlet. There is a 2 mm deep engraved reservoir that covers most of the width of the bottom cap. This is to insure the even distribution of injected fluid pressure at the bottom face of the sample. While a heat shrinkable membrane surrounded the sample and caps, the chosen liquid is injected into the bottom end of the sample by means of a syringe pump. The membrane is used to keep the sample and the caps in firm touche and is intended to prevent leakage from the samples circumference during the flow experiments. A pressure transducer is connected as close as possible to the inlet tube in order to measure the differential fluid pressure. The signal from this transducer, corresponding to the inlet pore pressure, is received, converted and recorded continuously with a sampling frequency of 5 seconds during the flow experiments by means of national instrument card and LabView software. At the top of the sample, a tube connected to the aluminium cap allows to collect the outlet fluid in a container.

The first step in the flow experiments is to assemble the experimental equipment (by connecting all its components) outside the experimental chamber at HZB or ILL. The syringe and tubing connecting the syringe to the aluminium base need to be filled with the desired fluid (water or heavy water depending on the experiment). The most important point in this step is to avoid any air bubbles in the system. The air trapper valves, connected to the inlet tubing, allows to get rid of any potential air bubbles inside the tube up to the base aluminium cap that touches the sample bottom. Then the saturated sample (see section 4.1.2), is placed on the base aluminium cap and then the top aluminium cap is fitted. Before putting the membrane, a few rounds of (PTFE) tape is evenly applied to cover all around the aluminium caps and the sample. The PTFE (as a polymer with near zero water absorption) tape, is used to provide a better sealing between the samples periphery and the membrane. Once the assembly is kept aligned, its confined (very small pressure) by using a shrinkable membrane. The membrane used for the experiments was Fluorinated Ethylene Propylene (FEP) membrane with 0.5 millimetre thickness that shrinks from diameter of 43mm to 32mm. This type of membrane is chosen for its low interaction with neutrons. The selection of proper membrane for neutron imaging application is discussed by Etxegarai (2019). The membrane then placed around the sample and heated using a heat gun to shrink. It is observed that some droplets of fluid were expelled from the (already saturated) samples outlet due to the heating. Expansion of fluid in the pores and slight confinement applied to the sample from shrinking

of the membrane seems to be responsible for this to happen. In some experiments the top cap is not used and a longer heat shrink tubing is used instead to provide a reservoir at the top of the sample to collect the outlet fluid. No significant flow at sample-matrix interface was observed by checking radiographies during the experiments.

The whole assembly containing the sample is then taken into the experimental chamber and placed on the rotary stage between the beam and the detector by attaching an aluminium stand to the base aluminium cap. Figure 4.5 shows the prepared sample and its positioning on the rotating table. After adjusting the position of the stage with respect to the neutron beam entry point and detector, the liquid outlet tubing is fitted and guided into a container for collecting

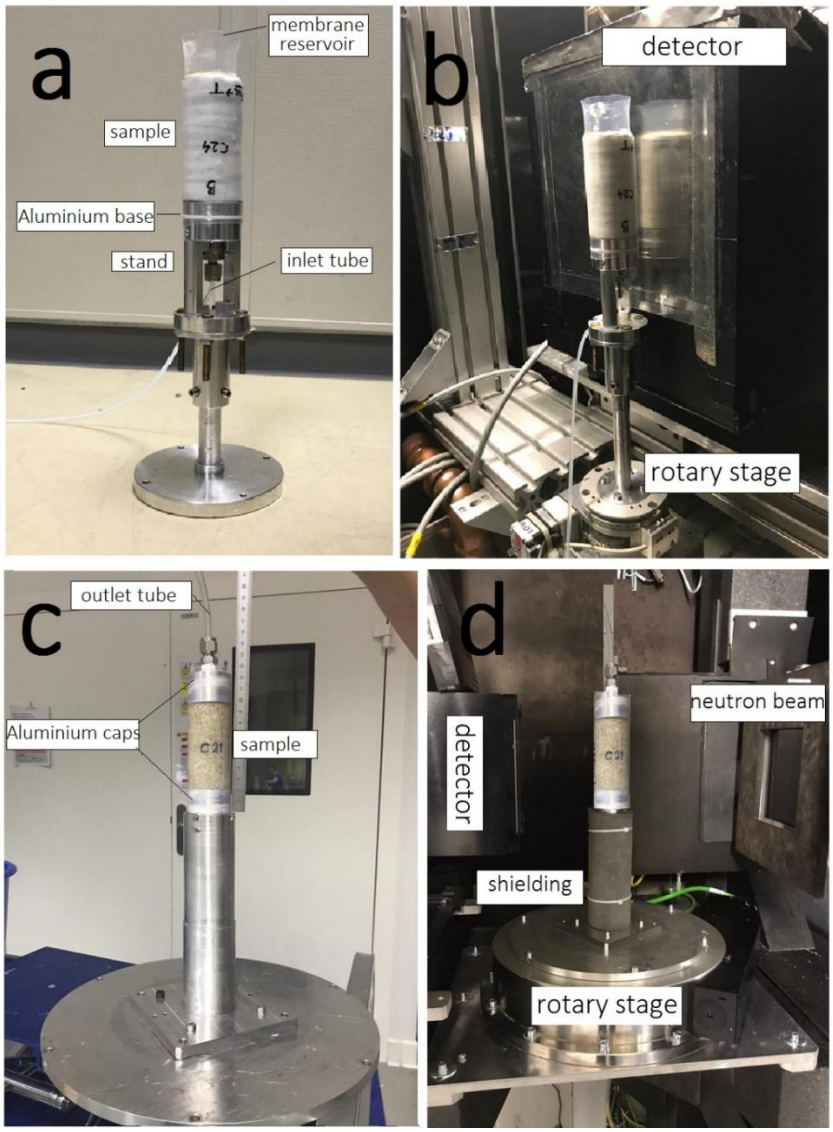

Figure 4-5 Photos of the sample and flow set-up prepared for flow experiments. a) a prepared sample with one aluminium base and a membrane reservoir left at the top for collection of outlet fluid, b) the sample placed on the rotary table in the beam at HZB (b), c) a prepared sample with two aluminium caps connected to inlet and outlet tubes, d) the sample placed on the rotary table between the neutron beam and detector at ILL.

the outlet fluid. This equipment is positioned so that the sample can be freely rotated in through the 180 degree angle required for the tomography acquisition. Shielding (Boron Carbide sheets) is used to cover the parts of the aluminium base and the attached stand in the neutron flight path in order to reduce their activation and thus the required cooling off period of the equipment before it could be handled and reused. The pump is located outside the experimental chamber and the start and end of the flow experiment as well as the flow rate are controlled manually from outside the experimental chamber.

4.2 Material

Four types of carbonate rocks were used in this study: Coquina; Oolitic limestone; Travertine and Biolithite. A brief geological description of these rocks is presented in this section followed by a detailed characterisation of their texture and pore structures.

The Coquina type Limestone, from the Provence Region of France consists mainly of shelly fragments. A block of this rock has been collected from a quarry at Crillion le Brave, south west of Bedoin. In this area, the Coquina unit with the geological age of 20 to 16 million years ago (Burdigalian age) directly overlies the Crillon le Brave Conglomerate (which is 38 to 34 million years old, (Priabonian age). So there was either a significant period of non-deposition (a disconformity) or deposition followed by erosion – an unconformity of at least 14 Ma. Below Crillon le Brave Conglomerate is the Ferruginous Sands which are not well dated and sit directly on the Bedoin sands. Above the Crillon le Brave Coquina are younger Miocene rocks and sediments units (Geological map of Provence region, France; http://infoterre.brgm.fr/).

The Oolitic limestone is from the Bath Oolite member which has about a 15 meter thickness in the Bath area, England. It consists mainly of Ooids, spherical grains formed as concentric layers composed mainly of calcium carbonate. This unit with the geological age of 195 to 135 million years ago (Bathonian) was deposited in shallow marine environment. With a sharp change, it sits on generally non-Ooidal, Pisoidal and shelly limestone of Twinhoe Member. The Travertine and the Biolithite come from a quarry in Northern Greece, which belongs to a company. Most of the geology is confidential, thus, only description based on the acquired measurements in this thesis will be discussed here.

4.3 Material characterisation

4.3.1 Hand specimen rock description and prepared samples

All the samples investigated in this study have been cored from rock blocks. In this section, the characteristics of each rock type based on the observation from rock blocks and examination of hand specimens are presented. Also, the coring direction of the samples and their naming convention is provided.

For the Coquina limestone, a block with dimensions of approximately 20*20*30cm had been collected from the outcrop. Examination of hand specimens indicated that this material can be described as a highly porous fine-grained and grain-supported carbonate grainstone (figure 4.6) which consists of poorly cemented shelly fragments with a tan-grey colour. In the rock block, a few thin layers or laminae (with approximately 2-4 mm millimetre thickness) can be distinguished in the block based on variation in colour and looser grins within the layers. These almost parallel layers are successively distributed within a 2-3 cm thick zone in bottom of the block. Core plugs of a diameter of 38 mm and a length of approximately 80 mm, were cored in two different direction with regards to these layers. Samples cored normal to the blocks layers are named C11, C12, C13 and C16; samples elevation within the blocks height varies, thus, the presence of layers within the height of each sample is not always at the same position (height). The second group of samples including C21, C22, C23 and C24 are cored parallel or sub-parallel to the layers; the first two encompass some of the layers while the other two are cored outside the layered zone in the block. A schematic image has been shown in figure 4.7 that shows approximate position of the samples cored from the rock block with regards to the layered zone. In this schematic figure, three samples are shown as example including the sample from outside layered zone (C21) and two other samples from inside the layered zone including the one perpendicular to the layered zone (C13) and the one parallel to the layered zone (C24) samples.

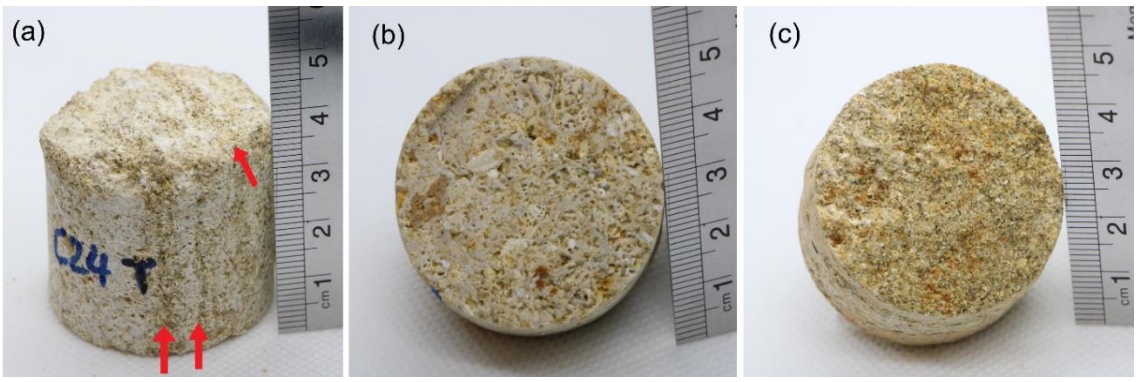

Figure 4-6 hand specimen of the Coquina sample (a) see the vertically oriented layers with somehow different colour (indicated by red arrows). The shelly fragments and some pore spaces between them are easily visible (b). An exposed surface of sandy layer with distinct texture and finer grain (c) in which the pore spaces are not visible with naked eye.

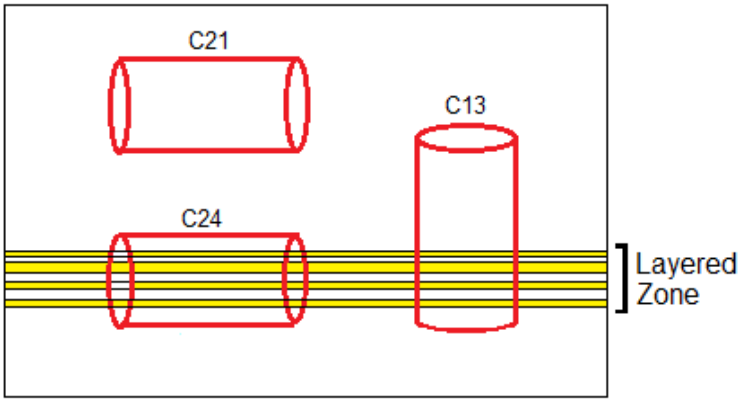

Figure 4-7 Schematic representation of samples position cored from the Coquina rock block with regards to layered zone. Three samples are shown as example including the sample from outside layered zone (C21) and two other samples from inside the layered zone including the one cored perpendicular to the layered zone (C13) and other one cored parallel to the layered zone (C24).

During the coring and taking the cores out of the block, some core plugs were split in the interface of these layers (normal to the core long axis). Exposed surface of this layer in broken samples showed that the layer has considerable amount of silt and sand size grains that look different from shelly fragments (figure 4.7 b,c). Existence of these layers can be due to a change in some combination of sediment supply, deposition and preservation of what is deposited. While many of pore spaces between shelly particles are almost visible (figure 4.7.b), pores in silty/sandy layers are much smaller to be seen with naked eye (figure 4.7.c).

The Biolithite samples were cored from a block of approximately 15*20*30 cm. In hand specimen, it looks a porous rock with red to tan-brown colour (figure 4.8). The pores have a very elongated oval shape that tend to have a very similar orientation throughout the sample. Big shells (a few centimetres size) are rarely observed in the rock that caused random distribution of larger pores in the samples. It seems that the orientation of pores can play significant role in inserting anisotropy in pore network properties like pore connectivity. To examine this, the coring was carried out in 3 orthogonal directions. Samples B11, B12, B13 and B14 in first direction and samples B21, B22, B23 and B24 in the second direction both having pores that are dominantly elongated parallel to the coring direction. Samples B31, B32 and B33 were cored the third direction (perpendicular to the first and second direction) and had elongated pores that were dominantly oriented approximately perpendicular to the coring direction. The dominant elongation of pores with regards to the coring direction will be easier to distinguish in X-ray tomography images that will be presented in the following sections. After coring and trimming the plugs, a natural fracture was observed in samples B13 and B14 with approximately 40^{o} orientation to the direction of coring. The fracture in both samples seems to have been partially filled with cement.

Figure 4-8 Hand specimen of the Biolithite sample, see the elongated pores in the zoomed area.

An interesting observation on the cored sample was a significant difference of their weight that was discernible even by handling the samples. Samples of same sizes, had weight ranging from 120 to 180 grams. Variation in the degree of cementation in different regions of the sample seems to be responsible for such differences. While zones with partial cementation and less pore space were obvious in heavier samples, lighter samples had less cemented and more porous appearance.

Ooilitic limestone samples were cored from a block with size of approximately 20*20*50cm. They are made up mainly of ooids, with medium- to coarse-grained appearance and dominantly cream, light grey to white colour. Bioclastic content is not observed in this block and the rock looks quite homogeneous in texture. A total of 12 samples were cored in two perpendicular direction (6 samples of each direction) and named O11 to O16 and O21 to O26. Figure 4.9.a shows the hand specimen of the Oolitic limestone used in this study.

Travertine samples was cored from a block of approximately 15*20*30 cm size. This was a white coloured Travertine with a wide range of pore sizes. Eight samples were cored in two perpendicular direction and samples were named as T11 to T14 and T21 to T24. A distribution of cracks and veins with no obvious pattern are observed in the surface of cored samples. These have various sizes and some of them seems to be sealed by cement of slightly darker colours (figure 4.9.b).

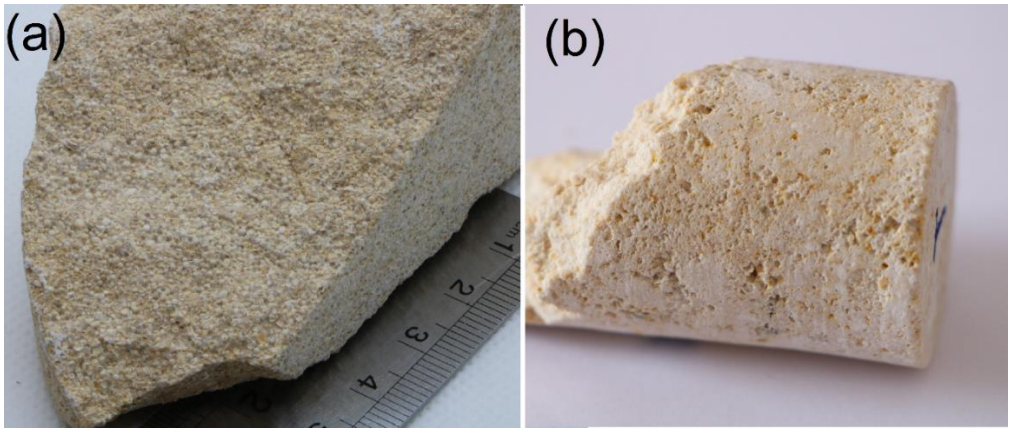

Figure 4-9 hand specimen of the Oolitic limestone (a) and Travertine (b)

4.3.2 Thin section rock description

Thin sections that were prepared from the Coquina and Ooltic limestone rocks were examined using a petrographic microscope. For the Coquina rock, thin sections were prepared from two zones of the sample; one from the body of the rock consisted mainly of shelly fragments and another one from the exposed surface of the sandy/silty layer. Photomicrographs from Coquina rock are displayed in figure 4.10 a-c. As shown in the images, intact and broken shells with preserved internal structure are in contact in a grain- supported frame lacking mud. Thin fringes of calcareous crystals (probably aragonite) precipitated on the edges of shell fragments and act as cement when these crystalline fringes intersect and hold the particle together. In the photomicrographs of the thin section prepared from layer surface (figure 4.11 d-f) some quartz and olivine grain of sand size are observed in between carbonate particles. The black areas in all thin section views are open spaces including inter-particle and intra-particle pores that vary in size and geometry.

Photomicrographs from Oolitic limestone are presented in figure 4.11. The texture can be described as medium to coarse grained packstone to grainstone. The grains consist of ooids, some peloids and few tiny shells. Grains are in point contact and calcite spar cement can be seen in between the grains. Based on visual examination, it seems that there is low intergranular porosity while totally or partially dissolved ooids provided secondary intra-granular moldic porosity. However, in most of dissolved ooids, the outer layer is preserved and a rim of crystallised cement is formed inside this layer that isolate the pore space of each ooid. Evidence of grain crushing can be observed in figure 4.11-b which connects pore spaces inside two ooids.

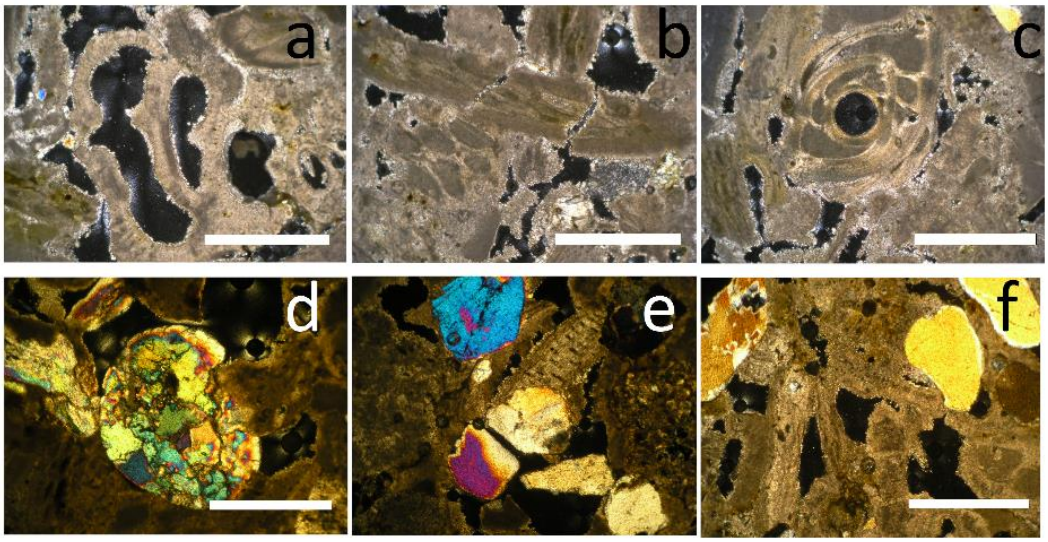

Figure 4-10 Photomicrographs of Coquina sample showing shelly fragments and a thin fringe of calcareous crystals (probably aragonite) precipitated on the edges of shell (a,b and c, under plain polarised light) and quarts and olivine sand grains in between shelly fragments (d,e and f, under cross polarised light). The black areas are pore spaces. The scale bar shows 400 micron.

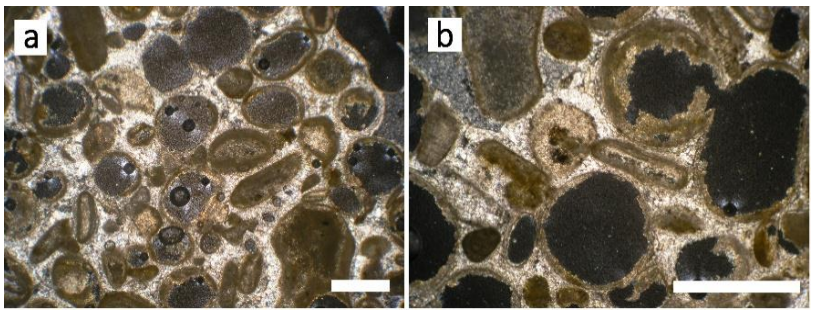

Figure 4-11 Photomicrographs of Oolitic limestone sample showing medium to coarse grained ooids. Calcite spar cement filled the spaces between grains. Totally or partially dissolved ooids provided secondary intra-granular moldic porosity. In most of dissolved ooids, the outer layer is preserved and a rim of crystalized cement is formed inside this layer that isolate the pore space of each ooid. The scale bar shows 500 micron.

4.3.3 Sample descriptions based on direct observation of X-ray tomographies

In this work, the 3D characterisation of the materials structure has been mainly carried out by focusing on X-ray tomography images with resolutions ranging from 5 to 53 μm. X-ray tomography (Chapter 3) offers superb capability of visualising the structure/texture of the sample in 3D. X-ray analysis includes both qualitative (e.g. direct observation of the visualised 3D volumes) and quantitative (e.g. measuring specific properties of interests) interpretation of the data. The first step for quantitative analysis is the distinction between the grain/matrix and the pore network; this can be achieved due to different densities (e.g. grains have higher density than pores). In Coquina samples, variation in the samples texture is investigated. Figure 4.12 shows reconstructed X-ray tomography images from C22 and C23

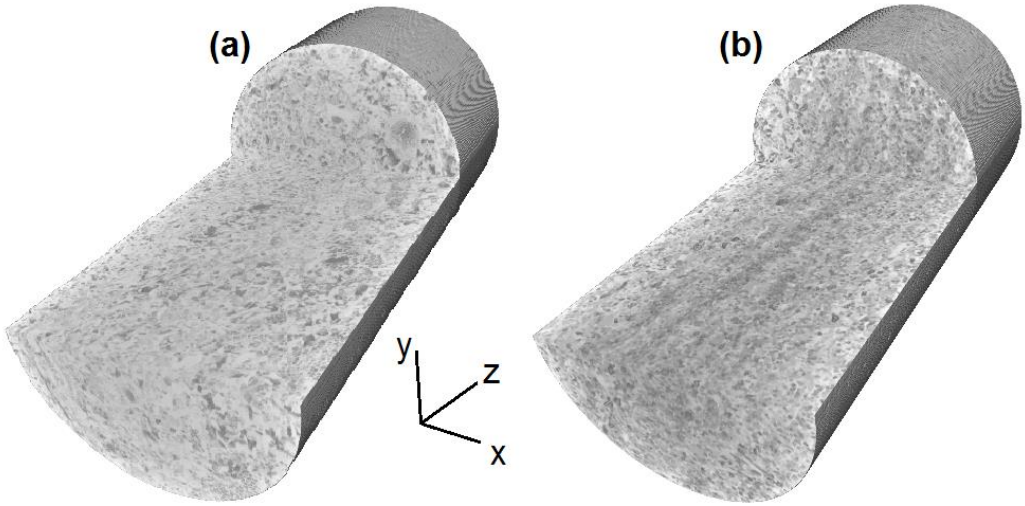

Figure 4-12 Reconstructed volume using X-ray tomography (50 micron voxel size) for whole core samples of 38mm diameter, grains and pores are in bright and darker colours respectively, a) sample C22 cored outside the layered zone and b) sample C23 cored inside the layered zone; stripe zones with distinct grey-scale value represent layers with possibly different characteristics.

samples. The resolution of the images is 50 micron voxel size. In these grey-scale images, grains have light colour (higher grey-scale value) whereas darker colours (lower grey-scale value) represent pore spaces. The spatial variations in distribution of pores and their size distribution can be observed in sample C22. Moreover, thin tabular zones (a few mm thick) with distinct grey-scale values can be observed in C23 sample (cored from the layered zone of the block) representing the layers with different density characteristics.

In order to have more accurate description of rocks texture (grain size, shape and arrangement), two small pieces of rock from inside and outside of the layered region were collected. Thanks to the smaller size of the samples, X-ray scanning with higher resolution is possible that enables us to resolve more details. Two 3D volumes with dimensions of 5*5*7mm were extracted from reconstructed high- resolution X-ray tomography images with a resolution of 5 micron voxel size (figure 4.13a,b). Obvious textural differences are observed in the 3D images; the material outside the layer (left image) mainly consists of irregularly shaped and arranged shelly fragments of different sizes (half to a few millimetres length). Inside the layer the material is characterised by a considerable proportion of sand size grains with more uniform size (about 0.5 to 1 mm) and shapes in between the shelly fragments that caused more compact grain arrangement and less and smaller pore spaces as a result. In both images, besides inter-particle porosity, intra-particle pores can be seen inside skeletal fragments that seems to be isolated.

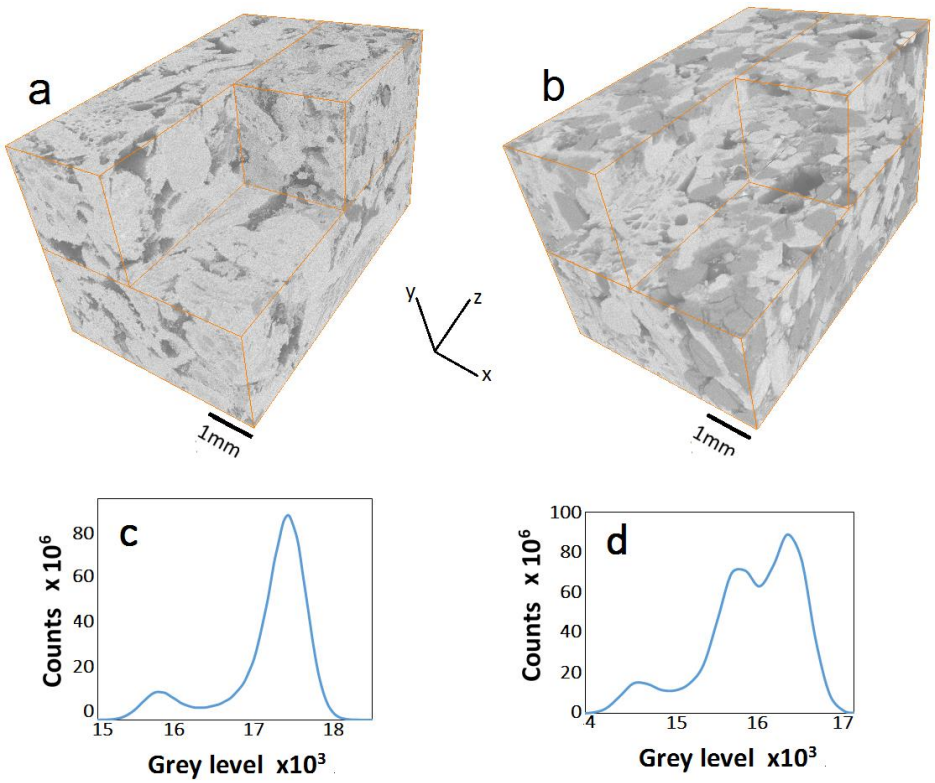

Figure 4-13 Extracted 3D volumes of high resolution X-ray tomographies of Coquina (5 micron voxel size), a) rock outside the layer mainly consisted of irregularly shaped and arranged shelly fragments in different sizes (half to a few millimetre) and b) rock inside the layer has considerable amount of sands in sizes about 0.5mm - 1mm are observed in between shelly fragments that caused more compact grain arrangement and less and smaller pore spaces as a result. Histogram of X-ray tomography images for: C) sample outside the layered zone with two peaks and d) sample from layered zone with 3 peaks. Grains and void spaces are in bright and darker colours respectively.

Given the same image acquisition parameters for these two X-ray tomographies, obvious different grey-scale colours between sand and carbonate particles in images indicate potential variation in grains mineralogy. The grey-scale histograms that show the pixels intensity distribution corresponding to 3D volume of each sample also reveal the grains compositional variation. As shown in figure 4.13-c,d, there are two peaks in histogram of the image in which sample consists mainly of carbonate grains (sample from outside the layered zone). The peaks correspond to the air-filled pore spaces and carbonate grains. But, for the sample from inside the layered zone, three peaks can be distinguished in the image histogram that indicate the existence of new material with different composition (quartz sand grains).

Extracted volumes from X-ray tomography images (10 micron voxel size) of Biolithite, Oolitic limestone and Travertine with dimension of 7*7*7mm are presented in figure 4.14. In the Biolithite rocks image (4.14a), the solid components of rock have uniform grey-scale colour. Based on Dunham classification of carbonate rocks (1962), this rock can be classed as Boundstone in which the rocks original components are bound together in place during the

deposition. So, inter-grown skeletal material is the typical textural characteristic of these rocks and has resulted in growth-framework pore type. Pores with mostly elongated shape, different sizes and somewhat parallel alignment are observed in this rock.

In the Oolitic limestone image (4.14b), spherical and semi-spherical ooids with sizes of approximately less than 0.5mm can be distinguished from the matrix. Moldic porosity is observed in the image where pore spaces preserve the spherical shape of the ooids while the nuclei is retained.

In the Travertine image (4.14c), the distinction between the solid components and the pore spaces is not easy. Some regions with larger and more visible solid components can be observed while some region with darker grey colour exist in which pores and solid components cannot be distinguished clearly at this resolution. A fibrous texture of crystals encompassing considerable amount of sub-resolution porosity can be a reason for this appearance. Grey-scale histograms of each volume are also presented below each image. While the histogram of the Biolithite rock shows two different peaks corresponding to air-filled pores and the solid components, for two other rock types, histogram has one peak. This is possibly because of the bigger pore size in Biolithite sample that have been resolved very good. On the other hand, existence of sub-resolution porosity in Travertine and Oolitic limestone samples causes kind of smoothening in the voxels grey-scale value which could explain such a single-peak histogram.

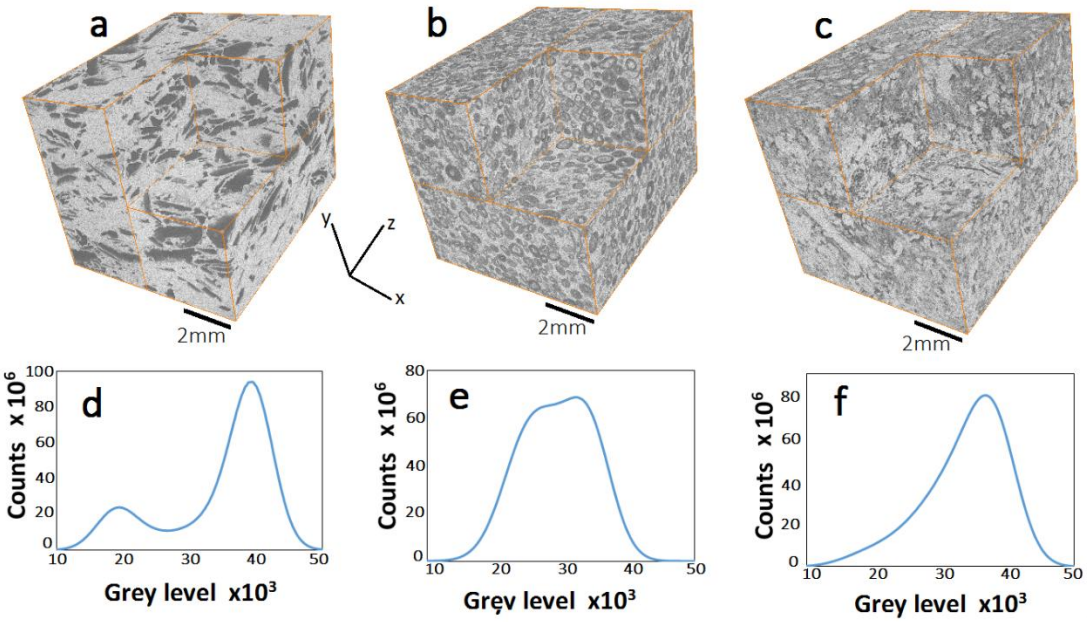

Figure 4-14 Extracted 3D volumes of high resolution X-ray tomographies **(**10 micron voxel size) of samples a) Biolithite, b) Oolitic lime stone and C) Travertine. The corresponding histogram is shown under the image of each sample (d,c and f). Grains and void spaces are in bright and darker colours respectively.

4.4 Mechanical behaviour

In this section, the mechanical behaviour of samples under triaxial compression at different confining pressures is discussed. Axial stress vs axial strain curves are presented and the mechanical properties of samples have been summarised in a table. The X-ray tomography images acquired from the deformed sample (after triaxial compression tests) are used to investigate the lab-induced deformation features in 3D like the fracture orientation, geometry and aperture. Also, X-ray tomography images of some intact samples have been presented to show the textural variations in samples before deformation.

For the Coquina rock, three samples were deformed under triaxial compression (at 2.5 MPa of confining pressure). To determine the proper confining pressure, spare Coquina samples were first deformed at different confining pressures (10, 5 and 2.5 MPa). While no signs of significant localised deformation were observed at higher confining pressures (5 and 10 MPs), shear fractures ware developed at 2.5 MPa. Since development of fracture network was of our interest (for flow experiments), the mechanical deformation of Coquina samples for flow experiment purpose was carried out at 2.5 MPa confining pressure. In order to investigate the impact of textural characteristics on the mechanical behaviour of the Coquina rock, one sample was cored from outside the layered zone (C22) and two samples were encompassing layers with different orientation (along each samples axis). For example, sample C13 was cored perpendicular to the layers while sample C24 was cored parallel to the layers. Figure 4.15 shows the curve of deviatoric stress versus axial strain for these samples.

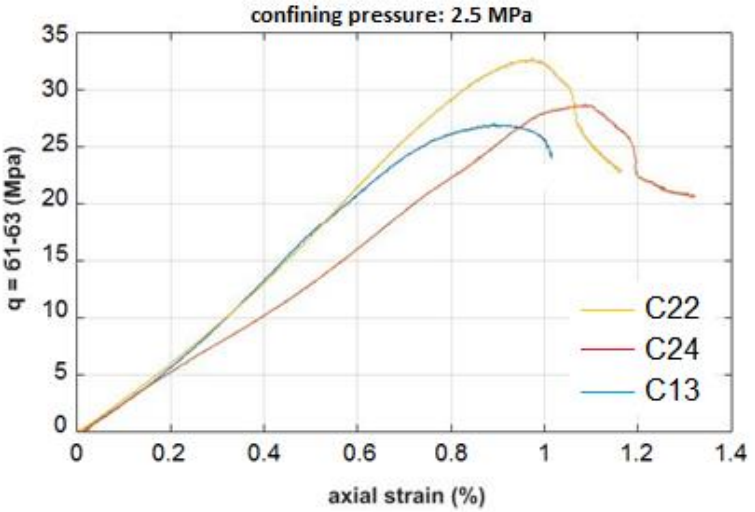

Figure 4-15 Deviatoric stress versus axial strain of triaxial loading test on samples C13 (cored normal to layers), C22 (from outside layered zone) and C24 (cored parallel to layers).

All samples show same linear trend up to a deviatoric stress of 5 MPa and corresponding axial strain of 0.2 percent. The strength of the sample from outside the layered zone, C22 (32.5 MPa) is higher than either samples within the layered zone C24 (28.5 MPa) or sample C13 (27MPa). For the samples cored in same direction, the sample that contains layering parallel to its length (C24) has lower resistance and is less stiff compared to the sample cored outside the layered zone however, the stress-strain curves resemble. The parallel layering seems to cause the sample to be less stiff and with lower resistance.

Comparing samples cored at two different directions (C22 and C13) shows that both samples have similar stiffness up to approximately 20 MPa but the sample with the layering normal to its length (C13) fails earlier and has a lower resistance. It looks like that the horizontal layering in sample C13 starts playing a role after a certain deviatoric stress, whereas before, the sample behaves similar to the other sample coming from outside the layered region (C22).

Vertical and horizontal slices of X-ray tomography images of samples C22 and C24 are shown in figures 4.16 and 4.17, respectively. A small aperture shear fracture inclined approximately 30 degree to the principal stress direction is observed in sample C22 (cored outside the layered zone). As observed in the horizontal slices, the fracture has an irregular shape in some regions (figure 4.16-d). Connected network of microcracks is observed when approaching to the bottom face of

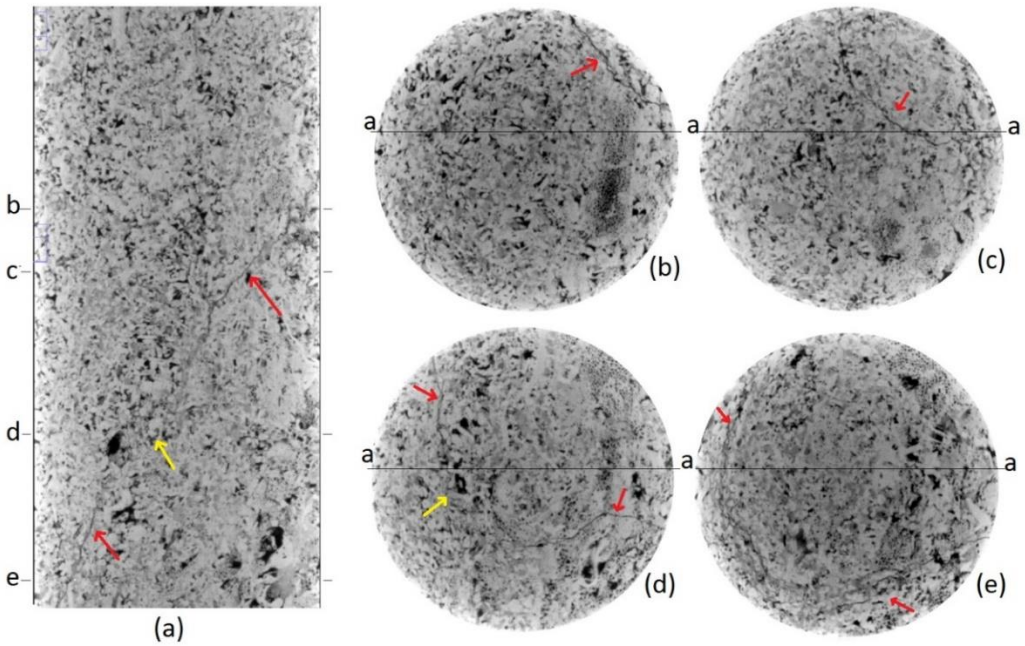

Figure 4-16 Vertical and horizontal slices of X-ray tomography images of samples C22 deformed under triaxial loading at 2.5 MPa confining pressure. Red arrows indicate the location of fracture while yellow arrows shows regions in which trace of the fracture is not clearly visible. Grains and void spaces are in bright and darker colours respectively.

the sample (figure 4.16.e). The fracture can hardly be traced in some regions as indicated by yellow arrows in (figure 4.17-a,d). It seems that due to the higher porosity of these regions, the strain has been accommodated mainly by rearrangement of grains.

In sample C24, it seems that the existence of vertically oriented layers (sample cored parallel to layering) has affected the fracture propagation. In addition to two steeply dipping shear failure surfaces observed at the top part of the sample, a vertical fracture has propagated parallel to the orientation of vertical layers (indicated by red colour in figure 4.17.f).

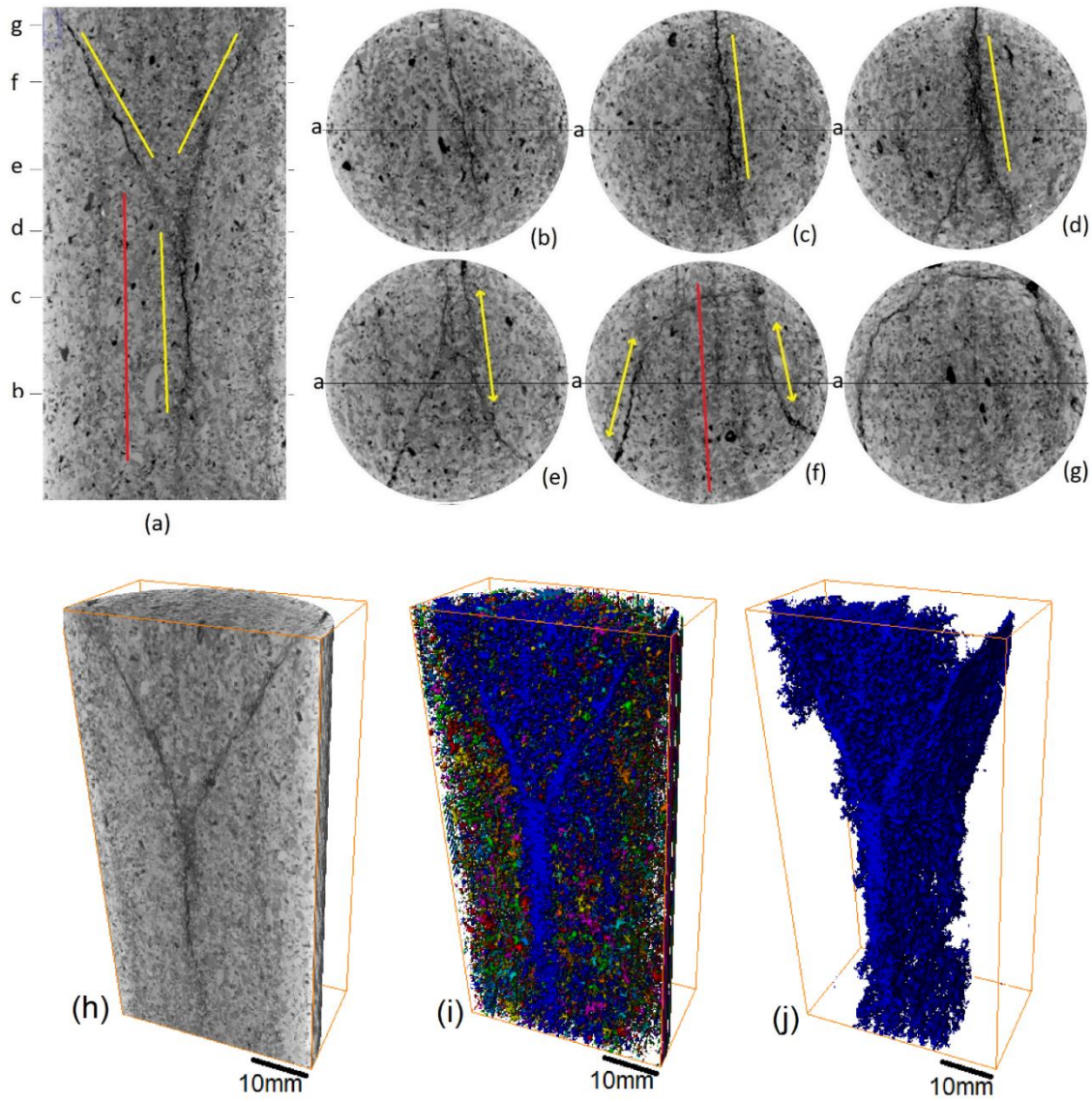

Figure 4-17 Vertical and horizontal slices of X-ray tomography images of samples C24 deformed under triaxial loading at 2.5 MPa confining pressure. Stripe patterns of darker and brighter colours that is more visible in slice (f) are due to the existence of layers of distinct textures. The yellow lines indicate the direction of the fractures propagating toward the bottom of the sample parallel to the layering direction (red line). The 3D rendering of the X-ray tomography image of sample C24 cut in half-cylinder shape (h) and the labelled pore network image (i) in which connected pores are displayed in same colour. The 3D rendering of the main connected pore network in the sample (j) extracted by filtering the image b. A well connected fracture network and pore network around it is observed.

It seems that occurrence of vertical layering has diverted the two steeply dipping shear fractures so that two fractures meet in the middle of the samples height and propagate in form of a single vertical fracture parallel and within one of vertically oriented layers down to the bottom end of the sample. The 3D rendering of the X-ray tomography image of sample C24 (cut in half-cylinder shape) is presented in figure 4.15.h in which the fracture network is observed. The pore network image of this sample (extracted from the X-ray tomography image) has been labelled (see chapter 3 for the method) so that connected pore networks are presented in same colours (figure 4.17.i). Also, the 3D rendering of the main pore network is extracted by filtering the labelled image and eliminating the smaller pore networks (figure 4.17.j) As seen in these images, the main pore network which is labelled in blue is distributed dominantly around the fracture network in this sample that communicate between the bottom and top ends of the core sample.

In sample C13-deformed, a steeply dipping fracture is propagated that crosses the horizontal layering in this sample. The fracture tip starts below ¼ of the samples height (indicated by the yellow arrow in the bottom of the figure 4.18.a and extends to the top in an almost vertical direction. The fracture has generally a tiny aperture (0.5 to 1mm) but it varies in different region and the highest aperture is observed in the samples central region. The fracture is hard to be traced in the region close to the top end of sample (indicated by the top yellow arrow in figure 4.18. a, where larger pore spaces are observed.

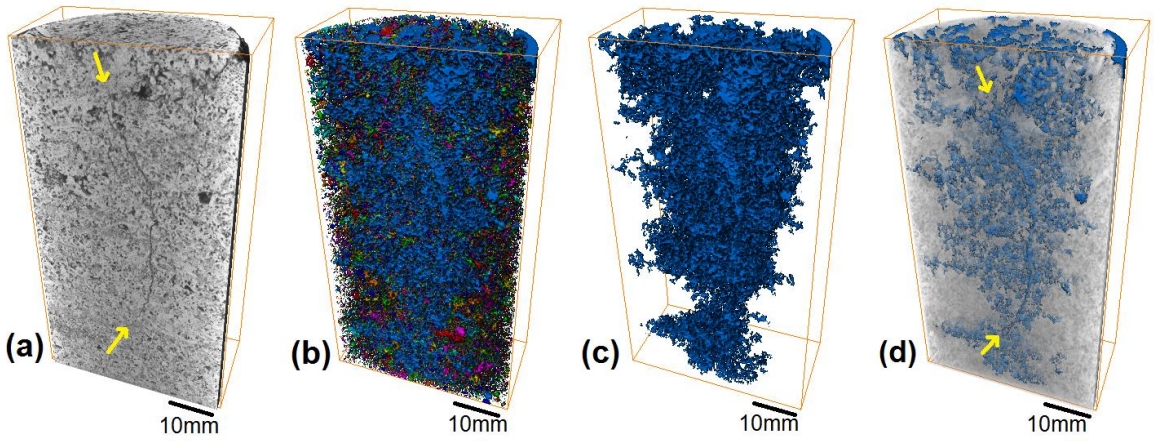

Figure 4-18 3D rendering of the X-ray tomography image of sample C13-deformed cut in half-cylinder shape (a), Grains and void spaces are in bright and darker colours respectively. The steeply dipped and almost vertically oriented fracture can be observed (fracture tips indicated by yellow arrows). 3D rendering of the labelled pore network image (b) in which connected pores are displayed in same colour. 3D rendering of the main connected pore network in the sample (b) extracted by filtering the image b and supperimposed to the X-ray tomography image (d).

The labelled pore network image of this sample is presented in figure 4.18.b. As seen in this figure, the main pore network which is labelled in blue communicate between the bottom and top ends of the core sample. The 3D rendering of the main pore network is extracted by filtering the labelled image and eliminating the smaller pore networks (figure 4.18.c) and is superimposed to the X-ray tomography image (figure 4.18.d). As seen in these images, the fracture is located within the main connected pore network and is expected to play a significant role in its connectivity.

After deformation, the permeability of the samples C13 and C24 were increased from 37 to 90 and 56 to 98 mD (lab-measured permeability values), respectively whereas permeability of sample C22 did not change. It seems that the well-connected network of open fractures that communicate between the top and bottom end of sample C24 is responsible for the increase of permeability. In sample C13, fracture crosses the horizontally oriented layers (layered zone in schematic figure 4.7) that are expected to have distinct pore network properties. As will be presented later in this chapter (section 4.5.5), there is significant permeability variation along the Coquina sample C16 which is cored perpendicular to the layered zone so that the layered zone generally show very low permeability values (almost below 50 mD) while zones with higher permeabilities can be observed above the layered zone. Given that the sample C13 is also cored in same orientation as sample C16 and in a close position to this sample, the similar trend of variation in permeability of the layered zone and the rest of sample is expected in sample C13 as well. It seems that the fracture has increased the permeability of this sample as a results of failure in structural integrity of the low-perm layered zone and increasing the permeability of this zone. On the other hand, very small aperture of the fracture as well as higher matrix permeability in sample C22 caused the fracture to be less influential in the permeability of the sample. Also the fracture does not connect the bottom and top end of the sample (like the other two sample) because the fracture tip starts from the samples periphery in mid-height of the sample.

For the Biolithite rock, the effect of porosity and coring direction on mechanical behaviour of samples was investigated. The Three samples B11, B23 and B33 with same range of lab-measured porosity (23-26% - porosimeter measurements) cored in three orthogonal directions were deformed under same confining pressure of 5 MPa. As shown in deviatoric stress versus axial strain curve in figure 4.19-a, multiple strain softening and hardening take place for all the three samples up to an axial strain of 1.5%. Samples B11 and B23 show somehow same linear trend and stiffness but sample B33 show lower stiffness and fail earlier than the other two samples. Sample B33 also has lower ultimate and residual strength than samples B11 and

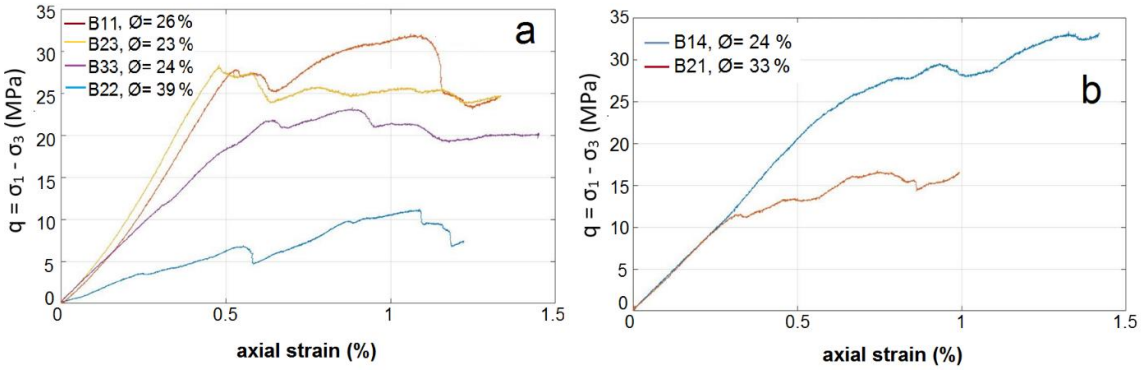

Figure 4-19 Deviatoric stress versus axial strain of triaxial loading test on Biolithite samples under 5MPa(a) and 10MPa (b) confining pressures.

B23. By the end of these experiments (after unloading) and a total axial strain of up to 1.4%, no obvious traces of fractures could be identified on the surface of the samples however some signs of local damages on the samples surface (kind of pore collapse and compaction) can be observed.

Vertical and horizontal slices of X-ray tomography images of these samples before deformation are presented in figure 4.20. Due to the coring in three orthogonal directions, orientation of pores with elongated shape are different in the samples. In samples B11 and B23, the pores dominantly have vertical orientation (pores elongation parallel to the samples vertical axis) while in the sample B33, pores are mainly oriented horizontally and are perpendicular to the samples vertical axis. This can make the collapse of pores much easier in sample B33 under the triaxial loading and it seems to be the main reason of lower young modulus and ultimate strength of the sample B33.

The deviatoric stress versus axial strain curve of samples B21 and B22 with higher porosity values (33 and 39% respectively) that are deformed under 10 and 5 MPa confining pressure respectively are shown in figure 4.20-a,b. Both samples show the same trend of multiple strain hardening and strain softening. Under 5 MPa confining pressure, highly porous sample B22 show significantly lower young modulus (lowest stiffness) and ultimate strength compared to the sample cored in same direction B23 with lower porosity. As shown in figure 4.20-b, under 10 MPa confining pressure, highly porous sample B21 has same stiffness with sample with lower porosity (B14) but shows almost half the yield point and ultimate strength of the sample B14.

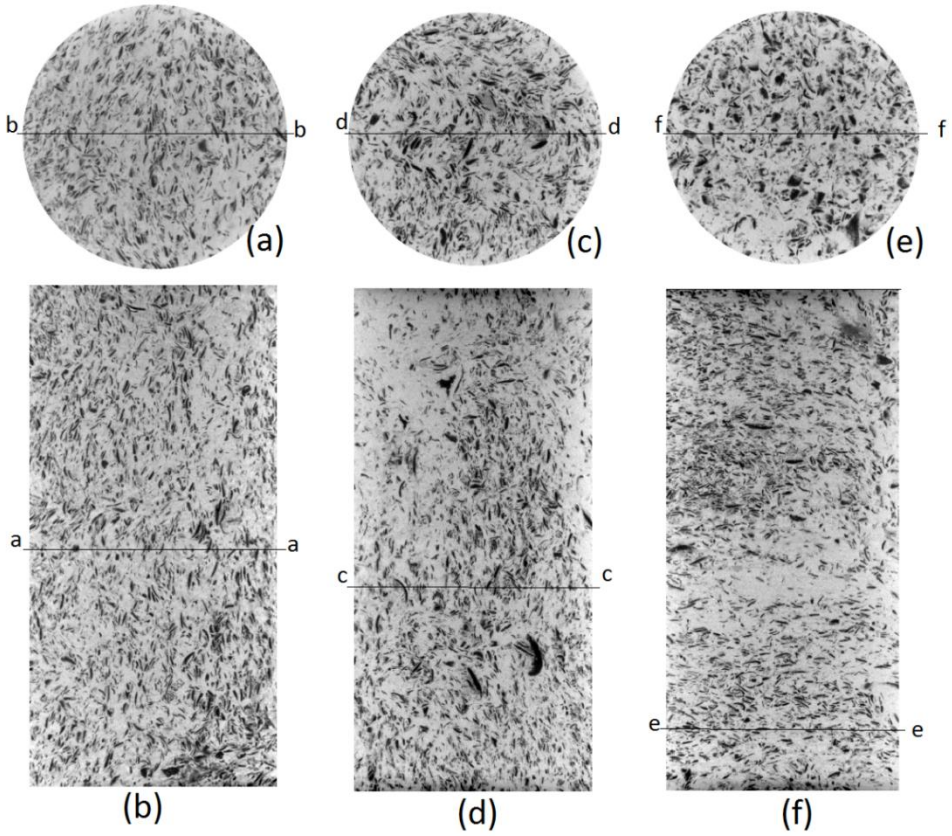

Figure 4-20 Vertical and horizontal slices of X-ray tomography images of samples B11 (a and b) B23 (c and d) and B33 (e and f). Pores with elongated shape are dominantly oriented vertically in samples B11 and B23 while they have mostly horizontal orientation in sample B33. Grains and void spaces are in bright and darker colours respectively.

Travertine samples were deformed under confining pressures of 5, 7.5 and 10 MPa. In each confining pressure, two samples cored in perpendicular directions were deformed. The deviatoric stress versus axial strain curve of samples are presented in figure 4.21. Samples T13, T11 and T15 (cored in direction 1) show a very weak strain softening after the yield point and have slightly smaller young modulus and ultimate strength than the samples T21, T22 and T24 (cored in direction 2) regardless of confining pressure. Samples T21, T22 and T24 show multiple weak strain hardening steps after sudden stress drops.

Seven samples from Oolitic limestone were deformed under different confining pressures ranging from 2 to 30 MPa. Deviatoric stress versus axial strain curves (figure 4.22), at 2 Mpa confining pressure, for sample O24 show a brittle response followed by strain softening step up to 1.5 percent of axial strain. By increasing confining pressure to 2.5, 3, 4 and 5 for samples O26, O11, O25 and O22 respectively, the mechanical response of samples gradually changes from strong strain softening to a weak strain softening while the yield strength is almost constant. At high confining pressures of 20 and 30 for samples O14 and O23 respectively, strong strain hardening can be observed.

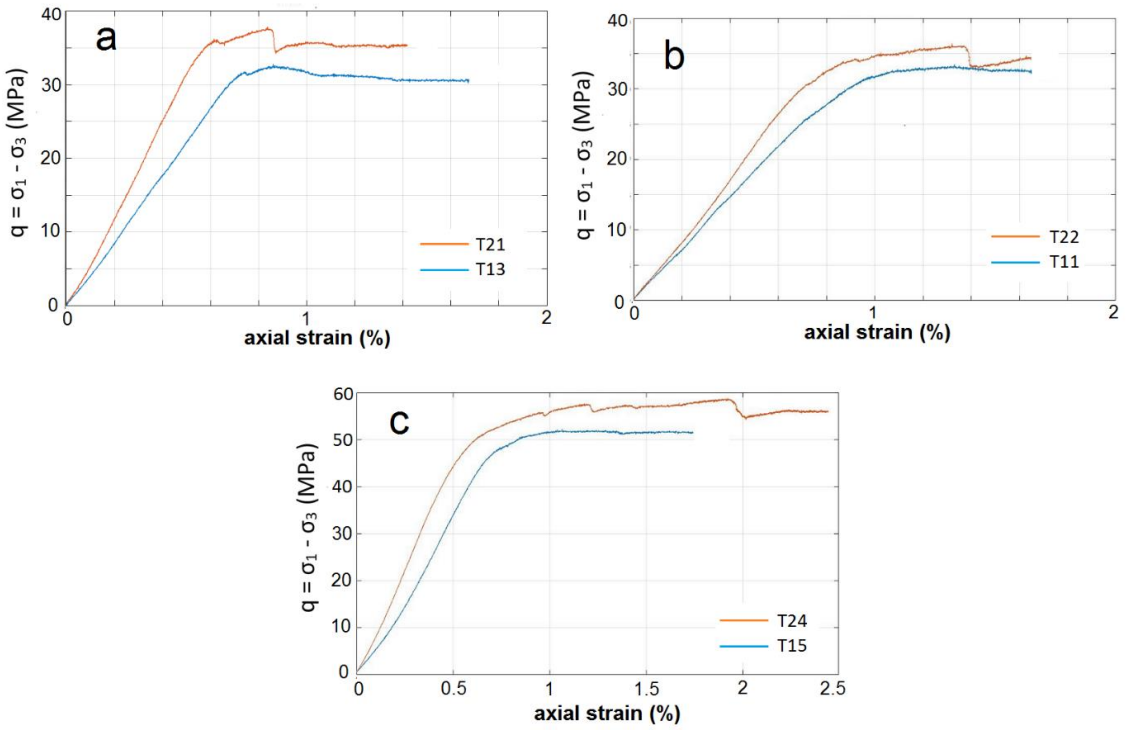

Figure 4-21 Deviatoric stress versus axial strain of triaxial loading test on Travertine samples under 5MPa(a), 7.5MPa(b) and 10MPa (c) confining pressures.

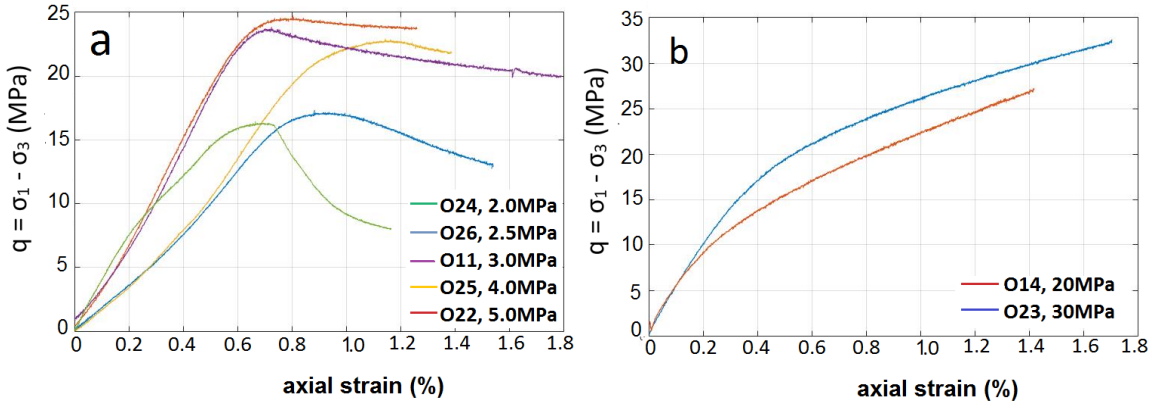

Figure 4-22 Deviatoric stress versus axial strain of triaxial loading test on Oolitic limestone under confining pressures ranging from 2 to 5 MPa (a) and 20 and 30 MPa (b).

4.5 Quantitative analysis on the pore system

As a first step for quantitative analysis on the samples pore system, the pore network image needs to be extracted from the X-ray tomography images acquired from the samples (see table 3.1 in chapter 3 for image acquisition parameters). In this study, X-rays images were reconstructed with commercial software Octopus at HZB and X-act software provided at ILL and Heriot-Watt University (see chapter 3, section 3.3.1 for more details on reconstruction).

Then, the Trainable Weka Segmentation (see Chapter 3) was used to segment all X-ray tomography images of the scanned samples to extract the pore network image. Computed pore network properties including porosity, specific surface area, connectivity density, coordination number and tortuosity of the samples are presented below. Also, to investigate the link between these pore network properties and the rock permeability, the pore network image of one of Coquina samples (extracted from the X-ray tomography image with 53 Micron voxel size) is used to compute the samples permeability using pressure-driven flow simulation and employing the lattice-Boltzmann method (LBM).

4.5.1 Porosity

The porosity calculation (see chapter 3) provided the total porosity as well as connected and isolated porosity values for each volume of pore network image. Calculated porosity values (from XRT images) for four different rock types are presented in table 4.1. The size of the volume studied and images resolution are also indicated. To be able to compare the image based calculated porosity values with the experimentally measured gas porosity, the pore network image of the whole core sample was used however these volumes might have undergone a slight crop at the boundaries to avoid the errors due to the artefacts. Pore network extracted from higher resolution tomography images focus on much smaller volume of the samples and cropped in cubic shape.

As seen in the table 4.1, digitally derived porosities are smaller than the gas porosity in all the samples. The differences between Helium porosity and digital porosity is about (2.8% to 4.15 %) in Coquina samples and (4.6% to 5.5%) in Biolithite samples. This values are much higher for Oolitic limestone (10.39% to 11.43%) and Travertine (8.5% to 10.64%). Some factors can influence the differences between digital porosity and experimentally measured gas porosity. For instance, sub-resolution porosity that is not visualised in the image can lead to under-calculation of digital porosity. On the other hand, digital porosity includes the entirely isolated pores which are common in carbonate rocks while these pores may not be measured experimentally since gas cannot enter them. As another crucial factor is the segmentation quality that is discussed in chapter 3. The normalised difference in digital porosity and the measured Helium porosity for Coquina samples in this study is ranging from 11% - 28 % (the difference between digital porosity and Helium porosity is divided by the Helium porosity).

Table 4-1 porosity, permeability, specific surface area and pore networks tortuosity of samples (from digital images)

Sample	Helium Porosity (%)	Permeability (mD)	Studied Volume (mm)	Voxel size (µm)	Ø (%) total	Connected pore		Isolated pores	
						Ø (%)	S (mm^{-1})	Ø (%)	S (mm^{-1})
I	-	-	5x5x7	5.5	18.43	17.21	53.05	1.22	189.18
II	-	-	5x5x7	5.5	14.84	13.57	82.79	1.27	252.69
C11	20.4	95	whole	42	17.57	16.59	13.58	0.98	26.41
C12	20.7	50	whole	42	15.49	14.28	13.95	1.21	26.36
C13	20.0	37	whole	52	15.86	14.56	18.57	1.30	35.10
C13 (D)	-	90	whole	-	-	-	-	-	-
C16	21.7	92	whole	53	17.55	16.10	15.29	1.45	25.68
C21	-	440	whole	47	18.52	17.46	12.63	1.06	21.71
C22	-	362	-	-	-	-	-	-	-
C22 (D)	-	368	whole	54	18.10	16.70	12.17	1.40	19.61
C23	21.2	84	whole	53	18.23	16.68	16.01	1.55	23.42
C24	-	50	-	-	-	-	-	-	-
C24 (D)	-	98	whole	54	18.10	17.00	18.61	1.09	34.23
B11	26.43	< 1	whole	53	20.94	19.19	12.81	1.75	19.13
B23	23.13	< 1	whole	53	18.53	15.77	13.87	2.76	18.12
B23-HR		-	7x7x7	10	25.23	19.87	26.43	5.36	61.62
B33	24.04	< 1	whole	53	18.58	16.31	14.57	2.27	18.89
O15	25.90	< 1	whole	53	14.47	11.62	-	2.84	-
O15-HR	-	-	7x7x7	10	19.47	18.6	77.2	0.87	317.84
O27	26.10	< 1	whole	53	15.71	13.16	-	2.55	-
T11	24.2	67	whole	53	15.62	13.78	-	1.84	-
T11-HR	-	-	7x7x7	10	20.25	19.32	73.61	0.93	160.14
T21	23.9	58	whole	53	13.26	10.55	-	2.71	-

Note: Specific surface area is presented by (S), sample from outside and inside of the layered zone are presented by (I) and (II) respectively. The suffix (D) in samples name means that the sample is deformed (lab-induced mechanical deformation). The ‘’whole’’ in studied volume size refers to the whole cylindrical volume of the scanned sample. The dash signs (-) means that the data is not available (not measured or not calculated).

The digital porosities calculated based on higher resolution images of Biolithite, Travertine and Oolitic limestone (10 µm voxel size) are closer to the measured Helium porosity values compared to the digital porosities calculated based on (50 µm voxel size) images. This can be because of the smaller pores (with sizes between 10 and 50 µm) that have been resolved

and contributed to the digital porosity. In Coquina rocks, porosity calculated based on higher resolution image (5 µm voxel size) acquired from inside the layered zone show smaller porosity (14.84%) than the one from outside the layered zone (18.43%).

4.5.2 Specific surface area

Calculated specific surface area values presented in table 4.1 shows that connected pore networks have generally lower value than isolated pores. There is also a significant difference between specific surface area values calculated from X-ray tomography images with different resolutions. Images with higher resolution (5 and 10 micron voxel size) show higher value (ranging from 53 mm-1 to 82.7mm-1 for connected pores) than images with lower resolution with specific surface area of 12 mm-1 – 18.6 mm-1. Higher resolution images can better resolve the pore surface roughness that results in higher specific surface area. This indicates the sensitivity of the specific surface area calculation to the image resolution. Depending on the application and the tested sample, different resolutions might be needed when analysing this property.

Calculations based on high resolution (5 µm voxel size) images of Coquina samples shows that the sample from inside the layered zone has higher specific surface area (82mm-1) than the sample from outside the layered zone (53 mm-1). This can be due to the smaller pore sizes in the sandy layers within the layered zone. In lower resolution images, samples selected from outside the layered zone (C21 and C22) have the smaller specific surface area values compared to the samples that encompass parts of layered zone. These two samples also have highest permeability among samples whereas sample C13 with highest specific surface area has lowest permeability. Higher values of the specific surface area may put a larger surface area per volume in contact with hypothetical fluids which may exert a higher friction on fluid flow and therefore lower permeability of the rock (Zambrano et al., 2017).

For the Oolitic limestone and Travertine, the specific surface area is only calculated for higher resolution images (10 µm voxel size) since the pore network images extracted from lower resolution images are not representative of the real pore system (due to considerable non-resolved pores). For higher resolution images, Biolithite has the lowest specific surface area whereas Oolitic limestone and Travertine have very high values. The relatively larger pores with simpler geometry in Biolithite compared to the very small pore size in Oolitic limestone and Travertine can explain this difference. The surface areas of the whole pore network (connected and isolated) and the mean pore size calculated based on high resolution (5 and 10 µm voxel size) X-ray tomography images are presented in table 4.2. The mean pore size

Table 4-2 calculated specific surface area and mean pore size based on X-ray tomography images of 5 and 10 µm voxel size for different samples

Sample		Voxel size (µm)	Mean pore size, D_{50} (µm)	Specific Surface Area (mm^{-1})
Coquina	I	5	788	62.05
	II	5	472	97.34
Biolithite	B23	10	1235	33.90
Oolitic limestone	O15	10	337	78.92
Travertine	T11	10	291	77.59

Note: sample from outside and inside of the layered zone are presented by (I) and (II) respectively. The mean pore sizes is calculated as mean equivalent pore diameter.

is calculated as D_{50} that represent the volumetric mean pore diameter (see section 3.3.3.2). As seen in this table, specific surface area values are inversely related to the mean pore sizes.

4.5.3 Pore connectivity

Connectivity properties of the pore network is examined by analysis of the pore skeleton extracted from the segmented pore network image as explained in chapter 3. Pore network connectivity is defined with connectivity density (CD) and average coordination number which are calculated for the pore networks extracted from the high resolution X-ray tomography images (5 and 10 µm voxel size) of samples Coquina (including two samples from inside and outside the layered zone with resolution of 5 µm), Biolithite, Travertine and Oolitic limestone (with resolution of 10 µm) as presented in table 4.3.

The pore network in the Biolithite sample is poorly connected with average coordination number (section 3.3.3.5) of 2.7 whereas the Travertine and Oolitic limestones have highly connected pore networks with average coordination numbers of 7.4 and 6.4 respectively. The high average coordination number of the Oolitic limestone is in contrast with the very low permeability of this rock. It can be expected that pore throat sizes are very small in this rock that resulted in low permeability of sample despite the abundance of connections between pores. Also, as intra-particle moldic porosity is dominant in this Oolitic limestone sample (see figure 4.11), the pores are well-connected where Ooliths are in contact (grain supported texture) whereas connectivity of the whole pore network is partially disrupted where the Ooliths are in a mud supported arrangement due to the existence of an extremely fine grained

Table 4-3 Results extracted from the skeleton model of the samples pore network

Sample	I	II	T11_HR	B23_HR	O15_HR
CD (mm-3)	101.17	212.01	149.71	8.2	46.69
Average Coordination Number	3.66	4.59	7.4	2.79	6.41

Note: Connectivity density is represented by (CD), sample from outside and inside of the layered zone are presented by (I) and (II) respectively.

mud size matrix around the Ooliths. Actually, groups of well-connected pores tend to be separated from nearby pores because they are surrounded by low porosity matrix. In the Coquina rock, the sample from inside the layered zone has a higher average coordination number (4.6) than the sample from outside the layered zone (3.6). The sample from inside the layered zone has smaller pores compared to the sample from outside the layered zone that seems to be connected through larger numbers of narrow pore throats.

Calculated connectivity density of the extracted pore network (section 3.3.3.3) also varies for different rock types. The low value of connectivity density (8.2 mm^{-3}) in the Biolithite is in good agreement with its low permeability and low average coordination number. Travertine and Coquina samples (both zones) on the other hand have higher connectivity density values (compared to those of the other two rocks), which are consistent with their higher permeability. In spite of a high average coordination number, the connectivity density is relatively small in the Oolitic limestone (46.69 mm^{-3}).

As a scalar value that represents the number of redundant connections per unit of rock volume, connectivity density (CD) can be highly dependent on pore size. It means that for pore networks with same range of porosity and coordination number, connectivity density can increase by decreasing the pore size. This point should be taken into account when comparing connectivity of rocks with significant difference in pore size range based on connectivity density values. For example, Coquina samples from inside the layered zone have connectivity density twice that of sample from outside the layered zone with almost same range of coordination number and even lower porosity in the layered zone. The finer pore spaces inside the layered zone results in higher number of redundant connection and high connectivity density.

4.5.4 Tortuosity

Tortuosity is calculated based on two methods described in chapter 3 (section 3.3.3.6) including minimum tortuosity and mean tortuosity. For the high-resolution X-ray tomography images of the tested samples, tortuosity is calculated in the three orthogonal directions (x, y and z) of the cubic volume. In each direction, the tortuosity calculated between the two opposite faces of the cubic volume. The standard deviation of values in three directions is also presented to show the anisotropy in the samples tortuosity. To investigate the effect of layering orientation on tortuosity of the Coquinas pore system, tortuosity is calculated in the z direction of whole core X-ray tomographies. Calculated tortuosity values are presented in table 4.4.

Table 4-4 Calculated tortuosity values in three x,y and z directions and their standard deviation for different samples.

sample	Mean tortuosity				Min tortuosity			
	x	y	z	stdev	x	y	z	stdev
I	1.91	2.09	2.15	0.12	1.08	1.1	1.08	0.01
II	1.89	2.5	2.57	0.37	1.07	1.07	1.16	0.05
B23_HR	2.69	1.59	1.42	0.69	1.74	1.14	1.13	0.35
O15_HR	1.76	1.85	1.89	0.07	1.09	1.12	1.16	0.04
T11_HR	2.05	1.96	1.76	0.15	1.12	1.1	1.1	0.01
C16	-	-	2.44		-	-	1.35	
C23	-	-	1.79		-	-	1.06	

Note: Tortuosity is calculated for three directions x,y and z. sample from outside and inside of the layered zone are presented by (I) and (II) respectively.

It is obvious that min tortuosity is smaller than mean tortuosity in all samples. Biolithite sample has the highest standard deviation value and the pore network tortuosity is significantly higher in x direction (T_{mean}: 2.69 and T_{min}:1.74) rather than the y and z directions (T_{mean}: 1.59 and 1.42; T_{min}:1.14 and 1.13 respectively). As shown in figure 4.23, a semi parallel distribution of oblate spheroid shaped pores resulted in an anisotropy in the pore system so that pores are elongated perpendicular to the direction x and parallel to directions y and z. Thus, flow paths can be more meandering when moving in the x direction causing higher tortuosity in this direction. On the other hand, Oolitic limestone and Travertine have almost similar tortuosity values in all three directions. For Coquina rock, sample from outside

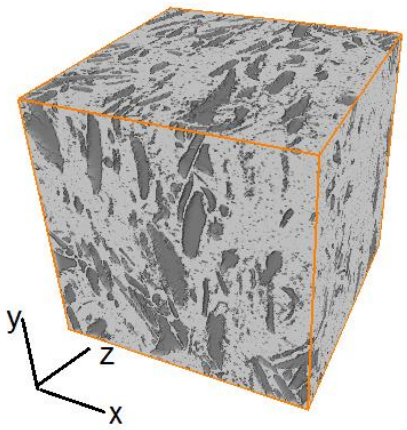

Figure 4-23 Extracted 3D volumes of high resolution X-ray tomography of sample B23 showing the anisotropic pore system so that pores are elongated perpendicular to the direction x and parallel to directions y and z. Grains and void spaces are in bright and darker colours respectively.

the layered zone shows both lower tortuosity and lower standard deviation than the sample from inside the layered zone. While min tortuosity in three directions is in same range for sample from inside the layered zone, mean tortuosity in directions y and z (2.50 and 2.57 respectively) are significantly higher than in direction x (1.89). Tortuosity values calculated in the z direction of the whole core Coquina samples show a significantly higher value for sample C16 (T_{mean}: 2.44 and T_{min}:1.35) which has layering perpendicular to the z direction than sample C23 (T_{mean}: 1.79 and T_{min}:1.06) with layering parallel to the z direction. In the former case, pathways inevitably cross the layers with variable porosity and pore size due to the different textures along the z direction resulting in more tortuous paths while in the latter case, pathways do not necessarily cross different layers.

4.5.5 Permeability

The pore network image extracted from the X-ray tomography image (53 µm voxel size) of one of Coquina samples (C16) was used to investigate the variation of permeability along the samples length and its correlation with the abovementioned pore network properties. To do this, the pore network image of the core sample C16 was split to 29 disc shaped (circular) sections along its length (with radius and thickness of 19000 and 2500 µm respectively). Then, pressure-driven flow simulation using the lattice-Boltzmann method, LBM (see chapter 3, section 3.4) was used to calculate permeability for each section. Pore network properties including porosity, specific surface area, connectivity density, tortuosity and pore coordination number were computed for each section. Sample C16 was selected because the existence of layers normal to its long axis enable us to capture the variation in permeability and pore network properties in different layers. Calculations have not been done in the first and last sections to avoid the effect of artifacts in bottom and top faces of the X-ray tomography image.

The calculated permeability and each pore network property are plotted versus section number showing their variation along the vertical direction of the sample (figure 4.24). As observed in these plots, there are considerable fluctuation in all plots along the samples length. There are wide range of permeability values ranging from 23 to 504 mD for different sections. Some sharp changes in permeability and pore network properties like specific surface area and porosity is observed. For example, section 12 has anomalously higher permeability and lower specific surface area compared to the sections just below and above it. This can indicate existence of a horizontal (normal to the samples length) thin (a few mm) layer with distinct pore network. The high variation of permeability suggests that the effect of lab-induced mechanical deformation on permeability of Coquina samples can significantly

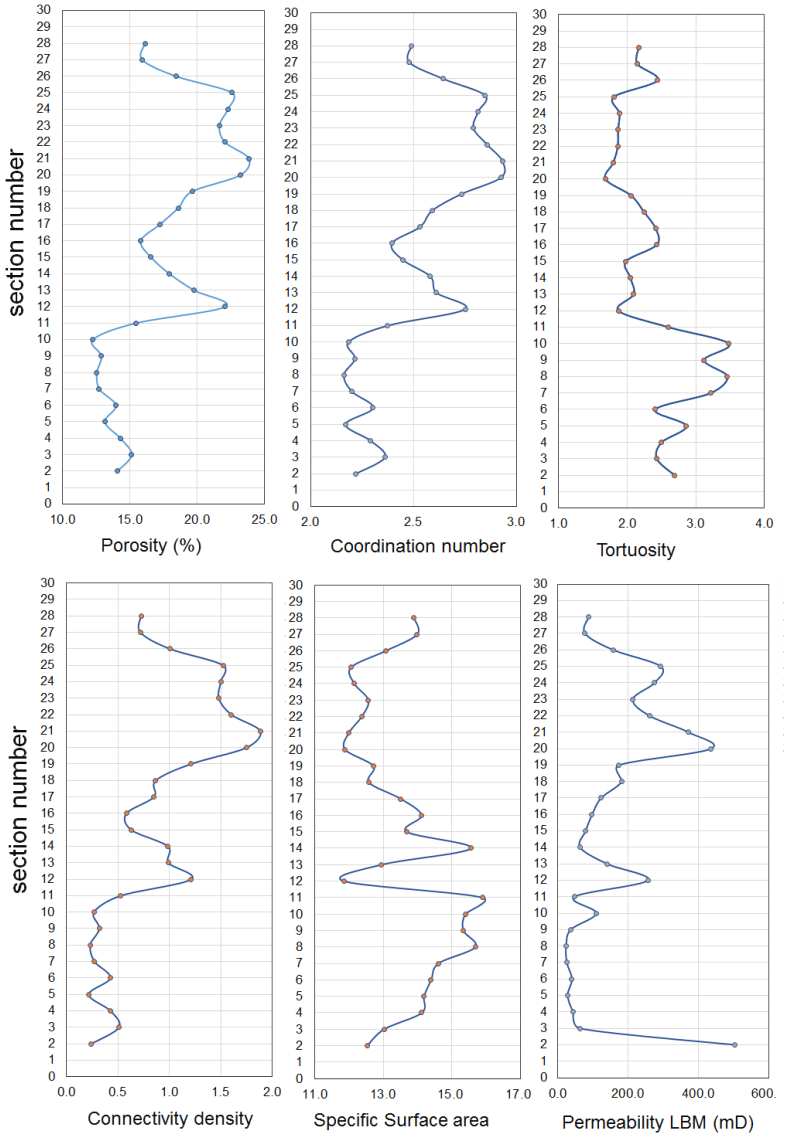

Figure 4-24 Plots of calculated permeability using LBM simulation and each pore network property vs section number of the sample C16

vary based on the distribution of permeability in the sample. For instance, as discussed before in section 4.4, the fracture did not significantly alter the permeability in high-perm sample (C22) while it considerably increased the permeability in the low-perm sample (C13) cored perpendicular to the layering orientation.

The correlative graphs of permeability and each pore network properties are presented in figure 4.25. As seen in these graphs, permeability is directly proportional to porosity, connectivity density and coordination number whereas its inversely proportional to the tortuosity and specific surface area. The specific surface area and porosity show stronger correlation with the calculated permeability. Dependency of permeability to pore network properties in this sample is in good agreement with the other studies on a carbonate grainstone sample (Tondi et al., 2015; Zambrano et al., 2018). This should be noted that the unresolved

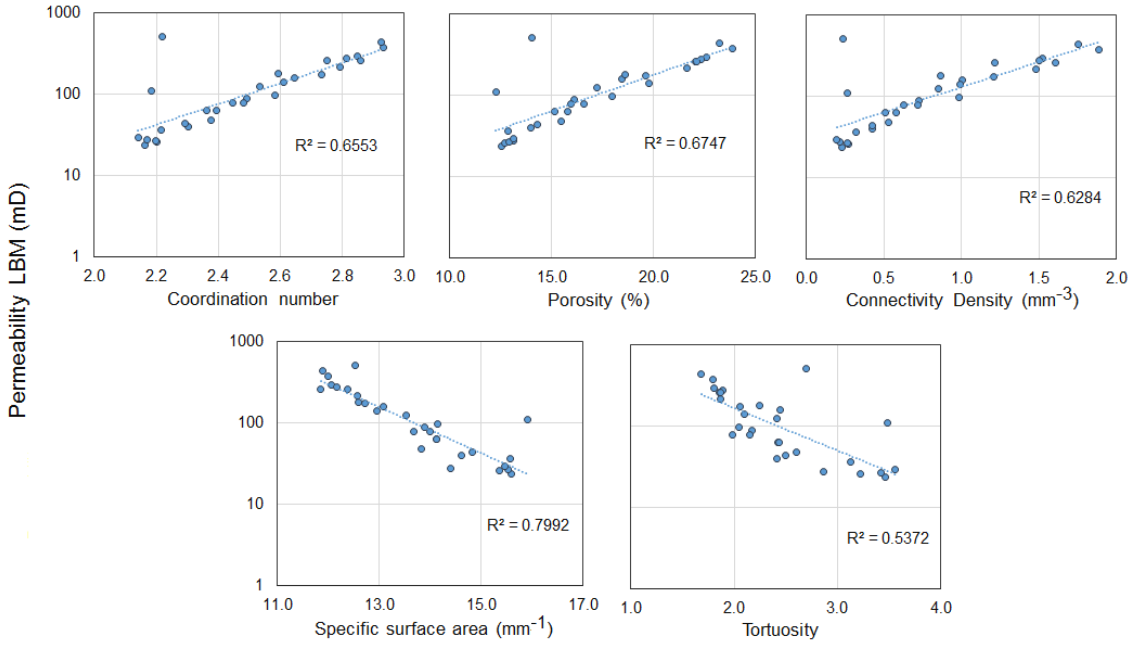

Figure 4-25 Correlation of calculated permeability using LBM simulation and each pore network property for sample C16.

micro-pores (sub resolution porosity) has not contributed in the calculated permeability values given the resolution of the X-ray-tomography image (53 µm voxel size) used for the flow simulation. The calculated permeability was compared to the measured permeability to get an understanding of the effect of un-resolved porosity on the calculated permeability. The permeability of the whole sample which was calculated from harmonic average of permeability values of all sections is equal to 74.97mD. This value is close to the lab-measured permeability for sample C16 (92mD). This can show a very low contribution of sub-resolution porosity (pores <53 µm) in absolute permeability of samples. This means that the used resolution of the image (53 µm) can resolve most of the connected pores of this sample.

4.6 Summary

In this chapter, four types of carbonate rocks used in this study were introduced and their textural features have been characterised based on analysis of hand specimens, thin sections and direct observation of X-ray tomography images. Then, mechanical behaviour of the samples coming from different directions of these rocks are presented (samples were subjected to triaxial compression) and the observed lab-induced deformation features were studied. Finally, pore system properties of the samples ware quantitatively investigated based on the extracted pore network images from X-ray tomography images. The objective is to characterise the spatial variations in pore network properties resulted from textural variation

due to depositional features and mechanical deformation features to help to better understand the observed fluid flow in these samples in next chapters. Furthermore, it has been investigated that how mechanical behaviour and the traces of lab-induced deformation (as expressed through section 4.4) in these particular rocks and under certain loading condition are controlled by textural features and potential textural variations in the samples. Here, a summary of these characterisations for each rock type is presented.

The **Coquina limestone**, is a carbonate grainstone from the Provence Region of France that consists mainly of shelly fragments. Distribution of layers with distinct textural characteristics is observed in this rock. These layers are distributed almost parallel to each other within a few cm thick zone. Thin sections and high-resolution X-ray tomography showed distinct textural characteristics in these layers. While the carbonate body mainly consisted of shelly carbonate fragments in non-uniform size and shape, these layers consist mainly of sand size grains with almost uniform size and shape. As observed based on the qualitative and quantitative analysis of X-ray tomography data (see sections 4.4 and 4.5) occurrence of these layers have affected both pore network properties and lab-induced deformation features and are expected to significantly control fluid flow within the samples. While the main carbonate body has higher porosity with larger interconnected pores, the sandy layers have lower porosity and smaller pores with higher specific surface areas that are connected through a large number of narrow channels. The orientation of these layers with regards to the flow direction in these sample is also expected to play crucial role in their flow properties. The calculated tortuosity values are significantly higher in the direction perpendicular to the layering compared to the direction parallel to the layering, which indicates anisotropy in pore system properties caused by the layers. High variance in lab-measured permeability values (ranging from 37 to 440mD) for samples that are all cored from same block but in different orientation and position with regards to the layered zone shows the significance of spatial variation in pore network properties. In general, samples that are cored outside the layered zone (samples C21 and C22) show higher permeability than other samples encompassing layers regardless of their coring direction. Calculated permeability and pore network properties in different sections of the Coquina sample (C16) show high fluctuation of these properties along the length of the sample which can be due to the existence of horizontally oriented layers with distinct pore network in this sample. The correlative graphs of permeability and each pore network properties showed that permeability is directly proportional to porosity whereas its inversely proportional to the tortuosity and specific surface area. This is in good agreement with the study on carbonate grainstone sample in Zambrano et al., (2018). Furthermore, correlations of connectivity density and coordination

number with permeability were also found in this chapter that showed a positive correlation of both parameters with permeability. Among these pore system properties, the specific surface area and porosity showed stronger correlation with the calculated permeability. Thus, these two parameters are chosen to be used (to be calculated for other samples) in next chapters where an estimation of the permeability and its variation in other Coquina samples is required to be made based on pore network properties.

The negative correlation between tortuosity and permeability in tested Coquina in this study is in contradiction with some results presented in Corbett et al., (2017) in which a Coquina rock type that has the lowest values of porosity and permeability among other Coquinas has also has the lowest tortuosity. As presented in their study, this Coquina sample has a particular pore type including a solution-seam related, fracture- like, porosity in micro-stylolites and (dis-)solution seams/channels. The mentioned contradiction between our study and the results in Corbett et al. (2017) highlights the significant role that the pore type can play in pore network properties of carbonate rocks.

Existence of layers and their orientation is also influential in mechanical deformation. For example, where the layering is parallel to the direction of axial stress, a vertical fracture has developed parallel to the layers. Induced mechanical deformation has increased the permeability of the samples that are cored in the layered zone.

In **Biolithite** rock, an inter-grown skeletal texture resulted in a growth-framework pore type. The almost parallel arrangement of oblate spheroid/ellipsoid shaped pores in this rock (as observed in the X-ray tomography images) has introduced an anisotropy in pore network properties and mechanical behaviour of samples. Also, high variances in measured helium porosity (ranging from 23 to 39%) of sample cored from different position in the Biolithite rock block is evidence of heterogeneous distribution of porosity in the rock block. The obtained results from triaxial compression tests suggest that variable porosity in the core samples can significantly control the mechanical properties. Samples with considerably high porosity values (33 and 39%) show significantly lower yield point and ultimate strength compared to samples cored in similar direction but with lower porosity values (23 and 24 %). These results are consistent with other studies investigating the effect of porosity in other types of carbonate rocks including Solnhofen limestone with fine-grained texture (Renner & Rummel, 1996) and chalk (Vajdova et al., 2004). All Biolithite samples showed the same trend of multiple strain hardening and strain softening events due to partial pore collapse and associated compaction under triaxial loading. The results from triaxial compression experiments also indicated that the samples in which oblate spheroid/ellipsoid shaped pores

are dominantly oriented horizontally (two larger axes of pores are normal to the long axis of the core sample) had lower bulk Youngs Modulus and Ultimate Strength compared to samples in which the pores are dominantly oriented vertically (two larger axes of pores are parallel to the long axis of the core sample). Although the effect of pore geometries like (pore aspect ratio) on the mechanical behaviour of porous rock has received a good attention (Bubeck et al., 2017), the results of the influence of pore orientation on mechanical deformation is much less reported (Griffiths et al., 2017) and are limited to numerical simulations. To our knowledge, this is the first time that the effect of pore orientation on mechanical behaviour of carbonate rock has been studied experimentally. The results confirms the finding of numerical simulation (Griffiths et al., 2017) where mechanical properties are found to be strongly dependent of the dominant pore orientation. The anisotropy in pore network properties caused by the geometry and distribution of pores is evident in calculated tortuosity values in different orthogonal directions. The tortuosity is significantly higher in the direction normal to the two larger axes and parallel to the shortest axis of pores and lower tortuosity in the other two orthogonal directions (parallel to the two larger axis). This is because the higher meandering of flow paths in the direction parallel to the shortest axis of pores. Employing such a simple and quick procedure to determine the directional dependency of tortuosity in reservoir rocks can be very useful. For instance, understanding of tortuosity anisotropy can provide very useful insight into anisotropy in parameters like effective diffusion coefficient that can have implication in for instance enhanced gas recovery processes (Yang et al., 2019). The low value of connectivity density (8.2 mm^{-3}) and average coordination number (2.7) in Biolithite is indicative of poorly connected pore network which is in good agreement with its low lab-measured permeability (<1mD). The calculated specific surface area is very low in this rock that can be related to relatively larger pores with simpler geometry.

Oolitic limestone can be characterised as a medium to coarse grained packstone to grainstone and as having a more homogeneous texture compared to the other tested rock types in this chapter. Based on thin section and X-ray tomography images, it seems that there is low inter-granular porosity while totally or partially dissolved Ooliths provide secondary intra-granular moldic porosity. In the high-resolution X-ray tomography, abundance of hollow spherical and semi-spherical Ooliths with sizes of approximately less than 0.4mm can be observed. The high calculated average coordination number (6.41) and medium value of connectivity density (46.69 mm^{-3}) of the Oolitic limestone is in contrast with the very low permeability of this rock (<1mD). It can be expected that pore throat sizes are very small in this rock that resulted in low permeability of sample despite the abundance of connections between pores.

In addition, as intra-particle moldic porosity is dominant in this Oolitic limestone sample (see figure 4.10), the pores are well-connected where Ooliths are in contact (grain supported texture) whereas connectivity of the whole pore network is partially disrupted where the Ooliths are in a mud supported arrangement due to the existence of an extremely fine-grained mud size matrix around the Ooliths. Actually, groups of well-connected pores tend to be separated from nearby pores because they are surrounded by low porosity matrix. The tortuosity of Oolitic limestone is low and there is no significant difference in tortuosity values in different directions.

Oolitic limestone samples were deformed under different confining pressures ranging from 2 to 30 MPa. At 2 Mpa confining pressure, a brittle response followed by strain softening is observed but by increasing confining pressure to 2.5, 3, 4 and 5MPa, the mechanical response of samples gradually changes from strong strain softening to a weak strain softening while the yield strength is almost constant. At high confining pressures of 20 and 30MPa, strong strain hardening is observed.

The **Travertine** rock used in this study is characterised by very small pore sizes (mean pore size of 291 μm) calculated based on 10μm resolution X-ray tomography image. In this resolution, distinction between the solid components and the pore spaces is not easy. Some regions with larger and more visible solid components can be observed while some region with darker grey colour exist in which pores and solid components cannot be distinguished clearly at this resolution. A fibrous texture of crystals encompassing considerable amount of sub-resolution porosity can be a reason for this appearance. Tested Travertine samples have high value of coordination number (7.4) and connectivity density (149 mm^{-3}). The tortuosity of Travertine is low and there is no significant difference in tortuosity values in different directions. The specific surface area in this sample is very high that is consistent with its very small pore size.

The mechanical properties of Travertine sample show a slight direction dependency. Two groups of Travertine samples cored in perpendicular direction were deformed under confining pressures of 5, 7.5 and 10 MPa. Samples T13, T11 and T15 (cored in direction 1) showed a very weak strain softening after the yield point and have slightly smaller young modulus and ultimate strength than the samples T21, T22 and T24 (cored in direction 2) regardless of confining pressure. Samples T21, T22 and T24 show multiple weak strain hardening steps after sudden stress drops.

The rock samples characterisation in this chapter provided a good insight into the pore system properties of different tested carbonate rocks that enabled us to choose the samples with most

interesting features for being tested under flow experiments coupled with Neutron tomography. Given the main focus of this study that is on investigating the impact of core-scale features on fluid flow, samples with most distinct features were chosen that were mainly from Coquina samples. Unlike the relatively homogeneous texture of Oolitic limestone, other three rock types including Coquina, Biolithite, and Travertine have shown different types of textural variations and core-scale features. Among these rocks, hydraulic properties of the Coquina rock were found to be more significantly affected by the core-scale features and textural variations as the samples cored from a same rock block showed more than one order of magnitude variation in measured permeability that was much higher than the permeability variation in other rock types. For the Coquina rock, the samples prepared from inside and outside the layered zone and in two perpendicular (C13) and parallel orientation (C21) to the layering direction showed a wide range of permeability values from 37 to 440. Quantitative analysis on X-ray tomography images also revealed a high spatial variations in pore network properties within Coquina samples so that a sharp changes in properties like porosity, specific surface area, coordination number and tortuosity was observed in different zones along the sample. The permeability calculated (using LBM method) for different zones within a layered Coquina sample (C16) also revealed high variation in permeability and sharp changes of permeability values along the length of core sample. These variations that highlights the significant impact of layering and textural variations on the hydraulic behaviour of the studied Coquina rocks, motivated us to choose Coquina rock for the flow experiments. Different Coquina samples cored from inside and outside of the layered zone and in two different orientation (parallel and perpendicular to the layering direction) were chosen for miscible and immiscible flow experiments in next chapters.

Chapter 5

4D Neutron imaging of miscible fluid flow

This chapter explores how textural variations due to depositional features and lab-induced mechanical deformation (fractures) in millimetres scale (within 38mm diameter core samples) control miscible fluid flow in tested carbonate rock samples. The morphology of the flow patterns, irregularity in the advancing fluid front, fluid speed distribution, relative concentration distribution and its evolution with time, hydrodynamic dispersion and fracture-matrix flow have been examined during miscible fluid flow experiments on two groups of Coquina samples including intact and mechanically deformed samples. For this purpose, high speed neutron tomography (HSNT) and image processing techniques have been employed to provide three dimensional visualisation of the fluid transport within the samples with time and quantitative measurements of its interplay with characterised core-scale features.

5.1 Tested Materials

In total, six Coquina core samples were tested and presented in this chapter. Miscible fluid flow experiments were carried out on two groups of samples. Samples tested in each group are listed in the following. The detailed description of these samples and their mechanical behaviour have been presented in Chapter 4.

The intact samples including C11, C12, and C13 were all cored in same direction but from different positions in the block. As described in Chapter 4, in the Coquina block from which the samples were cored, a few centimetres thickness zone can be identified in which several thin silty/sandy layers exist. The thickness of this zone and layers seems to be laterally variable in the block. Also, the texture of rock varies slightly in the vertical direction (along the depositional sequences). So, the three above-mentioned samples were extracted from different locations to cover examinations of both lateral and vertical variations in textural characteristics. While C12 and C13 cross the silty/sandy layered zone in two different lateral position, C13 is cut from above the layered zone and mainly consists of shelly fragments.

To investigate the interplay between fractures, layering and fluid flow in Coquina samples, three samples were selected and deformed under triaxial compression (see Chapter 4, section 4.4). The first selected sample was sample C13 on which the flow experiment and neutron imaging was performed before mechanical deformation (on intact sample). The second sample, C24, was cored from inside the layered zone and in the parallel direction to the layers. The last sample, C22, was cored from outside (above) the layered zone and parallel to the layering direction. The reason for selecting these sample was to understand the impact of fracture on fluid flow with regards to existence or lack of layering as well as the layering orientation (perpendicular and parallel to the core sample length).

5.2 Experimental set-up

The flow experiments coupled with high speed neutron imaging presented in this chapter were performed at NeXT-Grenoble instrument (ILL, Grenoble, in May 2018) and at Helmholtz-Zentrum Berlin (HZB, Berlin, in February 2019). The experimental workflow and equipment used during the tests are discussed in detail in Chapter 4. Here, specification of the flow experiments, used fluids, injection rate, samples initial saturation condition and other details of experimental campaigns are presented.

For miscible fluid flow experiments, samples are first saturated in heavy water (D_2O) under vacuum and then are placed in the flow setup (explained in chapter 4) and get prepared for

flow experiments. The samples were left under the vacuum about 12 hours until no bubbles could be seen at the sample surface meaning that the sample approached to its fully saturated condition. Also, some pre-test Neutron tomographies of the saturated samples were taken and checked by visual examination to make sure that no pockets of air are remained in the sample. However, saturation might slightly decrease at boundaries during handling (e.g. touching the sample) the sample for sample preparation (section 4.1.2). It was tried to wrap the sample with PTFE tape immediately after taking it out from the saturating vessel to minimise the loss of saturation at boundaries of the sample. During flow experiments, distilled water (H_2O) is injected into the core sample from its bottom end with a constant injection rate. The injection direction is from bottom end to top end of the vertically placed core sample and outlet fluid is collected from the top end of the sample that is at atmospheric pressure. Injection is continued until at least one pore volume of distilled water is injected into the sample. Heavy and light water are used because they have comparable hydro-mechanical behaviour while an order of magnitude difference in their neutron absorption provides enough contrast between them to be visualised and traced in neutron imaging. While the hydrogen in water attenuates much of the neutrons beam, deuterium in heavy water is more transparent to the neutrons. This makes the technique independent from the addition of any chemical dopants, which is needed in x-ray tomography studies to make contrast between different phases.

For choosing the flow rate for miscible fluid flow experiments, first, the maximum flow rate at which the movement of fluids can be captured by HSNT was determined. For this purpose, the highest temporal resolution that can be achieved in HSNT should be calculated as a determining factor for the maximum flow rate. This is because the flow rate higher than a certain value can result in a quick advancement of fluid in the sample (due to high fluid speed) during a signle HSNT and does not allow a successful tomography reconstruction. For calculating the maximum temporal resolution of HSNT itself, the number of projections and exposure time for each radiography should be calculated as determining factors for the total acquisition time of each HSNT. Based on the configuration of beam-line facilities (mainly the available flux of Neutron beam) and the advices of beam-line scientist, the fastest exposure time for our sample size was chosen to be 120 ms and 200 ms at ILL and HZB facilities respectively. For a good quality reconstruction of HSNTs, the optimum number of projections was defined to be 500 projections based on the previous experience (Etxegarai, 2019) of HSNT in the same size samples (38mm diameter core samples). Accordingly, the total acquisition time was calculated to be 60 and 100 second for HSNT at ILL and HZB facilities respectively.

To determine the maximum flow rate, some pre-test HSNT with temporal resolution of 100 second were carried out during fluid flow in a spare Coquina sample with variable flow rates. As found by (Etxegarai, 2019; Tudisco et al., 2019a), the fluid advancement of up to 10 pixel during a single HSNT acquisition (1 min duration) still allows reasonable results for tomographic reconstruction.

By assuming homogeneous distribution of fluid speed throughout the sample and given the pore volume and fluid injection rate, the average speed of front advancement can be calculated. The pore volume available for flow in a one millimeter height of the sample (given the 20.8% average porosity for Coquina samples) is approximately 0.235 ml. This means that 3.99 ml of the injected fluid is required until the fluid front advances for 10 voxel (1.7mm) in the vertical direction. Accordingly, the maximum fluid injection rate that can avoids more than 10 voxel advancement of the fluid during a single tomography is calculated that is equal to 2.35 ml/min. However, this calculation is only correct if the assumption of homogeneous advancement of the fluid in the sample be valid. However, due to the heterogeneous distribution of porosity and pore properties in the tested Coquina rocks, higher fluid advancement speed is expected in these samples. To get an idea of the fluid advancement speed in these samples, a series of test HSNTs (prior to running the main experiments) were acquired during fluid flow with variable flow rates below the maximum measured flow rate (2.35 ml/min). The advancement of fluid during each HSNT was measured by subtracting the first and last radiographies. Based on these analysis, it was found that at flow rate of 0.1 ml/min, the advancement of fluid is safely less than 10 voxel. Also, the HSNTs were reconstructed immediately in the facility and were checked by visual examination to make sure that the chosen imaging parameters (projection number and exposure time) and the chosen flow rate allows for a good quality reconstruction. In this way, the maximum flow rate that allows for a good quality reconstruction was determined that was equal to 0.1 ml/min. The field of view was optimised to cover the whole size of the sample as well as a portion of the aluminium base (flow inlet) that enabled us to assess the time when injected fluid touched the sample. About 200 to 400 HSNTs were acquired during the flow experiments to cover the full span of fluid entrance from inlet and its travel through the sample to reach to the outlet. The radiographies were being regularly checked (by visual examination) during the HSNT acquisition to follow the advancement of the injected fluid within the sample and to determine the time to terminate the experiment and image acquisition once the injected fluid flowed through the entire sample. Details of the imaging parameters are presented in Table 5.1.

Table 5-1 Details of the imaging parameters in two experimental rounds.

Flow experiment/ Beam-time	samples	Tomography acquisition time* (sec)	Number of projections	Voxel size (µm)	Exposure time** (ms)	FOV (mm x mm)
ILL, May. 2018	C11	60	500	170	120	105 x 105
	C12	60	500	170	120	105 x 105
	C13	60	500	170	120	105 x 105
HZB, Feb. 2019	C13-def	100	500	170	200	110 x 110
	C22	100	500	170	200	110 x 110
	C24	100	500	170	200	110 x 110

*Tomography acquisition time means the total time for acquisition of all radiographies over 180 degree rotation of the sample. **Exposure time is the time spent for each single radiography acquisition.

To estimate the relative influence of mechanical dispersion and diffusion in miscible displacement in our samples, the Peclet number (Pe) is calculated. This parameter is defined as the ratio between the rate of advection to the rate of diffusion in the transport of miscible fluids (equation 5.1).

Equation 5.1 $$\boldsymbol{Pe = \frac{vL}{D_m}}$$

where Dm is the molecular diffusion coefficient (m^2/s) of the fluid, L is the characteristic length (m) and v is the characteristic velocity in the pores (m/s). The characteristic velocity was calculated for the condition of fluid flow in the tested samples as $v = Q/(A\emptyset)$ where Q is the volumetric flow rate (m^3/s), A is the cross-sectional area of the core sample (m^2) and $\emptyset$ is the porosity. The characteristic velocity for experiments of this chapter is calculated using the flow rate of 0.1 ml/min, porosity of 0.2 (mean porosity of Coquina samples) and cross sectional area of 11.34 cm^2 (core sample radius of 19 mm) is calculated that is equal to 0.000007333m/s.

For laminar flow, which is the case for our flow experiments (given the density of (997 kg/m3), characteristic length of (0.000700 m) for pores, characteristic velocity of (0.000007333m/s) and dynamic viscosity of water (0.000798 Ns/m2) the calculated Reynolds number <1), 4 types of flow regimes are classified based on the Pe number (Bijeljic & Blunt, 2007).

- Restricted diffusion regime (Pe < 0.3) in that molecular diffusion mainly controls the transport processes.
- Transition regime (0.3 < Pe < 5) where both mechanical dispersion and diffusion contribute in spreading.
- Power law regime (5 < Pe < 300) where mechanical dispersion mainly controls the spreading and diffusion may have slight influence.
- Mechanical dispersion regime (Pe > 300) where only mechanical dispersion control the transport processes.

The calculated bulk characteristic velocity for the Coquina samples is 441 µm/min. However, the fluid speed fields show that the fluid speed raises even to over 1000 µm/min locally. The characteristic length, which is 700 x 10^{-6} m, is the mean pore size in Coquina samples calculated based on X-ray tomography images (of the whole core). The mutual diffusion coefficient D_m of heavy water in normal water at room temperature is equal to 2.21 x 10^{-9} m^2/s (Meng et al., 2018). The resulting Pe numbers considering bulk characteristic velocity and the maximum local fluid speed are 2.66 and 6.02 respectively. This indicates that the flow regime in the tested samples is expected to be in the transition to power law regimes. It should be noted that the calculated maximum flow rate (0.1 ml/min) is used to calculate the Peclet number. At this flow rate, the resulted flow regimes in which both mechanical dispersion and diffusion contribute in spreading and mixing suits the purpose of this study given our interest for exploring the interplay between core-scale features and the processes involved in both advective and diffusive miscible transport. Therefore, the flow rate of 0.1 ml/min is chosen for miscible fluid flow experiments.

For defining the spatial resolution of HSNTs, it was tried to achieve the highest possible spatial resolution for our sample size. Given the fixed configuration of source to detector distance in the used beam-line facilities, the sample was placed in closest position to the detector to increase the spatial resolution by decreasing Geometric Unsharpness (see figure 3.3). But it was tried to keep approximately 3 cm distance between the sample and the detector to minimize the impact of scattered Neutrons (section 3.2.3). Having above configuration, the spatial resolution of 170 µm was achieved for HSNTs.

5.3 Image analysis

All the acquired tomographies were reconstructed as discussed in Chapter 3. Figure 5.1 shows the central vertical slice of the reconstructed volume of sample C13 acquired at different time

steps during water-heavy water flow experiments. As shown in these images, advancement of the injected fluid can be observed based on changes in grey-scale values of the reconstructed images. The heavy water is pushed by injected water causing an increase in the grey-scale value (pixels with lighter colour) from the bottom of the sample. Grey-scale value profiles from the shown slices indicate the evolution of grey-scale value along the sample with time. Although the progress of the displacing phase can be seen in the images, defining the displacing fluid front is not easy in the images nor based on the grey-scale value plots. A gradual change is observed in the plots indicating a transition zone between the mainly water saturated and mainly heavy water saturated zones in the sample.

For quantitative analysis of acquired HSNTs, two codes written by Etxegarai (2019) were used to generate the fluid arrival time field and fluid speed field for each sample during the flow experiments as explained in Chapter 3. The fluid front shape and position in 3D at different time steps can be extracted by segmenting the generated fluid arrival time field. For example, for extracting the 3D morphology of water front at a given time (t_1), the fluid arrival time has been segmented so that only voxels with values equal and smaller than t_1 are visualised. Further image analysis have been carried out to assess the state of hydrodynamic dispersion during miscible fluid flow experiment.

To assess the distribution of phases concentration in samples and its evolution with time, differential imaging has been carried out. In this way, the HSNTs at different time steps are subtracted from the first HSNT where the sample is fully heavy water saturated. The resulted images that show the intensity difference due to the displacing or mixing of heavy water and injected water are normalized against the maximum intensity differences of fully heavy water and water filled voxels to reflect the relative concentration of phases.

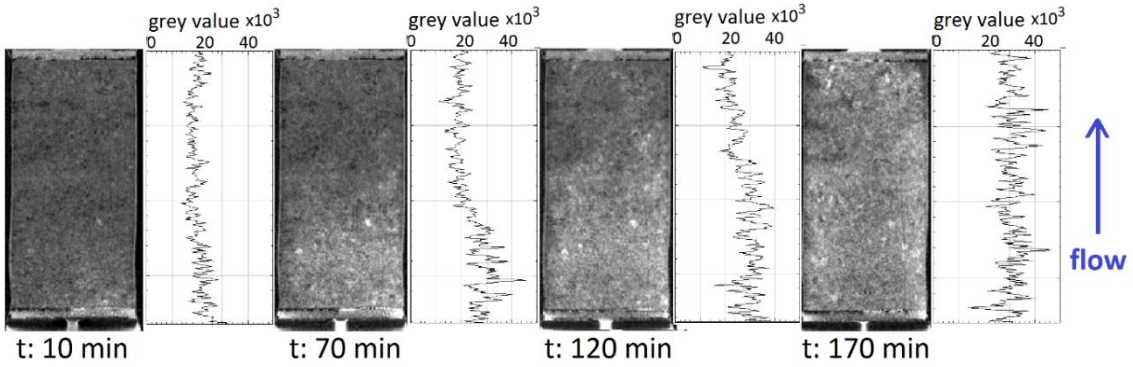

Figure 5.1 Vertical slices of reconstructed neutron tomographies of the Coquina sample C13, and grey-scale value profiles for the shown vertical slices of the reconstructed HSNTs (these are plotted along the height of the vertical slices using Plot function in ImageJ); one pore volume of water is injected into heavy water saturated sample, the lighter and darker colours correspond to water and heavy water respectively. The flow is from bottom to top.

To understand the influences of textural features on the observed processes, X-ray tomography images of samples have been used and sub-volume of these images have been analysed using the methods described in Chapter 3. In this way, the textural controls on distribution of pore system properties and the potential role they paly in the fluid transport processes have been explored.

5.4 Results

5.4.1 Miscible fluid flow patterns

The results from computed fluid arrival time field and fluid speed fields are presented in this section. The miscible fluid flow patterns and further quantitative analysis of the relative concentration distribution of fluid phases with regards to the textural features in the samples are investigated based on these results.

5.4.1.1 Textural variations - the presence of an anomalously large fossil fragment: Sample C11

This section presents results from C11 Coquina sample. This sample was cored from outside the layered zone in the Coquina block. Two vertical central slices, perpendicular to each other, and two horizontal slices from different height of the fluid arrival time field are presented in Figure 5.2. These images show that the distribution of the displacing fluid arrival time is not homogeneous in the sample. The displacing fluid (water) follows an expected time sequence from the bottom to the top part of the sample (injection was from the bottom end of the sample) but, many local millimetre-scale (like a few mm to ~20mm or tens of voxels to over 100 voxels) anomalies are observed. In a homogeneous sample, all pores at the same height are expected to be invaded by the displacing fluid in the same time frame. However, it is observed that there is a considerable lapse of fluid arrival time in neighbour regions in this sample (horizontal slices in Figure 5.2 c,d). This is particularly obvious in the mid-height horizontal sections of the sample, which reveal a region with anomalously later fluid arrival time. It can be inferred that the displacing fluid had bypassed this region by flowing through the adjacent regions in the sample (figure 5.2 a and d). The 3D rendering of the segmented fluid arrival time field in Figure 5.2 e shows the position of fluid front while passing this region.

In order to capture how concentration of the displacing phase (water) changes in this region, HSNTs acquired in times 50, 75, 100 and 125 minutes after the onset of flow experiment

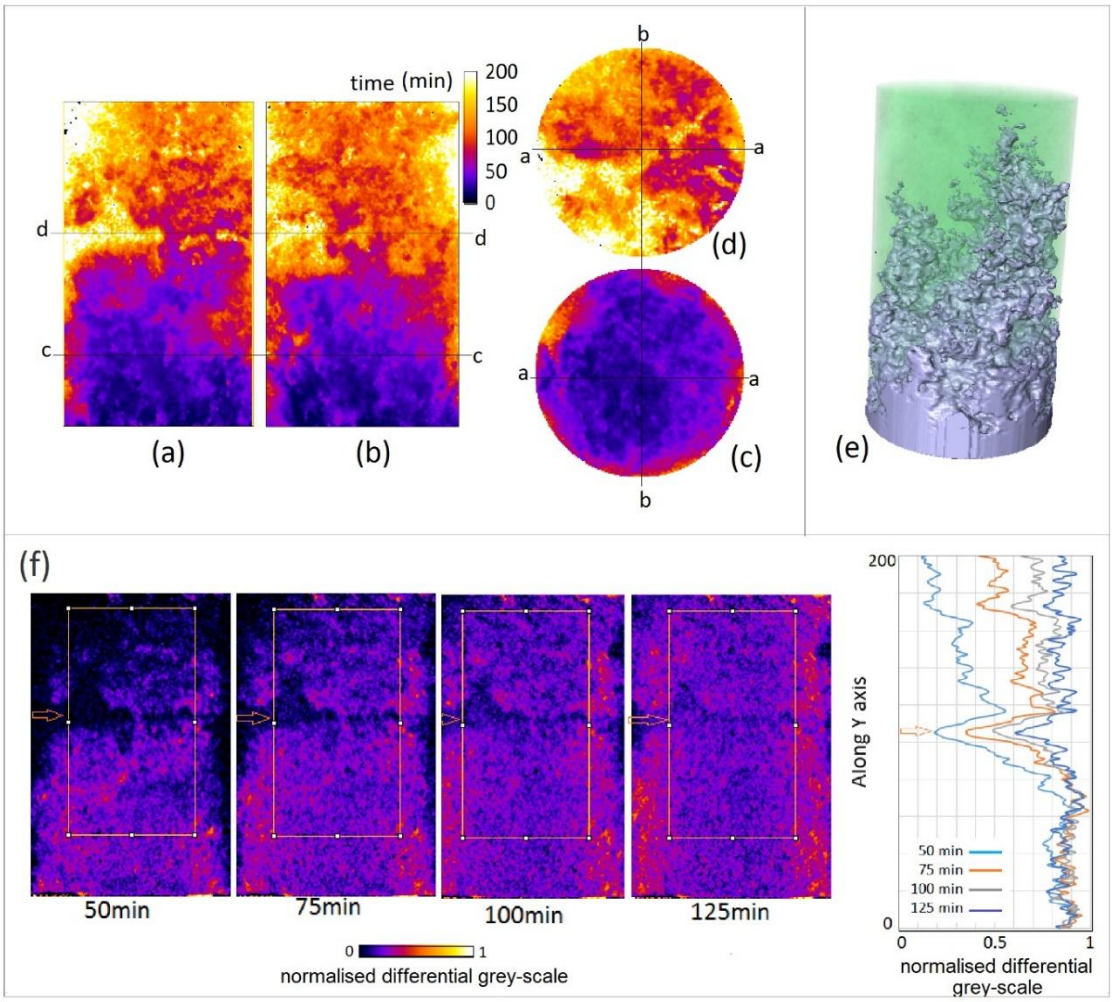

Figure 5.2 Two perpendicular vertical central slices of fluid arrival time field of sample C11 (a,b) and corresponding horizontal slices of them in indicated height of the sample (c,d) and 3D rendering of the position of fluid front in time:75min after flow experiments (e). Slices of the normalised differential grey-scale at 50, 75, 100 and 125 minutes after flow experiments that can be representative of water concentration (zero and one correspond to lowest and highest concentration of water, respectively) and corresponding graphs of normalised differential grey-scale along the Y axis from the indicated rectangular area on images (f), Outside the indicated rectangular, the higher differential grey-scale is observed at sample boundary due to the beam hardening artefact that may result in erroneous observed pattern.

were subtracted from the first HSNT, when the sample was heavy water saturated (see figure 5.2-f). The resulted images, which show the grey-scale difference due to the displacing or mixing of heavy water and water, were normalized against the maximum grey-scale differences of fully heavy water and water filled voxels. This can be directly linked to the relative concentration of the water in each voxel of the sample. However, the porosity also affect this grey-scale difference so that regions with lower porosity will have lower differential grey-scale value even if the water completely displaces the heavy water in that region. This suggests that the anomalies in porosity distribution should be taken into account while interpreting these data. As seen in these images, differential grey-scale is generally lower in the region that is identified with later arrival time. Given that the porosity in this

region is even higher than the surrounding regions (observed in X-ray tomography images that will be presented in the following, figure 5.4), relatively lower water concentration is concluded to be in this region. Average of normalised differential grey-scale plotted along the Y axis (i.e. height of the sample) of the selected rectangular (figure 5.2.f) show a sharp decrease of normalised differential grey-scale and as a result, lower water concentration in this region. Generally, higher differential grey-scale is observed in the boundaries of the sample compared to the central parts (in the normalised differential grey-scale images) that seems to be due to the beam hardening.

Vertical and horizontal slices of the computed fluid speed fields for this sample are presented in Figure 5.3. Distribution of fluid speed shows that the displacing fluid flows faster through preferential pathways. For instance, in Figure 5.3 a,d local distribution of high fluid speed can be observed in some regions, while there are neighbour regions with considerably lower fluid speed.

To better understand the observed flow behaviour of the sample, acquired X-ray tomography images were further analysed to obtain some pore-scale understanding. Figure 5.4, shows vertical and horizontal cross sections of the X-ray tomography image. The void spaces with variable sizes and shapes as a result of random arrangement of shelly fragments can be observed. There is a region (indicated by yellow arrows in the vertical slice) with anomalously different pore size, shape and distribution than that observed for the rest of

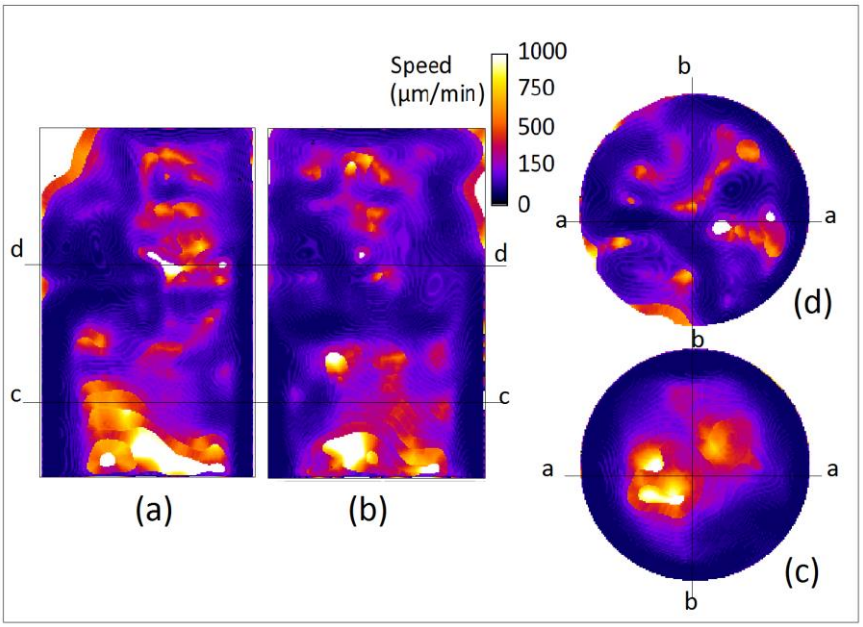

Figure 5.3 Two perpendicular vertical central slices of fluid speed field of sample C11 (a,b) and corresponding horizontal slices of them in indicated height of the sample (c,d)

sample. By zooming in this region (figure 5.3-c) a preserved structure is observed that seems to be related to a sponge fossil. This fossil with its own pore system that includes many pores with almost uniform shape and size, has a disc shape with a few millimetres thickness and about 15 millimetre diameter in its longest direction. Its position corresponds to the region characterised by later fluid arrival time and lower fluid speed.

Figure 5.4-d shows the 3D rendering of the pore spaces within this fossil fragment and the position of this fragment in the core sample. To investigate the connectivity of the pores in the sponge fossil, the segmented pore space image was labelled. In this way, connected pores are assigned with same label (colour). As shown in figure 5.4-e, pores of various colours indicate the abundance of isolated pores and poor connectivity of the void spaces that is in agreement with low fluid speed and later fluid arrival time in this region of the sample. In fact, the fossil fragment has acted as baffle and caused the displacing fluid (water) to flow through the adjacent volume of the sample. However, the slow change in the water concentration in this region observed from HSNT images, suggests that these pores are not entirely isolated. One explanation for this observation can be that the pores are connected through much smaller pores and pore throats that are not resolvable in the X-ray tomography image.

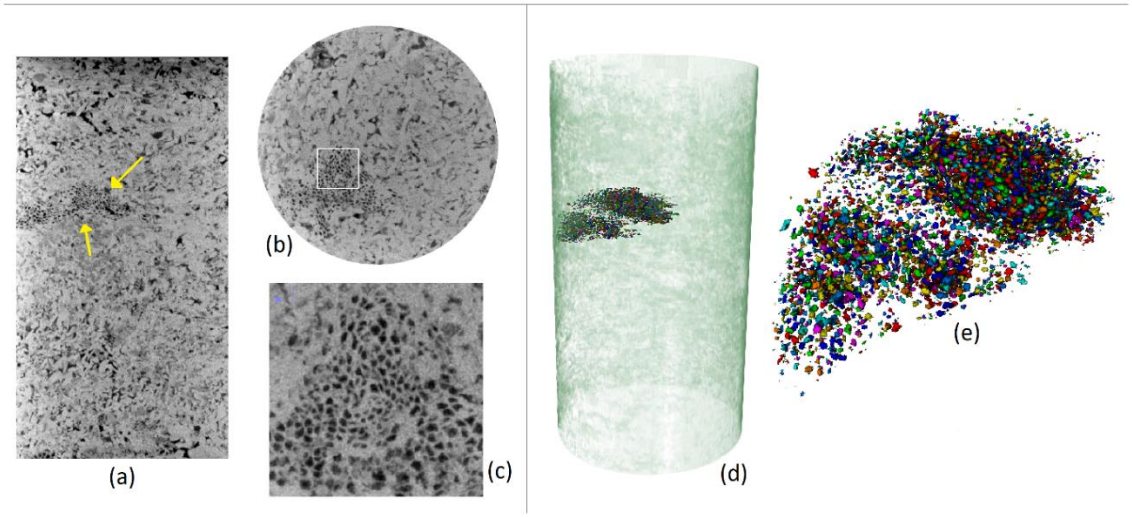

Figure 5.4 Vertical and horizontal cross section of the X-ray tomography image of sample C11 (a,b), yellow arrows indicate the region with anomalously different pore system. The zoomed images of this region (c) indicates a sponge fossil structure. Grains and void spaces are in grey and black colours respectively. The 3D rendering of the position of sponge fossil in the sample (d) and 3D rendering of the labelled sponges pore system (e), connected pores are assigned with same colour.

5.4.1.2 Textural variations – the presence of a horizontal high porosity sandy layer normal to the flow direction; Sample C12

Sample C12 is an intact Coquina sample. This sample has been cored perpendicular to the layered zone in the Coquina block. Two vertical central slices, perpendicular to each other, and two horizontal slices from different height of the fluid arrival time field are presented in figure 5.5. Generally, water arrival time increases from the centre of the core to its periphery meaning that the water flows earlier through the central part of the sample. The transition in voxels values from bottom to the top and from centre toward the periphery of the sample is gradual and no significant local and sharp variation can be observed in the water arrival time. The 3D rendering of the segmented fluid arrival time field indicating the front position in times 20 min and 60 min after the onset of the injection shows almost uniform conical shape of water progress in the sample. Actually, the water front has been stretched in the direction of flow. Water front has reached to the cores outlet almost 85 min after the injection started when considerable regions of samples were not invaded by the injected fluid (water) yet. Cross sectional slices of fluid speed field presented in figure 5.6 show higher fluid speed from the centre of the core to its periphery (fluid speed ranging from 0 to about 930 µm/min). In addition, some local changes in fluid speed are observed near the middle of the samples height (slightly above the indicated line c).

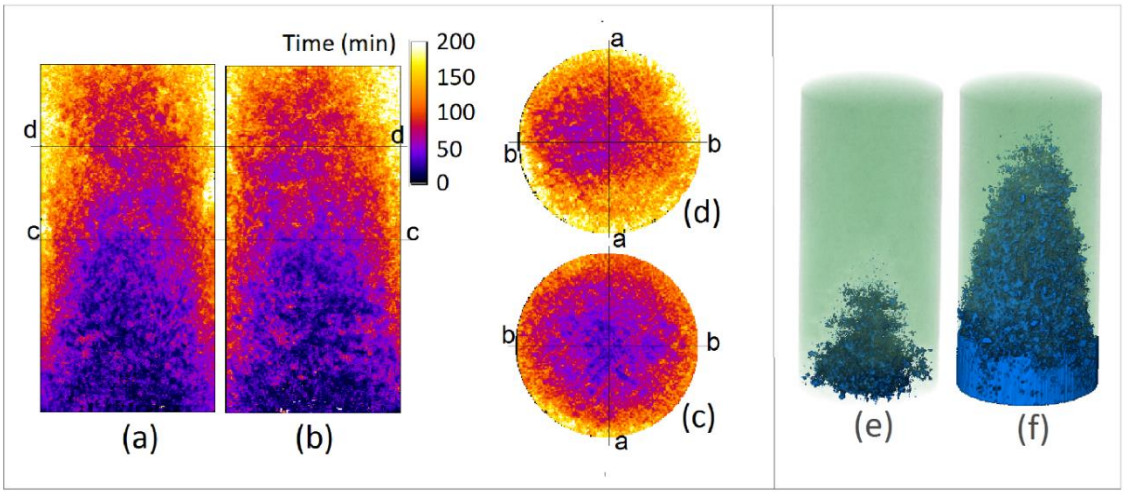

Figure 5.5 Two perpendicular vertical central slices of fluid arrival time field of sample C12 (a,b) and corresponding horizontal slices of them in indicated height of the sample (c,d) and 3D renderings of the position of fluid front in times: 20min (e) and 60min (f) after flow experiments.

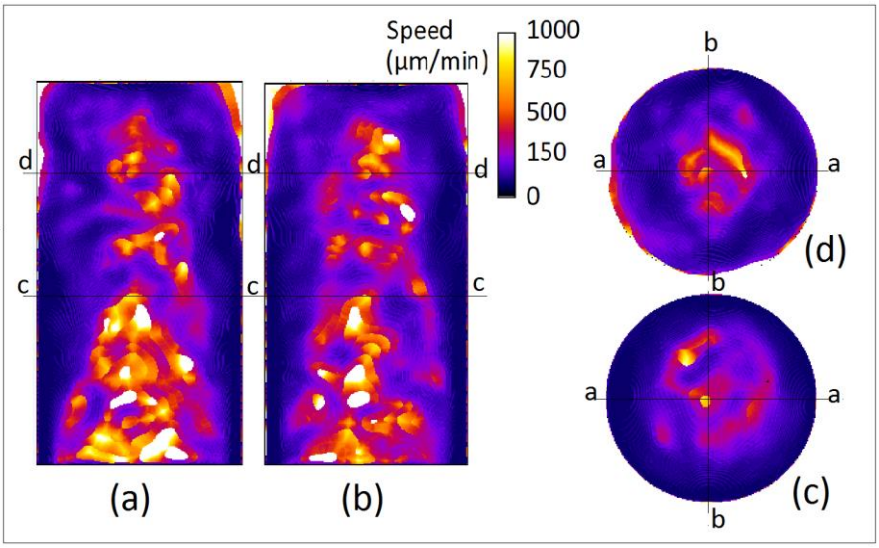

Figure 5.6 Two perpendicular vertical central slices of fluid speed field of sample C12 (a,b) and corresponding horizontal slices of them in indicated height of the sample (c,d)

The vertical and horizontal slices of X-ray tomography image of the sample C12 are presented in figure 5.7. A horizontal layer with different texture is identified in the middle of the samples height with about 1cm thickness (indicated by orange brackets). This layer that is related to the sandy layers in the Coquina block (described in material section of chapter 4), has darker grey-scale value and does not show a sharp boundary with the adjacent regions. The slice averaged porosity and pores specific surface area values that are plotted along the samples height are presented in figure 5.7-c. It shows that porosity increases significantly (about 10 percent) where the mentioned layer is located but the specific surface area is somehow constant along the samples height. The existence of this horizontal layer have had no significant impact on the water flow pattern however the higher porosity of this layer seems to be the reason for slight reduction of fluid speed in the mid-height of the sample (slightly above the line c in figure 5.6 a,b). No evident variation in pore network properties between the central part of the sample and the regions in samples periphery that can explain the earlier arrival time and higher fluid speed in the central part of the sample. Injection of water from a small circular opening in the center of the aluminum base can cause a conic shape water front in regions close to the inlet however, this cannot explain the conic shape advancement of the water front up to the outlet given the very small injection rate of water (that is 0.1 ml/min corresponding to almost 0.005 pore volume/min).

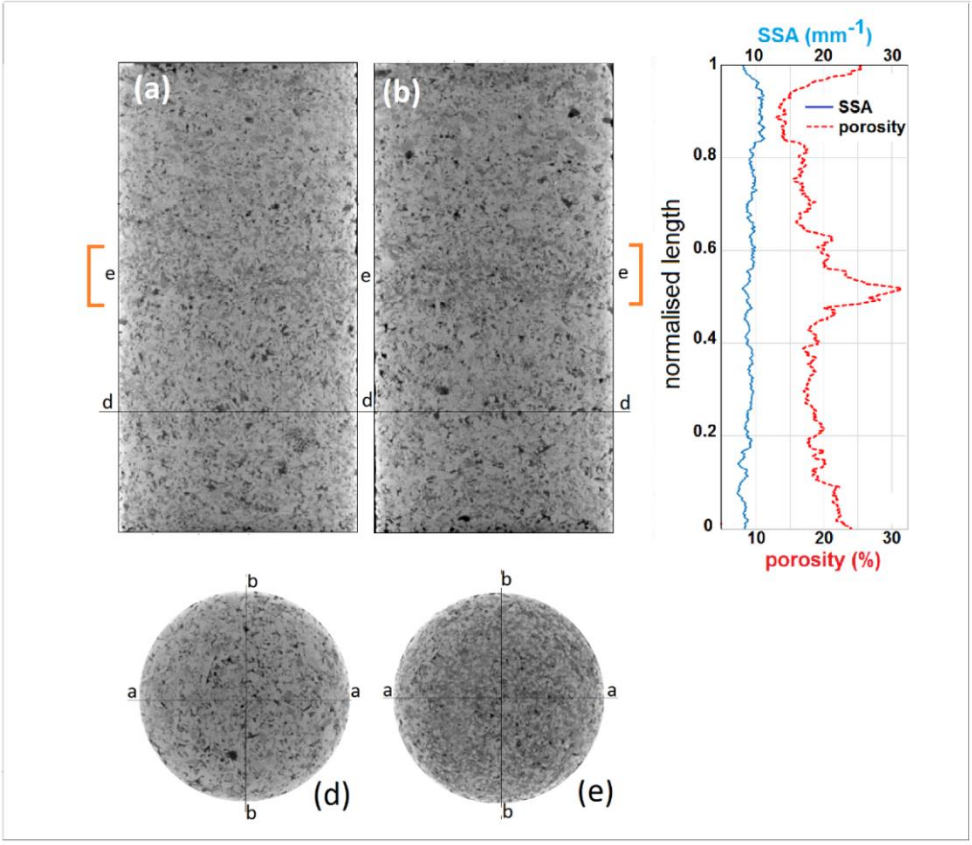

Figure 5.7 Vertical (a,b) and horizontal (d,e,) cross section of the X-ray tomography image of sample C12, Grains and void spaces are in grey and black colours respectively. Plots of porosity (red curve) and pores specific surface area (blue curve) along the samples length (c). The region in almost middle of the samples height indicated with orange brackets (horizontal slice e) shows significantly different texture.

5.4.1.3 Textural variations – the presence of layers with contrasting pore network properties normal to the flow direction: Sample C13

Sample C13 is an intact Coquina sample. This sample has been cored perpendicular to the layered zone in the Coquina block. Two vertical central slices, perpendicular to each other, and two horizontal slices from different height of the fluid arrival time field are presented in figure 5.8. By looking at vertical slices, a relatively sharp colour change, corresponding to arrival time difference, can be observed close to the mid-height of the sample (figure 5.8b) highlighted by a black line d. This time difference indicates that there is a considerable delay in water arrival time between regions above and below this point. As seen in the vertical slice (a) and horizontal slice (d), the water arrival time distribution becomes irregular and shows channelling when passing this region, indicating that water flows through some preferential paths. Also, advancing water fronts pattern seems to be altered at the level of horizontal slice c (indicated with black line c in the vertical slices). The fluid front below this point resembles the front in sample C12 (conic shape in which water arrival time increases from the central parts toward the boundaries of sample) while, above this point, the front advances with a

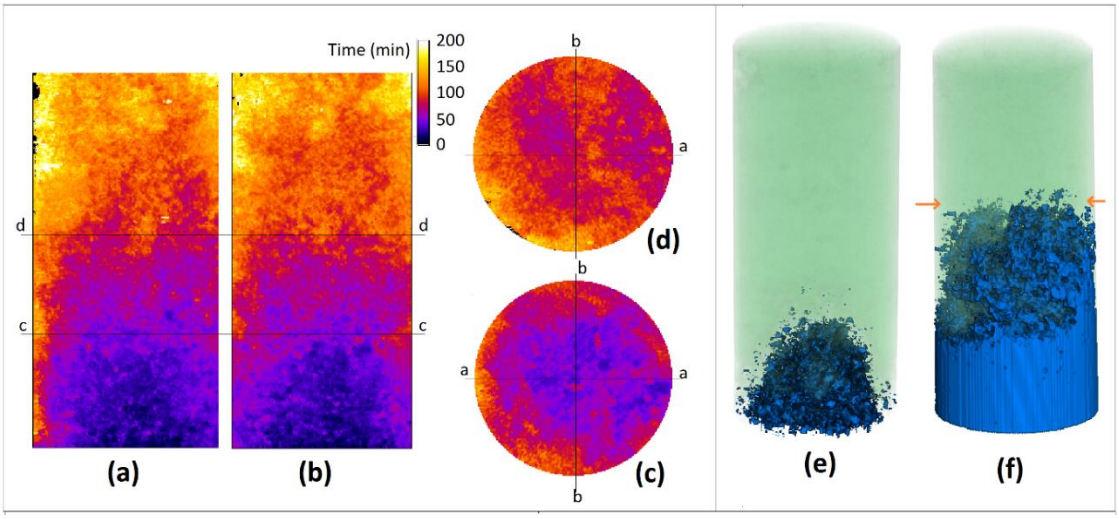

Figure 5.8 Two perpendicular vertical central slices of fluid arrival time field of sample C13 (a,b) and corresponding horizontal slices of them in indicated height of the sample (c,d) and 3D renderings of the position of fluid front in times: 20min (e) and 60min (f) after flow experiments.

more horizontal shape and transverse variation of arrival time decreases. This is more obvious in the 3D rendering of the fluid arrival time in time steps of 20 and 60 minutes after the onset of water injection (figures 5.8-e, f).

Cross sectional slices of fluid speed field of this sample are presented in figure 5.9. In general, the fluid speed is low at samples boundaries. The fluid speed distribution is irregular and local variation of fluid speed can be observed. In the region near the mid-height of the sample, a narrow low speed zone is observed in vertical slices of the fluid speed field figure 5.9-a,b). The horizontal slice corresponding to this region (figure 5.9-d) shows that the fluid speed is very low across the whole cross section except some narrow regions. A slight reduction in fluid speed is also observed at the level of horizontal slice c.

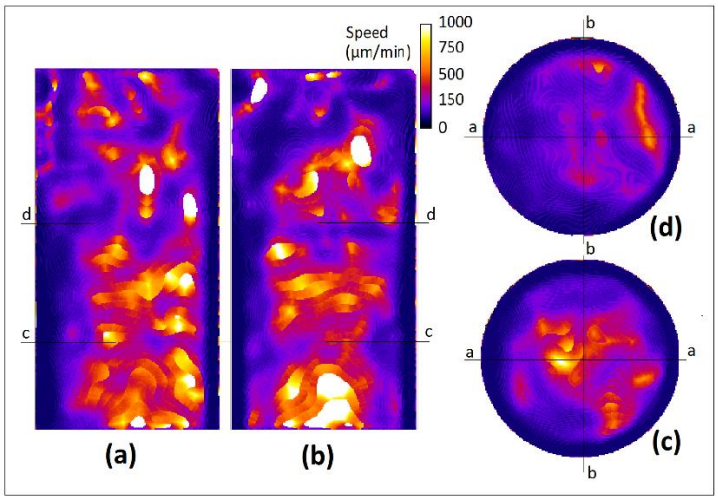

Figure 5.9 Two perpendicular vertical central slices of fluid speed field of sample C13 (a,b) and corresponding horizontal slices of them in indicated height of the sample (c,d)

The vertical and horizontal slices of X-ray tomography image of the sample C13 are presented in figure 5.10. Variation in pore size and shape can be observed in these images. In vertical slices (a and b), a narrow zone with a few millimetres thickness (indicated by black lines e) and slightly different grey-scale can be seen. Comparing horizontal slice corresponding to this narrow zone (slice e) with horizontal slices from the rest of sample (including slice d) reveals the significantly different texture of this region. Two disc-shape volumes with 38mm diameter and 5mm thickness were extracted from the X-ray tomography image at the location of (d) and (e) slices and the pore size distribution of these regions is plotted in (figure 5.7-f) that revealed significant difference in mean pore sizes of two regions.

The slice averaged porosity and pores specific surface area values plotted along the samples height are presented in figure 5.10-c. High fluctuation in these values are observed along the sample. The indicated red bracket in the profile shows relatively thick zone of low porosity and high specific surface area that seems to be responsible of altering the water front pattern as observed in the level of slice (c) of fluid arrival time field.

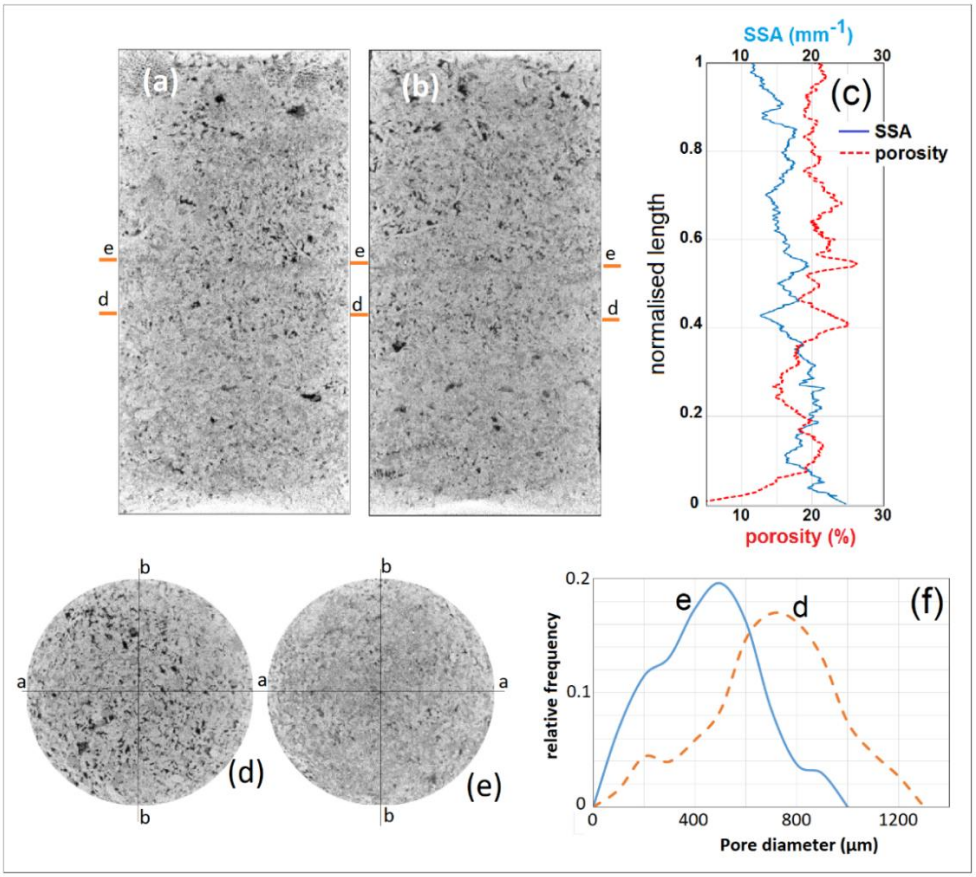

Figure 5.10 Vertical (a,b) and horizontal (d,e,) cross section of the X-ray tomography image of sample C13, Grains and void spaces are in grey and black colours respectively. Plot of porosity (red curve) and pores specific surface area (blue curve) along the samples height (c). The pore size distribution curves for two cropped regions near the d and e slices (f)

5.4.1.4 Textural variations – the presence of cross-layer lab-induced fracture: Sample C13 (deformed)

This section presents the results of flow experiments carried out on the sample C13 after being mechanically deformed at the laboratory scale. This sample was deformed under triaxial compression at 2.5 MPa confining pressure (see Section 4.4, Chapter 4). The fracture tip starts below ¼ of the samples height and extends to the top in an almost vertical direction (perpendicular to layering orientation in this sample) with a tiny aperture (0.5 to 1mm). The fracturing has increased the vertical (along the height of the sample) bulk permeability of the sample C13 from 30 to 90 mD. The flow experiment was carried out in this sample with same parameter as the intact sample (C13, section 5.4.1.1).

Cross sectional slices of the fluid arrival time field of this sample (C13-def) are shown in Figure 5.11. In these images, it is observed that the displacing fluid (water) front moves almost piston like up to ¼ height of the sample (as it was also shown in the case where the sample was intact) where it meets the fractures tip. After this point, heavy water existing in the fracture is displaced very quickly and water reaches the top of the sample through the fracture. As seen in the fluid arrival time field, once water fills the fracture, it starts to move laterally from the fracture into the matrix. However, the preferential water flow through the fracture caused a very small vertical progress of water within the matrix in the bottom part of the sample as soon as the fracture tip is reached. The maximum ΔP (differential pressure between the inlet and outlet of the core sample) recorded during the flow experiments is about 14 kPa that is much lower than maximum ΔP in intact sample (38 kPa) during flow at the same rate. The maximum ΔP and breakthrough time recorded during flow experiments for the deformed and undeformed C13 sample (as well as all other samples presented in this chapter) are presented in table 5.2. As seen in this table, the maximum ΔP and the breakthrough time are significantly lower in the deformed samples compared to the intact samples.

Table 5-2. The maximum ΔP, breakthrough time and the fraction of pore volume injected before breakthrough

sample	Breakthrough		Differential fluid pressure (KPa)
	Time (min)	Fraction of PV of water injected	
C11*	75	0.45	12
C12	85	0.41	19
C13	105	0.56	38
C13-deformed	60	0.31	14
C22	75	0.37	08
C24	65	0.32	11

* It should be noted that the length of the sample C11 is 56mm that is shorter than all other samples length (76mm)

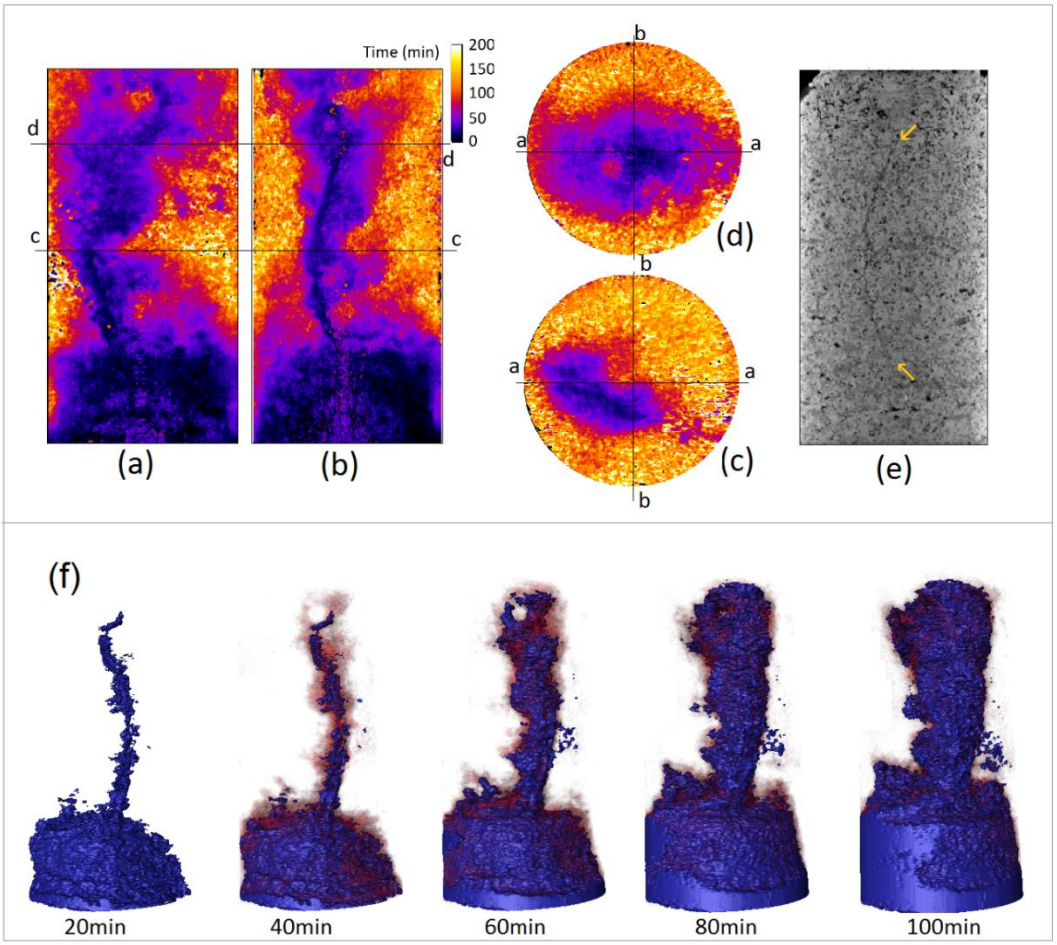

Figure 5.11 Two perpendicular vertical central slices of fluid arrival time field of sample C13-deformed (a,b) and corresponding horizontal slices of them in indicated height of the sample (c,d). Vertical slice of the X-ray tomography image of the sample (e) in which the fracture can be observed. The 3D renderings of the fluid arrival time field showing positions of advancing water in time steps: 20, 40, 60, 80 and 100 min after flow experiments (f) advancement of water between consecutive time steps is shown in red.

As shown in the speed map in Figure 5.12, the flow speed in the fracture and the bottom quarter of the sample (close to inlet) is very high. The fracture is surrounded (at its rimes) by low speed regions that indicates very slow movement of the front in these places. However, in the top part of the sample fluid speed slightly increases in the surrounding matrix.

Based on the fluid arrival time distribution, it can be inferred that water does not flow homogeneously from fracture to the matrix. Due to the horizontal orientation of zones with contrasting pore network properties in the matrix (discussed in section 5.4.1.3), it was expected to see variable intensity of fracture to matrix flow along the fracture. To better investigate the fracture to matrix flow, three grey-scale HSNTs acquired at 30, 60 and 90 minutes after the injection started were subtracted from the first HSNT (heavy water saturated sample) as described in section 5.4.1.1.

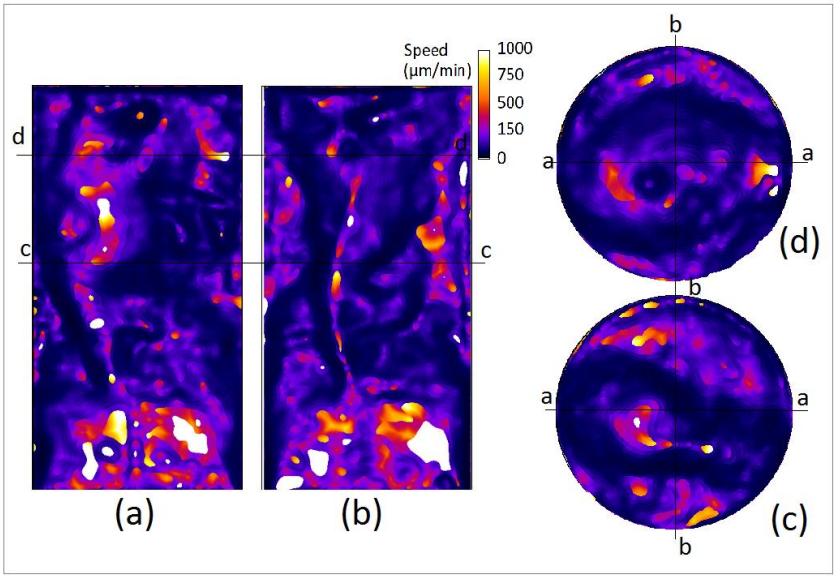

Figure 5.12 Two perpendicular vertical central slices of fluid speed field of sample C13-deformed (a,b) and corresponding horizontal slices of them in indicated height of the sample (c,d)

Figure 5.13 shows vertical and horizontal slices of normalised differential grey-scale image for sample C13-deformed. As we observe in the vertical slice (a) and horizontal slices at two

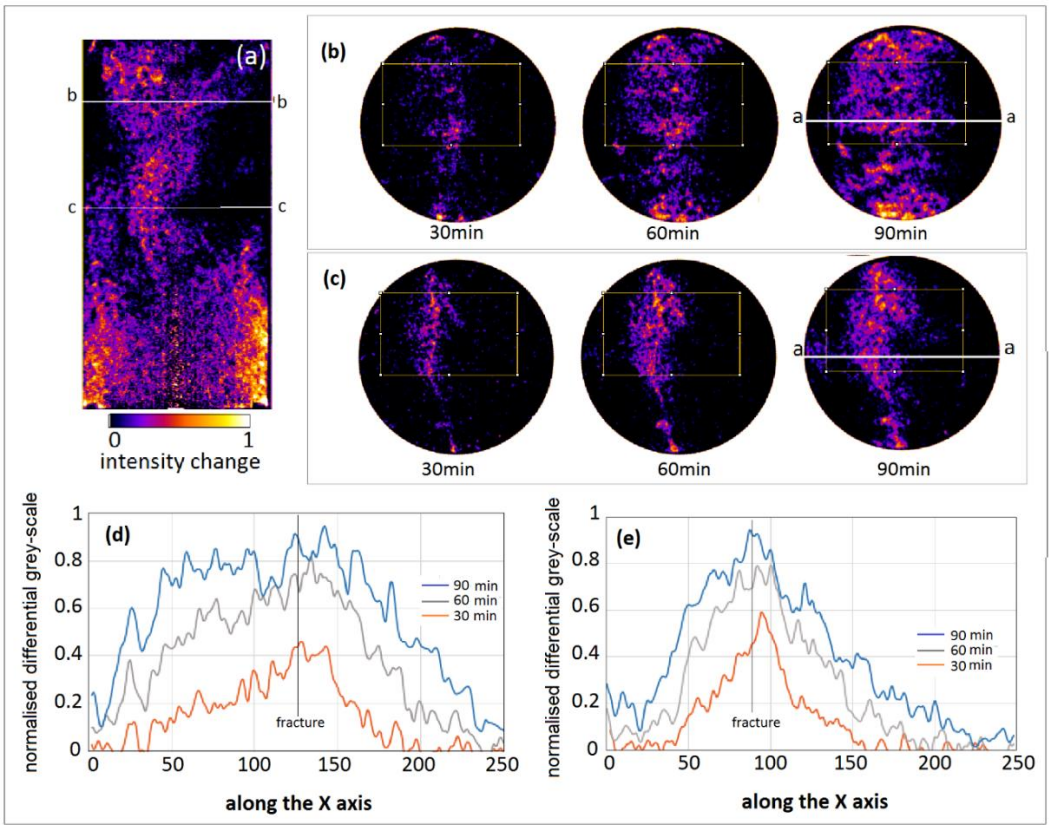

Figure 5.13 Horizontal (b and c) slices of the normalised differential grey-scale at 30, 60 and 90 minutes after flow experiments and vertical slice (a) at 90 min after flow experiment that can be representative of water concentration (zero and one correspond to lowest and highest concentration of water respectively). Graphs of normalised differential grey-scale (d and e) representing the relative water concentration with distance from the fracture in two horizontal slices of b and c respectively.

different heights of the sample by moving from the bottom to the top part of the fracture, water has invaded the matrix with greater lateral distance from the fracture. In Figure 5.13-d and e, average of normalised differential grey-scale is plotted along the length of a selected rectangle in the horizontal slices to show the relative water concentration with distance from the fracture. The position of fracture is indicated by a vertical black line in the graphs. Based on these graphs, different patterns of lateral concentration change within the matrix can be observed in two regions. In graph Figure 5.13-e (corresponding to the horizontal slice c) lateral decrease in water concentration is sharper while in graph d (corresponding to the horizontal slice b), this decrease is gentler and high concentration of water can be seen in the matrix in greater distances from the fracture.

5.4.1.5 Textural variations – the presence of a sandy layer parallel to the flow direction together with lab-indued fractures: Sample C24 (deformed)

Sample C24 is a Coquina sample that is cored within the layered zone of the Coquina block and parallel to the layering orientation. Lab-induced mechanical deformation under triaxial axisymmetric compression of the sample at low confining pressure (2.5 MPa) resulted in a fracture network (Figure 4.14 Chapter 4) that communicate between top and bottom faces of the sample. Occurrence of vertical layering has diverted the lab-induced fractures at the top half of the sample; these fractures propagate in the middle of the sample parallel to the direction of the layers (and they appear to be located at the interface of one of these layers) and keep propagating vertically toward the bottom of the sample. A fracture with about 1mm aperture has increased the vertical bulk permeability of the sample from 56 to 92 mD. Higher post-peak deformation in this sample compared to other samples resulted in creation of damage zone (microfractures) around the fractures that is observed in the X-ray tomography image of the deformed sample (Figure 5.15).

Cross sectional slices of the fluid arrival time field of this sample C24 are shown in Figure 5.14. As seen in these images, water flows through the fracture and reaches the outlet very quickly. While flow in this sample is dominated by the highly conductive fracture system that communicates between inlet and outlet, water flows relatively fast also on one side of the sample (early arrival time in the right side of the sample; Figure 5.14-a). The rest of the sample does not contribute much to the flow. The 3D renderings of the fluid arrival time field in different time steps (Figure 5.14-e) also show that water flows vertically through a narrow zone in the right side of sample and parallel to the fracture. Given the vertical orientation of layering in this sample, it seems that a vertical layer with higher conductivity led to this flow pattern.

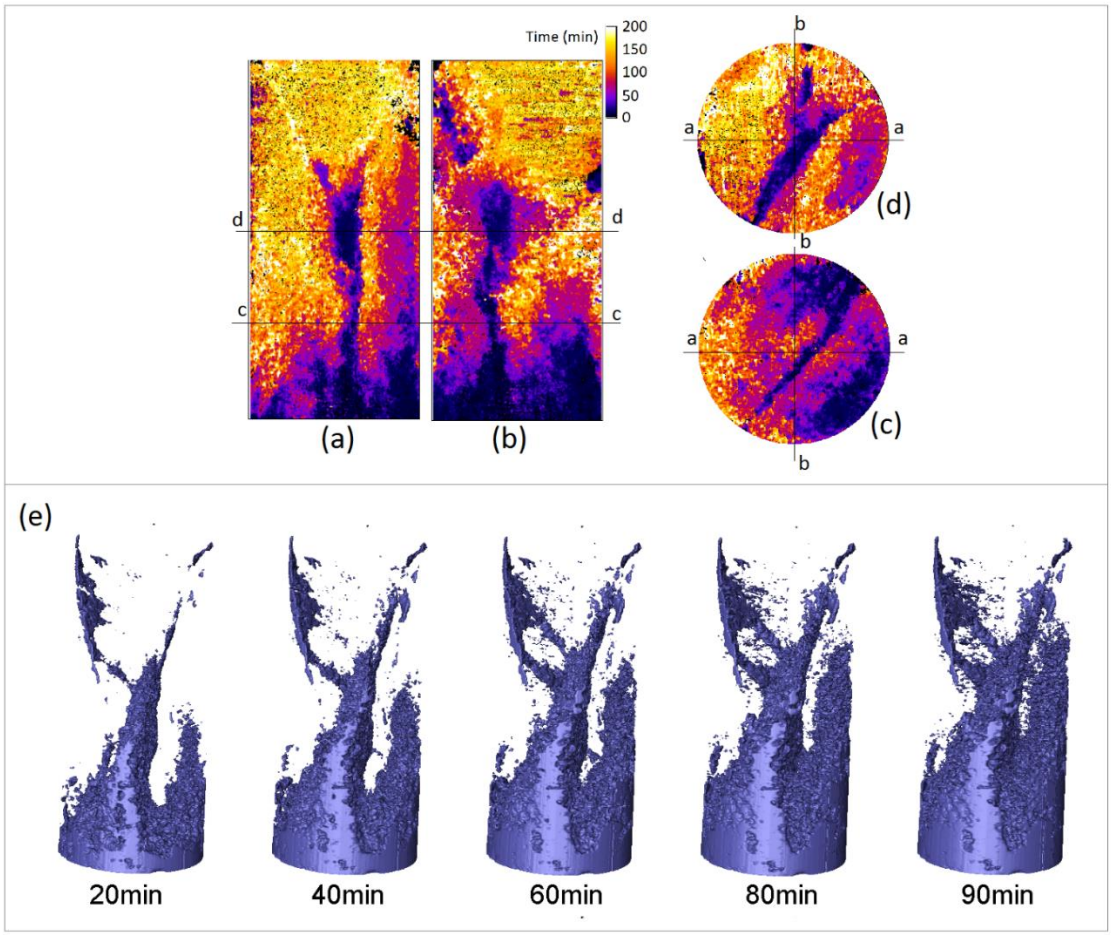

Figure 5.14 Two perpendicular vertical central slices of fluid arrival time field of sample C24 (a,b) and corresponding horizontal slices of them in indicated height of the sample (c,d) and 3D renderings of the positions of advancing water in time stepts: 20, 40, 60, 80 and 90 min after flow experiments (e).

As seen in the vertical slice (Figure 5.14-a), there is a sharp increase in water arrival time within a thin layer of matrix around the fracture that suggests a very low lateral fracture to matrix flow. On the other hand, gradual arrival time changes observed around the vertical layer on the right side of the sample shows lateral flow from highly conductive layer to the surrounding matrix. This can be observed also in the 3D renderings segmented fluid arrival time field in different time steps (Figure 5.14-e) where the thickness of the water increases significantly around the conductive layer (right side of the sample) while it remains almost constant around the vertical fracture .

To better investigate the miscible fluid displacing and mixing around the fracture and the conductive layer, normalised differential grey-scale images and graphs were calculated for three HSNTs acquired at 20, 60 and 80 minutes after the flow experiment as described in section (5.4.1.3). As shown in Figure 5.15, the mixing zone around the vertical part of the fracture is very narrow with a sharp boundary. The graphs of normalised differential grey-

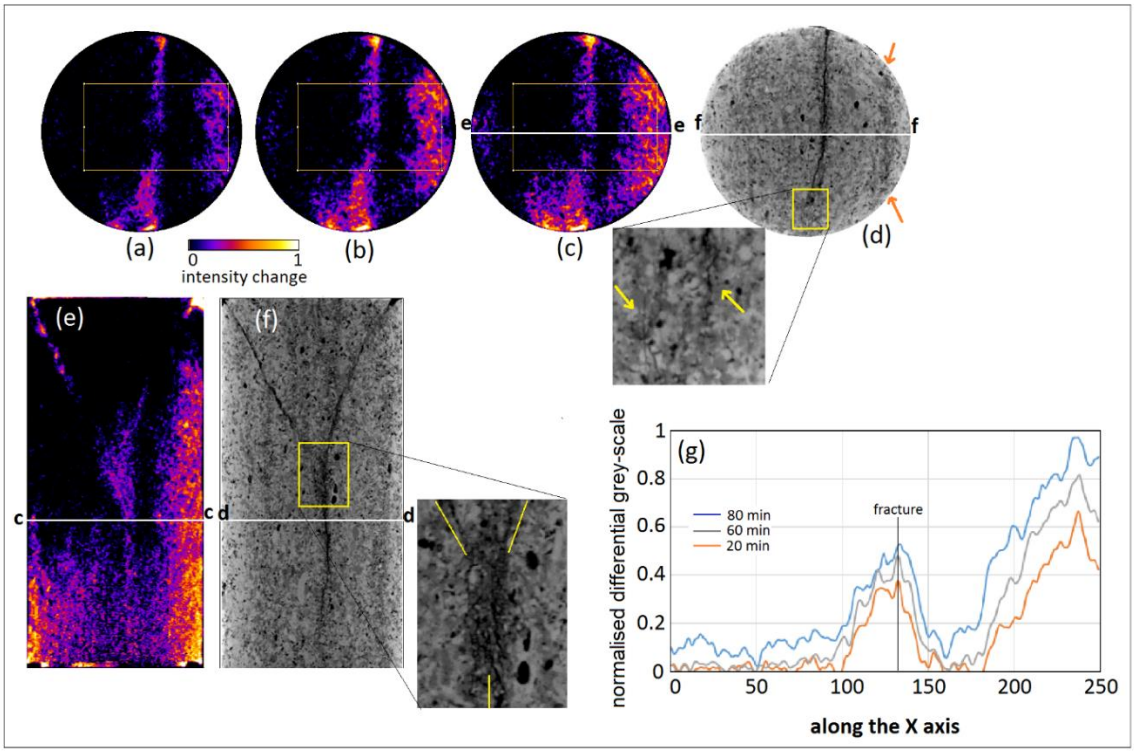

Figure 5.15 normalised differential grey-scale images at 20, 60 and 80 minutes after flow experiments (horizontal slices of a,b,c respectively and vertical slice e at 80 minute after flow experiments) (zero and one correspond to lowest and highest concentration of water respectively). Graphs of normalised differential grey-scale (g) representing the relative water concentration with distance from the fracture in horizontal slices. Horizontal (d) and central vertical slices (f) of X-ray tomography showing the fractures position.

scale also indicate that the concentration of water decreases sharply within a short distance from fracture and does not changed significantly with time. In the right side of the fracture, a vertical zone with high concentration of water is observed. In the cross sectional slice of the X-ray tomography (Figure 5.15-d) a narrow zone with distinct grey-scale value (indicated by orange arrows) is observed that seems to be a thin layer of different texture. While higher water concentration around this zone suggests higher conductivity of this layer compared to the adjacent matrix, lateral expanding of the mixing zone with time (visible in slices a, b and c) and decrease of water concentration with distance from this layer indicate a lateral flow from this layer into the surrounding matrix.

In vertical slice (e) it is observed that, in the middle of the samples height, the miscible displacement around the fracture has expanded. The corresponding vertical slices of X-ray tomography (zoomed area in slice f) shows a well-connected fracture (micro-cracks) network in the middle of the sample where two fractures meet the vertical fracture, which can explain the above observation. The spreading of the mixing zone at the bottom tip of fracture in

horizontal slices a, b and c is also related to the micro-cracks propagated from the fracture that can be seen in the zoomed area of the horizontal slices d.

5.4.1.6 Textural variations – the presence of high permeability matrix: Sample C22 (deformed) case study

Sample C22 is a Coquina sample cored from outside the layered zone in Coquina block. The bulk permeability of this sample in its intact condition (360mD) was higher compared to that of the other samples. However, lab-induced mechanical deformation (under the same condition as other Coquina samples), which introduced a fracture in this sample, has not significantly changed the permeability of the sample. The fracture tip starts from the bottom quarter of the sample and extends to the top end of the sample with almost 30° angle to the vertical axis (see Section 4.4 Chapter 4). Cross sectional slices of the fluid arrival time field of this sample C22 and corresponding slices of X-ray tomography image are shown in Figure 5.16. In general, a very chaotic distribution of fluid arrival time is observed. Variable pore

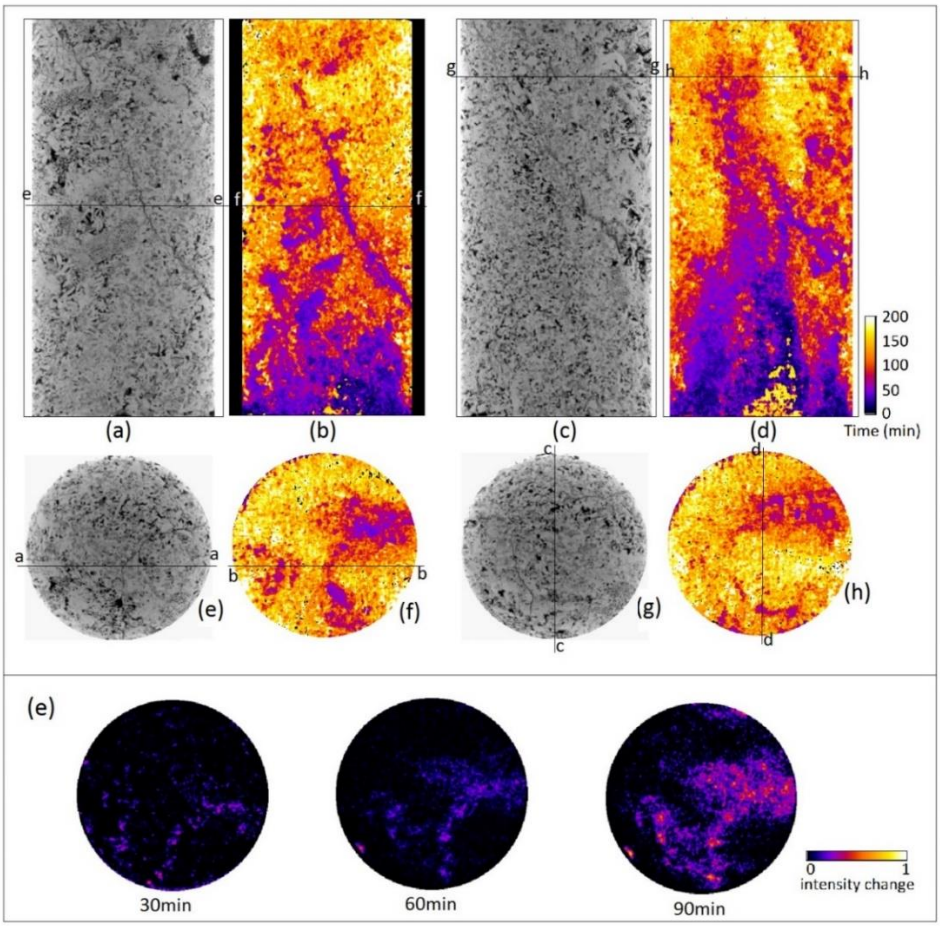

Figure 5.16 Two perpendicular vertical slices of fluid arrival time field (b and d) and corresponding slices of X-ray tomography image (a and c) of sample C22. Two horizontal slices of fluid arrival time field (f and h) in indicated height of the sample and corresponding slices of X-ray tomography image (a and c). Slices of normalised differential grey-scale images at 30, 60 and 90 minutes after flow experiments representing the water concentration (zero and one correspond to lowest and highest concentration of water respectively) around the fracture (e).

size and geometry, irregular spatial distribution of porosity and existence of large shelly fragments with their own intra-particle porosity have introduced complexities to the pore system of this sample. It is observed that miscible fluids displacement is affected by these complexities so that the water enters first into the highly porous (and possibly with higher hydraulic conductivity) regions that are randomly distributed in sample. Then, water slowly diffuses from highly porous regions to the surrounding pores. Once water reaches the fractures tip, it quickly moves up through the fracture and reaches the outlet resulting in early breakthrough (Figure 5.16-b and d). The fracture to matrix flow seems also to be affected by the local variation of porosity distribution. As observed in horizontal slice of fluid arrival time (f) and the corresponding slice of normalised differential grey-scale at time steps of 30, 60 and 90 minutes after flow (e), the water has not homogeneously flowed from the fracture into the matrix causing variable water concentration around the fracture.

5.4.2 Surface area of the leading front as a measure of irregularity of the fluid front

The occurrence of instability along a fluid-fluid displacement front during flow of miscible fluid in porous media is usually driven by hydrodynamic instability that tends to develop when there is considerable viscosity or density difference between fluid phases. These instabilities appear as development and growth of finger-like protrusions at the leading face of the advancing fluid and display different sizes and shapes. In our case in which the viscosity/density difference between the used miscible phases (water and heavy water) is negligible, the instability in the leading front can be mainly linked to variation of fluid speed in the leading fluid front that is caused by heterogeneity in the pore network properties. In this thesis, this instability is called irregularity of the fluid front.

As described in section 3.3.5, to have a quantitative measure of the extent of the irregularity of the fluid front and its evolution with time during miscible fluid displacement, we use calculated surface area of the leading front in samples at different times. Higher leading front surface area values represent the existence of more protrusions or existence of protrusions with more complex morphology at the face of the leading front. The surface area of the leading front also indicates the reactive interface available between miscible fluids for mixing.

Here, we investigate the evolution of the surface area of the leading front with time in two Coquina samples C12 and C13. These samples are cored in same direction (normal to the layering) by in different lateral position. These two samples have been chosen to investigate the effect of lateral variation in properties of the layered zone on miscible displacement.

Before evaluating the surface area of the leading front, the fluid arrival time fields were checked to ensure that the resulted fluid arrival time values are in agreement with mass conservation in the system. In fact, at different times before the breakthrough time, the cumulative count of voxels at which the fluid has arrived is expected to correlate with the volume of the fluid that has been injected until that given time. Given that the water has been injected at a constant rate and the injection rate was same for both samples, the number of voxels getting saturated with the advancing fluid in each time step are expected to be equal before the breakthrough of the injected fluid. This is expected to be valid when the samples are from same rock type with similar range of porosity and connected porosity. To check this, the number of voxels with a fluid arrival time value equal to or smaller than given time were counted from the fluid arrival time field and plotted versus time as shown in figure 5.17. As seen in this figure, both plots have a linear part at the beginning as the injection rate remains constant and this rate is the same in both samples. At a point that is attributed to the breakthrough time, plots deviate from linear state and the slope of plots becomes gentler. As indicated in the figure, sample C12 show earlier breakthrough time than sample C13 but, slope of the linear part of the plots for both sample is same that confirm the mass conservation in the system and the computed fluid arrival time fields.

The plots of the leading front surface area for two sample C12 and C13 are presented in figure 5.18. The 3D rendering of the leading front surface at indicated times after onset of flow experiments (20 min and 60 min for sample C12 and 20 min, 60 min and 75 min for sample C13) are also presented in figure 5.18. Since defining the exact boundary of the leading front is not possible, we calculated the outer surface area of the whole region invaded by the

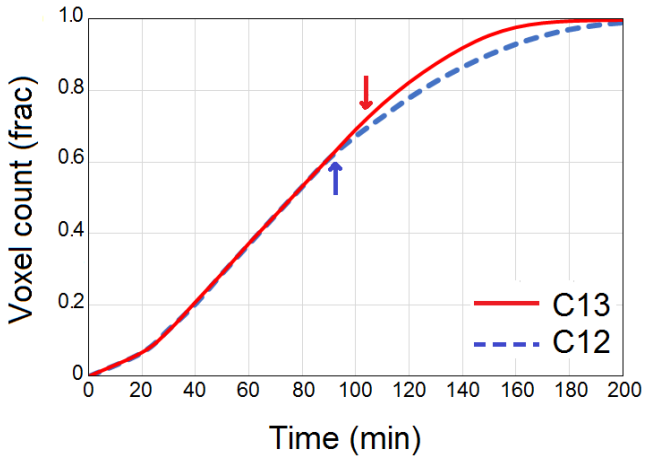

Figure 5.17 Cumulative plots of voxel counts versus fluid arrival time for sample C12 and C13. The red and blue arrows indicate approximating breakthrough points (where the plots deviate from the linear state) for sample C13 and C12 respectively.

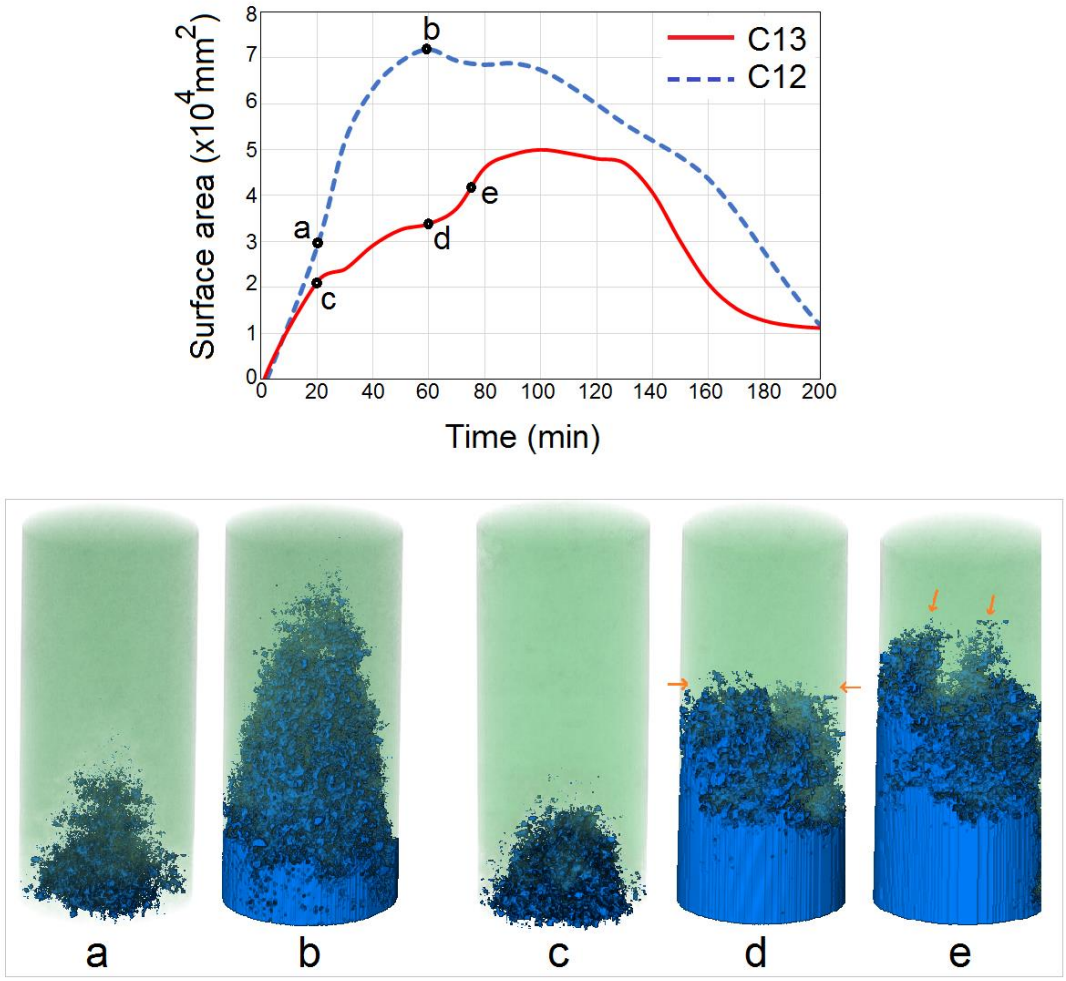

Figure 5.18 Plots of the leading fronts surface area versus time for samples C12 and C13. The 3D rendering of the leading fluid front surface at indicated times; for sample C12 (a and b in t = 20min and t = 60 min respectively) and for sample C13 (c, d and e for t = 20min, t =60min and t =75min respectively).

injected fluid in each time step. This means that the lateral face of the cylindrical sample is also included in the value of calculated front surface area. As shown in these plots, sample C12 shows generally higher values of leading front surface area compared to the sample C13. In sample C12, the leading front surface area increases with a steep slope in the first 60 minutes and start dropping after this point until reaching to the final surface area that is equal to the outer surface area of the whole cylindrical sample (~ 1.1 x 10^4 mm^2). This can be linked to the stretched geometry of the leading front (see figure 5.18-b) in this sample and existence of more smal-scale protrusions at the fronts surface. In sample C13, some sharp changes in the slope of plot are observed (particularly before the time = 80 min) so that the incremental rate of front surface area becomes slower at some points. It seems that at these points, the front reaches the horizontal layers with contrasting pore network properties in this sample as explored in section (5.4.1.3, figure 5.10) that result in stabilising the leading front and slowing

the growth of the protrusions at the front surface. This can be observed in Figure 5.18-d that leading fluid front becomes more flat at mid-height of the sample (at time = 60 min). Shortly after that, at time = 70 min, a rapidly developing and significant increase in the front surface area is observed in sample C13 that can be attributed to the channelling occurred in the leading front at middle of the sample of height as observed in the 3D rendering of the front surface (Figure 5.18-e). As investigated and presented in section 3.4.2.4, the calculation of the surface area of the fluid front can be highly sensitive to the spatial resolution of the used fluid arrival time field. This suggests that the effect of micro-scale roughness on the front surface can not be resolved and included in the surface area values that are calculated based on 170 µm voxel size fluid arrival time field in this section. However, the trend of changes in surface area caused by the macro-scale protrusions and finger-like irregularities are captured that allows investigating the effect of core scale features (layering) on irregularity of flow patterns. It is obvious that capturing the evolution of front surface area with time also depends on the frequency at which the surface area of the fluid front is calculated. In this section, the surface area is calculated at every 5 minutes of advancement of fluid front in samples that is quick enough to capture the features like initiating of fingering in the advancing fluid front.

5.4.3 Textural controls on hydrodynamic dispersion in Coquina samples

Spreading and mixing as the key transport processes in miscible fluid displacement result from mechanical dispersion and molecular diffusion. Mechanical dispersion has significant control on miscible displacement in porous media where complexities in pore space geometry cause small scale variation in the velocity field of displacing phase and fluid paths tortuosity. In this section, the impact of pore system heterogeneity on the miscible displacement of water and heavy water is analysed by indirect quantification of transition duration of miscible displacement (displacement of heavy water by the injected water).

As described in Chapter 3, a sigmoidal function is used to analyse the grey-scale evolution of each voxel in series of HSNT acquired during the flow experiments. This grey-scale evolution in each voxel is linked with the displacing fluid concentration changes over time at that voxel. While the time corresponding to the 50 percent of the full range of grey-scale evolution is considered as fluid arrival time, the steepness of the fitted sigmoidal indicates how fast the transition in miscible displacement has taken place at that voxel that can be linked to the local fluid speed. But, extracting the data of the absolute fluid speed based on the D-parameter is not of the purposes of this study. However, the spatial variation of D-parameter in samples is found as a useful parameter that can provide an insight into the relative potential of hydrodynamic dispersion during miscible fluid flow experiments in different samples

(section 3.3.6). This parameter can be compared to the pore-scale ‘’filling duration’’ parameter proposed by Van Offenwert et al., (2019) that generally depends on the pore size and pore-scale velocity variations during the miscible displacement. In Van Offenwert et al., (2019), the filling duration is defined as the time that takes until concentration of the injected fluid increase from 10 to 90 percent in the pore and is calculated based on the sigmoidal curve fitted on the evolution of the fluid concentration in each pore during time. This is similar to the sigmoidal curve fitted to the grey-scale evolution in each voxel of HSNTs with time (due to the concentration change of the injected fluids) during flow experiments (Chapter 3; figure 3.10). Thus, the steepness of the sigmoidal (D-parameter in this thesis) can be compared to the filling duration (Van Offenwert et al., (2019) so that the steeper and gentler slope of the sigmoidal curve (higher and lower D-parameter values respectively) can be linked to shorter and longer filling duration. The steepness of fitted sigmoidal is given by the D parameter and is computed for all voxels of the sample resulting in a D parameter field. The vertical cross sections of D parameter fields for samples C12 and C13 are presented in Figure 5.19.

As discussed in Chapter 3 (section 3.4.1), the spatial distribution of D-parameter values can be sensitive to the sigmoidal fitting error. As observed in error analysis (section 3.4.1), the distribution of sigmoidal fitting error in the sample is not uniform. Despite the generally low error of the sigmoidal fitting throughout the sample, non-uniform distribution of these error

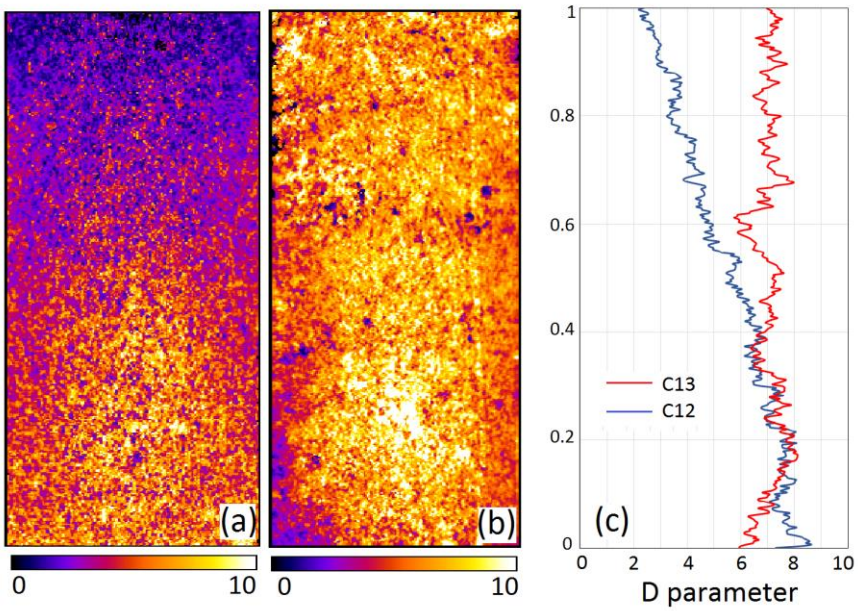

Figure 5.19 Cross sectional slices of the D parameter field of samples C12 (a) and C13 (intact)(b) and slice averaged D parameter values plotted along the height of the samples (c). The darker and lighter colours represent the lower and higher D parameter respectively. Higher D parameter value means shorter transition duration.

may introduce incorrect local variation to the calculated D-parameter. For instance, relatively higher error in sigmoidal fittings is observed in central parts of the sample compared to the samples boundaries. This may introduce uncertainties to the calculated D-parameter particularly when studying local small-scale (a few voxel scale) variations of D-parameter. As observed in figure 5.19, slightly lower D parameter values can be noticed in the cylindrical boundaries compared to the central parts of samples. While, lower fluid speed in the boundaries can be an explanation for this observation, non-uniform distribution of sigmoidal fitting error (lower error in boundaries) may also plays a role here. But, here, instead of local variation in D-parameter, the trends of variation in D-parameter along the length of sample is studied in order to get an insight into the state of longitudinal dispersion in samples. For this purpose, the D-parameter values are averaged over each horizontal slice and the slice averaged values (arithmetic average of D-parameters of all pixels within each horizontal slice) are plotted versus the slice number (along the length of the sample). This can reduce the effect of incorrect local D-parameter variations (in central parts and boundaries) and provide a data that is still useful as it shows the trend of D-parameter variation along the sample length. The slice averaged D-parameter profiles are presented in Figure 5.19-c. As seen in slice (a) and D parameter profiles of sample C12, the D parameter rises approximately linear along the samples height from inlet to outlet (along the flow direction). This indicates a longitudinal dispersion in this sample. For sample C13, there is no significant change in D parameter with the distance from the inlet however more local fluctuations can be seen, particularly in the region slightly above the middle of samples height. The histogram of D parameter values of the whole samples shows higher mean value for sample C13 and broader range in D parameter for sample C12 (Figure 5.20). The broader range in D parameter suggests higher variation in the displacing fluid speed that results in more dispersion.

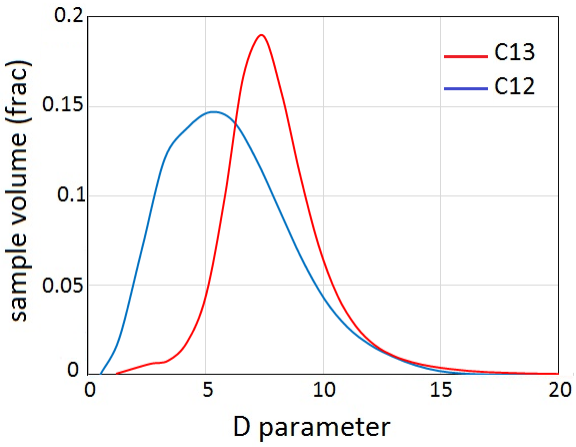

Figure 5.20 The histograms of D parameter for the sample derived from the D parameter fields show almost normal distribution. Sample C13 has higher mean value while sample C13 has broader range in D parameter that indicates higher dispersion.

Different extent of mechanical dispersion observed in two sample that were cored from same block and with same orientation. Comparing the results from pore system characterisation and in particular the porosity and specific surface area profiles of samples C12 and C13 (figures 5.7-c and 5.10-c respectively) reveal some variations that can explain the different behavior during the miscible displacement in these samples. More fluctuation in porosity and specific surface area along the samples height is observed in in sample C13 compared to sample C12. In the profiles of sample C13, especially for the bottom half of the sample, several points can be found where porosity decreases and specific surface area increases significantly that can be indicative of horizontal zones of lower hydraulic conductivity. This is in agreement with the measured gas permeability of sample C13 which is the lowest (30 mD) among all Coquina samples. Distribution of these zones that result in permeability contrast in the direction perpendicular to the flow direction seems to be the reason for lower longitudinal dispersion in sample C13. Low permeability zones perpendicular to the flow direction can moderate the variations of the displacing fluid speed caused by the pore-scale heterogeneity.

5.5 Summary and Discussion

The results presented in this chapter show how different scale (from mm to cm) textural variations due to depositional and diagenetic processes (such as layers with distinct textures parallel and perpendicular to the flow direction) and due to lab-induced deformation (such as fractures with different orientation and opening/aperture) control the miscible fluid displacement. 4D visualisation of fluid flow within the sample enables us to explore the role of these sub-core-scale variations (combination of lab-induced deformation and textural variations in tested samples) and their interaction with miscible fluid flow process.

As observed in sample C11, existence of a relatively large fragment with high intra-particle porosity acted as a baffle resulting in distortion of the displacing fluid front. The pore space image extracted from the X-ray tomography shows poor connectivity of the intra-particle porosity which caused later fluid arrival time, lower relative concentration of displacing fluid and lower fluid speed in this region. However, the grey-scale change observed in HSNTs in different time steps indicated that water concentration slowly increases in this region. This indicates that intra-particle porosity still contributes in miscible displacement but it will take longer for the fluid in these pores to be totally displaced by the displacing fluid. Therefore, it is expected to detect very small concentration of pore fluid in the outlet for long period of time after injection of displacing fluid due to a slow mixing between fluids occupying the

intra-particle and inter-particle pores. From geological point of view, these results highlight the significant role that the pore types and link between them (for instance connectivity between inter-particle and intra-particle pores) can play in evolution of concentration distribution during miscible displacement in carbonate rocks. This can have implication in solute and contaminant transport within these rocks.

The extent to which the pore connectivity can be precisely resolved in image-based pore-scale characterisation depends on the spatial resolution of the imaging technique. Several attempts have been made in recent years to resolve the tightest pores and pore throats by achieving high spatial resolution in X-ray micro-CT (Hebert et al., 2014; Pak et al., 2016) or scanning electron microscopy (SEM) images (Jim Buckman et al., 2017) however the size of the sample that can be visualised at high resolutions is usually limited. In fact, the trade-off between the sample size and spatial resolution of image means that a high resolution image that resolve tight pores and pore throats may not be able to provide details of features in larger scales like the interplay between different pore types (e.g. inter-particle and intra-particle pores). The results in this chapter showed that such details of larger scale features can be obtained by Neutron tomography acquired from the larger size sample (38 mm diameter and 76 mm length core sample) during flow experiments. For instance, Neutron tomography has the potential to indirectly provide insight into the state of connectivity between different pore types based on concentrations distribution evolution throughout the sample. This is thanks to the high contrast that can be achieved between miscible fluids (using HSNT) in a sample that is large enough to encompass different pore types. This suggests the potential of complimentary use of Neutron tomography and high resolution X-ray micro-CT to enhance our understanding of pore connectivity in carbonate rocks with multi-scale pore system.

Pore system characterisation of samples C13 and C12 showed similarities and differences in the two samples. Despite of similar range of porosity and pore size distribution, the variance of pore system properties along the height of samples are not the same. Higher fluctuation in the profiles of porosity and specific surface area along the height of sample C13 compared to sample C12, suggests the existence of several layers of contrasting transport properties in the pore network of sample C13 that are oriented normal to the core samples length. Layers with higher specific surface area and lower porosity are expected to cause local congestion in pore network of sample C13 that is in agreement with the lowest permeability of this sample compared to other Coquina samples. The influence of these variations in miscible displacement in these samples is well pronounced. Perpendicular to the flow orientation of layers with contrasting transport properties seems to play a role in stabilizing the front of

displacing fluid in sample C13. Given the wide range of pore sizes distribution and variable pore geometry that results in pore-scale heterogeneity in carbonate rocks, high longitudinal dispersion was expected during miscible displacement (Boone et al., 2016). While high longitudinal dispersion was observed in sample C12, existence of cross flow layers (layers perpendicular to the flow direction) of lower porosity and higher specific surface area moderated the fluid speed variation in the displacing fluid front resulting in low longitudinal dispersion in sample C13. This is in agreement with the result of pore-scale simulation of miscible displacement in 2D heterogeneous layered porous media (Afshari et al., 2018) in which layering perpendicular to the flow direction decreases the longitudinal dispersion.

The impact of the cross flow layering on the dispersion can be investigated locally and on the whole system. In terms of their impact on the whole system, the lower conductive cross-flow layers (like the one in sample C13) can reduce the longitudinal dispersion of the whole core sample by moderating the fluid speed variations caused by pore-scale heterogeneities however, in terms of local effects, they may introduce local zones of higher dispersion where some preferential paths in these layers can cause channeling in the displacing fluid. The significance of both effects can be highly dependent on contrast between transport properties of layers as well as the interval of layers and spacing between them that can be of interest for further studies.

The observations from the evolution of surface area of the leading front during the miscible fluid displacement in these two samples (C13 and C12) also indicates that cross-flow layers with contrasting transport properties (in sample C13) paly role in slowing the growth of the protrusions at leading fluid front surface. This implies that fluid speed variation in the leading front is moderated by flowing across layers with contrasting transport properties. While the volume of regions that has been invaded by the injected fluid is same (before breakthrough) in both sample, morphology and surface area of these regions are significantly different. These observations suggest that lateral variation in properties of layered zone can significantly influence the transport properties of samples cored within an even short lateral distance from each other.

The impact of lab-induced fracture in the hydraulic properties of tested Coquina samples was very dependent of the host rocks permeability, core-scale heterogeneity and anisotropy in their pore system. The role of fractures in increasing the rocks permeability was more pronounced in the samples with lower permeability. Permeability of samples C13, C24 and C22 were altered from 30, 56 and 362mD before deformation to 90, 98, 369mD after deformation respectively. The lab-induced fractures significantly reduced the maximum

differential fluid pressure and the breakthrough time during the flow experiments. The other important parameter is the particulars of the developed fracture systems such as where the fracture tips starts, its orientation, length, opening and the damage zone around the fracture.

Miscible displacement in sample C13 was seriously altered by the fracture. The fracture tip is located in the central part of the sample where a good amount of injected water can be fed into the fracture and move directly toward the outlet through the open vertical fracture. This caused that the vertical advancement of displacing fluid front in the matrix to be declined once it reached the fracture tip. The quick advancement of water in fracture reduced the breakthrough time from about 105 minutes in the intact sample to less than 60 minutes in the deformed sample. The fracture caused a decrease of differential pressure between the inlet and outlet of sample from 38 kPa in intact sample to 14 kPa in deformed sample as a result of failure in integrity of the low permeability layers oriented perpendicular to the flow direction.

The direction of fracture with regards to the layering in the samples seems to have a great influence in fracture to matrix flow. In sample C13, where a fracture crosses the layering, considerable transverse flow from fracture to matrix is observed while in sample C24, in which the vertical part of fracture is located within the one of vertical layers, no significant lateral flow from fracture to matrix is observed. On the other hand, relatively high lateral flow from a highly conductive vertical layer that is parallel to the fracture is observed from fluid arrival time field. Given the relatively large aperture of the vertical fracture, higher contrast between hydraulic conductivity of the fracture and surrounding matrix seems to be the reason of the very limited lateral fracture to matrix flow. However, local damage zones and microfracture network around the main fractures caused by the higher post-peak deformation in this sample resulted in higher fracture to matrix flow in some regions.

Very small aperture of the fracture as well as higher matrix permeability in sample C22 caused the fracture to be less influential in the permeability of the sample. The heterogeneous distribution of porosity (and possibly permeability) in this sample caused a complex miscible displacement patterns. The very heterogeneous flow from fracture to matrix that seems to be dependant of the porosity distribution of surrounding matrix added to these complexities.

As discussed in section (3.4.2.1), the lack of significant grey-scale change in some parts of the sample may increases the error of the sigmoidal fitting in those parts and can adversely affect the reliability of the calculated fluid arrival time and as a result, fluid speed values in those regions. This can introduce limitation to interpreting the results of fluid arrival time and fluid speed of the fractured samples in which the fluid flow is dominated by the fracture and

the injected fluid does not flow significantly into matrix, particularly in regions with higher distance from the fracture. However, the calculated fluid arrival time are still useful in providing the general flow patterns and the fluid arrival time within the fracture and its vicinity where significant fluid mixing has occurred. In these cases, (like the fractured samples C13, C22 and C24 presented in this chapter) the use of normalised differential grey-scale images can be helpful to better understand the fluid flow between fracture and matrix and investigate the evolution of the fluid concentrations with distance from the fracture.

In this study, high speed neutron tomography has been successfully employed to study miscible transport in tested samples. Although, HSNT was previously used for studying of water - heavy water displacement in intact and mechanically deformed sandstone (Tudisco et al., 2019; Etxegarai., 2019) and low-permeability carbonate (Zihms et al., 2017), but the use of this technique (HSNT) for quantitative analysis of miscible displacement processes like hydrodynamic dispersion and morphology of flow pattern is presented for the first time in this thesis. The advantages of using this technique over the X-ray tomography, which has been recently applied as a practical technique to study processes in miscible transport (Boone et al., 2016; Van Offenwert et al., 2019), are worth noting. Thanks to the sensitivity of neutrons to the different hydrogen isotopes, using heavy water in miscible displacement experiments provides significant contrast against normal water while closely resemble water from physical and chemical point of view. On the contrary, in x-ray tomography technique, considerable density difference between miscible fluids is necessary to get enough contrast between the fluids. This requires using of high concentration of chemical solutions whose reaction with minerals in rocks may not be desired in many cases. Moreover, high density differences of fluids introduce density driven transport. On the other hand, the chemically and biologically inert nature of heavy water and its similar hydro-mechanical behaviour to water makes it an ideal tracer that can be used in miscible displacement experiments coupled with neutron imaging. In this way, the results can be more representative of the effective transport properties of groundwater in natural aquifer.

Due to the short acquisition time in high speed neutron tomographies, the weak signal to noise ratio can be problematic for quantitative analysis. It can introduce random noises that may exert uncertainty when evaluating the grey-scale value evolution in each single voxel and as a result on calculated arrival time value and D-parameter. In fact, grey-scale evolution in each voxel during a series of (for instance 300) HSNTs, is considered to be solely due to the Neutron attenuation change corresponding to that voxel caused by changes in concentration of hydrogen-rich fluid occupying the voxel. However, occurrence of random noises in some

of tomograpgies can result in erroneous grey-scale for a voxel that does not represent the real attenuation value of that voxel. The abundance of erroneous grey-values (due to random noises) for a voxel can result in dispersity in the grey-scale evolution data points and increases the error of the fitted sigmoidal for that voxel. As observed from the error analysis (section 3.4.1), the error in sigmoidal fittings is generally low however, non-uniform distribution of these errors can introduce uncertainties to the calculated D-parameter particularly when studying local small-scale (a few voxel scale) variations of D-parameter. For instance, relatively higher error in sigmoidal fittings is observed in central parts of the sample compared to the samples boundaries. This can be directly linked to the higher noise to signal ratio in central parts where the beam travels through thicker part of the sample (higher cross-sectional distance). To reduce the impact of random noises when analyzing the solute concentration field derived from high speed laboratory-based Micro-CT data, Van Offenwert et al., (2019) a method to average the grey-scale value of voxels over each individual pore body and calculated the averaged solute concentration for each pore rather than each voxel. They showed that coarse gridding these values per individual pore significantly lowers the uncertainty in the solute concentration data. To alleviate the impact of random noises in our work, the D-parameter values were averaged over horizontal slices and the values were plotted versus slice number (converted to normalised samples length afterward). Although the 3D nature of the data is sacrificed in this way, the obtained data still provide useful insight on the state of longitudinal dispersion based on the trend of D-parameter variation along the samples length. As presented in the results, almost linear decreasing trend of D-parameter from the inlet toward outlet of the sample C12 indicates increasing the filling duration that can be linked to longitudinal dispersion in this sample.

In comparison to the existing knowledge in the field of miscible fluid transport, the results presented in this chapter provide new insights into this field in terms of both actual findings as well as methodological procedures employed. As reviewed in Chapter 2 (section 2.4.6), advances in 3D and 4D visualisation techniques have provided a good opportunity to resolve processes involved in miscible fluid displacement (e.g. mixing and dispersion) in pore-scale (Van Offenwert et al., 2019; Hasan et al., 2020) and core-scale (Boon et al., 2017). However, to the best of our knowledge, employing these techniques for experimental investigation of miscible displacement in natural layered rocks is not reported in literature yet. Despite the considerable interest in miscible fluid displacement in layered porous media, the experimental studies in this fields are limited to employing conventional methods (Starr et al., 1985; Swami et al., 2013) that provide a global measurement and breakthrough curves and lack the information on local processes within the samples. However, this chapter presented, for the

first time, the experimental results that revealed the processes involved in miscible fluid transport across layers of contrasting pore network properties and how they impact the longitudinal dispersion and morphology (stability) of the fluid front. In addition, the 4D nature of experimental results in this chapter enabled the analysis of 3D flow patterns, concentration distribution (3D) and their evolution with time with respect to different features like fractures or stagnant zones in the sample.

In terms of methodological procedures employed in this chapter, it should be noted that new image analysis procedures developed in this PhD, provided a step forward in terms of extracting quantitative data from HSNT data sets compared to the existing methods. In fact the developed procedures used the output of the sigmoidal fitting method developed by (Etxegarai., 2019) as an input for further quantitative analysis. The results showed a very good potential of the developed procedure to provide extra information on fluid front irregularity (instability) and hydrodynamic dispersion (based on D-parameter calculation) that can support and explain the observations of miscible fluid displacement processes associated with core-scale features like layering.

Chapter 6

4D Neutron imaging of immiscible fluid flow

This chapter explores how initial textural variations due to depositional features and lab-induced mechanical deformation at the millimetre scale (within 38mm diameter core plugs) control two-phase immiscible fluid displacement in the carbonate rocks during fluid flow experiments. The morphology of the advancing fluid front, 3D distribution of fluid speed, the phases saturation distribution evolution with time and fracture-matrix flow within the sample have been examined during two-phase heavy water-Decane (wetting and non-wetting phases, respectively) flow experiments on intact as well as mechanically deformed Coquina and Travertine samples. Syn-flow High Speed Neutron Tomography (HSNT) has been employed to capture in 3D the movement of the advancing fluid within the sample. To obtain information on the 3D distribution of phases (saturation), higher resolution neutron tomographies have been acquired after steps of fractional flow and when the injection is paused.

X-ray tomographies of dry samples have also been analysed both qualitatively and quantitatively to obtain detailed information of textural features, distribution of layers and layering orientation, distribution of fractures and spatial variations of pore network properties. These information are combined with results from immiscible fluid flow experiments to understand the flow processes during multiphase flow with an implication to better predict the flow behaviour of carbonate rocks with different sort of complexity in their pore systems.

6.1 Tested Samples

In total, four Coquina core plugs including one mechanically (laboratory) deformed sample and three intact samples plus a mechanically (laboratory) deformed Travertine sample were tested (flow experiments and neutron imaging) and are presented in this chapter. Table 6.1 provides some details about the tested samples. The detailed description of these samples together with the mechanical behaviour of the deformed sample have been presented in chapter 4.

To investigate the displacement of immiscible fluids across and along the layers of contrasting pore network properties as explored before (in chapters 4 and 5), two intact samples C16 and C23 were cored perpendicular and parallel to the layering direction, respectively. The next intact sample studied in herein is C21, which was cored parallel to the layering orientation but from outside of the layered zone in the Coquina block (no layer within the sample), and it has higher absolute permeability compared to other Coquina samples. The immiscible fluid displacement in fractured samples was investigated on sample C13-deformed (cored normal to the layering orientation) that was tested also for miscible fluid flow experiment (chapter 5) and one mechanically deformed Travertine sample called T13.

The wetting properties of the tested rock samples that has crucial importance in displacement of immiscible fluids was investigated by fluid-solid contact angle measurement. As defined by Craig (1971), wettability represents the tendency of a fluid to spread on or adhere to a solid surface in the presence of another immiscible fluid. The wettability of both Coquina and Travertine rock samples were determined by measuring the contact angle of oil phase (Decane in this study) in presence of water as shown in figure 6.1. The oil contact angle for Coquina and Travertine are 104 and 98 degrees, respectively, which indicates water wet condition for both rock samples.

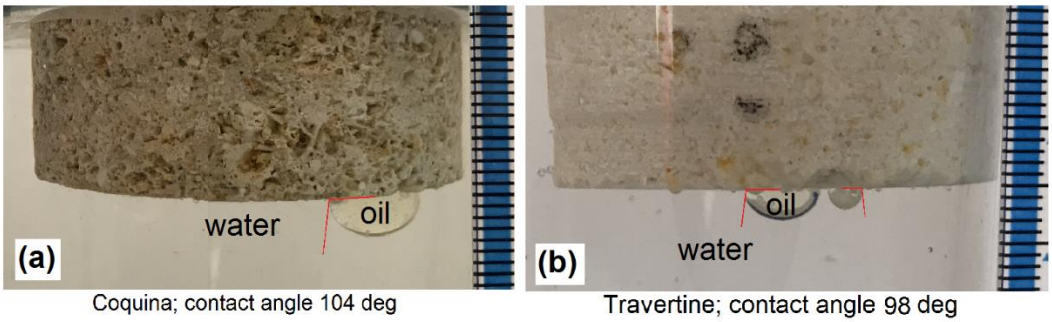

Figure 6-1 Photos of oil droplets on Coquina (a) and Travertine (b) samples in presence of water and measured contact angles.

Table 6-1 A brief description of the tested samples presented in this chapter

Samples name	Rock type	Intact / deformed	Description
C13-deformed	Coquina	Deformed	Cored normal to the layering orientation and mechanically deformed under triaxial loading (2.5 MPa Pc)
C16	Coquina	Intact	Cored normal to the layering orientation
C23	Coquina	Intact	Cored parallel to the layering orientation
C21	Coquina	Intact	Cored from outside the layered zone
T13	Travertine	Deformed	Mechanically deformed under triaxial loading (2.5 MPa Pc)

6.2 Experimental set-up

The flow experiments coupled with neutron imaging, which are presented in this chapter, were performed at NeXT-Grenoble instrument (ILL, Grenoble, in July 2019) and at Helmholtz-Zentrum Berlin (HZB, Berlin, in November 2019). The experiments workflow and the used equipment during these tests are explained in detail in chapter 4 (section 4.1). Here, specification of the flow experiments, including the used fluids, the injection rates, the samples primary saturation and other details of experimental campaigns are presented.

Two experimental protocols were employed during the flow experimental campaigns of this chapter. In the first protocol, samples were first saturated in Decane (oil phase) under vacuum and then placed in the flow setup (detailed in chapter 4, section 4.1.2) and get prepared for the flow experiments. Samples were submerged in Decane under the vacuum for several hours to make sure that they have reached as close as possible to the fully oil saturated condition. Samples were taken out from the saturation vessel only when no bubbles of air was coming out from the sample (after regular checking). However, we acknowledge that a very small fraction of the porosity may not get saturated by Decane (and remained air filled) but

we make an assumption that the fraction of air-filled porosity is a very small and negligible. Also, some pre-test Neutron tomographies of the saturated samples were taken and checked by visual examination to make sure that no air-filled macro-pores are remained in the sample. During the flow experiments, heavy water (heavy water) was injected into the core sample from its bottom with the constant injection rate. The samples have pore volume ranging from 16-19 ml. Heavy water was used as the aqua phase in these experiments for contrast reasons; Decane contains hydrogen, which has a high neutron attenuation coefficient (attenuates much the neutrons), while deuterium in heavy water is more transparent to neutrons due to its very low neutron attenuation coefficient. Thus, by previously saturating the sample in Decane and injecting afterwards heavy water, we were able to visualise and trace the immiscible displacement by means of neutron imaging.

By running some test flow experiments at different flow rates prior to running the main flow experiment at the Neutron facility, the flow rate of 0.05 ml/min was chosen for the immiscible fluid flow experiments. This flow rate that is half the flow rate in miscible experiments (Chapter 5), was chosen to avoid high differential fluid pressures that may result in leakage at sample-membrane interface. The Capillary Number calculated at this flow rate is equal to 6.39×10^{-8} (given the characteristic velocity of 3.67×10^{-6} m/s, dynamic viscosity of 0.890 mN/m^2 and 0.859 mN/m^2 for water and Decane respectively, and interfacial tension between Decane and water of 51.1 mN/m) that indicates a capillary dominant flow regime. The characteristic velocity is obtained by dividing the flow rate by the cross-sectional area of pore spaces (see section 5.2). At such a capillary dominant regime, and given that the interface between the sample and the membrane is sealed with PTFE tape, the assumption is made that the imbibition through the sample-membrane interface is prevented.

About 200 HSNTs were acquired during the flow experiments for each sample to cover the full span of fluid entrance from inlet and its travel through the sample to reach to the outlet. The radiographies were being regularly checked (by visual examination) during the HSNT acquisition to follow the advancement of the injected fluid within the sample and to determine the time to terminate the experiment and image acquisition once the injected fluid flowed through the entire sample. The spatial resolutions of 170 µm for HSNTs was achieved by having the similar configuration that is explained in section 5.2 (for miscible fluid flow experiments). To define the acquisition time of each HSNT (temporal resolution), the same procedure explained in section 5.2 was employed to estimate the speed of advancement of the injected fluid in the sample. Some pre-test HSNTs with different acquisition time were acquired during the injection of the heavy water (into some spare Coquina samples) at the

constant rate of 0.05 ml/min and the advancement of the heavy water was measured by subtracting the first and last radiographies of each HSNT. For different HSNT acquisition time, number of projections was kept the constant (500 projections was found suitable as discussed in section 5.2) while the exposure time for each projection was changed. Based on this analysis, it was found that at the flow rate of 0.05 ml/min, the advancement of fluid is safely less than 10 voxel even if the HSNT acquisition time increases to 2 min. For this acquisition time, the exposure time can be increased to 0.240 second (double the exposure time in miscible experiments) that allows a higher signal to noise ratio. Finally, the HSNTs were reconstructed immediately in the facility and were checked by visual examination to make sure that the chosen imaging parameters (projection number and exposure time) at the chosen flow rate allows for a good quality reconstruction.

By the end of the HSNT series acquisition after the injection of approximately one pore volume of heavy water into the sample, the injection at a higher rate (incremental rates of 0.1, 0.2 and 0.5ml/min) was continued until another pore volume of heavy water was injected into the sample (there was no HSNT acquisition during that period). Then the injection was stopped and the sample was left untouched for 30 minutes to allow the fluid movement to be stabilised within the sample. Finally, a single neutron tomography (NT) with higher spatial resolution (85 µm) compared to that of the HSNTs (170 µm) was acquired for each sample to capture the 3D distribution of the two phases within the samples.

In the second protocol, the flow experiments were carried out on the mixed Decane - heavy water saturated samples to examine the multiphase displacement in a condition that is more representative of (the oil) reservoir condition in terms of initial fluid occupancy. For this purpose, samples were first saturated in heavy water under vacuum and then were placed in the flow setup where 4 pore volumes of Decane was injected into the sample (outside the beam) under high flow rate (5 ml/min). After stopping the injection and waiting for 30 minutes, the first neutron tomography (spatial resolution of 85 µm) was acquired from the sample in mixed saturation condition. Then, four steps of fluid injection were carried out. In each step, a further ¼ pore volume of heavy water was injected into the sample at a flow rate of 0.05 ml/min in the same flow direction (from bottom to top end). At the end of each step, the heavy water injection was paused and the sample was left untouched for 30 minutes to allow the fluid movement to be stabilised within the sample. Then, a neutron tomography with spatial resolution of 85 µm was acquired.

Details of the imaging parameters for both protocols are presented in table 6.2. In both experimental protocols, the injection direction was from bottom to the top end of the

Table 6-2 Details of the imaging parameters in each experimental campaign.

Flow experiment/ Beam-time	Neutron tomography	Tomography acquisition time	Number of projections	Voxel size (µm)	Exposure time	FOV (mm x mm)
ILL, July. 2019	High speed NT	120s	500	170	240ms	105 x 105
	Static NT	20min	600	85	2s	105 x 105
HZB, Nov. 2019	Static NT	23min	700	85	2s	110 x 110

vertically placed core sample and outlet fluid was collected from the top end of the sample, that was at an atmospheric pressure (equal to 101 kPa). The differential fluid pressure was measured and recorded using a pressure transducer installed close to the inlet base (see set-up figures 4.4 and 4.5). Table 6.3 show the maximum differential fluid pressure in each sample during immiscible fluid flow experiments.

6.3 Image analysis

All the acquired tomographies were reconstructed as detailed in chapter 3 (section 3.3.1). Each voxel of the reconstructed image has a grey-scale value that corresponds to the neutron attenuation coefficient. The voxels with lower grey-scale value (darker colour in the image) corresponds to the materials with low neutron attenuation coefficient like deuterium and voxels with higher grey-scale values (lighter colour in the image) represent the existence of materials with high neutron attenuation coefficient like hydrogen. Figure 6.2 illustrates an example neutron tomography images during Decane - heavy water flow experiments; it shows the central vertical slice from neutron tomography images of a samples acquired at different time steps. As shown in these images, the advancement of the injected heavy water into the Decane-saturated sample affects the grey-scale values of the images. Displacing the (pre-existing) oil with the injected heavy water resulted in a decrease in grey-scale value that can be observed from the bottom of the sample towards the top in consecutive time steps. Even though advancement of the displacing phase can be seen in the images, defining the exact position of the displacing fluid leading front is not straightforward from the images due to the existence of considerable amount of unaffected oil left behind.

Table 6-3 Maximum differential fluid pressure in each sample during immiscible fluid flow experiments

Sample	Max differential fluid pressure (kPa)
C13-Deformed	25
C16	63
C21	12
C23	35
T13	22

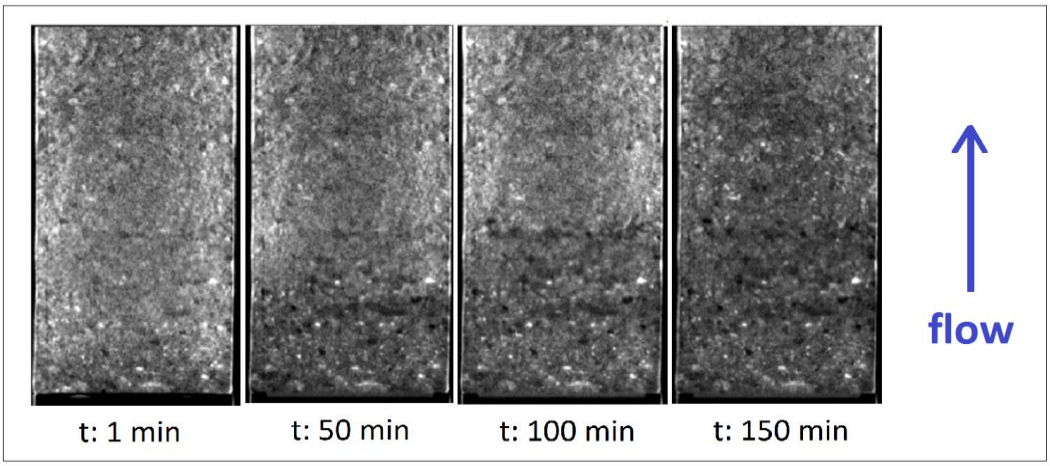

Figure 6-2 Example of vertical slices of reconstructed neutron tomographies; water flow into oil (Decane) saturated sample, the lighter and darker colours correspond to Decane and heavy water, respectively. The flow is from bottom to top.

For the quantitative analysis of these high speed neutron tomographies, two codes written by (Etxegarai, 2019) were employed to determine the fluid arrival time field and flow speed field for each sample during the flow experiments as detailed in Chapter 3. The shape and position of the fluid front in 3D at different time steps can be extracted by segmenting the generated fluid arrival time field. Moreover, the neutron tomographies acquired at the end of the flow experiments (static fluid condition once the injection is paused) can be segmented to establish the 3D distribution of fluid phases and phases saturation profiles along the sample length. For a series of static neutron tomographies acquired during the fractional flow in samples, so-called differential images have been calculated by subtracting the consecutive tomographies from the initial tomography (acquired before the fractional flow onset) to reveal the 3D distribution of sections of the pore system where immiscible displacement is dominant.

X-ray tomographies of dry samples have also been analysed both qualitatively and quantitatively (based on methods described in Chapter 3). This includes the visual examination of textural variation and position of layers and fractures within the samples volume to calculate variations in pore network properties.

6.4 Results

6.4.1 Immiscible fluid flow patterns

In this section, the results of fluid flow experiments that were carried out using the first experimental protocol (explained in section 6.2) are presented. These include the fluid arrival time field and the fluid speed field for each sample from which patterns and speed of the

displacing phase advancement can be studied in 3D. Then, phases saturation distribution within the sample and saturation profiles are presented and correlated with the character of the textural variation.

6.4.1.1 Immiscible displacement in fractured heterogeneous Coquina - Sample C13-deformed

This is a sample of Coquina, containing a lab-induced fracture. This sample was previously tested (chapter 5, section 5.4.1.3) when discussing miscible fluid flow experiments. As mentioned before, the fracturing has increased the vertical (or axial) macroscopic permeability of the sample C13 from 30 to 90 mD. The fracture tip starts below ¼ of the samples height and extends to the top in an almost vertical direction with a tiny aperture, 0.5 to 1mm, (figure 6.3-h,g, and figure 4.17 in Chapter 4). Cross sectional slices of the fluid arrival time field of this sample are shown in figure 6.3. As shown in these images, the distribution of the displacing fluid (heavy water) arrival time is relatively homogeneous (the rate of displacement from the injection point along the sample axis tried to find the fracture position in the HSNTs and investigate the saturation state around it. In the first HSNT taken when the sample was almost fully oil saturated, the fracture is hardly traceable (figure 6.4-a,b) due to the low contrast caused by the similar attenuation between the oil-filled fracture, and the oil-filled matrix. A while (60 minutes) after the injection of the displacing phase (heavy water), it can be observed that the fracture can be more readily observed in the regions of the sample already invaded by the heavy water (figure 6.4- a,b; slices of tomography taken 60 min after the flow started). This is because of the contrast between the oil in the fracture and heavy water that invaded the surrounding matrix earlier. It seems that heavy water flow from matrix into the fracture due to the co-current imbibition creates a film of heavy water in the matrix-fracture interface in early stages that does not hydraulically displace the oil within the fracture. Figure 6.4- c,d shows the plots of grey-scale value along the X axis of the indicated yellow rectangle in horizontal and vertical slices of HSNTs acquired at 1 and 60 minutes after the flow experiment. The evolution of the mean grey-scale value with distance from the fracture (that is located almost in the middle of the X axis) is shown in these plots. We observe that the grey-scale value is almost constant with distance from the fracture at the first HSNT while at the 60 min later HSNT, the grey-scale value changes at the rim of the fracture (along x direction), so that the lowest grey-scale values are observed in the vicinity of fracture-matrix interface (indicated by red arrows).

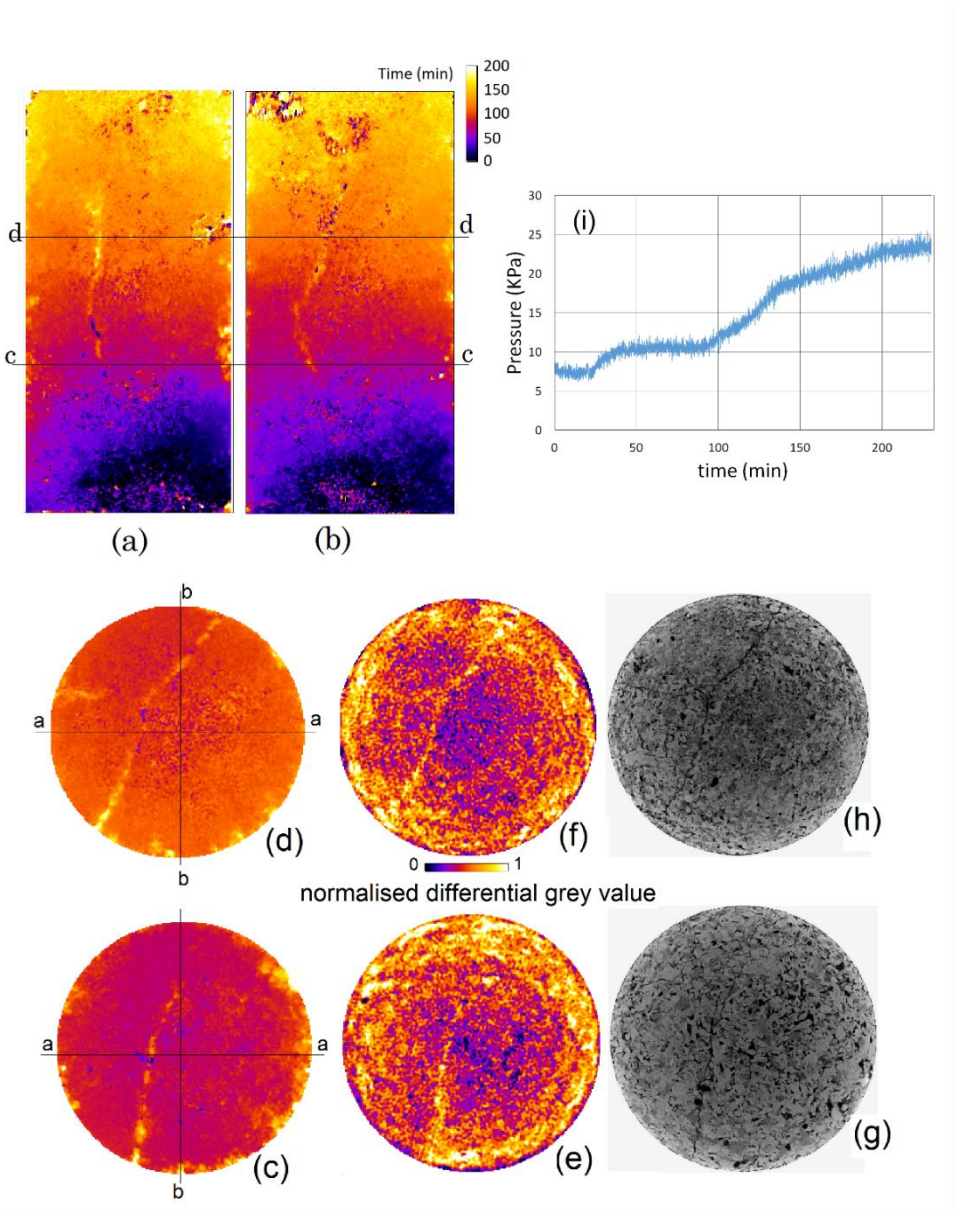

Figure 6-3 Two mutually perpendicular centrally placed vertical slices though the the fluid (heavy water) arrival time field for deformed sample C13 (a,b) and corresponding horizontal slices through the same data at the indicated sample height (c,d). Horizontal slices of the normalised differential grey-scale value at 150 min after the onset of flow experiments, the darker and lighter colours represent regions with higher and lower amount of displaced fluid, respectively). The horizontal slices of the X-ray tomography image of the dry sample (corresponding to the axial positions of c and d) in which the location of fracture is observed (g and h). The plot of differential fluid pressure (ΔP) versus time (i).

is quite uniform with lateral position) and the incremental arrival time sequence from bottom to the top part of the sample suggests a piston-like displacement. However, a narrow zone (1 to 3 mm thick) with delayed fluid (heavy water) arrival time (with lighter colour compared to the surrounding regions in the fluid arrival time field) is observed. The position of this zone correlates well with the location of the fracture observed from the X-ray tomography images

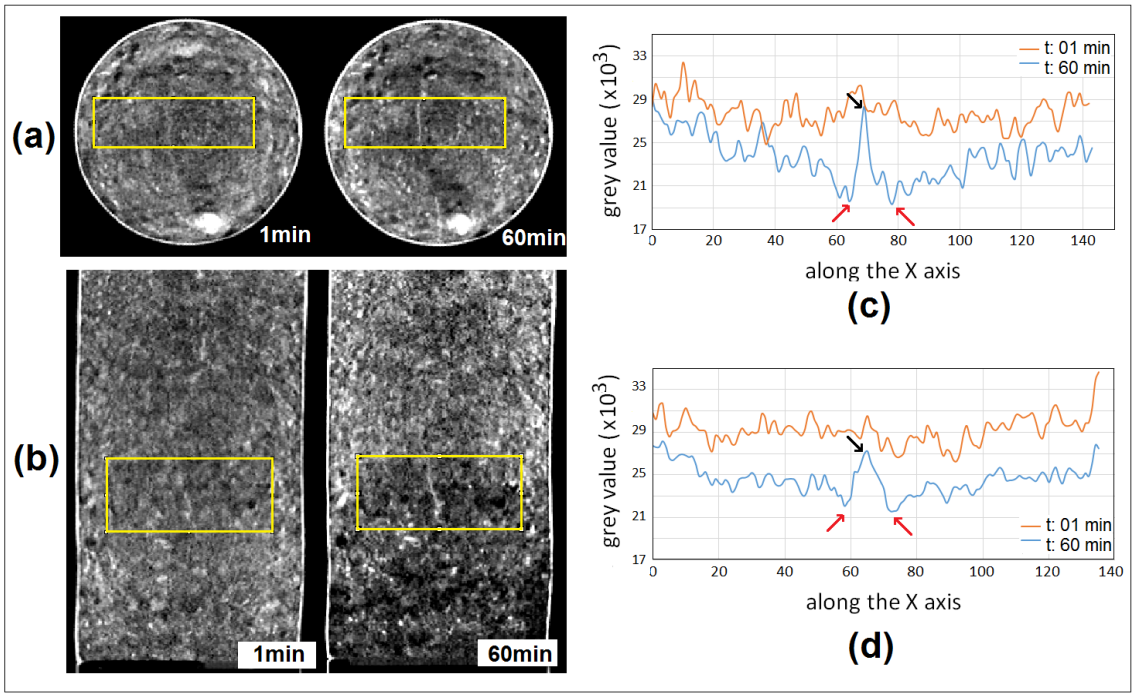

Figure 6-4 Horizontal (a) and vertical slices of the HSNTs acquired 1 and 60 minutes after the start of the flow experiments, lighter and darker colours (higher and lower grey scale values respectively) represent the regions with high saturation of oil (Decane) and heavy water, respectively. The plots of grey-scale value (c and d) along the length of the indicated yellow rectangular encompassing the fracture that show the mean grey-scale value with distance from the fracture, the black arrows indicate the location of the fracture, the lowest grey-scale values (red arrows) are observed in fracture vicinity that represent higher saturation of water in matrix near the fracture.

of the dry sample (figure 6.3-g,h). This suggests that the displacing phases leading front is delayed in the vicinity of the fracture. To further explore the origin for this observation, we Nonetheless, the grey-scale value has not changed significantly in the fracture itself (indicated by black arrows): this shows the absence of significant flow of heavy water flow into the fracture in early stages. The lowest grey-scale values in the vicinity of the fracture-matrix interface represents the highest saturation of heavy water in these regions. This can be due to creation of a film of heavy water in the fracture matrix interface in early stages. This causes accumulation of the heavy water in the matrix near the fracture and only after reaching high heavy water saturation, the heavy water start hydraulically displace the oil within the fracture. Given the spatial resolution of 170 µm (voxel size), the formed film of heavy water can not be visualised in early stages however, it cause a relative reduction of grey-scale value in voxels in these regions. This could justify why a delay of several minutes is observed in the displacing fluid arrival time in the fracture as compared to the surrounding matrix.

Figure 6.3-i shows the recorded differential fluid pressure (ΔP) as a function of time during flow experiment. As shown in this plot, after a slight increase at the beginning of the injection, inlet fluid pressure remains constant until t =100 min, after which it starts increasing and the

incremental rate of pressure build up is moderated at t = 135 min. From this point, the pressure rises at a gentler rate until the end of experiment. Based on the fluid arrival time field (figure 6.3), the leading front of the displacing phase reaches the middle of the sample where there is a narrow horizontal layer (normal to the general direction of flow and with lower permeability; explored in chapters 4 and 5) at t = 100 min and it seems to be the reason for the increased pressure at this point. In addition, the part of fracture crossing this low permeability zone started being filled by the displacing fluid around t =130 min and that seems to be the reason for the fluid pressures incremental rate to be gentler at this time.

In some parts of the fracture, the displacing phase has invaded the matrix and fracture at the same time and no delay in the heavy water arrival time is observed in the fracture. It is observed in the X-ray tomography image of this sample that in these regions, the matrix surrounding the fracture has bigger mean pores and/or pore throat sizes and consequently capillary pressure gradient between matrix and fracture is smaller compared to the regions in which the existence of very small micro-pores in the surrounding matrix caused creation of a film of heavy water in fracture-matrix interface in the early stages.

By subtracting the initial from the final HSNT images, regions of dominant immiscible displacement in the sample are visualised. This 3D image, in which the value of each voxel represents the grey-scale value difference due to the displacement of the Decane by the injected heavy water, was then normalised against the highest grey-scale value difference. Two representative horizontal slices of this volume are reported in figure 6.3- e,f. Generally, a relatively higher normalised grey-scale value difference is observed at the samples periphery due to the beam hardening artefact in HSNTs. By a more detailed look at these images, a zone with higher normalised grey-scale value difference (lighter colour) can be observed. Its position correlates with the position of the fracture in the corresponding X-ray tomography slices. This suggests that despite of a delay in flowing of displacing phase from matrix into the fracture, heavy water finally entered the fracture and displaced the oil within the fracture.

Cross sectional slices of the fluid speed field of this sample are presented in figure 6.5. The fluid speed distribution is irregular and local fluctuations of fluid speed can be observed. In general, some low speed regions are distributed in the form of horizontal lenses (can be seen in vertical slices of the fluid speed field figure 6.5-a,b) which is in agreement with the existence of cross-flow layers of contrasting pore system properties in this sample. Also, a contrast in the fluid speed can be observed in the vicinity of the fracture in the sample but it is not observed around the whole fracture. This contrast is marked by a very slow fluid speed

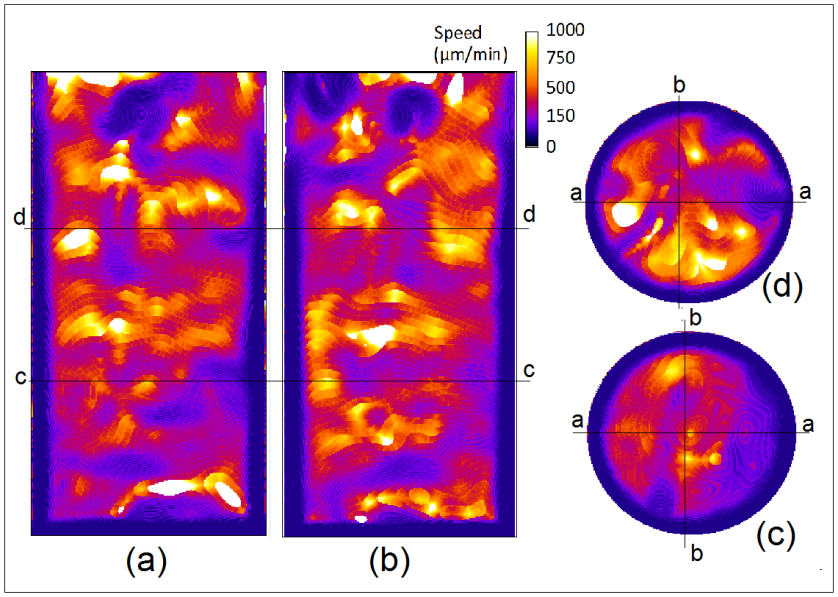

Figure 6-5 Two perpendicular vertical central slices of fluid speed field of sample C13-deformed (a,b) and corresponding horizontal slices of them at indicated sample height (c,d)

in the rim around the fracture. It is also observed that fluid speed inside this otherwise low-speed rim is high in some parts of the fracture (figure 6.5-d).

6.4.1.2 Cross-layer immiscible displacement in Coquina: - Sample C16

Sample C16 is a Coquina sample that has been cored perpendicular to the layered zone so that the bottom half of the core plug is within the layered zone. Cross sectional slices of the fluid arrival time field of this sample are shown in figure 6.6. As seen in the vertical slices (a and b), a sharp transition in the fluid (heavy water) arrival time value is present almost in the middle of the samples height. A horizontal boundary can be assumed (at samples mid-height indicated by arrows) in this region that divides the sample into two halves. A remarkable gap in fluid arrival time values below and above this horizontal boundary is observed. The mean fluid arrival time value at regions right below and above this boundary (with vertical distance of a few mm) are 70 and 100 minutes respectively meaning a 30-minute gaps in arrival time while this gap is much smaller for same vertical distances in other regions of sample. This indicates a slowing of the displacing (heavy water) phase advancement at this point. In the bottom half of the sample, other sharp transitions in fluid arrival time are observed while in the top half of the sample the transition is gradual and the rate of changes of fluid arrival time is rather homogeneous. The very bottom of the sample surprisingly shows late fluid arrival while the region just above this part shows earlier fluid arrival time. This is more obvious in figure (6.8-b) which shows the slice averaged fluid arrival time plotted along the samples height. As seen in this plot, three sharp fluctuations in fluid arrival time are observed in the bottom half of

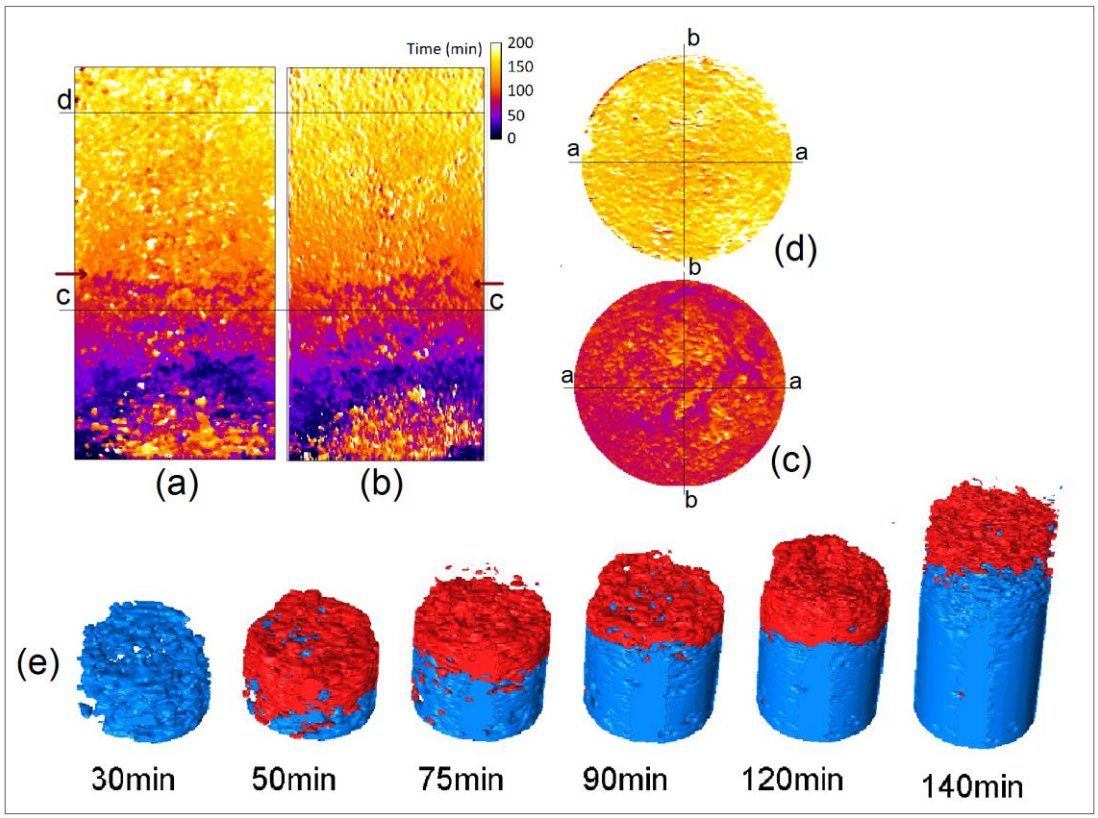

Figure 6-6 Two perpendicular vertical central slices of fluid arrival time field of sample C16 (a,b) and corresponding horizontal slices of them in indicated height of the sample (c,d) and 3D renderings of the position of displacing fluid leading front in times; Red represents the volume of the sample transited by the leading front since the last time step displayed. The fluid injection rate was constant during the flow experiment.

the sample (indicated by red arrows). This part of the sample encompasses the layered zone in which sandy/silty thin layers with distinct texture exist (as explored before and presented in chapter 4). These sharp changes can be linked to the existence of layers with variable pore size, absolute permeability, wettability and initial water saturation. Given that initial water saturation in the whole sample is zero and the flow rate is small (0.05 ml/min equivalent to ~0.005 PV/min), capillary pressure contrast caused by the variable pore and/or pore throat sizes and possibly variable wettability (sandy layers are expected to be more strongly water-wet in the tested Coquina rock) of these layers seems to have dominant role in the observed anomalies during immiscible displacement in this sample. The sandy layers can be saturated with the displacing phase (heavy water) earlier than the surrounding region due to their higher capillary pressure. This can cause the non-wetting phase (here Decane) to be trapped upstream of layers with higher capillary pressure through the mechanism commonly known as capillary heterogeneity trapping.

The X-ray tomography image of the sample C16 was used to characterise the pore properties of different layers. The vertical and horizontal slices of X-ray tomography image of the

sample C16 are presented in figure 6.7. Comparing horizontal slice extracted at different height of the sample (d and e) reveals the significantly different texture. The slice averaged porosity and pores specific surface area values plotted along the samples height are presented in figure 6.8-c. High fluctuation in these values are observed along the height of the sample. The sharp increase of porosity and decrease of specific surface area in the indicated location (d) can suggest the existence of a horizontal layer with relatively larger pore size compared to the indicated location (e) with lower porosity and higher specific surface area. To quantify the pore size difference, two disc-shape volumes with 38mm diameter and 5mm thickness were extracted from the X-ray tomography image at the indicated locations of (d) and (e) and the cumulative pore size distribution of these regions were plotted (figure 6.7-f). From these plots, mean pore size, D_{50} (section 3.3.3.2) of 415 µm and 783 µm were obtained for zones at indicated heights of e and d respectively.

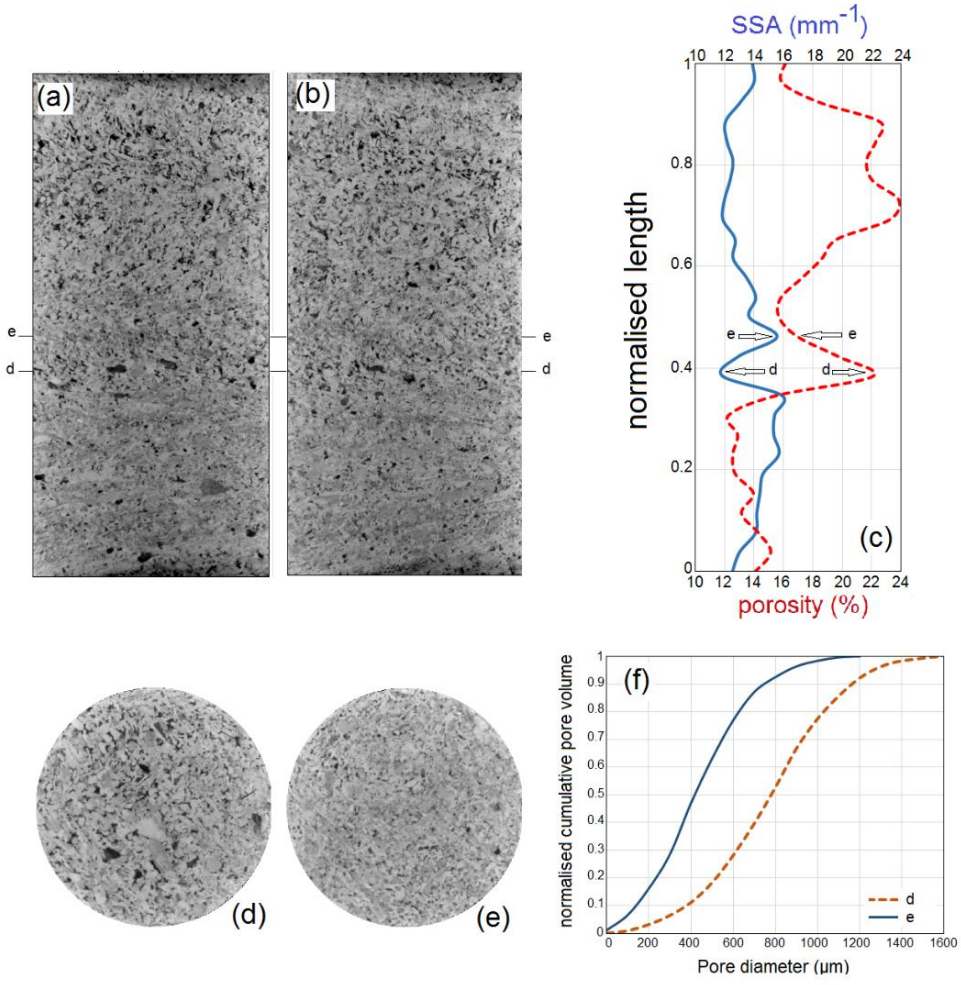

Figure 6-7 Vertical (a,b) and horizontal (d,e,) cross section of the X-ray tomography image of sample C16, and plot of porosity (red curve) and pores specific surface area (blue curve) along the samples height (c). The cumulative pore size distribution curves for two cropped regions near the d and e slices (f)

To further explore the impact of capillary pressure heterogeneity on oil entrapment in this sample, the first HSNT was subtracted from the last one (acquired after injection of approximately 1 PV of heavy water into the sample). The result is a 3D image in which the voxel values represent how far from equality the two phases saturation is: the greater this value is, the higher the saturation of heavy water and vice-versa. The slice averaged grey-scale value difference plotted along the samples height is presented in figure (6.8-a). As seen in this graph, sharp fluctuations in grey-scale values difference in the bottom half of the sample reflect the impact of capillary pressure heterogeneity on final phases saturation. Picks in grey-scale value differences (orange arrows) that indicate higher saturation of heavy water, correlate very well with those sections of the sample with anomalously early fluid arrival time figure (6.8-b) meaning that the layers with higher capillary pressure have finally held higher saturation of the wetting (heavy water) phase. The oil in between these layers and particularly at the bottom of the sample seems to be trapped due to the capillary heterogeneity.

Cross sectional slices of the fluid speed field of sample C16 are presented in figure 6.9. As observed in these images, in general, fluid speed is higher in the top half of the sample even though, there are some regions with locally lower fluid speed values. In the bottom half of

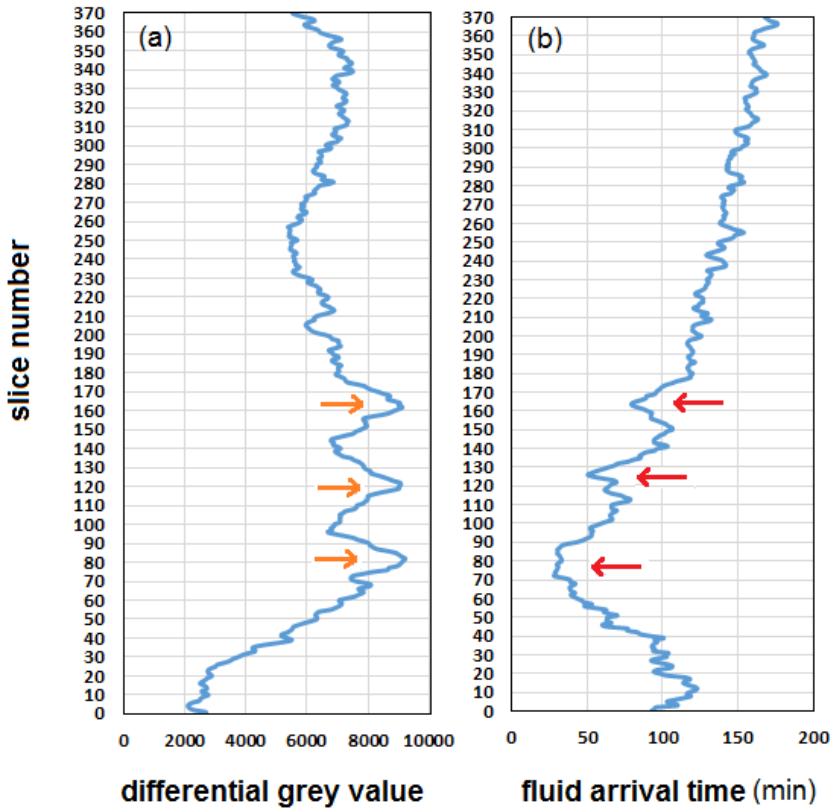

Figure 6-8 Plots of slice averaged differential grey-scale value (between first and last HSNTs) (a) and slice averaged fluid arrival time (b) versus slice number (along the samples height)

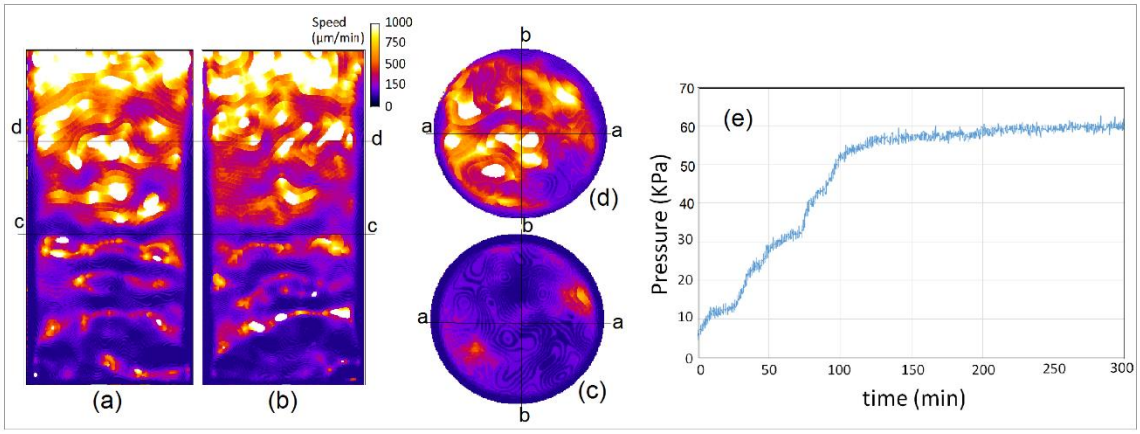

Figure 6-9 Two perpendicular vertical central slices of fluid speed field of sample C16 (a,b) and corresponding horizontal slices of them in indicated height of the sample (c,d); The plot of differential fluid pressure (ΔP) versus time (e). Cross-layer flow of the displacing phase through layers that act as a capillary barriers increased the fluid pressure. Once the displacing phase passes the last layer in the bottom half of the sample at time = 100 min, the pressure stops increasing and becomes almost constant (at 60 kPa).

the sample, a sequence of horizontally distributed zones with high and low fluid speed is observed that can be due to the existence of layers with significant contrast in capillary pressures caused by the significant difference in their mean pore size as observed in figure 5.7-f, (layers with D_{50} of 415 µm and 783 µm). The quick uptake of injected fluid by the layers with higher capillary pressure results in fast advancement of displacing fluid (heavy water) front and consequently higher calculated fluid speed. On the other hand, it seems that the wetting phase saturation hold-up at the interface of layers with higher and lower capillary pressures reduces the speed of the displacing phase. In fact, we speculate that due to the negative capillary pressure gradient, heavy water is held within the layer with high capillary pressure and does not flow into the next layer with lower capillary pressure until the saturation of heavy water in this layer (high capillary pressure) reaches a high level. This is why a considerable gap in fluid arrival time and consequently the zones with low fluid speed is observed.

A plot of differential fluid pressure (ΔP) during the flow experiment of sample C16 is shown in figure 6.9-e. As seen in this graph, the differential fluid pressure increases in several steps and becomes almost constant after 100 minutes. Different steps of pressure increase seem to be due to the cross-layer flow in the bottom half of the sample. In fact, the layers that act as a capillary barrier exist in the bottom half of the sample. When the displacing phase (heavy water) reaches to each of these layers, the fluid pressure increases. Once the displacing phase passes the last layer in the bottom half of the sample at time = 100 min, as observed in the time map, the pressure stops increasing and becomes almost constant (at 60 KPa) until the end of flow experiment.

6.4.1.3 Layer parallel immiscible displacement in Coquina: Sample C23

Sample C23 is a Coquina sample that has been cored within the layered zone and its long axis is almost parallel to the layering direction. Cross sectional slices of the fluid arrival time field of this sample are shown in figure 6.10. As seen in the vertical slices (a), distribution of the fluid arrival time is uneven, showing that the leading front of the displacing fluid (heavy water) arrives earlier in the central part of the sample and its arrival time increases with distance from the centre. Some regions (zones) with earlier fluid arrival time are also observed in the corresponding horizontal slices at different heights of the sample (figure 6.10 c and d). The fluid arrival time gradually increases with distance from these zones. The 3D renderings of the fluid arrival time field in different time steps (figure 6.10-f) also show uneven advancement of displacing fluid leading front. It seems that the preferential flow (of displacing phase) through vertical layers of contrasting pore system properties resulted in the observed uneven fluid arrival time distribution.

By looking at the distribution/orientation of these layers in the corresponding cross sectional slices of X-ray tomography image of this sample (figure 6.11 g,h), a good correlation between the regions with earlier fluid arrival time and the position of sandy layers is observed. As described in chapter 4, distribution of these layers is identifiable based on their distinct grey-scale value (darker regions) in the X-ray tomography image. Given the small injection rate

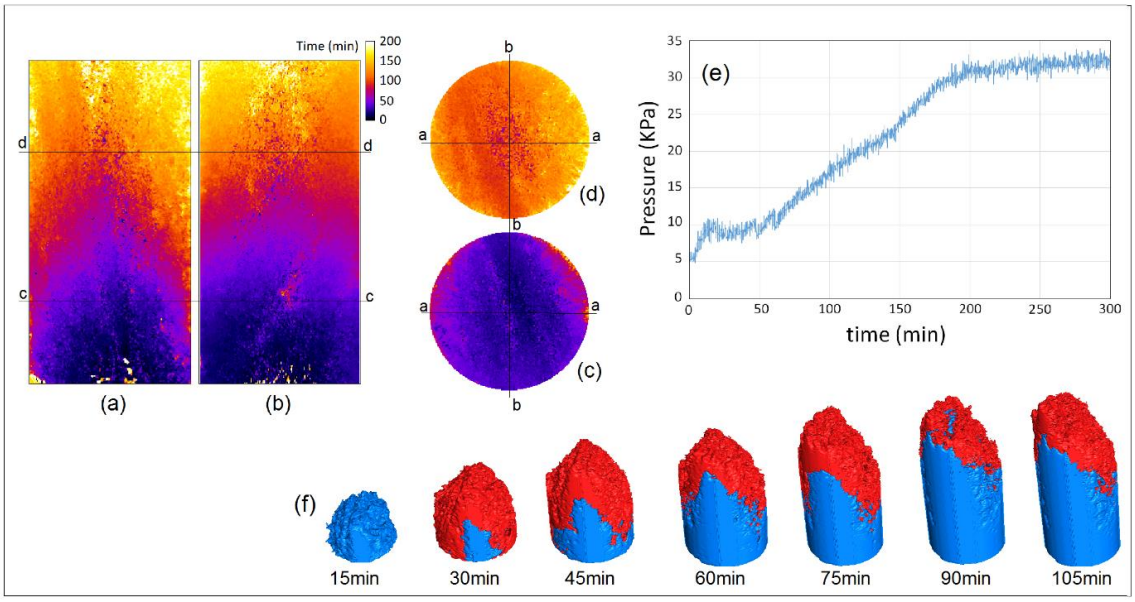

Figure 6-10 Two perpendicular vertical central slices of fluid arrival time field of sample C23 (a,b) and corresponding horizontal slices of them in indicated height of the sample (c,d). The plot of differential fluid pressure (ΔP) versus time (e). The 3D renderings of the position of displacing fluid leading front along time (f), the blue and red show regions invaded by the displacing fluid from the beginning of the flow experiments and from the previous presented time step, respectively.

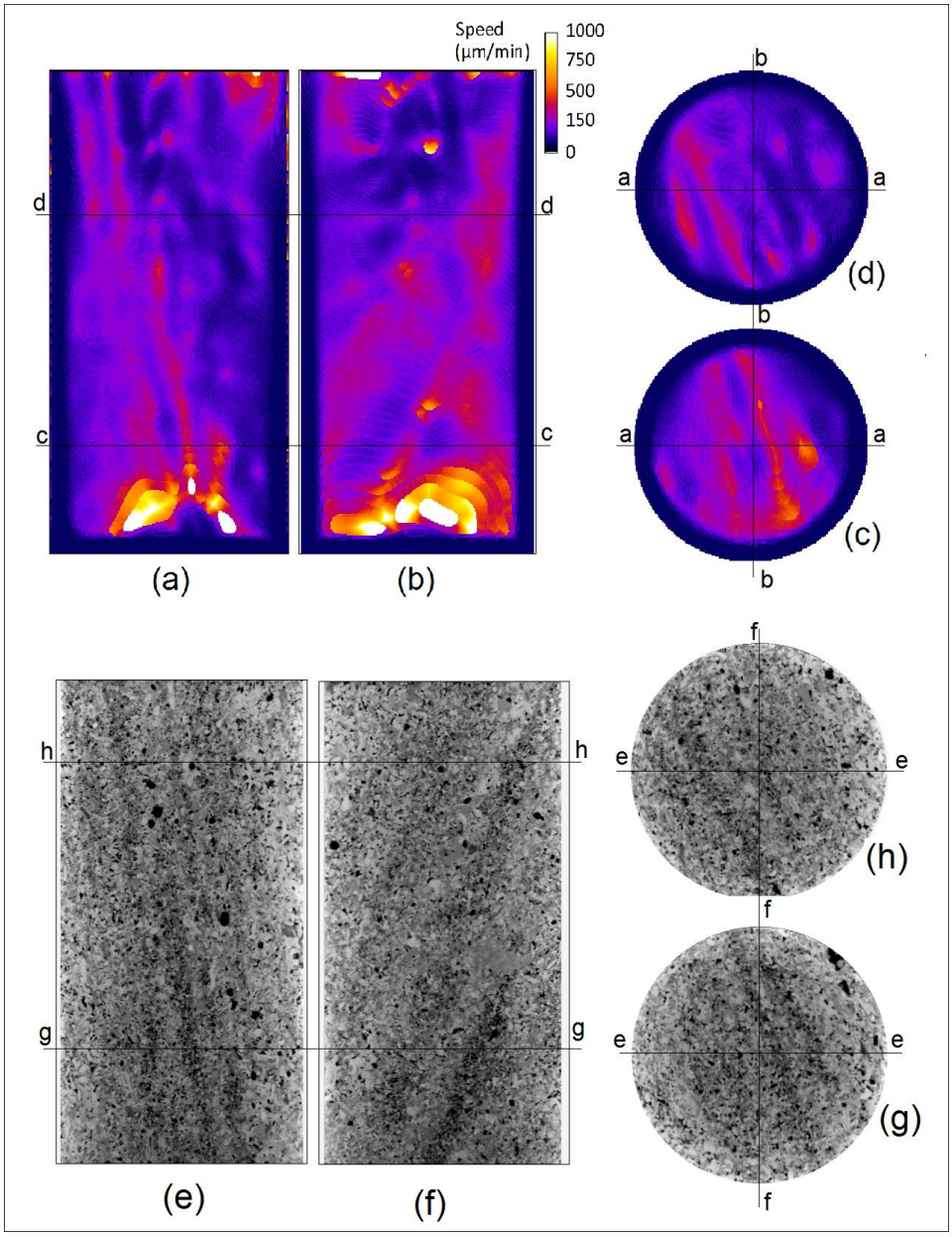

Figure 6-11 Two perpendicular vertical central slices of fluid speed field of sample C23 (a,b) and corresponding horizontal slices at the indicated heights (c,d); Two perpendicular vertical central slices of X-ray tomography image of the sample C23 (e,f) and corresponding horizontal slices of them in indicated height of the sample (g,h).

(~0.005 PV/min) and zero initial saturation of the wetting phase (heavy water) it seems that the higher capillary pressure in the sandy layers has played the key role in faster heavy water uptake in these layers compared to the surrounding rock. On the other hand, the arrival time transition around these layers looks gradual and no sharp changes in fluid arrival time is observed between these layers and the surrounding rock. The displacing phase (heavy water) reaches the outlet (sample top) around 100 minutes after the injection which is approximately 50 minute earlier than in sample C16 (cross layer flow). Also, the maximum differential fluid

pressure for this sample is about half the maximum differential fluid pressure for sample C16 (with layering perpendicular to the flow direction).

Cross sectional slices of fluid speed field of sample C23 are presented in figure 6.11. In these images, narrow zones with higher fluid speeds are observed. These are surrounded by regions with lower fluid speed. The distribution of high speed zones is well correlated with the position of sandy layers as observed in the corresponding X-ray tomography cross sectional images (figure 6.11 e,h). Vertical steeply inclined layers (which are about 10 degrees off axis-parallel) with high fluid speed that communicate between the inlet and outlet of the sample can result in early arrival of displacing phase (heavy water) at the samples outlet and reduce the fluid pressure. However, as the layers are not exactly parallel to the sample axis, not all layers in contact with the sample base reach the samples top. Considerable parts of the sample that have very low fluid speed seem to be bypassed by the displacing phase (heavy water). These regions of the sample do not have significant contribution to the flow (sample as a system here) compared to the layers with high fluid speed.

6.4.1.4 Immiscible displacement in heterogeneous high-perm Coquina- Sample C21

Sample C21 is a Coquina sample cored outside the layered zone and parallel to the layering direction. This sample has the highest measured permeability (440 mD) among the samples cored from the Coquina block (see table 4.1). Cross sectional slices of the fluid arrival time field of this sample are shown in figure 6.12. As seen in these images, the injected fluid has reached the top parts of the sample relatively quickly (around 90 min after injection started), when compared to the other Coquina samples (discussed previously in this chapter). This means that at the breakthrough time, only 4.5 ml (approximately 25 percent of the sample pore volume) of the heavy water was injected into the sample. This suggests that the heavy water has flowed through the preferential paths to reach to the sample outlet. A considerable part of the sample, near the bottom end, shows a very late fluid arrival time. It should be noted that for most of the voxels in this region, sigmoidal fitting (see section 3.3.5) failed and NaN (Not-a-Number) value voxels were created due to the lack of grey-scale changes in these voxels during the test (constant grey-scale throughout the flow experiment). These voxels were then removed by filtering the fluid arrival time field using the remove NaNs filter in ImageJ. This filter replaces NaN voxels images by the median of the neighbour voxels within the defined radius. It can be implied that the lack of grey-scale evolution indicates that no significant fluid displacement has occurred in this region. As seen in horizontal slice C, almost half of the samples cross sectional area has early fluid arrival time, showing that this

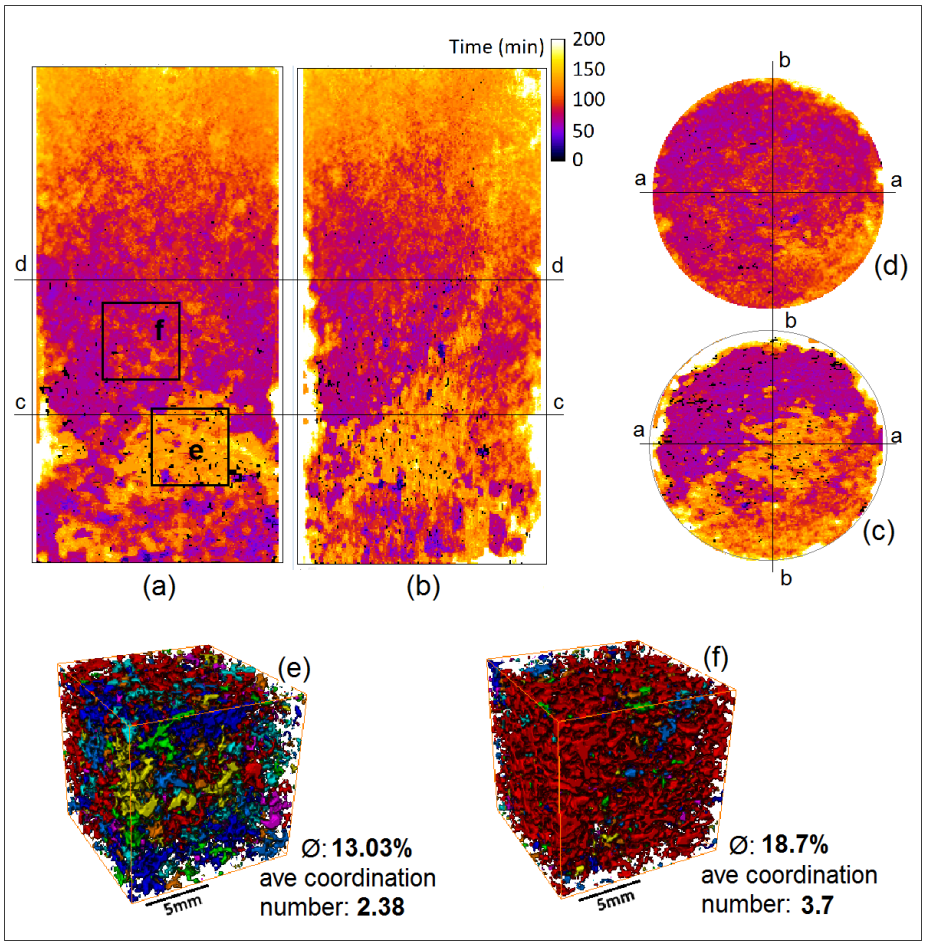

Figure 6-12 Two perpendicular vertical central slices of fluid arrival time field of sample C21 (a,b) and corresponding horizontal slices of them in indicated height of the sample (c,d). Rendering of 3D pore spaces extracted from the X-ray tomography image in two regions indicated in the fluid arrival time slice (e,f); connected pore spaces are presented in same colours.

part has contributed in immiscible displacement in the early stages and acted as a conduit for upper parts of sample, where displacing phase (heavy water) has invaded almost the whole cross sectional area of the sample (horizontal slice D).

The 3D void space image of the sample, segmented from the X-ray tomography image, was used to extract two sub volumes (cubes of 250x250x250 voxels) of the pore space from the unswept region and a region with early arrival time above that, indicated by e and f respectively. Figures 6.12 e,f show the 3D rendering of the labelled pore spaces in which connected pore spaces are presented in the same colour. Also, the porosity and average coordination number of the pore spaces are calculated for the two sub volumes. X-ray image results suggest that both pore connectivity and porosity in the unswept region (Ø:13.03 and average coordination number: 2.38, figure 6.12e) is lower than those within the region where earlier fluid arrival time was observed (Ø:18.7 and average coordination number 3.7, figure 6.12f). It seems that due to the low porosity and poor connectivity of pores, the volume of the

water flowed into this region is very small so that the grey-scale changes of the voxels in this region is not high enough that allow an accurate calculation of the fluid arrival time.

Cross sectional slices of fluid speed field of sample C21 are presented in figure 6.13. As seen in these images, the highest fluid speed is observed in the middle of the samples height while the lowest fluid speed is observed in a rim around the unswept region. As seen in horizontal slice C, the fluid speed in the half of the samples cross section is very high. Although, considerable part of the samples cross section has not significantly contributed to the fluid displacement, the maximum recorded differential fluid pressure during the flow experiment was very low in this sample (12 kPa). This suggests the existence of a well-connected network of smaller pores with higher capillary pressure that are communicating between the inlet and outlet of the sample. In fact, it seems that a good continuity in capillary pathways between the inlet and outlet provide preferential flow paths that result in the quick uptake and breakthrough of heavy water in the sample.

6.4.1.5 Immiscible displacement in Travertine containing laboratory induced deformation band - Sample T13 – deformed

Sample T13 is a Travertine sample mechanically deformed under 5 MPa confining pressure. As described in chapter 4, this sample shows a very weak strain softening after the yield point and has undergone 1.75% axial strain. After the triaxial compression test, signs of localised deformation can be observed on the samples surface, which indicate the development of an agently inclined-deformation band. Cross sectional slices of the fluid arrival time field of this

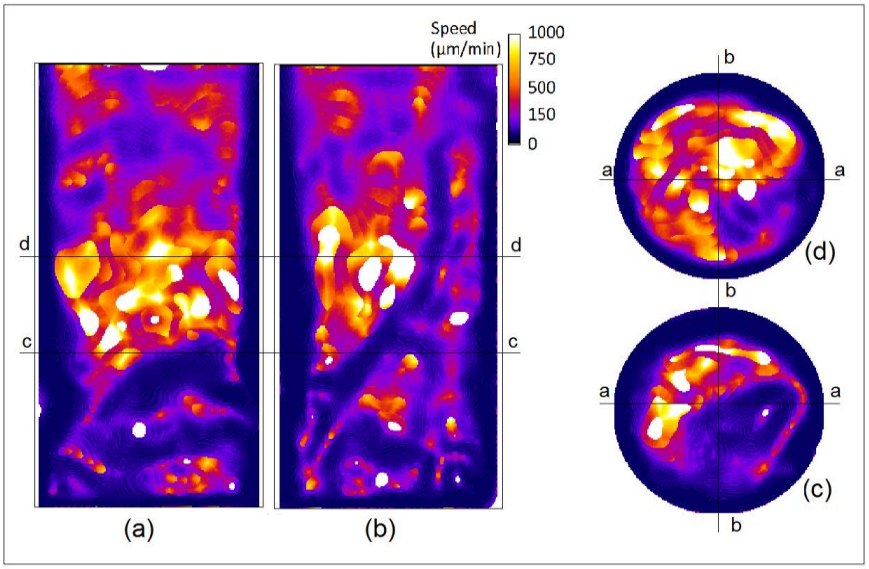

Figure 6-13 Two perpendicular vertical central slices of fluid speed field of sample C21 (a,b) and corresponding horizontal slices of them in indicated height of the sample (c,d)

sample are shown in figure 6.14. The distribution of fluid arrival time is very variable and several local anomalies are observed so that regions with very late fluid arrival time are surrounded with regions with early arrival time. Like other tested samples, this could be due to the flowing of the injected phase through the preferential paths that can cause some parts of the sample to be bypassed by the displacing phase (heavy water). To explore this, the 3D image of the normalised differential grey-scale of the sample was also extracted by subtracting the final and initial HSNTs (differences of grey-scale values in each voxel is normalised against the highest grey-scale value difference). As shown in the cross sectional slices of this image (figure 6.14 e-g) the distribution of the normalised grey-scale value

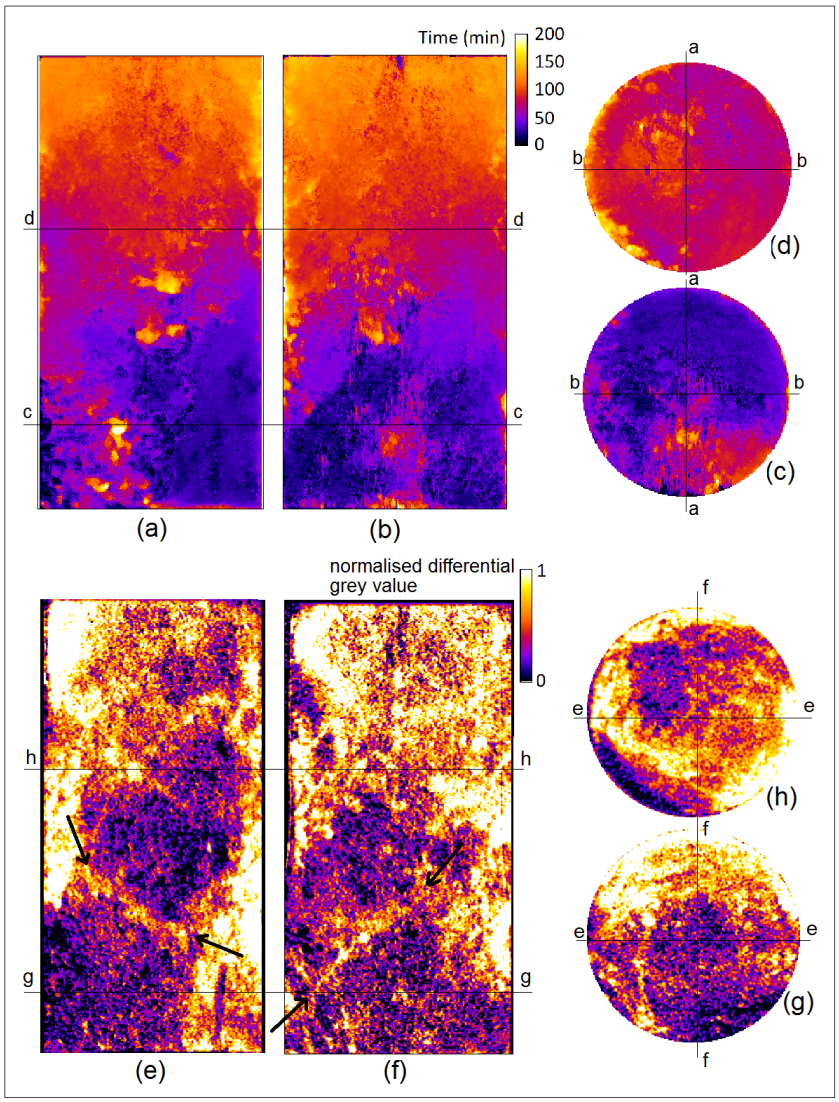

Figure 6-14 Two perpendicular vertical central slices of fluid arrival time field of sample T13 (a,b) and corresponding horizontal slices at the indicated heights of the sample (c,d). Corresponding vertical and horizontal slices of the normalised differential grey-scale value at 200 min after flow experiments, the darker and lighter colours represent regions of highest and lowest displaced oil respectively). Inclined narrow band (a few millimetres thickness) with anomalously high normalised differential grey-scale value are indicated by black arrows on these images.

difference is very heterogeneous. Considerable parts of the sample in the bottom have very low (close to zero) normalised differential grey-scale value meaning that no significant fluid displacement has occurred there. However, in the upper part of the sample, high values of normalised differential grey-scale value are observed that show significant fluid displacement. By looking at the vertical slices (e and f) in more detail, an inclined narrow zone (a few millimetres thickness) with anomalously high normalised differential grey-scale value can be identified. The position of the observed zone matches well with the earlier arrival time regions (fluid arrival time field). This zone can be related to the laboratory induced deformation band. It is speculated that this deformation band could have been populated by grain damage resulting to very fine fractures and potentially altered pore sizes, and thus, characterised by higher capillary pressure compared to the surrounding matrix so that the wetting phase (heavy water) flows earlier through this zone. Unfortunately, the post-deformation X-ray tomography image of this sample is not available for further examination.

Existence of the conduit band that communicates between the inlet and middle part of the sample provides a preferential fluid flow path that causes considerable part of the sample at the bottom part of the sample to be bypassed by the displacing phase (heavy water). This resulted in relatively quick arrival of the displacing fluid at the samples top part and consequently at the samples outlet (approximately 90 min after the injection). Also, very low differential fluid pressure has been recorded during the experiment (maximum 20 kPa) in this sample.

Cross sectional slices of fluid speed field of this sample are presented in figure 6.15. The mean calculated fluid speed in this sample is 505 µm/min and local variation in fluid speed is observed particularly in the bottom half of the sample. In this part of the sample, distribution of regions with high and low fluid speed matches well with the distribution of regions with high and low differential grey-scale, respectively indicating that the injected fluid flowed with higher speed through the preferential flow paths. In the top half of the sample, the fluid speed is lower and distributed less heterogeneously.

6.4.2 Saturation profiles

As mentioned before, in protocol 1, after acquisition of HSNTS during the injection of approximately one pore volume of heavy water into fully oil saturated samples, an injection at a higher rate (incremental rates of 0.1, 0.2 and 0.5ml/min) was continued until another pore volume of heavy water was injected into each sample. A single NT with 85 µm voxel size was acquired for each sample after the final injection of 2 PV of heavy water. The NT image

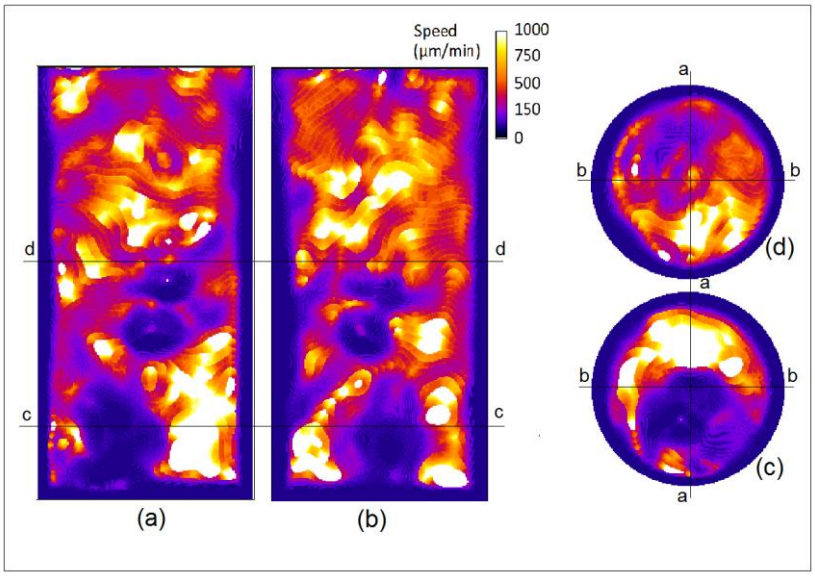

Figure 6-15 Two perpendicular vertical central slices of fluid speed field of sample T13 (a,b) and corresponding horizontal slices of them in indicated height of the sample (c,d)

of each sample was then segmented using Weka trainable segmentation method (chapter 3, section 3.3.3.1) into three phases of Decane, heavy water and solid parts of the sample. The slice averaged fluid saturation were calculated based on this segmented image. In fact, the ratio between the area occupied by each phase (in each horizontal slice) and the total area of that slice was plotted versus the slice number to produce the saturation profile of each phase along the samples height. To make sure that no air is remaining in the sample, it was checked that the sum of area occupied with Decane, heavy water and solid phases be equal to the total area of horizontal slice.

As seen in figure 6.16, the saturation profiles for the oil phase along the samples height are presented for four Coquina samples C13, C16, C21 and C23. In general, two distinct types of saturation profiles are observed, one for each of the two groups of samples cored parallel (C21 and C23) and perpendicular (C13-deformed and C16) to the layering orientation. While in the latter case, there are local variations (fluctuations) in the oil saturation value along the samples height, the oil saturation is relatively constant along the sample height in the former group. In samples C13 and C16, sharp increases and decreases of the oil saturation along the sample reflect the occurrence of horizontal layers with contrasting pore system properties as explored before. In samples C21 and C23 however, these variations are averaged over each horizontal slice so that no sharp fluctuations is observed in oil saturation profiles along the samples height.

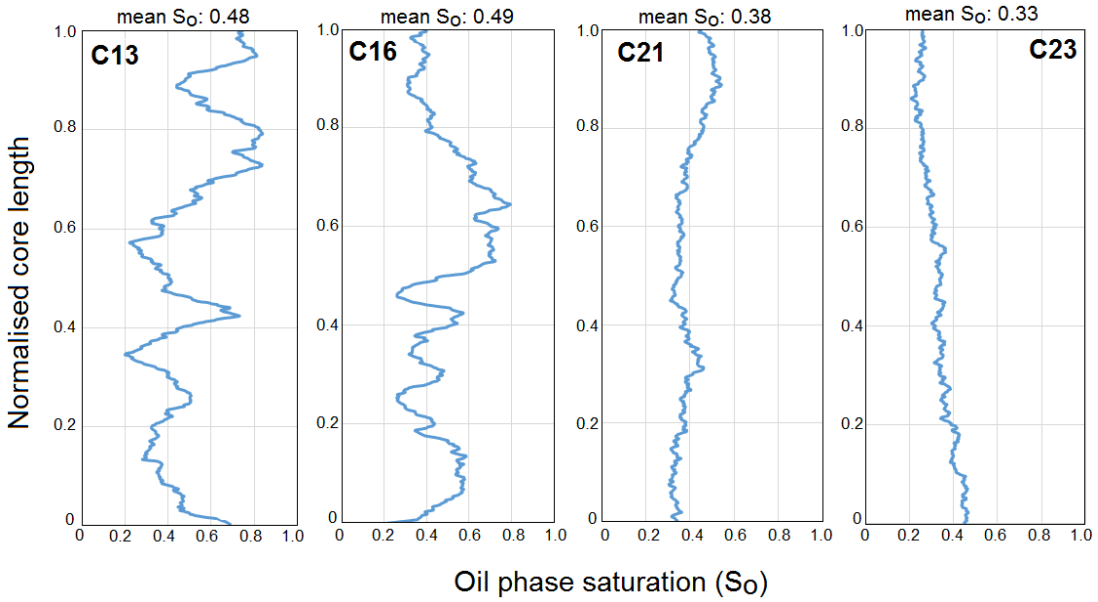

Figure 6-16 Profiles of the remaining oil phase saturation along the samples height after injection of 2 PV of heavy water for four Coquina samples including C13 deformed and C16 (cored perpendicular to the layering orientation), C21 and C23 (cored almost parallel to the layering orientation)

The final distribution of phases saturation within the samples can be influenced by parameters that have different scales. The distinct pore system properties of each individual layer can control the fluid displacement within that layer. At larger length scales, the spatial distribution/orientation of these layers with respect to the flow direction controls the interplay between layers and, as a result, affects the fluid displacement in the whole sample and final saturation distribution. As observed in the saturation profiles of samples C13 and C16, the maximum oil saturation in some parts of samples is remained very high (over 0.8) after 2 pore volume of heavy water injection which is much higher than the maximum oil saturation in samples with parallel layer flow. Also, the mean oil saturation is higher in samples C13 and C16 (0.48 and 0.49 respectively) compared to samples C21 and C23 (0.38 and 0.33 respectively). As detailed before (section 6.4.1.2), capillary trapping of the non-wetting phase, which can be more pronounced in the samples with cross (perpendicular to) flow distribution of layers of contrasting capillary pressure (C13 and C16), seems to result in a high amount of oil to be trapped in these samples. Despite the existence of a lab-induced fracture in sample C13, the final oil saturation and saturation profile in this sample are similar to the one for intact sample C16.

Given the spatial resolution of 85 µm for the Neutron tomography images used for calculating the phases saturation, effect of sub-resolution pores that are not properly resolved in these images should be investigated. In fact, for the above calculations, the assumption has been made that each voxels is solely occupied by a single phase that can be either Decane, heavy

water or solid component of the rock. However, this is not exactly true since some voxels may be partially resolved so that a single voxel may be occupied by fraction of different phases. During the image segmentation process using WEKA (section 3.3.3), the partially resolved voxels will be finally classified in one of the Decane, heavy water or solid component based on the computed probability of each voxel for belonging to a given phase. This probability of each voxel to belong to each given phase has a value ranging from zero to one for lowest and highest probability respectively (Arganda-Carreras et al., 2017). The probability of a voxel to a given phase should be close to one if the voxel is solely occupied by that phase. But, for a partially resolved voxel that is occupied with three different phases (like in our case; Decane, heavy water and solid component), for instance, probability of a voxel to Decane, heavy water and solid component may be calculated as 0.40, 0.35 and 0.25 respectively. In this case, the voxel will be classified as Decane phase (as it has the highest probability for Decane among other phases), although a fraction of its volume is occupied by two other phases. This can result in error in calculation of phases saturation. Here, in order to estimate the proportion of partially resolved pores in the image that lead to erroneous saturation calculation, the probability field is obtained (as an output of the WEKA segmentation) for a three-phase Neutron tomography image of one Coquina sample (C16). As you see in figure (6.17), a vertical slice of the Neutron tomography image (a) of this sample and the corresponding segmented image (b) are presented in which three phases including Decane, heavy water and solid component are segmented. In the second row of the figure (6.17), the corresponding probability maps for Decane (c), heavy water (d) and solid components (e) are presented. In these images, only voxels with a probability values of over 0.9 to each given phase are visualised (in white colour). The proportion of these voxels to the total voxels in the image are then calculated. By overlying these probability maps (c, d and e), all the voxels with probability value over 0.9 to any of the three phases are visualised in white colour (f). From this image (f), the voxels that does not have probability values over 0.9 to none of the phases are considered as partially resolved voxels that their assignment to any of the three classes can be erroneous. In fact, we assume that voxels with probability value over 0.9, will properly resolve a given phase (with negligible error) while voxels with no probability values over 0.9 to any of the phases will have error in their classification. The threshold 0.9 is chosen based on visual examination of the voxel values in the central parts of the well-resolved large pore spaces that their fluid occupancy is clearly observable in the Neutron tomography image. It is observed in figure 6.17-f, that many of the voxels with probability value below the 0.9 (visualised in black colour) are in the rims of pore spaces that confirms their partially resolved state. The proportion of voxels with probability over 0.9 to

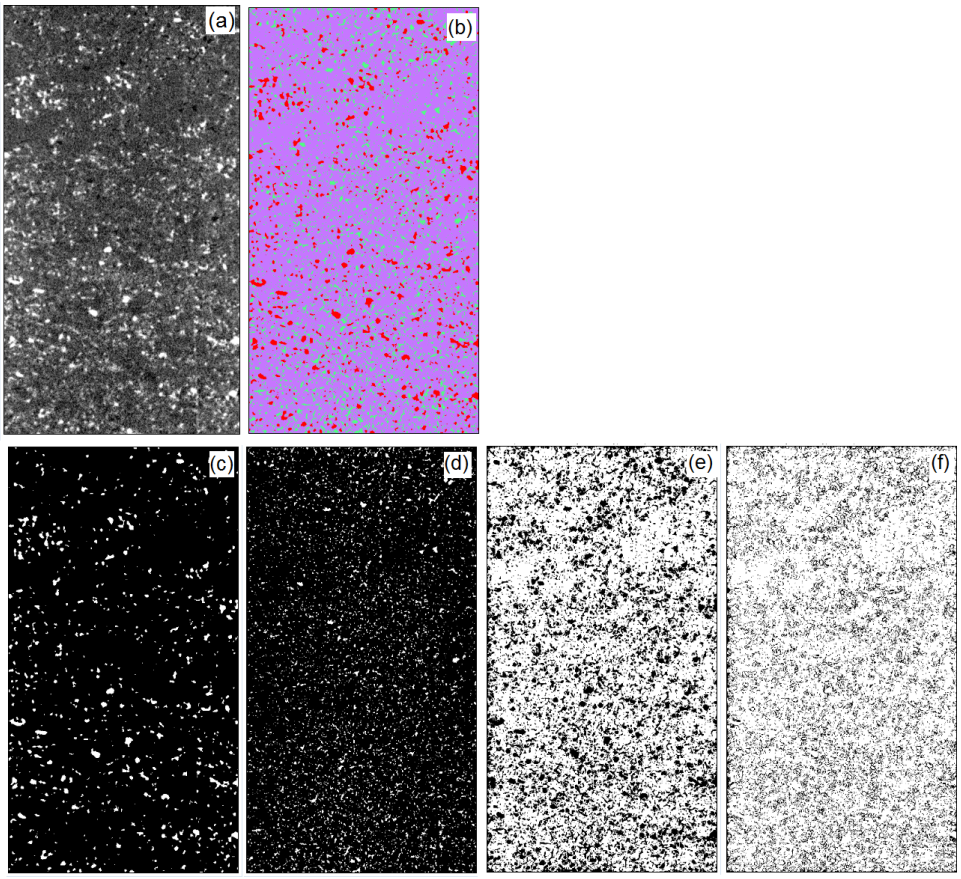

Figure 6-17 The vertical slice of grey-scale Neutron tomography image (a) with 85µm voxel size taken from sample C16 after injection of 2 pore volume of heavy water into Decane saturated sample. The bright, dark and grey colours represent Decane, heavy water and solid components of the rock respectively. The corresponding segmented image using WEKA method (b) presenting Decane, heavy water and solid components of the rock in red, green and purple colours respectively. Corresponding slices of probability maps representing the probability of voxels to be assigned to Decane (c), heavy water (d) and solid component (e) respectively. Voxels with a probability values of over 0.9 and below 0.9 are visualised in white and black colours respectively. By overlying the probability maps (c, d and e), all the voxels with probability value over 0.9 to any of the three phases are visualised in white colour in slice (f). In slice (f), the voxels that does not have probability values over 0.9 to none of the phases are visualised in black.

the Decane, heavy water and solid components (to the total voxel count of the image) are calculated that are equal to 4.73 %, 7.51 % and 71.67 % respectively. The proportion of the partially resolved voxels (probability below 0.9) are then calculated that is equal to 16.09 % of the total voxels in the image. The relatively large proportion of partially resolved voxels may introduce considerable uncertainty to the calculated phases saturation. With regards to the lab-measured porosity of this sample (21.7%), the proportion of the pore space that is properly resolved (both heavy water filled and Decane filled pore spaces with probability of over 0.9) is equal to 56.4 % of the total porosity. This means that the fluid occupancy calculated for the rest of pore spaces can only be an approximated value.

6.4.3 Differential imaging

Variation in the rocks pore system, caused by textural variation due to depositional features or mechanical deformation, can influence the way in which different voids contribute to fluid flow. The proportion of pore spaces contributing to two phase immiscible displacement in Coquina samples was determined by investigating the difference between neutron tomography images acquired after steps of fractional flow in the samples. For this purpose, a high resolution neutron tomography (85 µm voxel size) was acquired from Coquina samples with the initial two phases (oil and heavy water) saturated condition. This tomography was subtracted from a high resolution neutron tomography acquired after flooding the samples with one pore volume of heavy water. The detail of flow parameters in this experiment is presented in section 6.2-second flow protocols. The result is a 3D differential image (see section 3.3.8) for each sample in which the voxel values correspond to the intensity of the grey-scale value changes due to the displacement of fluids (oil and heavy water).

By segmenting the differential grey-scale image, a 3D image of the distribution of regions with differential grey-scale value over 2000 (grey-scale unit) was extracted. The regions with differential grey-scale values over this threshold were considered as pore spaces in which significant fluid displacement has been happened. Here, the proportion of these pore spaces to the samples volume is defined as contributing porosity. The slice averaged contributing porosity was then calculated based on the segmented differential image. Figure 6.18 shows the slice averaged contributing porosity as well as total porosity extracted from the X-ray tomography images of the samples (as detailed in chapters 3 and 4). In general, the gap

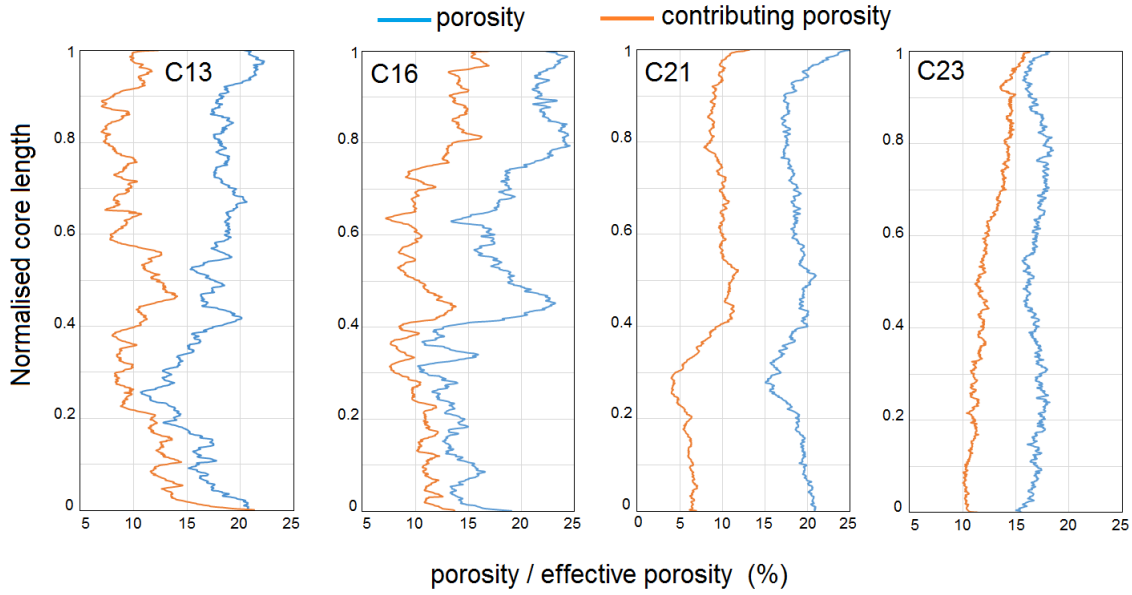

Figure 6-18 plots of slice averaged porosity (blue line) and effective porosity (orange line) along the samples height for four Coquina samples C13, C16, C21 and C23

between contributing porosity and the porosity varies in different samples and even in each individual sample along its height.

In sample C16, a positive correlation is observed between contributing porosity and porosity along the samples height, however the gap between these two values varies along the height of the sample. A change in the gap between porosity and contributing porosity is obvious at a point around 0.4 of the samples height. Below this point, the difference between porosity and contributing porosity values is low (2-5% difference) while this difference increases to 7-10% above this point. This means that a higher proportion of pore spaces contribute to fluid flow in the bottom 40% of the samples height. By looking at porosity and specific surface area profiles along the height of sample C16 (figure 6.7-c), it is observed that in the bottom 40 % of the sample height, the porosity is generally lower and the specific surface area is generally higher compared to the upper parts of the sample. The different pore size in bottom part and upper parts of the sample is also obvious in the vertical slices of the X-ray tomography image of this sample (figure 6.7). This observation suggests that the higher proportion of pores with smaller pore size and higher capillary pressure result in relatively more heavy water imbibition in the bottom part of the sample compared to the upper parts. This can explain the relatively higher contributing porosity in the bottom 40 % of the sample height.

In sample C13, an increase in the difference between porosity and effective porosity is observed at regions above 25%of the sample height, where the fracture tip starts. From this point up to the samples outlet, the flow is dominated by the fracture that reduces the pore spaces contributing to a flow in the surrounding matrix. In samples C21 and C23, the local fluctuations in porosity and effective porosity values along the samples are smaller. In sample C21, the highest difference between porosity and effective porosity is observed, which can be related to flow through the preferential high permeability paths in this sample.

6.5 Summary and further discussion

The results presented in this chapter show the significant role that textural variations, due to depositional features and mechanical deformation, can play in immiscible fluid displacement (heavy water displacing oil) in the tested Coquina and Travertine samples. Complementary using of HSNT (170µm voxel size), high resolution neutron tomography (85 µm voxel size) and X-ray tomography provided valuable insights into immiscible fluid displacement processes caused by sub-core-scale variations.

The impact of mechanical deformation in immiscible displacement can vary depending on the deformation condition and the host rock properties. The observed flow patterns within mechanically deformed Coquina (C13) and Travertine (T13) samples revealed a significant difference. In sample T13, the injected fluid (heavy water) has flowed mainly through the developed deformation band (associated with the laboratory induced deformation in this sample). The stress-strain curve (figure 4.20) suggest compaction induced to this sample; although no post-deformation X-ray tomography has taken place, we speculate that the developed deformation band is characterised by grain fracturing and pore collapse leading to very fine pore and microfracture sizes and as a result, this zone is characterised with higher capillary pressure compared to the surrounding matrix. Preferential flow of the wetting phase (heavy water) through this deformation band , which is characterised by higher capillary pressure caused that a considerable part of the sample is bypassed by the displacing phase heavy water) resulting in poor sweep efficiency in this sample. In sample C13 on the other hand, the laboratory induced mechanical deformation introduced a fracture (with 0.5 to 1mm aperture) that has not acted as a preferred flow path at the beginning and instead the injected fluid has invaded the matrix earlier than the fracture. However, the fracture has been finally filled with the injected fluid (heavy water) and also became a conduit. In fact, as explained before, the injected fluid has flowed into the fracture with several minutes of delay compared to the surrounding matrix. The mechanical deformation under low confining pressure created an open vertical fracture in sample C13. It seems that flow of the wetting phase (heavy water) from matrix into the fracture due to the co-current imbibition creates a film of heavy water in the matrix-fracture interface in early stages and does not hydraulically displace the oil within the fracture. Given the spatial resolution of 170 μm (voxel size), the formed film of heavy water can not be visualised in early stages however, it cause a relative reduction of grey-scale value in voxels in these regions. Although, the creation of the heavy water film is not visualised, but the time when the heavy water has hydraulically displaced the oil in the fracture is resolved. In sample C13, the flow from the matrix into the fracture is not impeded but only delayed for several minutes. This still had significant influence in the improved macroscopic sweep efficiency in this sample and needs to be considered in assessing immiscible fluid displacement in water wet fractured systems where the initial water saturation is low.

Some experimental observations of immiscible displacement in a fabricated fracture-matrix system using Magnetic Resonance Imaging (MRI) have been reported before (E. Aspenes et al., 2002) as reviewed in Chapter 2. In their study, same fluids (e.g. heavy water and Decane) have been used as immiscible phases. As observed by Aspenes et al., (2002), in a fracture-

matrix system with an strongly water wet matrix, the wetting phase (heavy water) forms a film in fracture-matrix interface and does not flow into the fracture until water saturation in the matrix reaches its spontaneous imbibition endpoint (Swi=70%). Based on the results in this chapter (sample C13-deformed), the similar process (creation of a film of wetting phase in matrix-fracture interface when wetting phase saturation in the matrix is low) seems to be responsible for the delayed flow of the heavy water from matrix into the fracture even in moderately water wet condition of our sample. However, it can be expected that this delay can increase by approaching to a strongly water wet condition. The MRI images presented in their study are captured in 2D and in orthogonal directions along and perpendicular to the fracture. The 2D nature on data, allowed the whole cross-section within a simple geometry fabricated fracture aperture to be captured and 2D distribution of fluid phases to be investigated. However, the HSNT in our study has provided 4D data that allowed investigating the immiscible displacement processes in a fractured carbonate rock with a complex geometry fracture. Thanks to the 4D nature of data and quantitative image analysis, the delay in heavy water arrival time within the fracture (compared to surrounding matrix) is quantified. Also, a good approximation of saturation distribution of phases and its evolution with time can be obtained within the fracture and in any distance from fracture within the matrix.

The existence of layers of contrasting pore system properties remarkably affected the immiscible fluid displacement efficiency. This effect was significantly dependent on the spatial distribution and orientation of these layers with respect to the flow direction. As observed in the fluid arrival time results, quick uptake of the wetting phase (heavy water) into the layers (with higher capillary pressure) oriented semi-parallel to the length of the sample (flow along the length of the sample (C23)) resulted in early heavy water breakthrough along these layers. In contrast, in samples with cross flow layers (C16), a later heavy water breakthrough time caused by the wetting phase (heavy water) saturation hold up by capillary mechanism in the horizontal layers (with higher capillary pressure) was observed. The wetting phase saturation hold up can be identified in this sample based on the sharp contrast in fluid arrival time values observed in some horizontal levels along the samples height. Capillary pressure contrasts between layers can cause accumulation of the non-wetting phase (Decane) trapped upstream of the layers with high capillary pressure. This is consistent with the sharp fluctuations observed in the oil saturation profiles of this sample and the high saturation of remaining Decane (0.49) at the end of the test (after injection of two pore volumes of heavy water). These observations are in agreement with the experimental and numerical results of previous studies(Krevor et al., 2011; Debbabi et al., 2017) in which the

capillary pressure contrasts at layers interface are found to cause the formation of saturation discontinuities at layer boundaries and fluid entrapment. However, it should be noted that the observation in Krevor et al., (2011) is made based on static X-ray tomography scan once the flow is stabilised after at least 10 pore volume of water injection however, the observation here is based on the heavy water arrival time at different layers during the injection of one pore volume of heavy water. But, saturation distribution is also checked after two pore volumes of heavy water injection based on Neutron tomography image acquired in static condition that still show high fluctuation in oil saturation along the core length indicating the entrapped oil in some layers. As observed in the differential grey-scale images, the proportion of pore spaces contributing to the fluid flow is affected by the distribution of these layers. The fluid pressure drops downstream of these layers can significantly reduce the amount of pore space contributing in flow and as a result, increases the amount of entrapped non-wetting phase.

The use of differential imaging for defining contributing porosity as a new procedure developed in this study, showed potential to reveal very small fractions of fluids displacement during immiscible fluid displacement. Given the voxel size of 85 μm in Neutron tomography images, displacement of oil (Decane) in micro-pores (sub-resolution) cannot be fully resolved however, the slight change in grey-scale value of a voxel can be a sign for a partial fluid displacement over a fraction of the volume of a single voxel. In fact, a micro-pore may occupy only a fraction of a voxel volume so that even full displacement of oil in this micro-pore does not incur a huge change in grey-scale value of that voxel but it does change the grey-scale of that voxel slightly. Therefore, the data obtained from differential imaging lack information about the geometry or accurate location of the displaced fluid and micro-pores however it still provide a good approximation of the extent of fluids displacement and the distribution of pore spaces contributing in fluid displacement.

In sample C23, the displacing fluid leading front moves faster in some vertically distributed layers. However, the transition of fluid arrival time between these layers and the surrounding layers looks gradual and no sharp changes in fluid arrival time is observed. Based on previous studies, transverse capillary pressure gradients may cause capillary crossflow that can reduce the distance between the leading edges of the injected phase in the different layers distributed parallel to the flow direction (Yokoyama & Lake, 1981; Debbabi et al., 2017). At the beginning of the flow experiment in sample C23, when the capillary force is expected to be dominant due to the low initial water saturation in the sample and the small flow rate, capillary

crossflow can be responsible for gradual fluid arrival time transition between layers and moderating the distance between the leading fluid fronts in different layers.

In sample C21, the early breakthrough of the heavy water (when only about 25 percent of the sample pore volume of heavy water was injected into the sample) suggests that the heavy water has flowed through the preferential paths to reach to the sample outlet. Also, the very low maximum differential fluid pressure recorded in this sample (12 kPa) suggests that there is a good continuity in capillary pathways (network of well-connected smaller pores with high capillary pressure) between the inlet and outlet of the sample. This is in contrast with sample C16 in which the differential fluid pressure sharply increases once the advancing heavy water front meets the capillary barriers zones (with larger mean pore size and lower capillary pressure).

As observed in the fluid arrival time field of sample C21, there is a region in the bottom part of the sample that lack an accurate calculation of fluid arrival time. It seems that due to the low porosity and poor connectivity of pores in this region (as explored from pore network characterisation), the volume of the heavy water imbibed into this region is very small and does not form a well-connected cluster of the wetting phase. Therefore, the grey-scale changes in the voxels (of HSNTs) in this region (due to fluid displacement) is not high enough to allow a good fitting of a sigmoidal curve. This can suggests the limitation in the spatial resolution of f HSNTs that can not resolve the grey-scale changes in micro-pores (sub-resolution pores). In fact, the grey-scale changes due to the fluid displacement in micro-pores (occupying only a small fraction of a voxel volume) is not detected properly when it is averaged by the low grey-scale change corresponding to the material occupying the rest of a voxel space. Despite the limitation of partially resolved voxels, as discussed above, even a slight change in a grey-scale value of a partially resolved voxel can be still analysed and inferred as partial fluid displacement (in a fraction of a voxel) in differential imaging where the used Neutron tomography images have less image noises (high signal to noise ratio achieved by longer acquisition time of about 20 minute). However, in HSNTs, due to the shorter acquisition time (1-2 min) and lower signal to noise ratio compared to the static Neutron tomographies, the slight changes in grey-scale values of a given voxel may not be discriminated from the images noise level in that voxel. This makes the fitting of the sigmoidal curve challenging and sometimes impossible in these voxels.

The results and outcomes from this chapter can have different implication in the field of immiscible fluid flow within heterogeneous carbonate rocks. While our understanding of immiscible fluid displacement mechanisms associated with pore-scale complexities in

carbonate rocks have been developed by recent uses of 3D and 4D imaging techniques (Andrew et al., 2015; S Schlüter et al., 2016; Pak et al., 2015), full-field experimental studies on the influence of core-scale features on these mechanisms are lacking in the literature. The results in this chapter provided new insights into 4D observations of immiscible fluid flow patterns associated with core-scale (millimetre to centimetre) features including layering, layering orientation, mechanical deformation and textural variations. These observation are not only helpful to explore processes and mechanisms, but also can provide experimental data sets for evaluating the performance of simulations and relevant models. For instance, as reviewed in Chapter 2, pore-scale models bridge predictions of transport properties from sub-pore to core-scale and more importantly, they provide sensitivity analyses of pore-scale features on macroscopic transport observations and offer explanations for anomalous flow behaviours (Mehmani et al., 2020). However, qualitative and quantitative comparisons between different models, and with experimental data, are rare (Zhao et al., 2019). Zhao et al. (2019) compared the performance of different pore-scale modelling methods with the experimental data from 2D micromodels. However, the authors has mentioned that the heterogeneity in real rocks such as carbonates can have an effect on their correlations due to the wider pore-size distribution in these rocks compared to their micromodel. The results from this chapter showed that the HSNT and image analysis procedures employed in this chapter have the potential to provide experimental data of 3D flow patterns that can be used for qualitative and quantitative evaluation of relevant modelling methods.

Despite the proven capability of HSNT in capturing the movement of hydrogen-rich fluids (e.g. water flow in both dry and D_2O-saturated sample) in porous rocks in in core-scale (Etxegarai., 2019; Tudisco et al., 2019; Tengattini et al., 2021), employing this technique to study oil (as a Hydrogen-rich fluid) displacement in porous rocks in core-scale could not be found in the literature. This study showed that HSNT can be successfully employed for visualisation and full field investigation of the immiscible fluid transport in core-scale (38mm diameter core sample). Thanks to the high contrast that can be achieved between heavy water and oil phases in neutron imaging, the immiscible fluid displacement can be investigated without the need for salts and chemical dopants that are needed in X-ray tomography. This can be a great advantage for investigating low salinity waterflooding using this technique. (Murison et al., 2015) have proposed neutron imaging as a useful tool for studying mutliphase phenomena in porous media at pore-scale where the results are known to be dependant on salinity of fluids like low salinity water, surfactant, and polymer flooding. Although the underlying mechanisms of low salinity water flooding is well known at the molecular scale,

neutron imaging can provide a good opportunity to experimentally investigate the effect of water salinity at the oil recovery in core-scale.

Chapter 7

Conclusions and perspective for future researches:

7.1 Conclusions

In this thesis, the miscible and immiscible fluid transport processes within carbonate rocks having different types of complexities in their pore system caused by their textural variation due to depositional and lab-induced mechanical deformation features have been experimentally investigated. The main objective of this work was to deepen understanding of the influence of these core-scale complexities on pore network properties and fluid transport processes by means of direct and real time observation using full field techniques. Exploring the capability of Neutron imaging to temporally and spatially resolve the fluid transport process at core-scale was other objective of this study. For this purpose, first, some of samples were subjected to triaxial compression (at the laboratory scale) to induce mechanical deformational features. Then, we characterised the textural characteristics due to depositional and lab-induced mechanical deformation features (e.g. lamination, layering, fractures etc.) and their influence on the spatial distribution of pore network properties within different carbonate rocks by means of experimental methods and mainly X-ray micro-computed tomography (micro-CT) and image analysis. Miscible and immiscible fluid transport within 38mm diameter and 76mm length core samples was imaged using in-situ High Speed Neutron Tomography (HSNT). By means of quantitative image analysis methods, the interaction between aforementioned core-scale features with miscible and immiscible fluid displacement processes was quantified.

Reviewing the literature as presented in Chapter 2, showed that, in recent years, full-field techniques and particularly X-ray micro-CT has been widely used to study miscible and immiscible fluid displacement mechanisms in porous rocks. Most of these studies focus on phenomena occurring at the pore-scale during fluid flow within a few millimetre size samples. However, exploring the impact of larger scale (core-scale/ a few mm to cm scale) features like fractures, lamination or layering and other rock textural heterogeneity features on fluid flow via a direct observation method requires scanning larger samples that may have some limitations in terms of achieving desired temporal and spatial resolution. In order for a larger sample to be scanned, a sufficiently strong signal from the beam after it has been attenuated by passage though the object is required. Imaging with high temporal resolution that requires a shorter image acquisition time can adversely affect the image quality by reducing the signal to noise ratio.

Sensitivity of Neutrons to Hydrogen and its isotope, Deuterium, and the high fluxes of Neutrons available for imaging at Neutron beamline facilities as well as the very low neutron attenuation coefficient of geological materials as presented in Chapter 3, can make Neutron imaging an ideal tool for visualising the multiphase flow at core-scale at useful spatial and temporal resolution. In Neutron imaging, displacement of a hydrogen-rich fluid like water or most hydrocarbon-based oils by a Deuterium-rich fluid like heavy water (or vice versa) can be visualised because the contrast between the Neutron attenuation coefficients of these two isotopes (Hydrogen and Deuterium) and of suitably chosen liquids containing them, is sufficient to identify the position of each one.

In Chapter 4, four carbonate rocks, Coquina limestone, Biolithite, Travertine and Oolitic limestone were studied. The textural features of these rocks, the variation of these features within the samples and the potential influence of these features on the pore network properties and mechanical behaviour of these rocks were characterised. The results of these characterisations that were carried out using experimental methods and analysis of X-ray tomography data, led to choosing the most interesting samples for flow experiments. Among the studied carbonate rocks, textural characteristics of Coquina limestone were found to more significantly control its pore network/flow properties when compared to other three rock types. Accordingly, and given the time constrains (PhD period), mainly Coquina samples were picked for flow experiments which were performed in the neutron beam. The occurrence of a series of thin (a few mm thick) semi-parallel layers with distinct textural characteristics in the Coquina limestone introduced zones with contrasting pore network properties and permeability values in some of the samples. Permeability values calculated (based on

pressure-driven flow simulation using the lattice-Boltzmann method) for different sections along the length of a single core sample of Coquina limestone revealed a significant variation in permeability of different zones within the sample, ranging from 23 to 504mD. This is in accordance with a wide range of permeability values from 37 to 440 mD that was measured for Coquina samples cored from the same block but in different positions and orientation with regards to the layers. The existence of layers and their orientation to loading direction during the triaxial compression experiments was also influential in mechanical deformation that developed within the tested material. For example, under the same confining pressure, a shear fracture was developed in the sample cored outside the layered zone. Samples with layers oriented parallel to their long axis were weaker than the previous ones when subjected to triaxial compression and developed vertical fractures along the rim of the layers. Furthermore, the lab-induced fractures were found to significantly alter the pore system of the samples and thus, were initially expected to play crucial role in the hydraulic behaviour of the sample. However, their impact was found to significantly vary with both fracture properties and host rock characteristics.

By employing HSNT, the advancement of water (H_2O) in previously heavy water (D_2O) saturated samples (miscible fluids flow) and advancement of heavy water in previously Decane saturated samples (immiscible fluids flow) was visualised in 3D and with time. By further image analysis, the fluid arrival time and fluid speed fields from which the local variations in the advancing fluid speed and the arrival time of the injected fluid at each voxel is presented were computed. A good quantification of irregularity of the advancing fluid front with time, saturation / relative concentration evolution of phases in 3D with time, and longitudinal dispersion during miscible displacement were then obtained. Processes like capillary heterogeneity trapping and fracture to matrix flow during immiscible fluid displacement were also identified. The above results obtained by Neutron tomography were then linked to the textural characteristics of the material due to depositional and lab-induced deformational features as those inferred by means of the X-ray tomography performed on the same samples.

The results from miscible fluid flow experiments (Chapter 5) showed that the existence of layers with significant contrast in their pore network properties (e.g. porosity, permeability, specific surface area etc.) oriented normal to the intended flow direction, can stabilise the advancing fluid front and reduce the longitudinal dispersion by moderating the fluid speed variation in the displacing fluid front. The computed surface area of the advancing fluid front at different times was defined as a measure of irregularity of the fluid front. The higher surface

area of the advancing fluid front represent the existence of more protrusions or existence of protrusions with more complex morphology at the leading front face that can be implicitly a representative of the higher variation in fluid speed in the leading fluid front. The results showed that this value (surface area) remains 3-4 times smaller in the sample with several layers (with contrasting pore network properties) oriented normal to the flow direction compared to the sample that was not significantly affected by layers.

In samples with lab-induced fractures, flow distribution is dominated by the fracture network so that the injected water flows quickly through the fracture and reaches the outlet. A variable rate of water flow from fracture into the matrix was observed in samples with fractures perpendicular and parallel to the layering orientation. In the former case, generally higher fracture to matrix flow is observed compared to the latter case so that the fluid mixing zone in the matrix around the fracture is larger in the former case. However, there are more local variations, and the fracture-matrix flow was found to be linked to other parameters including the particulars of the developed fracture systems. Examples are where the fracture tips start, its orientation, length, and opening and the damage zone around the fracture as well as surrounding matrix properties.

The results from immiscible flow experiments (Chapter 6) indicated the significance of the samples sub-core-scale capillary heterogeneity on immiscible displacement where the heavy water (wetting phase) was injected into Decane (non-wetting phase) saturated sample. Analysing the HSNT data and anomalies in the computed fluid arrival time fields successfully revealed the immiscible displacement phenomena related to the capillary heterogeneities.

Existence of layers with distinct texture as well as lab-induced fractures/mechanical deformation features within the Coquina and Travertine samples introduced zones with contrasting capillary pressure characteristics. Layers with a smaller mean pore size introduced zones with a higher capillary pressure that imbibed the injected heavy water (wetting phase) earlier than surrounding regions. In the case of parallel layer flow, earlier progress of heavy water in the layer with higher capillary pressure compared to surrounding layers resulted in an uneven fluid front advancement and earlier breakthrough of heavy water. Flow across layers with significant capillary pressure contrast however, resulted in wetting-phase saturation hold up at a layer with higher capillary pressure values and accumulation of the non-wetting phase upstream of these layers. The displacing fluid front was more stable and a piston like advancement was observed in latter case.

The anomaly in the fluid arrival time field of the Coquina sample having a lab-induced fracture (oriented parallel to the sample long axis) revealed that the advancing fluid front has

been retarded in a narrow zone (~1 mm width) where the fracture exists. It was found that the injected fluid has flowed into the fracture with several minutes of delay compared to the surrounding matrix. It seems that flow of the wetting phase (heavy water) from matrix into the fracture due to the co-current imbibition creates a film of heavy water in the matrix-fracture interface in early stages and does not hydraulically displace the oil within the fracture. Given the spatial resolution of 170 µm (voxel size), the formed film of heavy water can not be visualised in early stages however, it cause a relative reduction of grey-scale value of voxels in these regions. Although, the creation of the heavy water film is not visualised, but the time when the heavy water has hydraulically displaced the oil in the fracture is resolved. In the deformed Travertine sample on the other hand, early flow of heavy water through a narrow band was observed. The compactant mechanical deformation in this sample is expected to have induced a band with very fine pore sizes and as a result, with higher capillary pressure compared to the surrounding matrix that gets imbibed earlier with the wetting phase. This band acted as a preferential flow path that caused the considerable part of the sample to be bypassed by the displacing phase and resulted in poor sweep efficiency in this sample.

The results from differential Neutron tomography images acquired before and after injecting 1 to 2 pore volume of heavy water into samples indicated that the existence of preferential flow paths such as a fracture and a higher permeability zone or layer communicating between inlet and outlet of the sample significantly reduce the proportion of pore space contributing in immiscible displacement. On the other hand, the proportion of the pore space that contribute to flow is higher at a region behind the slow layers (layers hindering the flow) that are oriented normal to the flow direction. In these regions, a higher proportion of tiny pore spaces and pore throats contribute to immiscible displacement due to the increased fluid pressure.

7.2 Perspective for future research:

In this thesis, it was shown that a combination of Neutron and X-ray imaging along with quantitative image analysis has a great potential to temporally and spatially resolve the dynamic processes during miscible and immiscible fluid flow in carbonate rock at the core-scale. The results indicated that the effect of local sub-core-scale textural features (e.g. fractures or textural heterogeneity) on the processes such as irregularity in the advancing fluid front, hydrodynamic dispersion during miscible displacement, two phase fluid flow in fracture-matrix system and capillary heterogeneity trapping during immiscible fluid displacement can be captured and quantified. The experimental approach employed in this

thesis can be readily followed for further experimental studies in a wide range of applications such as solute transport in porous rock and contaminant groundwater remediation, flow in Enhanced Geothermal Systems, enhanced oil recovery and transport/displacement of dissolved CO_2 during geological storage of CO_2. By following the same approaches, further researches can study the effect of other variables such as flow rate, fluid properties, different sorts of heterogeneity features and different types of reservoir rocks on the mentioned processes. For instance, three-dimensional structure of viscous fingering and its development in time for miscible and immiscible fluid displacement can be quantified as a function of Peclet number, viscosity ratio or capillary number.

Thanks to the high contrast that can be achieved between heavy water and oil phases in neutron imaging, the immiscible fluid displacement can be investigated without the need for the salts and chemical dopants that are needed in X-ray tomography. This can be a great advantage for investigating low salinity waterflooding using this technique. Although the underlying mechanisms of low salinity water flooding is well known at the molecular scale, neutron imaging can provide a good opportunity to experimentally investigate the effect of water salinity at the oil recovery in core-scale.

In this study, miscible fluid displacement was examined during continuous injection experiments meaning that the water was continuously injected into heavy water saturated samples. In this case, a sigmoidal function fitted to the grey-scale evolution within voxels that represent the relative concentration evolution of the injected phase with time. Future experiments using the same approach can focus on pulse tracer injection during flow experiments to study the spatial concentration evolution after the breakthrough point. The calculated Peclet number for the miscible fluid flow experiments in this thesis indicated a dominant contribution of advection compared to diffusion to miscible displacement. Further experiments at smaller Peclet number can be interesting to study the slower processes like diffusion and back-diffusion in fractured rocks or rocks with stagnant zones. In the case of capturing these slower processes, the Neutron tomography acquisition time can also slightly increased in order to gain higher signal to noise ratio that allows more accurate quantification of spatial concentration evolution.

In terms of image analysis, by fitting a sigmoidal function to the evolution of grey-scale values of HSNTs captured during flow experiments, useful parameters including C-parameter (used as fluid arrival time) and D-parameter (representing the steepness of the curve) were quantified in this study. The other two parameters that can be obtained from the fitted sigmoidal function are the A and B parameters (see section 3.3.5) from which the range of

grey-scale changes in voxels can be quantified. The extent to which the grey-scale changes in each voxel can depends on the location of that voxel with regards to the pore space. This is itself controlled by the spatial resolution of the image so that the grey-scale change associated with a specific physics, can be dependent of the volume of the voxel relative to the actual pore size of the sample. Therefore, the A and B parameters can be further analysed in future in order to estimate the spatial resolution of the image at which a specific physics can be properly resolved.

From an experimental point of view, further development of the flow setup and sample environment is required to make the flow experiment possible at higher flow rates. A fluid flow cell that can apply high confining pressure is then required. This is particularly required for running flow experiments with lower permeability rocks where fluids need to be injected at higher pressures. The advantage of Neutrons in passing through metals can be taken to design and use a metal flow cells that withstand the high confining pressure.

References

Afshari, S., Hejazi, S. H., & Kantzas, A. (2018). Longitudinal dispersion in heterogeneous layered porous media during stable and unstable pore-scale miscible displacements. *Advances in Water Resources*, *119*, 125–141. https://doi.org/https://doi.org/10.1016/j.advwatres.2018.06.005

Alhammadi, A. M., Gao, Y., Akai, T., Blunt, M. J., & Bijeljic, B. (2020). Pore-scale X-ray imaging with measurement of relative permeability, capillary pressure and oil recovery in a mixed-wet micro-porous carbonate reservoir rock. *Fuel*, *268*(June 2019), 117018. https://doi.org/10.1016/j.fuel.2020.117018

Alhosani, A., Scanziani, A., Lin, Q., Pan, Z., Bijeljic, B., & Blunt, M. J. (2019). In situ pore-scale analysis of oil recovery during three-phase near-miscible CO2 injection in a water-wet carbonate rock. *Advances in Water Resources*, *134*, 103432. https://doi.org/https://doi.org/10.1016/j.advwatres.2019.103432

Aliakbardoust, E., & Rahimpour-Bonab, H. (2013). Effects of pore geometry and rock properties on water saturation of a carbonate reservoir. *Journal of Petroleum Science and Engineering*, *112*, 296–309. https://doi.org/https://doi.org/10.1016/j.petrol.2013.11.018

Ambrose, J. (1973). Computerized transverse axial scanning (tomography): Part 2. Clinical application. *The British Journal of Radiology*, *46*(552), 1023–1047. https://doi.org/10.1259/0007-1285-46-552-1023

Anderson, I. S., McGreevy, R. L., and Bilheux, H. Z. (2009), Neutron imaging and applicatio*ns, Springer Science+ Business Media, Vol. 200, No. 2209, pp. 987.*

Andrew, M., Bijeljic, B., & Blunt, M. J. (2014). Pore-scale contact angle measurements at reservoir conditions using X-ray microtomography. *Advances in Water Resources*, *68*, 24–31. https://doi.org/https://doi.org/10.1016/j.advwatres.2014.02.014

Andrew, M., Menke, H., Blunt, M. J., & Bijeljic, B. (2015). The Imaging of Dynamic Multiphase Fluid Flow Using Synchrotron-Based X-ray Microtomography at Reservoir Conditions. *Transport in Porous Media*, *110*(1), 1–24. https://doi.org/10.1007/s11242-015-0553-2

Antonellini, M., Petracchini, L., Billi, A., & Scrocca, D. (2014). First reported occurrence of deformation bands in a platform limestone, the Jurassic Calcare Massiccio Fm., northern Apennines, Italy. *Tectonophysics*, *628*, 85–104. https://doi.org/10.1016/j.tecto.2014.04.034

Arganda-Carreras, I., Kaynig, V., Rueden, C., Eliceiri, K. W., Schindelin, J., Cardona, A., & Sebastian Seung, H. (2017). Trainable Weka Segmentation: a machine learning tool for microscopy pixel classification. *Bioinformatics*, *33*(15), 2424–2426. https://doi.org/10.1093/bioinformatics/btx180

Armstrong, R. T., Georgiadis, A., Ott, H., Klemin, D., & Berg, S. (2014). Critical capillary number: Desaturation studied with fast X-ray computed microtomography. *Geophysical Research Letters*, *41*(1), 55–60. https://doi.org/10.1002/2013GL058075

Arns, C. H. (2004). A comparison of pore size distributions derived by NMR and X-ray-CT techniques. *Physica A: Statistical Mechanics and Its Applications*, *339*(1), 159–165. https://doi.org/https://doi.org/10.1016/j.physa.2004.03.033

Aspenes, E., Graue, A., Baldwin, B. A., Moradi, A., Stevens, J., & Tobola, D. P. (2002). Fluid

Flow in Fractures Visualized by MRI during Waterfloods at Various Wettability Conditions - Emphasis on Fracture Width and Flow Rate. *Proceedings - SPE Annual Technical Conference and Exhibition*, 69–80. https://doi.org/10.2118/77338-ms

Aspenes, Eirik, Ersland, G., Graue, A., Stevens, J., & Baldwin, B. A. (2008). Wetting phase bridges establish capillary continuity across open fractures and increase oil recovery in mixed-wet fractured chalk. *Transport in Porous Media*, *74*(1), 35–47. https://doi.org/10.1007/s11242-007-9179-3

ASTM (American Society for Testing, Materials), (2012). Standards & Publications. http://www.astm.org/Standard/ (Accessed 03/05/12).

Baruchel, J., Buffiere, J. Y., & Maire, E. (2000). *X-ray tomography in material science*. Hermes science publications. http://inis.iaea.org/search/search.aspx?orig_q=RN:31031064

Baud, P., Vinciguerra, S., David, C., Cavallo, A., Walker, E., & Reuschlé, T. (2009). Compaction and failure in high porosity carbonates: Mechanical data and microstructural observations. *Pure and Applied Geophysics*, *166*(5–7), 869–898. https://doi.org/10.1007/s00024-009-0493-2

Baud, Patrick, Exner, U., Lommatzsch, M., Reuschlé, T., & Wong, T. F. (2017). Mechanical behavior, failure mode, and transport properties in a porous carbonate. *Journal of Geophysical Research: Solid Earth*, *122*(9), 7363–7387. https://doi.org/10.1002/2017JB014060

Baxevanis, T., Papamichos, E., Flornes, O., & Larsen, I. (2006). Compaction bands and induced permeability reduction in Tuffeau de Maastricht calcarenite. *Acta Geotechnica*, *1*(2), 123–135. https://doi.org/10.1007/s11440-006-0011-y

Berg, S., Saxena, N., Shaik, M., & Pradhan, C. (2018). Generation of ground truth images to validate micro-CT image-processing pipelines. *The Leading Edge*, *37*(6), 412–420. https://doi.org/10.1190/tle37060412.1

Beucher, S., & Meyer, F. (1993). The Morphological Approach to Segmentation: The Watershed Transformation. In *Mathematical Morphology in Image Processing: Vol. Vol. 34* (pp. 433–481). https://doi.org/10.1201/9781482277234-12

Bijeljic, B., & Blunt, M. J. (2007). Pore-scale modeling of transverse dispersion in porous media. *Water Resources Research*, *43*(12). https://doi.org/https://doi.org/10.1029/2006WR005700

Bingham, P., Polsky, Y., Anovitz, L., Carmichael, J., Bilheux, H., Jacobsen, D., & Hussey, D. (2015). Neutron Radiography of Fluid Flow for Geothermal Energy Research. *Physics Procedia*, *69*(October 2014), 464–471. https://doi.org/10.1016/j.phpro.2015.07.065

Blunt, M. J., Bijeljic, B., Dong, H., Gharbi, O., Iglauer, S., Mostaghimi, P., Paluszny, A., & Pentland, C. (2013). Pore-scale imaging and modelling. *Advances in Water Resources*, *51*, 197–216. https://doi.org/10.1016/j.advwatres.2012.03.003

Boek, E. S., & Venturoli, M. (2010). Lattice-Boltzmann studies of fluid flow in porous media with realistic rock geometries. *Computers & Mathematics with Applications*, *59*(7), 2305–2314. https://doi.org/https://doi.org/10.1016/j.camwa.2009.08.063

Boon, M., Bijeljic, B., & Krevor, S. (2017). Observations of the impact of rock heterogeneity on solute spreading and mixing. *Water Resources Research*, *53*(6), 4624–4642. https://doi.org/https://doi.org/10.1002/2016WR019912

Boon, M., Bijeljic, B., Niu, B., & Krevor, S. (2016). Observations of 3-D transverse

dispersion and dilution in natural consolidated rock by X-ray tomography. *Advances in Water Resources*, *96*, 266–281. https://doi.org/https://doi.org/10.1016/j.advwatres.2016.07.020

Boone, M., Bultreys, T., Masschaele, B., Van Loo, D., Van Hoorebeke, L., & Cnudde, V. (2016). In-situ , real time micro-CT imaging of pore scale processes , the next frontier for laboratory based micro-CT scanning. *International Syposium of the Sociaty of Core Analysts*, 1–12.

Bubeck, A., Walker, R. J., Healy, D., Dobbs, M., & Holwell, D. A. (2017). Pore geometry as a control on rock strength. *Earth and Planetary Science Letters*, *457*(October), 38–48. https://doi.org/10.1016/j.epsl.2016.09.050

Buckman, James. (2014). Use of automated image acquisition and stitching in scanning electron microscopy: Imaging of large scale areas of materials at high resolution. *Microscopy and Analysis*, *28*, S13–S15.

Buckman, Jim, Bankole, S. A., Zihms, S., Lewis, H., Couples, G., & Corbett, P. W. M. (2017). Quantifying porosity through automated image collection and batch image processing: Case study of three carbonates and an aragonite cemented sandstone. *Geosciences (Switzerland)*, *7*(3). https://doi.org/10.3390/geosciences7030070

Chadwick, J. (1932). Possible Existence of a Neutron. *Nature*, *129*(3252), 312. https://doi.org/10.1038/129312a0

Charalampidou, E.-M., Hall, S. A., Stanchits, S., Viggiani, G., & Lewis, H. (2014). Shear-enhanced compaction band identification at the laboratory scale using acoustic and full-field methods. *International Journal of Rock Mechanics and Mining Sciences*, *67*, 240–252. https://doi.org/https://doi.org/10.1016/j.ijrmms.2013.05.006

Charalampidou, E. M., Tudisco, E., Etxegrai, M., Couples, G., Kardjilov, N., Hall, S., & Berlin, H. Z. (2017). *Assesment of Localised Deformaton in Sandstones Via High Speed Neutron Tomography*. *June*, 2–3.

Chen, G.-H., Tokalkanahalli, R., Zhuang, T., Nett, B. E., & Hsieh, J. (2006). Development and evaluation of an exact fan-beam reconstruction algorithm using an equal weighting scheme via locally compensated filtered backprojection (LCFBP). *Medical Physics*, *33*(2), 475–481. https://doi.org/10.1118/1.2165416

Chen, X., Roshan, H., Lv, A., Hu, M., & Regenauer-Lieb, K. (2020). The dynamic evolution of compaction bands in highly porous carbonates: the role of local heterogeneity for nucleation and propagation. *Progress in Earth and Planetary Science*, *7*(1), 28. https://doi.org/10.1186/s40645-020-00344-0

Cilona, A., Baud, P., Tondi, E., Agosta, F., Vinciguerra, S., Rustichelli, A., & Spiers, C. J. (2012). Deformation bands in porous carbonate grainstones: Field and laboratory observations. *Journal of Structural Geology*, *45*, 137–157. https://doi.org/10.1016/j.jsg.2012.04.012

Cilona, A., Faulkner, D. R., Tondi, E., Agosta, F., Mancini, L., Rustichelli, A., Baud, P., & Vinciguerra, S. (2014). The effects of rock heterogeneity on compaction localization in porous carbonates. *Journal of Structural Geology*, *67*(PA), 75–93. https://doi.org/10.1016/j.jsg.2014.07.008

Cnudde, V., & Boone, M. N. (2013). High-resolution X-ray computed tomography in geosciences: A review of the current technology and applications. *Earth-Science Reviews*, *123*, 1–17. https://doi.org/10.1016/j.earscirev.2013.04.003

Corbett, P. W. M., Wang, H., Câmara, R. N., Tavares, A. C., Borghi de Almeida, L. F., Perosi,

F., Machado, A., Jiang, Z., Ma, J., & Bagueira, R. (2017). Using the porosity exponent (m) and pore-scale resistivity modelling to understand pore fabric types in coquinas (Barremian-Aptian) of the Morro do Chaves Formation, NE Brazil. *Marine and Petroleum Geology*, *88*, 628–647. https://doi.org/10.1016/j.marpetgeo.2017.08.032

Cordonnier, B., Pluymakers, A., Tengattini, A., Marti, S., Kaestner, A., Fusseis, F., & Renard, F. (2019). Neutron Imaging of Cadmium Sorption and Transport in Porous Rocks. *Frontiers in Earth Science*, *7*(November), 1–11. https://doi.org/10.3389/feart.2019.00306

Datta, S. S., Ramakrishnan, T. S., & Weitz, D. A. (2014). Mobilization of a trapped non-wetting fluid from a three-dimensional porous medium. *Physics of Fluids*, *26*(2). https://doi.org/10.1063/1.4866641

Debbabi, Y., Jackson, M. D., Hampson, G. J., & Salinas, P. (2017). Capillary Heterogeneity Trapping and Crossflow in Layered Porous Media. *Transport in Porous Media*, *120*(1), 183–206. https://doi.org/10.1007/s11242-017-0915-z

Ersland, G., Fernø, M. A., Graue, A., Baldwin, B. A., & Stevens, J. (2010). Complementary imaging of oil recovery mechanisms in fractured reservoirs. *Chemical Engineering Journal*, *158*(1), 32–38. https://doi.org/10.1016/j.cej.2008.11.049

Etris, E. L., Brumfield, D. S., Ehrlich, R., & Crabtree, S. J. (1988). Relations between pores, throats and permeability: A petrographic/physical analysis of some carbonate grainstones and packstones. *Carbonates and Evaporites*, *3*(1), 17–32. https://doi.org/10.1007/BF03174409

Etxegarai Aldamiz-Etxebarria M (2019). Coupled hydro-mechanics of reservoir rocks studied by quantitative in-situ neutron imaging. PhD thesis. Université Grenoble Alpes.

Ferno, M. a., Ersland, G., Haugen, a., Graue, a., Stevens, J., & Howard, J. J. (2007). Visualizing Fluid Flow With Mri in Oil-Wet Fractured Carbonate Rock. *Sca*, *2002*, 112.

Gao, Y., Qaseminejad Raeini, A., Blunt, M. J., & Bijeljic, B. (2019). Pore occupancy, relative permeability and flow intermittency measurements using X-ray micro-tomography in a complex carbonate. *Advances in Water Resources*, *129*(November 2018), 56–69. https://doi.org/10.1016/j.advwatres.2019.04.007

Gao, Z., & Hu, Q. (2013). Estimating permeability using median pore-throat radius obtained from mercury intrusion porosimetry. *Journal of Geophysics and Engineering*, *10*(2). https://doi.org/10.1088/1742-2132/10/2/025014

Garfi, G., John, C. M., Berg, S., & Krevor, S. (2020). The Sensitivity of Estimates of Multiphase Fluid and Solid Properties of Porous Rocks to Image Processing. *Transport in Porous Media*, *131*(3), 985–1005. https://doi.org/10.1007/s11242-019-01374-z

Ghanbarian, B., Hunt, A. G., Ewing, R. P., & Sahimi, M. (2013). Tortuosity in Porous Media: A Critical Review. *Soil Science Society of America Journal*, *77*(5), 1461–1477. https://doi.org/https://doi.org/10.2136/sssaj2012.0435

Gordon, R., Bender, R., & Herman, G. T. (1970). Algebraic Reconstruction Techniques (ART) for three-dimensional electron microscopy and X-ray photography. *Journal of Theoretical Biology*, *29*(3), 471–481. https://doi.org/https://doi.org/10.1016/0022-5193(70)90109-8

Graafsma, H., & Martin, T. (2008). *DETECTORS FOR SYNCHROTRON TOMOGRAPHY*.

Griffiths, L., Heap, M. J., Xu, T., Chen, C., & Baud, P. (2017). The influence of pore geometry and orientation on the strength and stiffness of porous rock. *Journal of Structural Geology*, *96*. https://doi.org/10.1016/j.jsg.2017.02.006

H., K. F., Dayakar, P., & S., H. D. (2012). Water Distribution Variation in Partially Saturated Granular Materials Using Neutron Imaging. *Journal of Geotechnical and Geoenvironmental Engineering*, *138*(2), 147–154. https://doi.org/10.1061/(ASCE)GT.1943-5606.0000583

Hall, S. A., Hughes, D., & Rowe, S. (2010). Local characterisation of fluid flow in sandstone with localised deformation features through fast neutron imaging. *EPJ Web of Conferences*, *6*(June). https://doi.org/10.1051/epjconf/20100622008

Hall, Stephen A. (2013). Characterization of fluid flow in a shear band in porous rock using neutron radiography. *Geophysical Research Letters*, *40*(11), 2613–2618. https://doi.org/10.1002/grl.50528

Hasan, S., Niasar, V., Karadimitriou, N. K., Godinho, J. R. A., Vo, N. T., An, S., Rabbani, A., & Steeb, H. (2020). Direct characterization of solute transport in unsaturated porous media using fast X-ray synchrotron microtomography. *Proceedings of the National Academy of Sciences of the United States of America*, *117*(38), 23443–23449. https://doi.org/10.1073/pnas.2011716117

Hassanein, R. K. V. (2006). *Correction methods for the quantitative evaluation of thermal neutron tomography*. ETH.

Hassanein, R., Lehmann, E., & Vontobel, P. (2005). Methods of scattering corrections for quantitative neutron radiography. *Nuclear Instruments and Methods in Physics Research Section A: Accelerators, Spectrometers, Detectors and Associated Equipment*, *542*, 353–360. https://doi.org/10.1016/j.nima.2005.01.161

Hebert, V., Garing, C., Luquot, L., Pezard, P., & Gouze, P. (2014). Multi-scale X-ray tomography analysis of carbonate porosity. *Geological Society London Special Publications*, *406*. https://doi.org/10.1144/SP406.12

Hoek, E., & Franklin, J. A. (1968). A simple triaxial cell for field and laboratory testing of rock. *Trans. Instn Min. Metall.*, *77*, A22-26. http://linkinghub.elsevier.com/retrieve/pii/S1365160905000948%5Cnhttp://linkinghub.elsevier.com/retrieve/pii/S1365160904002965%5Cnhttp://www.rocscience.com/hoek/references/H2004e.pdf%5Cnhttp://www.springerlink.com/openurl.asp?genre=article&id=doi:10.1007/

Holtzman, R. (2016). Effects of Pore-Scale Disorder on Fluid Displacement in Partially-Wettable Porous Media. *Scientific Reports*, *6*(October), 1–10. https://doi.org/10.1038/srep36221

Hossain, Z. (2011). *Relative Permeability Prediction from Image Analysis of Thin Sections*. *All Days*. https://doi.org/10.2118/143606-MS

Hounsfield, G. N. (1973). Computerized transverse axial scanning (tomography). 1. Description of system. *The British Journal of Radiology*, *46*(552), 1016–1022. https://doi.org/10.1259/0007-1285-46-552-1016

Iassonov, P., Gebrenegus, T., & Tuller, M. (2009). Segmentation of X-ray computed tomography images of porous materials: A crucial step for characterization and quantitative analysis of pore structures. *Water Resources Research*, *45*(9). https://doi.org/https://doi.org/10.1029/2009WR008087

Jasti, J. K., & Fogler, H. S. (1992). Application of neutron radiography to image flow phenomena in porous media. *AIChE Journal*, *38*(4), 481–488. https://doi.org/https://doi.org/10.1002/aic.690380402

Kang, W., Yang, Q.-Q., & Liang, R.-P. (2009). *The Comparative Research on Image*

Segmentation Algorithms. *2*, 703–707. https://doi.org/10.1109/ETCS.2009.417

Kardjilov, N., de Beer, F., Hassanein, R., Lehmann, E., & Vontobel, P. (2005). Scattering corrections in neutron radiography using point scattered functions. *Nuclear Instruments and Methods in Physics Research Section A: Accelerators, Spectrometers, Detectors and Associated Equipment*, *542*, 336–341. https://doi.org/10.1016/j.nima.2005.01.159

Kardjilov, N., Hilger, A., Manke, I., Woracek, R., & Banhart, J. (2016). CONRAD-2: the new neutron imaging instrument at the Helmholtz-Zentrum Berlin. *Journal of Applied Crystallography*, *49*(1), 195–202. https://doi.org/https://doi.org/10.1107/S1600576715023353

Keehm, Y. (2004). Permeability prediction from thin sections: 3D reconstruction and Lattice-Boltzmann flow simulation. *Geophysical Research Letters*, *31*(4), 3–6. https://doi.org/10.1029/2003GL018761

Ketcham, R. A., & Carlson, W. D. (2001). Acquisition, optimization and interpretation of X-ray computed tomographic imagery: applications to the geosciences. *Computers & Geosciences*, *27*(4), 381–400. https://doi.org/https://doi.org/10.1016/S0098-3004(00)00116-3

Khishvand, M., Alizadeh, A. H., & Piri, M. (2016). In-situ characterization of wettability and pore-scale displacements during two- and three-phase flow in natural porous media. *Advances in Water Resources*, *97*, 279–298. https://doi.org/10.1016/j.advwatres.2016.10.009

Knackstedt, M., Arns, C., Ghous, A., Sakellariou, A., Senden, T., Sheppard, A., Sok, R., Averdunk, H., Pinczewski, V., & Padhy, G. (2006). *ANU-Digital Collections: 3D imaging and flow characterization of the pore space of carbonate core samples*.

Krevor, S. C. M., Pini, R., Li, B., & Benson, S. M. (2011). Capillary heterogeneity trapping of CO2 in a sandstone rock at reservoir conditions. *Geophysical Research Letters*, *38*(15), 1–5. https://doi.org/10.1029/2011GL048239

Lewis, H., Tengattini, A., Couples, G., Tudisco, E., Hall, S., Etxegarai, M., & Edlmann, K. (2017). Neutron radiography and tomography used to characterise water flow through a low permeability carbonate altered by an experimentally induced fracture network. *3rd International Conference on Tomography of Materials and Structures*, *June*.

Liu, Z., Herring, A., Arns, C., Berg, S., & Armstrong, R. T. (2017). Pore-Scale Characterization of Two-Phase Flow Using Integral Geometry. *Transport in Porous Media*, *118*(1), 99–117. https://doi.org/10.1007/s11242-017-0849-5

Looyestijn, W., Cense, A., Hofman, J., Marcelis, F., & Makurat, A. (2009). *Visualisation of Micro Fracture Network in an Oilwet Carbonate*. 1–6.

Mehmani, A., Verma, R., & Prodanović, M. (2020). Pore-scale modeling of carbonates. *Marine and Petroleum Geology*, *114*(November 2019), 104141. https://doi.org/10.1016/j.marpetgeo.2019.104141

Meng, W., Xia, Y., Chen, Y., & Pu, X. (2018). Measuring the mutual diffusion coefficient of heavy water in normal water using a double liquid-core cylindrical lens. *Scientific Reports*, *August*, 1–7. https://doi.org/10.1038/s41598-018-30650-z

Menke, H. P., Reynolds, C. A., Andrew, M. G., Pereira Nunes, J. P., Bijeljic, B., & Blunt, M. J. (2018). 4D multi-scale imaging of reactive flow in carbonates: Assessing the impact of heterogeneity on dissolution regimes using streamlines at multiple length scales. *Chemical Geology*, *481*(September 2017), 27–37. https://doi.org/10.1016/j.chemgeo.2018.01.016

Murison, J., Moosavi, R., Schulz, M., Schillinger, B., & Schröter, M. (2015). Neutron Tomography as a Tool to Study Immiscible Fluids in Porous Media without Chemical Dopants. *Energy and Fuels*, *29*(10), 6271–6276. https://doi.org/10.1021/acs.energyfuels.5b01403

Olivier, P., Cantegrel-Gassiot, L., Laveissière, J., & Guillonneau, N. (2005). Analysis of multiphase flow behavior in vugular carbonates using X-ray CT scanning. *Petrophysics*, *46*(6), 424–433.

Ortenzi, A., & Dichicco, M. C. (2014). 20+ years of pore network characterization on carbonate reservoir thin sections: What did we learn? *Society of Petroleum Engineers - 30th Abu Dhabi International Petroleum Exhibition and Conference, ADIPEC 2014: Challenges and Opportunities for the Next 30 Years*, *3*, 2431–2440. https://doi.org/10.2118/171903-ms

Otsu, N. (1979). A Threshold Selection Method from Gray-Level Histograms. *IEEE Transactions on Systems, Man, and Cybernetics*, *9*(1), 62–66. https://doi.org/10.1109/TSMC.1979.4310076

Pak, T., Butler, I. B., Geiger, S., Dijke, M. I. J. van, & Sorbie, K. S. (2015). Droplet fragmentation: 3D imaging of a previously unidentified pore-scale process during multiphase flow in porous media. *Proceedings of the National Academy of Sciences*, *112*(7), 1947–1952. https://doi.org/10.1073/PNAS.1420202112

Pak, T., Butler, I. B., Geiger, S., van Dijke, M. I. J., Jiang, Z., & Surmas, R. (2016). Multiscale pore-network representation of heterogeneous carbonate rocks. *Water Resources Research*, *52*(7), 5433–5441. https://doi.org/https://doi.org/10.1002/2016WR018719

Pak, T., Butler, I. B., Geiger, S., Van Dijke, M. I. J., & Sorbie, K. S. (2015). Droplet fragmentation: 3D imaging of a previously unidentified pore-scale process during multiphase flow in porous media. *Proceedings of the National Academy of Sciences of the United States of America*, *112*(7), 1947–1952. https://doi.org/10.1073/pnas.1420202112

Purcell, W. R. (1949). Capillary Pressures - Their Measurement Using Mercury and the Calculation of Permeability Therefrom. *Journal of Petroleum Technology*, *1*(02), 39–48. https://doi.org/10.2118/949039-G

Rabbani, A., Assadi, A., Kharrat, R., Dashti, N., & Ayatollahi, S. (2017). Estimation of carbonates permeability using pore network parameters extracted from thin section images and comparison with experimental data. *Journal of Natural Gas Science and Engineering*, *42*, 85–98. https://doi.org/10.1016/j.jngse.2017.02.045

Rath, A., Exner, U., Tschegg, C., Grasemann, B., Laner, R., & Draganits, E. (2011). Diagenetic control of deformation mechanisms in deformation bands in a carbonate grainstone. *AAPG Bulletin*, *95*(8), 1369–1381. https://doi.org/10.1306/01031110118

Renner, J., & Rummel, F. (1996). The effect of experimental and microstructural parameters on the transition from brittle failure to cataclastic flow of carbonate rocks. *Tectonophysics*, *258*(1), 151–169. https://doi.org/https://doi.org/10.1016/0040-1951(95)00192-1

Rezaee, M. R., Jafari, A., & Kazemzadeh, E. (2006). Relationships between permeability, porosity and pore throat size in carbonate rocks using regression analysis and neural networks. *Journal of Geophysics and Engineering*, *3*(4), 370–376. https://doi.org/10.1088/1742-2132/3/4/008

Rustichelli, A., Tondi, E., Agosta, F., Cilona, A., & Giorgioni, M. (2012). Development and distribution of bed-parallel compaction bands and pressure solution seams in carbonates

(Bolognano Formation, Majella Mountain, Italy). *Journal of Structural Geology*, *37*, 181–199. https://doi.org/https://doi.org/10.1016/j.jsg.2012.01.007

Schlüter, S, Berg, S., Rücker, M., Armstrong, R. T., Vogel, H.-J., Hilfer, R., & Wildenschild, D. (2016). Pore-scale displacement mechanisms as a source of hysteresis for two-phase flow in porous media. *Water Resources Research*, *52*(3), 2194–2205. https://doi.org/https://doi.org/10.1002/2015WR018254

Schlüter, Steffen, Sheppard, A., Brown, K., & Wildenschild, D. (2014). Image processing of multiphase images obtained via X-ray microtomography: A review. *Water Resources Research*, *50*(4), 3615–3639. https://doi.org/https://doi.org/10.1002/2014WR015256

Scriven, L. E. (1994). Porous media: Geometry and transport by Pierre M. Adler, butterworth-heinemann, stoneham, ma, 1992, 544 pp. *AIChE Journal*, *40*(2), 380–381. https://doi.org/https://doi.org/10.1002/aic.690400220

Shepp, L. A., & Vardi, Y. (1982). Maximum Likelihood Reconstruction for Emission Tomography. *IEEE Transactions on Medical Imaging*, *1*(2), 113–122. https://doi.org/10.1109/TMI.1982.4307558

Shin, H. S., Kim, K. Y., & Pande, G. N. (2013). Porosity and Pore-Size Distribution of Geomaterials from X-ray CT Scans. *Springer Series in Geomechanics and Geoengineering*, *3*, 177–186. https://doi.org/10.1007/978-3-642-32492-5_21

Silin, D., & Patzek, T. (2006). Pore space morphology analysis using maximal inscribed spheres. *Physica A: Statistical Mechanics and Its Applications*, *371*(2), 336–360. https://doi.org/https://doi.org/10.1016/j.physa.2006.04.048

Starr, R. C., Gillham, R. W., & Sudicky, E. A. (1985). Experimental Investigation of Solute Transport in Stratified Porous Media: 2. The Reactive Case. *Water Resources Research*, *21*(7), 1043–1050. https://doi.org/https://doi.org/10.1029/WR021i007p01043

Swami, D., Sharma, P. K., & Ojha, C. S. P. (2013). Experimental investigation of solute transport in stratified porous media. *ISH Journal of Hydraulic Engineering*, *19*(3), 145–153. https://doi.org/10.1080/09715010.2013.793930

Tahmasebi, P., & Sahimi, M. (2012). Reconstruction of three-dimensional porous media using a single thin section. *Phys. Rev. E*, *85*(6), 66709. https://doi.org/10.1103/PhysRevE.85.066709

Tang, Y., & Aral, M. M. (1992). Contaminant transport in layered porous media: 1. General solution. *Water Resources Research*, *28*(5), 1389–1397. https://doi.org/https://doi.org/10.1029/92WR00292

Tengattini, A., Lenoir, N., Andò, E., Giroud, B., Atkins, D., Beaucour, J., & Viggiani, G. (2020). NeXT-Grenoble, the Neutron and X-ray tomograph in Grenoble. *Nuclear Instruments and Methods in Physics Research Section A: Accelerators, Spectrometers, Detectors and Associated Equipment*, *968*, 163939. https://doi.org/https://doi.org/10.1016/j.nima.2020.163939

Tengattini, A., Lenoir, N., Andò, E., & Viggiani, G. (2021). Neutron imaging for geomechanics: A review. *Geomechanics for Energy and the Environment*, *27*, 100206. https://doi.org/https://doi.org/10.1016/j.gete.2020.100206

The Schlumberger Oilfield Glossary | Oilfield Glossary. (n.d.). https://glossary.oilfield.slb.com/

ThermoFisher Scientific. (2018). Avizo 9 user´s guide. *Thermo Scientific Avizo Software 9 User's Guide*, 96–99.

Tondi, E., Rustichelli, A., Cilona, A., Balsamo, F., Storti, F., Napoli, G., Agosta, F., Renda, P., & Giorgioni, M. (2015). Hydraulic properties of fault zones in porous carbonates, examples from central and southern Italy. *Italian Journal of Geosciences*, *134*, 1–36. https://doi.org/10.3301/IJG.2015.08

Tudisco, E., Etxegarai, M., Hall, S. A., Charalampidou, E.-M., Couples, G. D., Lewis, H., Tengattini, A., & Kardjilov, N. (2019a). Fast 4-D Imaging of Fluid Flow in Rock by High-Speed Neutron Tomography. *Journal of Geophysical Research: Solid Earth*, *124*(4), 3557–3569. https://doi.org/https://doi.org/10.1029/2018JB016522

Tudisco, E., Etxegarai, M., Hall, S. A., Charalampidou, E. M., Couples, G. D., Lewis, H., Tengattini, A., & Kardjilov, N. (2019b). Fast 4-D Imaging of Fluid Flow in Rock by High-Speed Neutron Tomography. *Journal of Geophysical Research: Solid Earth*, *124*(4), 3557–3569. https://doi.org/10.1029/2018JB016522

Tudisco, E., Hall, S. A., Charalampidou, E. M., Kardjilov, N., Hilger, A., & Sone, H. (2015). Full-field Measurements of Strain Localisation in Sandstone by Neutron Tomography and 3D-Volumetric Digital Image Correlation. *Physics Procedia*, *69*, 509–515. https://doi.org/https://doi.org/10.1016/j.phpro.2015.07.072

Vajdova, V., Baud, P., & Wong, T. (2004). Compaction, dilatancy, and failure in porous carbonate rocks. *Journal of Geophysical Research: Solid Earth*, *109*(B5). https://doi.org/https://doi.org/10.1029/2003JB002508

van Aarle, W., Palenstijn, W. J., De Beenhouwer, J., Altantzis, T., Bals, S., Batenburg, K. J., & Sijbers, J. (2015). The ASTRA Toolbox: A platform for advanced algorithm development in electron tomography. *Ultramicroscopy*, *157*, 35–47. https://doi.org/https://doi.org/10.1016/j.ultramic.2015.05.002

Van Offenwert, S., Cnudde, V., & Bultreys, T. (2019). Pore-Scale Visualization and Quantification of Transient Solute Transport Using Fast Microcomputed Tomography. *Water Resources Research*, *55*(11), 9279–9291. https://doi.org/10.1029/2019WR025880

Wardlaw, N. C., McKellar, M., & Yu, L. (1988). Pore and throat size distributions determined by mercury porosimetry and by direct observation. *Carbonates and Evaporites*, *3*(1), 1–16. https://doi.org/10.1007/BF03174408

Wei, Y., Wang, G., & Hsieh, J. (2005). Relation between the filtered backprojection algorithm and the backprojection algorithm in CT. *IEEE Signal Processing Letters*, *12*(9), 633–636. https://doi.org/10.1109/LSP.2005.851615

Williams, S., Hilger, A., Kardjilov, N., Manke, I., Strobl, M., Douissard, P., Martin, T., Riesemeier, H., & Banhart, J. (2012). Detection system for microimaging with neutrons. *Journal of Instrumentation*, *7*, P02014. https://doi.org/10.1088/1748-0221/7/02/P02014

Wu, Y., Tahmasebi, P., Lin, C., Zahid, M. A., Dong, C., Golab, A. N., & Ren, L. (2019). A comprehensive study on geometric, topological and fractal characterizations of pore systems in low-permeability reservoirs based on SEM, MICP, NMR, and X-ray CT experiments. *Marine and Petroleum Geology*, *103*, 12–28. https://doi.org/https://doi.org/10.1016/j.marpetgeo.2019.02.003

Yang, K., Li, M., Ling, N., May, E., Connolly, P., Esteban, L., Clennell, M., Mahmoud, M., El Husseiny, A., Adebayo, A., Elsayed, M., & Johns, M. (2019). Quantitative Tortuosity Measurements of Carbonate Rocks Using Pulsed Field Gradient NMR. *Transport in Porous Media*, *130*. https://doi.org/10.1007/s11242-019-01341-8

Yao, J., Hu, R., Wang, C., & Yang, Y. (2015). Multiscale pore structure analysis in carbonate rocks. *International Journal for Multiscale Computational Engineering*, *13*(1), 1–9.

https://doi.org/10.1615/IntJMultCompEng.2014010500

Yehya, M., Andò, E., Dufour, F., & Tengattini, A. (2018). Fluid-flow measurements in low permeability media with high pressure gradients using neutron imaging: Application to concrete. *Nuclear Instruments and Methods in Physics Research, Section A: Accelerators, Spectrometers, Detectors and Associated Equipment*, *890*(December 2017), 35–42. https://doi.org/10.1016/j.nima.2018.02.039

Yokoyama, Y., & Lake, L. W. (1981). *The Effects of Capillary Pressure on Immiscible Displacements in Stratified Porous Media* . https://doi.org/10.2118/10109-MS

Zack, G. W., Rogers, W. E., & Latt, S. A. (1977). Automatic measurement of sister chromatid exchange frequency. *The Journal of Histochemistry and Cytochemistry : Official Journal of the Histochemistry Society*, *25*(7), 741–753. https://doi.org/10.1177/25.7.70454

Zambrano, M., Hameed, F., Anders, K., Mancini, L., & Tondi, E. (2019). Implementation of Dynamic Neutron Radiography and Integrated X-Ray and Neutron Tomography in Porous Carbonate Reservoir Rocks. *Frontiers in Earth Science*, *7*(December). https://doi.org/10.3389/feart.2019.00329

Zambrano, M., Tondi, E., Mancini, L., Arzilli, F., Lanzafame, G., Materazzi, M., & Torrieri, S. (2017). 3D Pore-network quantitative analysis in deformed carbonate grainstones. *Marine and Petroleum Geology*, *82*, 251–264. https://doi.org/10.1016/j.marpetgeo.2017.02.001

Zambrano, M., Tondi, E., Mancini, L., Lanzafame, G., Trias, F. X., Arzilli, F., Materazzi, M., & Torrieri, S. (2018). Fluid flow simulation and permeability computation in deformed porous carbonate grainstones. *Advances in Water Resources*, *115*, 95–111. https://doi.org/10.1016/j.advwatres.2018.02.016

Zhang, D., Zhang, R., Chen, S., & Soll, W. E. (2000). Pore scale study of flow in porous media: Scale dependency, REV, and statistical REV. *Geophysical Research Letters*, *27*(8), 1195–1198. https://doi.org/https://doi.org/10.1029/1999GL011101

Zhao, B., MacMinn, C. W., Primkulov, B. K., Chen, Y., Valocchi, A. J., Zhao, J., Kang, Q., Bruning, K., McClure, J. E., Miller, C. T., Fakhari, A., Bolster, D., Hiller, T., Brinkmann, M., Cueto-Felgueroso, L., Cogswell, D. A., Verma, R., Prodanović, M., Maes, J., … Juanes, R. (2019). Comprehensive comparison of pore-scale models for multiphase flow in porous media. *Proceedings of the National Academy of Sciences of the United States of America*, *116*(28), 13799–13806. https://doi.org/10.1073/pnas.1901619116

Zhu, W., Baud, P., & Wong, T. (2010). Micromechanics of cataclastic pore collapse in limestone. *Journal of Geophysical Research: Solid Earth*, *115*(B4). https://doi.org/https://doi.org/10.1029/2009JB006610

Zihms, S., Lewis, H., Charalampidou, E.-M., Couples, G., Hall, S., Tudisco, E., Andò, E., Tengattini, A., & Atkins, D. (2017). *Network Connectivity in low-permeability Carbonates*. https://doi.org/10.6084/m9.figshare.4872893.v1

Zitha, P. L. J., Nguyen, Q. P., & Currie, P. K. (2003). Effect of Flow Velocity and Rock Layering on Foam Flow: An X-ray Computed Tomography Study. *SPE - Asia Pacific Oil and Gas Conference*, 498–511. https://doi.org/10.2523/80530-ms